Numerical simulation of the mechanical behavior of the ITER cable-in-conduit conductoras,

Hugues Bajas

ÉCOLE CENTRALE DES ARTS ET MANUFACTURES « ÉCOLE CENTRALE PARIS »

THÈSE

présentée par

BAJAS Hugues

pour l'obtention du

GRADE DE DOCTEUR

Spécialité : Mécanique

Laboratoire d'accueil : Mécanique des Sols Structures et Materiaux (MSSMat)

Numerical simulation of the mechanical behavior of the ITER cable-in-conduit conductors

Acknowledgments

This thesis has been achieved in the laboratory of “Mécanique des Sols, Structure et Materiaux” of the École Centrale Paris and co-funded by CEA/DRFC and ITER Organization.

The work was initiated and partly directed by Professor Claude Prioul, who until the day of his retirement showed kind concern and consideration regarding the understanding of cable mechanics. Professor Hachmi Ben Dhia subsequently took over and gave all the support and attention that was needed. For their unselfish and unfailing support I wish to express all my respect and gratitude.

However, this work would not have been possible without the major contributions of Damien Durville from LMSSMat. I owe my deepest gratitude for his help in all what concerned the Multifil model. I am also heartily thankful to my supervisors, Arnaud Devred and Daniel Ciazynski, whose encouragement, supervision and support from the preliminary to the concluding level, enabled me to fulfill most of the ITER requirements. I wish to deeply thank Professor David Larbalestier and Patrice Cartraud to have accepted to review this thesis.

Lastly, I offer my regards and blessings to all of those who supported me in any respect during the completion of this thesis. I wish to thank, Arend Nijhuis, Véronique Aubin, Alexandre Torre and Matthew Jewell, for the insights they shared during various meetings. I would also like to thank my colleagues and the staff at the LMSSMat for the use of facilities and more particularly Sylviane Bourgeois and Sokona Konate for their help in setting up the experiments presented in this thesis.

Last but not the least, I wish to express my love and gratitude to my family, my friends and my dearest fellow Camille, for giving me the strength to continue, for their understanding during hard times, I thank you so much.

Abstract

The ITER Cable-In-Conduit Conductors (CICC) are composed of an assembly of pure copper wires and composite superconducting strands (with embedded brittle Nb_3Sn microfilaments) cabled together and inserted in a stainless steel jacket. If the current carrying capacities of individual ITER strand are clearly identified by a dependence of the critical current on the applied strain and by a statistical quantification of possible microfilaments breakage, the characterization of cable-in-conduit is not yet fully achieved.

In order to assess the local strains at the scale of the strands responsible for the degradations of the electrical performances, a global modeling of the mechanical behavior of CICCs from their initial forming to the application of magnetic loading is proposed by means of finite element simulation. The simulation code, Multifil, dedicated to the modeling of entangled media is adapted to handle with the specific loadings of CICCs operating conditions.

In the proposed approach, each wire or strand of the studied conductor sample is modelled using a kinematically enriched beam model and contact-friction interactions between wires are detected and accounted for. During this thesis, particular pseudo-periodic conditions have been developed to prescribe appropriate boundary conditions at the ends of the cable. Contact conditions with moving rigid tools are considered to model the initial forming of the conductor and the presence of the jacket during the application of loadings. The global problem is solved using an implicit solver.

The simulation is used first to determine the initial geometry of the conductor. A theoretical configuration where all wires are described by helicoidal functions corresponding to the different cabling stages is deformed and compacted by rigid tools into a cylindrical or petal-shape form to get the initial configuration. An elastoplastic behavior is considered in the axial direction of strands. A transverse orthotropic elastic model is used in the transverse directions to attempt to reproduce the plastic deformation due to the pinching of the strand. The material properties are identified upon experimental data from the tests of single Nb_3Sn strands and OFHC copper wires. The validation of the cable model in both the axial and the transverse directions will be presented with comparison of the loading curves to experimental measurements.

The different stages experienced by CICCs during their service life, namely the annealing induced by the heat treatment, the axial compression generated during cool-down by the differential of thermal expansion with the jacket and the application of magnetic Lorentz forces are successively simulated on the ITER CS and TF conductors (considering one petal). Analysis of the local axial strains demonstrates a high non-uniformity, with combination of bending and axial compression at the local scale. At last, the outputs of the model are feeding two electromagnetic codes in order to retrieve the electrical properties of the conductors.

Key words: ITER, cable-in-conduit conductor, Multifil, finite element, simulation, mechanical behavior, contact/friction interaction, strain, bending

Chapter I: Strain effect assessment in Cable-in-Conduit Conductors

1 Introduction to the ITER project and the superconducting cables for magnets

1.1 The International Thermonuclear Experimental Reactor

The International Thermonuclear Experimental Reactor ITER is the future experimental fusion reactor that is currently built in Cadarache, south of France. The construction has started in 2007 after the international agreement officially signed on 21 November 2006 by the involved nations (Europe, Japan, China, Russia, USA, the republic of Korea and India). ITER, "*the way*" in Latin, is the essential next step in the development of fusion and will be the world's biggest fusion energy research project. ITER main objective is to demonstrate the scientific and technological feasibility of steady-state fusion power production.

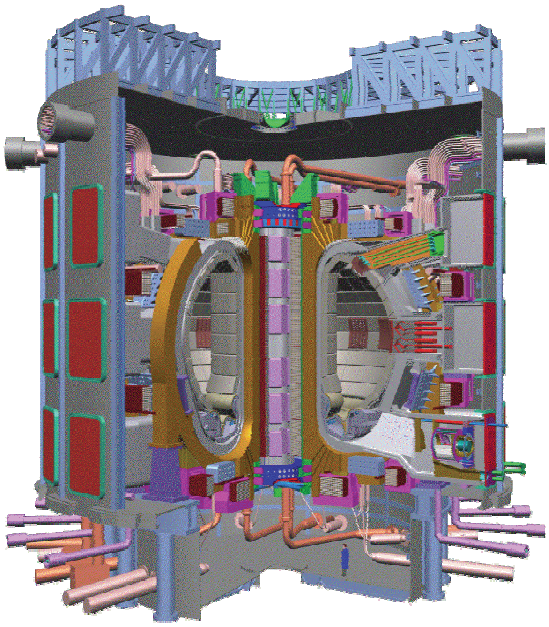

Fig. 1.1. The International Thermonuclear Experimental Reactor.

The main challenge in fusion is to be able to create a medium of sufficient energy to initiate the fusion reaction between deuterium and tritium. The needed energy is around 10 keV which can be attained in plasma with high ionic temperature of about 10^8 K during several hundred seconds. The ITER reactor will create and maintain the fusion plasma by the magnetic confinement technique. The magnetic confinement uses the so-called tokamak machines. Tokamaks are specific devices able to create and maintain high temperature plasma enclosed inside a *magnetic bottle*. The plasma is trapped or *confined* inside a torus shape magnetic field. The enclosure of the field asks for the field lines to run helicoidally around the torus centre. This magnetic shape is achieved by the superposition of a vertical and a horizontal magnetic field. Tokamaks make use of toroidal coils to generate horizontal field lines and a transformer coil, the central solenoid, to induce pulse current in the plasma (acceleration of the charged particles) [Libeyre 2009][Mitchell 2009]. The current flowing in

the plasma creates the vertical field lines. At last, the poloidal coils help fixing the vertical position of the plasma inside the container, the vacuum vessel. The current in the plasma should be 15MA to reach the fusion ignition point.

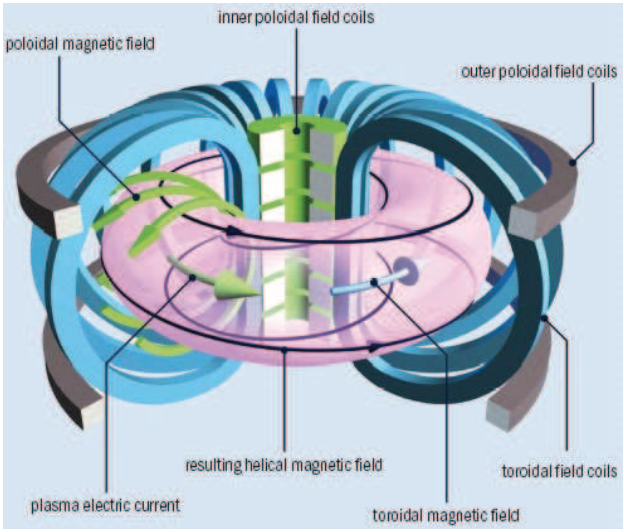

Fig.1.2. Magnetic confinement technique for plasma fusion.

http://www.euronuclear.org/info/encyclopedia/t/tokamak.htm

1.1.1 ITER coils

For the fusion plasma confinement, ITER needs the creation of a stable 5.3 T toroidal magnetic field. The ITER toroidal magnetic field (840m^3 and 6.2m major radius) is created by a complex of magnets composed of 48 superconducting coils:

- 18 Toroidal Field (TF) coils
- 1 Central Solenoid (CS) with 6 pancakes around modules
- 6 Poloidal Field (PF) coils
- 9 pairs of Correction Coils (CC)

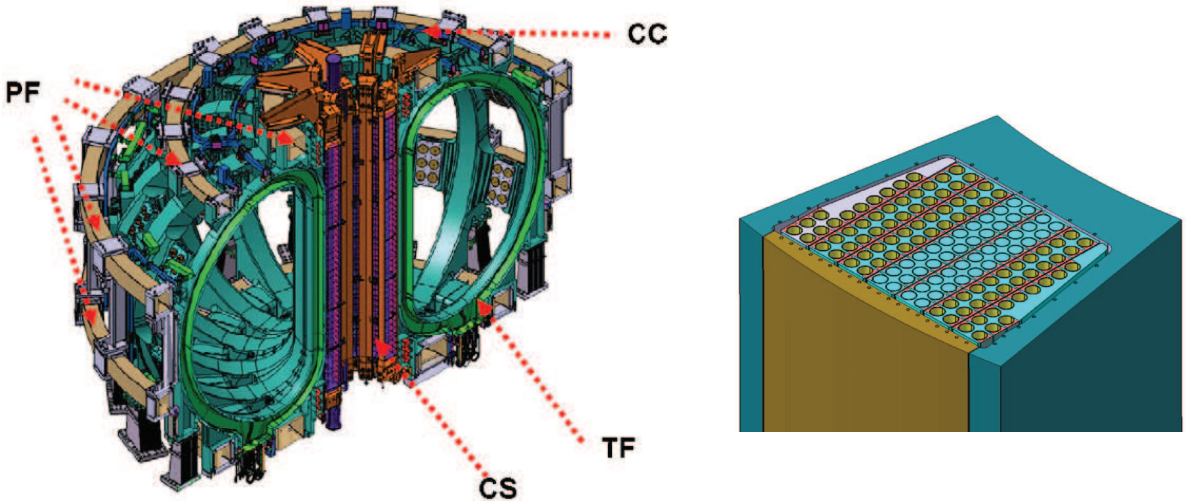

a) b)

Fig. 1.3. a) The four kinds of magnets of the ITER magnetic system. b) The TF coil equatorial cross-section with the array of round conductors (11x13) [Mitchell 2009].

Inside the coils, arrays of round conductors (11x13) are carrying their current in parallel creating the required magnetic field. The operating currents are 40–45 kA for the conductors of the CS, 68 kA for the TF coils, 45–55 kA for the PF coils, and 16kA for the CC coils. In order to reach these high currents, superconducting materials are used for the conductor of the coils. The Niobium-Titanium, NbTi superconductor is used for the poloidal and correcting coils whereas the niobium-tin, Nb_3Sn is used for the toroidal and coils and the central solenoid. The choice of Nb_3Sn superconductor is mandatory to maintain the superconducting state in high magnetic field that can reach 14T where the critical current density of NbTi material is not sufficient. The superconducting properties of the material only appear at cryogenics temperature 15K. But the external magnetic field asks to decrease the temperature down to 4.5K to maintain the superconducting state [Wilson 1986], [Tixador 1995]. The conductors are cooled down to cryogenic temperature by the circulation of supercritical helium at the vicinity of the conductors.

1.1.2 Cable-in-conduit conductors

To face up large temperature and field variations, the ITER conductor relies on the Cable-In-Conduit Conductor technology [Dresner 1995]. The conductors are composed of thousand of superconducting wires of a diameter of 0.8 mm cabled together around a central spiral and inserted inside a metallic jacket. For stability concern, the cable can also include some pure copper wire. The conductor is cooled down by superfluid Helium that flows through the interstices in-between the strands and through the central channel. *CICCs* offer excellent stability in regard with temperature and field variations and appear to be the only technical way to design conductors fulfilling ITER qualifications [Duchateau 2002]. The plasma can show instability that would eventually lead to its termination with abrupt temperature drops. The energy that was stored in the plasma suddenly dumps into the rest of the tokamak (vacumm vessel and coils). The energy deposits on the conductors in the form of temperature increase should be actively removed not to lose the superconducting state. The acceptable temperature for the cool down of the superconductor is defined by the ITER specification and should not exceed 5.7K [Mitchell 2001]. The heat exchange area (or wet surface) between strands and helium flow is large enough (typically N*□*d*l ~3m per section) to ensure the required heat exchange rate.

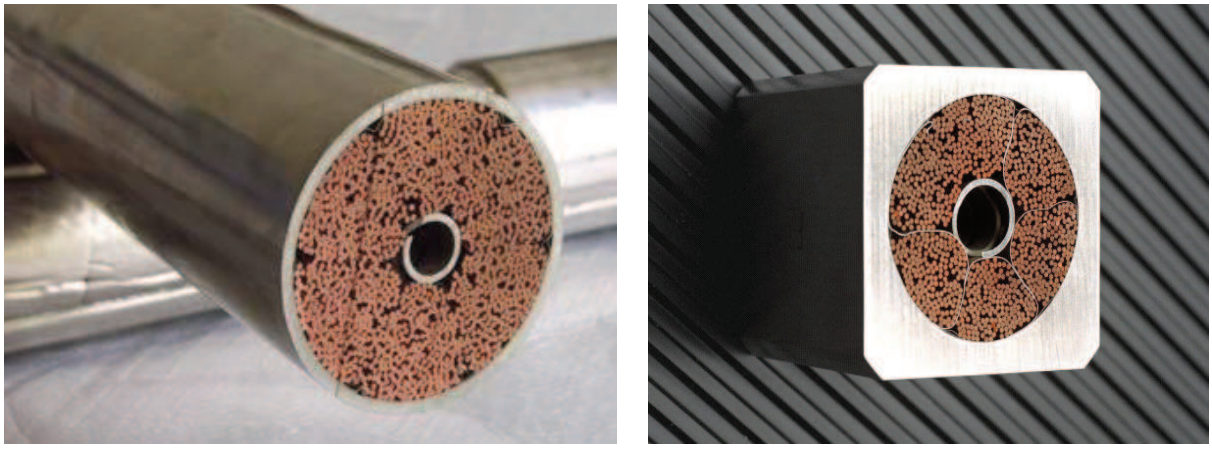

Fig. 1.4. ITER TF and CS cable-in-conduit conductors. Thousand of strands are cable together and inserted in a Stainless Steel conduit. Six petals surround the central spiral. (Courtesy of A. Devred).

1.1.3 Composite strands

The ITER superconducting strands are composite structure made of twisted Nb_3Sn micro filaments bundles embedded in a metallic matrix surrounded by a tantalum anti-diffusion barrier 4µm thick and by an outer copper shell that is 140µm thick [Lee 2000 - 01]. The decomposition of the superconducting materials into micro-filaments embedded in stabilizing high conductivity (high Residual Resistivity Ratio) matrix along and their twisting are mandatory for the stability of the superconducting properties [Ekin 1978][Ciazynski 1985]. Two different manufacturing processes are used for the production of ITER Nb_3Sn strands: the Bronze route (Br) and the Internal Tin (IT) processes. In Fig. 1.5 a) and b), examples of the two kind of strands used for ITER are presented, from [Jewell 2010]. The principal difference lies in the organization of Nb_3Sn micro-filaments and in their size that may vary from 4µm for the Br to few tens of µm for IT. The bronze route and internal tin processes differ in the location of the tin source for the creation of the Nb_3Sn superconducting material. Regarding the bronze route, the tin source is the bronze (α–CuSn) matrix in which the hexagonal bundles of Nb filaments are embedded whereas for the internal tin, pure tin cores are surrounded by filaments arranged in crown of typically four rows [Lee 2003-05]. Originally, the strands are delivered 'un-reacted', the niobium and the tin are not alloyed and physically separated. In order to form the Nb_3Sn alloy a heat treatment up to ~650°C for few hundred hours is performed. The heat treatment aims at diffusing the tin into the niobium across the distance of the filament radius in order to form the Nb_3Sn superconducting material [Lee 2005 a b], [Fisher 2003], [Naus 2002]. In the mean time, the tantalum diffusion barrier prevents the tin to alloy with the pure copper shell whereas the chromium plate prevents strand-to-strand sintering during the heat treatment reaction [Hibbs 1995]. The strands are coated by a 2µm chromium plate in order to increase the inter-strands contact resistance [Nijhuis 1999]. The ternary Nb_3Sn strands also include Ti-stabilizing filaments so as to strengthen the Nb_3Sn filaments [Cheggour 2010]. During the heat treatment, the temperature rate of change should be accurately controlled so as to obtain the proper stoichiometry of tin in the Nb_3Sn filaments [Kasaba 2001], [Markiewicz 2002], [Godeke 2005], [Jewell 2005-08], [Chaowu 2009]. Micro-scale analysis of ITER strands is of high concern for qualifications. State-of-the-art microscopic observation techniques are carried on at the Applied Superconductivity Center under the guidance of David Larbalestier and Peter Lee The Scanning Electron Microscopy (SEM) method is used to measure the dimensions of the different parts of the composite and to analyze the chemical compositions of the different material such as the tin concentration in the Nb_3Sn or the Ti alloying (ternary Cu-Nb-Sn system) for instance. The uniformity of the filaments and the material composition can be accurately quantified [Lee 2003 - 2008].

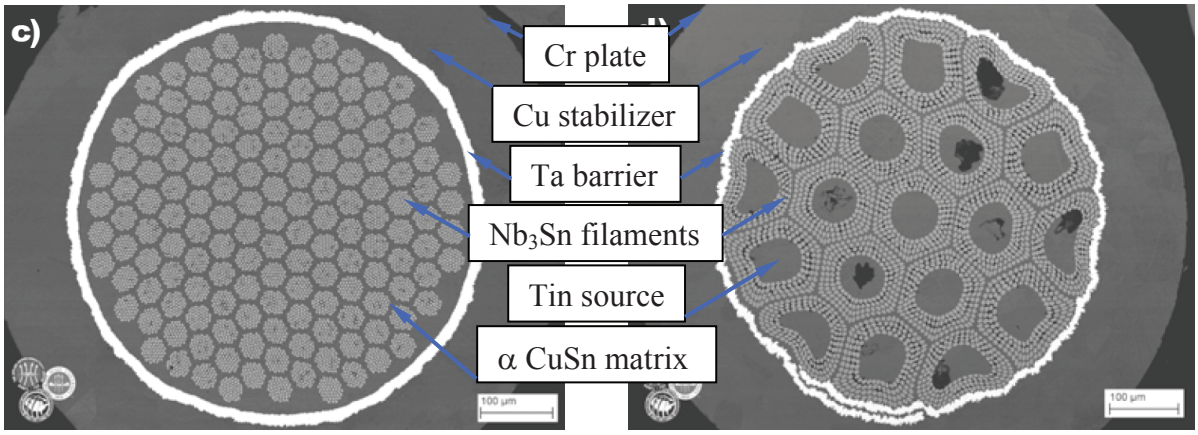

a) b)

Fig. 1.5. SEM views of the composite superconducting strands for ITER. a) EAS Br and b) OST IT strand [Jewell 2008].

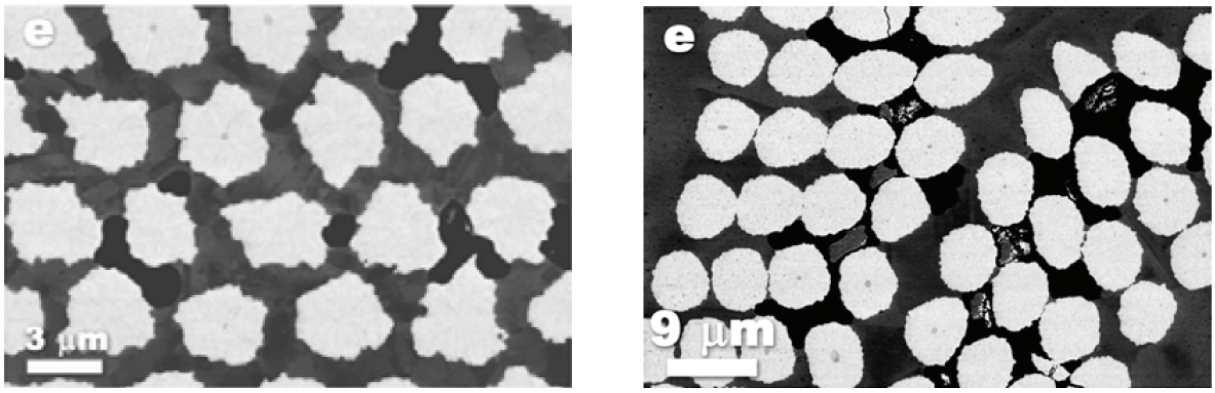

a) b)

Fig. 1.6. Detailed SEM views of the Nb_3Sn filaments with indications on the sizes. a) EAS and b) OST strands [Jewell 2008].

1.1.4 The mechanical loading applied to the strands in cable-in-conductors

Due to the typical operating conditions of *CICCs*, the cable inside the jacket is submitted to three different loadings from three different origins:

- First, during the cool down from the heat treatment temperature to the cryogenic temperature, the mismatch between the coefficient of thermal expansion of the cable and the jacket causes an axial compression of the cable. The amplitude of the compression may reach from -0.3 to -0.7% depending on the jacket thickness and material, see for instance [Martovetski 2005].
- Second, the combination of high current and high magnetic field creates a Lorentz force of around 1kN/m that is acting orthogonally to the strands [Duchateau 2004].
- Third, the combination of the background magnetic field and the transport current produce a loading that tends to spread the coils in its outward direction (radially). Under operating conditions, this bursting effect, typical of large scale coils, stresses the mechanical part of the magnets that in turn put the cable-in-conduit under tension. This generated the so-called tensile "hoop strain" assessed around +0.15% [Zanino 2005].

During their service life, the ITER conductors should undergo several thousand electromagnetic cycles and hundred warm up cool down. These loadings applied to cable create some local strains at the scale of the strands that deform the embedded microfilaments in return [Mitchell 2003]. For several decades, experiments have shown that the potential of the Nb_3Sn strands is not fully utilised in *CICC* due to high strains that develop in the strands of loaded cable. Occurrence of strain appears to be an intrinsic limitation of cable-in-conduit technology. For the estimation of the structural, the thermal and the electromagnetic effects on the cable-in-conduit conductors, one may refer to [Salpietro *et Al 1999*], [Kato *et Al* 2001], [Zanino *et Al* 2003], [Martovetsky 2004], [Mitchell 2006]. In the next paragraph, it is shown that the superconducting properties of the Nb_3Sn material are highly sensitive to the deformation.

1.2 Dependence of the conductivity properties on the strains for strands and conductors

1.2.1 The Nb_3Sn strands characterization

a. Nb_3Sn superconducting properties

- **The critical current**

The main parameter regarding the superconducting properties of the strand is the critical current density J_c [A/mm²] that is defined as the maximum possible current I_c [A] that can flow through the superconducting material $S_{non\ Cu}$ [mm²] without transition to the resistive state [Wilson 1986]:

$$J_c = I_c / S_{non\ Cu} \qquad \textbf{eqn. 1.1}$$

If the current density exceeds the critical value the material no longer stands in its superconducting state. The current then leaves the filaments that have become resistive toward the copper shell stabilizer that exhibits lower resistivity. As long as the superconducting state is not recovered, some heat is generated in the material. If the current density further increases a thermal run-way occurs indicating the *quench* of the conductor. The transition between superconducting and resistive state is observed through the development of an electric field across the conductor that can be detected by voltage drop measurement [Ekin 1978], [Ciazynski 1985]. The transition is classically investigated by probing the strand with voltage taps placed at different locations along the strands. The measurement of the critical current, the I_c test, consists to gradually ramp up the current at constant temperature and to measure the voltage drop. In the superconducting state, there is no resistance and no electric field develops: the measured voltage is null. As the current increases to certain extend a voltage starts to be measured preceding a sudden voltage run away typical of the loss of superconducting state. Since the transition to the resistive state can be smooth, a criterion on the detected electric field should be set to define the critical current. The common value in the literature is 10µV/m which is also used in ITER requirements. For an electric field criterion E_c= 10µV/m, the measured critical current I_c goes up to several hundred Amperes at the ITER operating conditions (4.2 K and 12 T), see for instance [Ilyin 2007].

- **The *n-index***

An important point concerns the gradual transition to the resistive state of Nb_3Sn-based strands. The evolution of the electric field with the transport current I during the transition to the resistive state can be expressed using the n-power law of the current I divided by the critical current I_c [Wilson 1986]:

$$E = E_c \left[\frac{I}{I_c} \right]^n \qquad \textbf{eqn. 1.2}$$

The exponent n is basically retrieved from the slope of the double logarithm scale of the relation. It basically reflects the sharpness of the transition with lower *n-index* corresponding to broader resistive transition. The *n-index* of single strand is usually measured at 4.2K and

12T and is typically 20-30 for internal tin and 30-50 for bronze route [Bruzzone 2004]. Various authors suggest that the *n-index* mostly depends on the critical current I_c with increasing value for higher current and propose the following formulation, e.g. [Taylor 2005 c]:

$$n = 1 + 4 \cdot \left[I_c(B,T,\varepsilon) \right]^{0.41} \qquad \textbf{eqn. 1.3}$$

As the different laboratories and various papers specify, the *n-index* of single strand can be considered as a quality factor for the performances as low values tend to indicate non-uniform current distribution, non-uniform material properties or broken filaments, [Taylor 2002], [Bruzzone 2003], [Nijhuis 2005], [Godeke 2006].

b. The strain dependence of the properties

- **Reversible losses due to strains**

Since the 1980's and the work of Jack Ekin, it is well established that the current carrying capacity of Nb_3Sn depends on the external magnetic field B, the temperature T and the strain ε sustained by the filament [Ekin 1980-2010]. For the Nb_3Sn strand, it is possible to define a four-dimensional surface that states the performance boundaries between the resistive and the superconducting state:

$$J_c = f(B,T,\varepsilon) \qquad \textbf{eqn. 1.4}$$

For fusion application, the field may typically vary from 7 to 13 T, the temperature from 4.2 K to 15 K and the strain from -1.0 % to +0.3 %. Within these ranges, the critical current density is of the order of hundreds A/mm². As an example, the evolution of the critical current I_c as function of the temperature T(K), the field B(T) and the strain ε(%) is presented in Fig. 1.7, from [Ilyin 2007 a]. From these curves, it can be stated that the critical current of OST Nb_3Sn strand at T = 4.2 K, B=11 T and ε= 0% is I_c=300 A. For the same field and temperature but a strain of -0.6%, the critical current drops in a reversible way by 50% down to 150 A. At these external conditions, no current superior to 150 A can flow through the superconducting filaments without transition to the resistive state. An axial strain greater than 0.2 % causes irreversible degradations of the critical current. At such tensile strain, the brittle Nb_3Sn filaments are expected to gradually be damaged through the formation of micro-cracks as exposed in the next paragraphs.

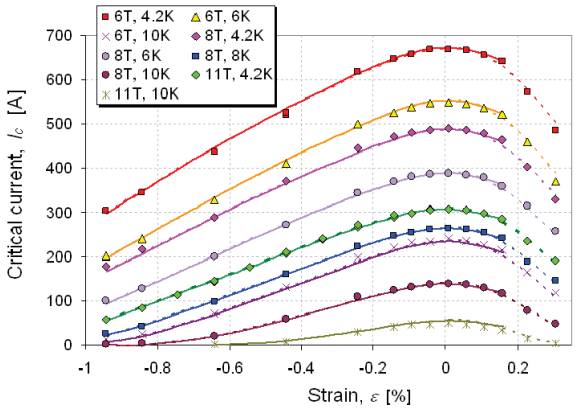

Fig. 1.7. Characterization of the dependence of the critical current I_c of Nb_3Sn strand on the external magnetic field, temperature and axial strain. Strand from OST [Ilyin 2007 a].

- **Irreversible losses due to the micro-cracks of the Nb_3Sn filaments**

A major work on the microfilament fracture analysis of ITER strands has been done by M.C. Jewell at the Applied Superconductivity Center and latter by Y. Miyoshi at the University of Twente [Jewell 2003], [Jewell 2008], [Miyoshi 2009]. Observing the presence of cracks at the nano-scale requires advanced polishing techniques to prepare the surface that will later be probed by Scanning Electron Microscopic method. In Fig. 1.8, the SEM views of polished and etched longitudinal cross-section are shown for bronze route EAS and internal tin OST strands after I_c test for a maximum axial tensile strain greater than 1 % ($I_c \sim 0.1\ I_{c\ max}$). The pictures illustrate the Nb_3Sn filament breakage due to applied strain. Jewell and Miyoshi emphasize the different fracture mechanisms that take place between the two strand architectures. The internal tin strands with twice larger filament diameter than bronze route (6.3µm for OST and 3.5µm for EAS) and smaller filament spacing (1.4µm for OST and 1µm for EAS) exhibit collective cracking that even crosses the tin core region. Unlike IT, the bronze route presents dispersed cracks with wider spatial distribution.

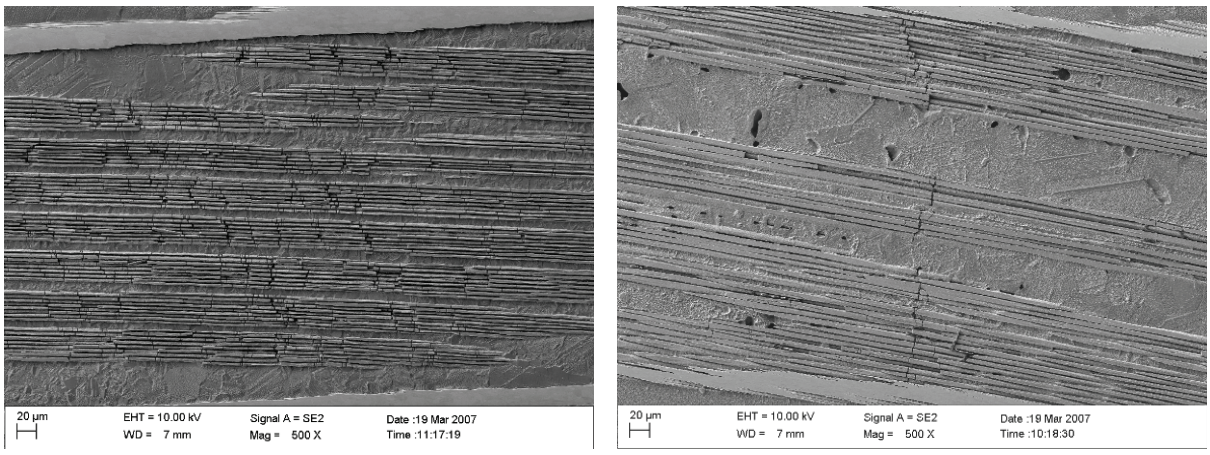

a) b)

Fig. 1.8. Occurrence of dispersed and collective cracks in bronze route and internal tin strands [Jewell 2008].

For both strand types, intensive SEM observations attempt to correlate the density of cracks found in longitudinal cross-sections with the degradation of the critical current and the *n-index* of the strands. As an example in Fig. 1.9 a) from [Miyoshi 2009], the evolution of the number of cracks per millimeter with the applied strain is presented. Miyoshi's results complete the observations made by Jewell on the onset of crack initiation ε_c for bronze route and internal tin strands, respectively 0.8 % and 0.3 %. Fig. 1.9 b) shows the concordance of the SEM method with the irreversible degradation of the superconducting properties from [Nijhuis 2008 a]. The variations of the critical current and the *n-index* are given as function of the applied axial strain (with regular unloading of the sample). From an initial I_c = 300 A, the performances of the strand are irreversibly degraded for strain greater than +0.25%. For a tensile strain of 0.5%, the I_c decreases down to 125A with partial recovery after strain release (220 A). The *n-index* irreversibly dramatically drops after 0.3% from 29 to 10.

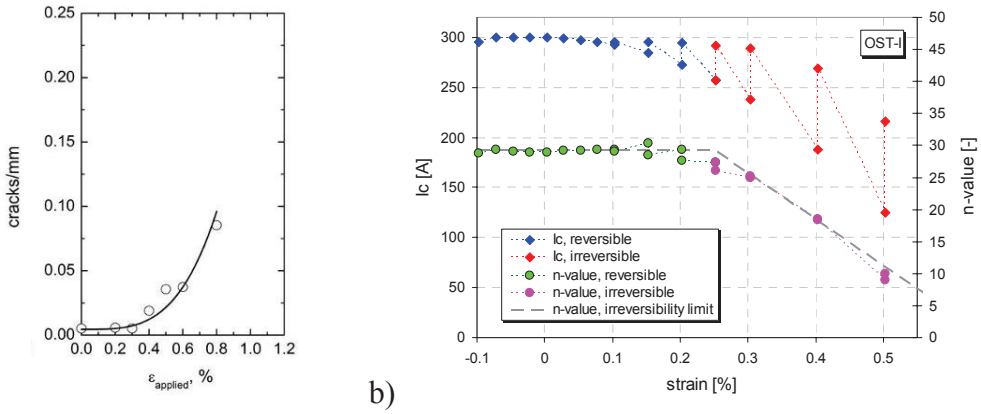

Fig. 1.9. a) Observation of the crack onset at an applied strain of 0.3% for OST internal tin strand [Miyoshi 2009]. b) Measurement of the irreversible degradations of the critical current and the *n-index* of OST internal tin strand (at 4.2 K and 12 T), [Nijhuis 2008 a].

c. The strand characterization by the Ekin's model

The experimental curves representative of the superconducting critical state of Nb_3Sn-based strands have been used to derive what is now called the Universal Scaling Law of the critical current I_c [Ekin 1980-2010]. This scaling law allows representing the global superconducting behavior for a given range of temperature, field and strain. Ekin has defined the scaling law for the *pinning force density* F_p discovering that it can be written in separable form. The respective contributions of the temperature, magnetic field and strain on the pinning force density can be expressed by three separable functions with direct relation between the pinning force density and the critical current of the strands. This decomposition relies on analytical model developed by J.Ekin and later by A.Godeke based on the Maki-De Gennes relation to approximate the critical field dependence on temperature and strain and the dependence of the normalized Ginzburg-Landau parameter on temperature and strain [Godeke 1999-2008]. The development relies on the shape invariance of the pinning force density. According to Ekin, the unified scaling law for the flux-pinning force per unit conductor length in practical high-field superconductors is expressed in its separable form by:

$$F_p = I_c(B,T,\varepsilon)\cdot B = C\,s(\varepsilon)\,h(t)\,f_p(b) \qquad \textbf{eqn. 1.5}$$

Different laboratories have proposed various formulations for the $s(\varepsilon)$, h(t) and $f_p(b)$ functions supported by intensive experimental measurements. After consensus, ITER has fixed the scaling law as follows [Bottura 2008]:

$$I_c(B,T,\varepsilon) = \frac{C}{B}\,s(\varepsilon)\,h(t)\,f_p(b) \qquad \textbf{eqn. 1.6}$$

The separable temperature and magnetic field functions are characterized as follows:

$$h(t) = \left(1-t^{1.52}\right)\left(1-t^2\right) \qquad \textbf{eqn. 1.7}$$

$$f_p(b) = b^{0.5}(1-b)^2 \qquad \textbf{eqn. 1.8}$$

With the reduced temperature t and the reduced field b defined as follows:

$$t = \frac{T}{T^*_{c0}(\varepsilon)} \qquad \textbf{eqn. 1.9}$$

$$b = \frac{B}{B^*_{c2}(T,\varepsilon)} \qquad \textbf{eqn. 1.10}$$

The effective critical temperature $T^*_{\mathbf{c0}}$ and the effective upper critical field $B^*_{\mathbf{c20}}$ depends on the strain using the earlier *s(ε)* function as follows:

$$T^*_{c0}(\varepsilon) = T^*_{c0\max} s(\varepsilon)^{1/3}$$
$$B^*_{c2}(T,\varepsilon) = B^*_{c20\max} s(\varepsilon)\left(1 - t^{1.52}\right) \qquad \textbf{eqn. 1.11}$$

The parameters $B^*_{\mathbf{c20\ max}}$ and $T^*_{\mathbf{c0\ max}}$ are respectively the maximum critical field at zero temperature and zero intrinsic strain and the maximum critical temperature at zero field and zero intrinsic strain. To characterize the function *s(ε)*, the parameter $\varepsilon_{\max}$ is defined as the tensile strain needed to reach the maximum critical current during the stretching test. Then, the effective strain ε to take into account in the formulation reads:

$$\varepsilon = \varepsilon_{applied} - \varepsilon_{\max} \qquad \textbf{eqn. 1.12}$$

The hydrostatic and deviatoric invariants are considered in the theory on the superconducting state. Comparison of hydrostatic pressure and axial strain experiments on the critical properties of A15 materials have shown that the influence of the deviatoric strain (the change of shape proportional to equivalent strain) is much stronger that the influence of the hydrostatic strain (the change in volume) and hence the deviatoric strain invariant is chosen to describe the influence of deformations on the critical parameters. The chosen formulation of the dimensionless strain part *s(ε)* is based on the *deviatoric strain model* developed by the complementary works of [ten Haken 1999] [A.Godeke 1999-2009], [Cheggour 2002], [Markiewicz 2004-06], [Arbelaez 2009].

$$s(\varepsilon) = 1 + \frac{1}{1 - C_{a1}\varepsilon_{0,a}}\left[C_{a1}\left(\sqrt{\varepsilon_{sh}^2 + \varepsilon_{0,a}^2} - \sqrt{\left(\varepsilon - \varepsilon_{sh}\right)^2 + \varepsilon_{0,a}^2} \right) - C_{a2}\varepsilon \right] \qquad \textbf{eqn. 1.13}$$

$$\varepsilon_{sh} = \frac{C_{a2}\varepsilon_{0,a}}{\sqrt{C_{a1}^2 - C_{a2}^2}} \qquad \textbf{eqn. 1.14}$$

The terms $\varepsilon_{0,a}$,C_{a1} and C_{a2} are respectively the non-axial residual strain and two fitting constants. The parameter $\varepsilon_{0,a}$ is actually corrected by the factor expressed in eqn. 1.14 that shifts its value to ε_{sh}. The parameterization needs the identification of the seven parameters of the law that necessitates limited experimental data [Nijhuis 2006]. The advantage of the scaling law is that it remains valid for the typical strain range expected in ITER conductors, saying between -1% and +0.5%. In Fig. 1.10, the parameters for the OST internal tin strand are listed in the table and the $I_c(\varepsilon)$ is plotted for T = 4.2 K and B = 12 T.

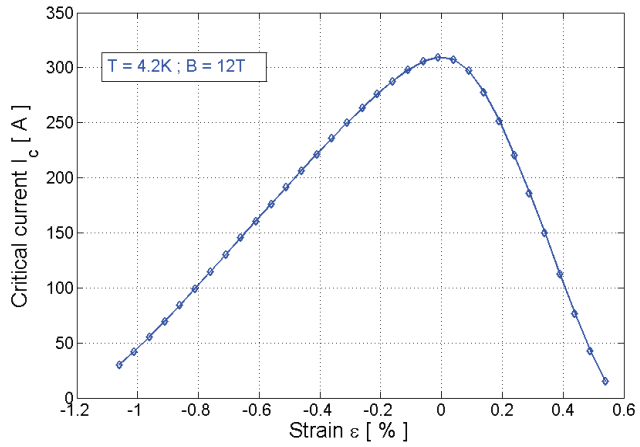

C_{a1}	37.22
C_{a2}	0.0
$\varepsilon_{0,a}(\%)$	0.21
$\varepsilon_m(\%)$	0.13
$B^*_{C2max}(T)$	29.76
$T^*_{C0max}(K)$	16.21
C(AT)	17390

Fig. 1.10. Example of the use of the deviatoric strain model to compute the critical current as function of the axial strain .

1.2.2 The Cable-in-conduit conductors characterization

a. Critical current

The critical current of *CICC* can be determined in the same way as for the single strands. However, the measurements give an average I_c that is not necessarily equal for different strands of the cable considering the possible redistribution of the current between the strands. Besides, the *n-index* that is found for the *CICC V-I* curves is usually lower than the single strand value

b. Current sharing temperature

Regarding the *CICC* characterization, another important parameter is measured which is the same as for single strands, the *current sharing temperature* T_{cs} (K) which is defined at $E=E_c$ when all but the temperature parameters are fixed in the above relation. In *CICC*, the transition to resistive state is not as sharp as it is in single strand when the temperature increases at constant field and current. The Nb_3Sn filaments and strands do not experimence transition simultaneously everywhere in the cable. A sharing of the current between filaments or between strands rather occurs that causes the observed smooth collective behavior. In order to measure the T_{cs} of a conductor, the temperature of the helium flow is slowly increased at constant current and constant external magnetic field. As the temperature evolves the electric field is measured, the voltage is then plotted against the temperature. According to ITER design rules, the *current sharing temperature* T_{cs} (K) of a *CICC* is defined as the temperature at which an electric field of 10μV/m is detected. An example, of T_{cs} measurement is given in Fig. 1.17, from [Mitchell 2003 b].

1.3 The degradation of the superconducting performance in cable-in-conduit conductors

1.3.1 The test results on the ITER model coils

In 2000–2002, the first step on the ITER development has been carried on with the construction and the tests of two ITER full size model coils, the Central Solenoid Model Coils and the Toroidal Field Model Coil [Salpietro 1999], [Kato 2001], [Mizoguchi 2001],

[Mitchell 2001]. The cable-in-conduit conductors inside coils are respectively composed of 1152 strands and 720 strands for the CSMC and the TFMC. The designs of the conductor are indicated in Table 1.1, from [Mitchell 2002]. For the estimation of the current sharing temperature of the two model coil, the maximum magnetic fields and current sustained by the conductor are also indicated. The temperature of current sharing, T_{cs} of the model coils using an electric field criterion E_c= 0.1mV are estimated – see Fig. 1.17 and reported in Table 1.1.

	TFMC	CSMC
Pattern	(2 sc + 1 Cu) x 3 x 5 x 4 x 6	3 x 4 x 4 x 4 x 6
TP (mm)	45-85-125-160-400	45-74-123-160-380
VF (%)	36	36
External magnetic field	5.1-11.8T	8.5-13T
Operating current kA	80	46
Measured T_{cs} (K)	8.5	6.5

Table 1.1. The ITER model coils design parameters and operating conditions. The estimation of the current sharing temperature is also shown.

In his "Review of Nb_3Sn conductors for ITER", Daniel Ciazynski summarizes the results of the tests of the two model coils. First, the T_{cs} decreases with the intensity of the electromagnetic loading. Second T_{cs} drops with the number of loading cycles and/or quench of the conductor. Third, the final *n-index* of the strands is found to be half of the initial value [Ciazynski 2007].

1.3.2 The results of *CICCs* tested at SULTAN facility

After the test of the model coils, further investigations on Cable-In-Conduit Conductors have been performed at the SULTAN facility. The facility allows several meters long conductors to be tested in ITER operating conditions (significantly higher than for the model coils). Sophisticated measurement techniques are used for the measurement of the current sharing temperature. In 2006, four ITER-like *CICCs* have been tested at SULTAN [Ciazynski 2007], [Bruzzone 2007]. The conductors are all identical except that the Nb_3Sn strands are from different suppliers. Compared to those of the model coils, these strands are called "advanced" with higher critical current (1000 A/mm^2 at 4.2 K and 12T) – see for instance [Vostner 2006].

In Fig. 1.11, the result of the T_{cs} measurement is shown for the four tested conductors. The figure illustrates the continuous degradation of the T_{cs} with the number of Lorentz loading cycles with T_{cs} below the ITER specification (5.7 K with the TF conductor). The numerous papers dedicated to the study of the model coils and other *CICCs* attribute the T_{cs} degradations with cycles to the effects of the deformations at the scale of the strands. The cabled strands undergo severe bending due to the Lorentz forces with possible consecutive filament breakages. [Mitchell 2003-10], [Ciazynski 2007-08], [Martovetski 2004-05], [Bruzzone 2003-04-09 a].

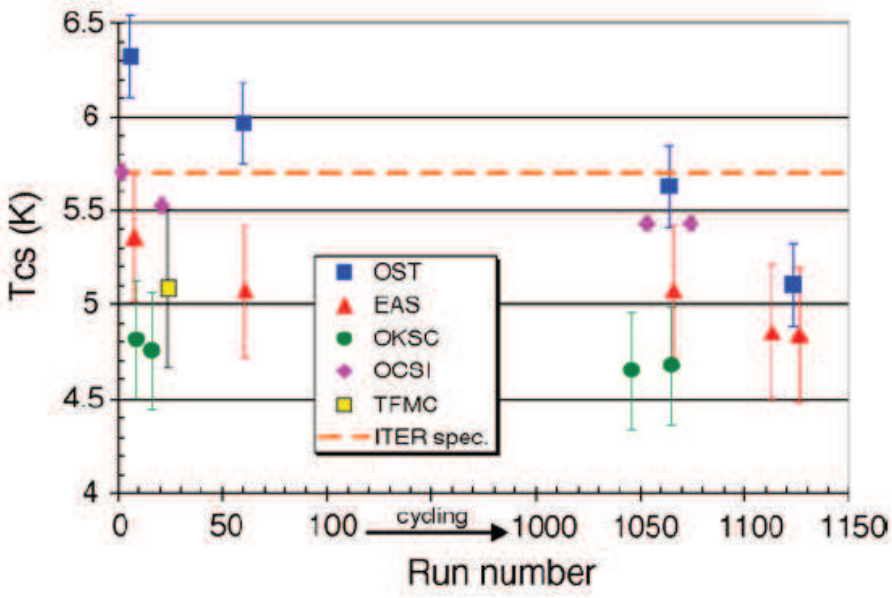

Fig. 1.11. Observation of the T_{cs} degradation with the number of Lorentz loadings. The field is 11 T and the current is 68 kA to be shared between 720 strands in the OST and OKSC and 1080 strands in the EAS and OCSI, i.e. respectively 94 A and 62 A per strand.

2 *Investigations on the detrimental effects of the strain in cable-in-conduit conductor*

2.1 Variation of the single strand properties for different mechanical loadings

In order to understand the cable-in-conduit conductor, a first approach is to characterize the behavior of a single strand submitted to different loadings. Three types of loading can be applied to the strands to produce pure uniaxial strain, pure bending strain and pure transverse stress. The experimental procedures to test the strands have been published in the works of J.Ekin since 1980's and later by Nijhuis and Godeke, Hampshire and Taylor or Nunoya.

2.1.1 The axial loading of the strand

For the application of pure axial strain (tensile and compressive), the Twente University uses the so-called Pacman device [Godeke 2004] while the Durham University and the NIST laboratories prefer the Walters spring [Taylor 2005]. The Japan Atomic Energy Agency proposes to use the horseshoe-shape ring [Nunoya 2007], [Yoshihiko 2007]. Fig. 1.12 from [Nijhuis 2008] summarizes the dependence of the critical current (I_c / $I_{c\ max}$) on the axial strains for various Nb_3Sn strands. The applied strain ranges from compressive (-1%) to tensile strain (> +0.6 %). The temperature and the background field are 4.2 K and 12 T. The dependence on the strain is very similar for the various strands which can be related to Ekin's universal model of Nb_3Sn strand earlier described.

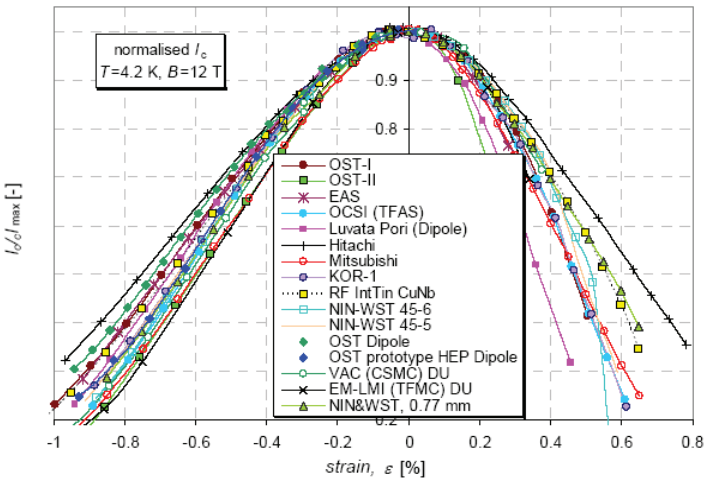

Fig. 1.12. Illustration of the conductivity loss due to applied axial strain to the strand. [Nijhuis 2008 a].

2.1.2 Bending loading

a. Mechanical behavior

Inside a cable-in-conduit, the strands are expected to deform by bending in addition to pure compression. The Twente Laboratory has proposed a specific device that allows prescribing a bending strain to single strands (TARSIS) [Nijhuis 2006 a]. The bending is created by placing a strand at the circumference of a barrel between two jaws that present some bulges around. The vertical displacement of the upper cap produces the desired bending strain on the sample. The strand is assumed not bounded at its ends so that only pure bending is applied. The pinching that may occur between the strand and the bulges is of a second order. In Fig. 1.13 a), a picture of the device is shown and the result of the force-displacement plot measured by the loading cell and extensometers is exposed. The applied load goes up to 6 kN/m while the vertical deflection mounts up to 140 µm. The sample can be cyclically loaded to reveal occurrence of plastic deformation – see Fig. 1.13 b). The accurate measurement of the loading curves could later help any numerical model of strands.

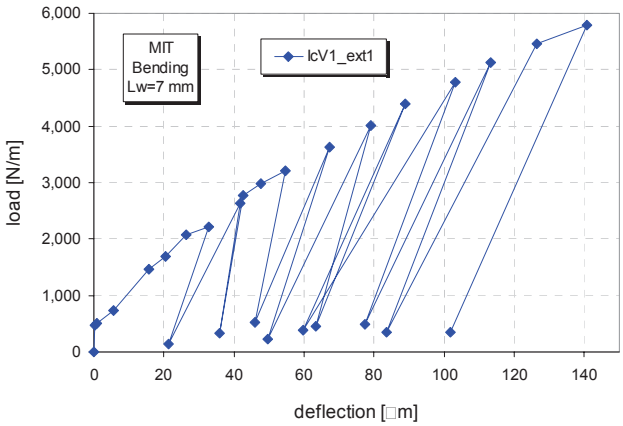

a) b)

Fig. 1.13. Bending TARSIS device and an example of the force-displacement characteristic of MIT strand at 4.2 K (Courtesy of Nijhuis).

b. Degradation of the electrical properties due to bending

In Fig. 1.14 a), the critical current is plotted against the applied load and in b) against the corresponding peak bending strain. This strain is calculated from the measured deflection and corresponds to the maximum axial strain at the outer radius of the filament region. For the range of applied load, the peak bending strain sustained by the filament goes from zero to 1.7 %. Direct comparison between both graphs of Fig. 1.14 allows relating the applied vertical load to the strain, e.g. 3 kN/m corresponds to 0.7 %. The property of the strand reversibly degrades for loads lower than 1.5 kN/m then partially recovers as the load is released. A drop of more than 50 % of the critical current is measured for loads greater than 4.5 kN/m that is not recovered after the release. The irreversible behavior that is observed can be interpreted as the effect of the yielding of the copper and bronze matrix on the strain state of the Nb_3Sn filament or as filament breakage.

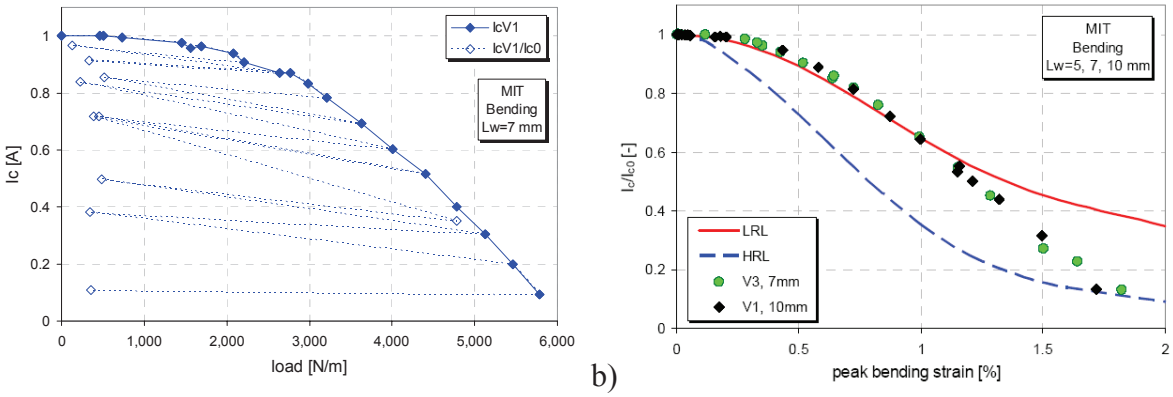

Fig. 1.14. Critical current irreversible degradation with bending and comparison with models [Nijhuis 2008 a].

c. The question of the inter-filament current redistribution

The properties of Nb_3Sn strand are not only affected by the applied bending strain but also by the inter-filament electrical resistivity. It indicated that some redistribution of current from filament to filament effectively occurs within the strands when bending is involved [Nijhuis 2004 a- 09][Ciazynski 1985 - 10][Mitchell 2004]. In 2004, Mitchell proposed two models to describe the evolution of the critical current with bending strain noting that it depends on the twist pitch of the filament and on the internal resistance of the strands. The first model allows the current to transfer at low voltage level and is written LRL for Low Resistance Limit. The second model corresponds to the extreme case where the interstrand resistivity is so high that no current transfer is possible. The model is referred to as the High Resistance Limit HRL**.** In Fig. 1.14 b), the LRL match the curve up to a peak bending strain up to 1%. But then the experience tends toward the HRL. In 2010, Ciazynski and Torre propose an analytical formulation to compute the critical current of strands submitted to bending [Ciazynski 2010]. So far the effects of the bending on the Nb_3Sn strand electrical properties are not clearly modelled.

2.1.3 Pinching loading

a. Mechanical behavior

Another experiment is performed at Twente University realizes to test the effect of pure contact load between crossing strands [Nijhuis 2006 b]. Radial strands are pressed against a

strand that runs around a barrel by an upper cap. The strands are crossing at 90° - see Fig. 1.15 a). In Fig. 1.15 b), the transverse stress-strain loading curve is presented. The curve is non linear at the beginning and then linear up to 275MPa (10%). The transverse stress is calculated by the applied force divided by the square of the strand diameter (σ_t=F/d²). The strain is defined as the ratio of the measured displacement (extensometer) to the strand diameter (ε_t=u/d). After the test, the strand is plastically deformed (surface imprint).

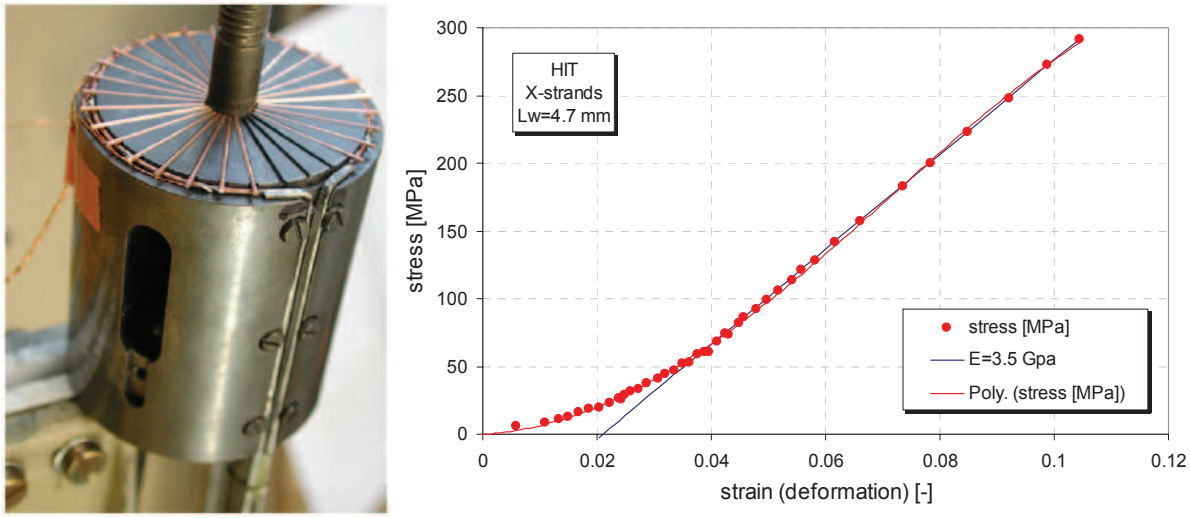

a) b)

Fig. 1.15. TARSIS crossing strands probe and an example of the stress-strain characteristic of HT strand at 4.2K [Nijhuis 2006 b].

b. Degradation of the electrical properties due to bending

In Fig. 1.16 a), the variation of the critical current I_c with the transverse stress (successively applied and released) show that irreversible degradation occurs for contact stresses greater than 100 MPa. The critical current degrades up to 30% for a contact stress of 250MPa and is not recovered after load release (60%). The *n-index* also decreases with the contact from 34 down to 10 at 250MPa. Nonetheless these are high values of stress that correspond to transverse deformation of about 8% of the strand diameter.

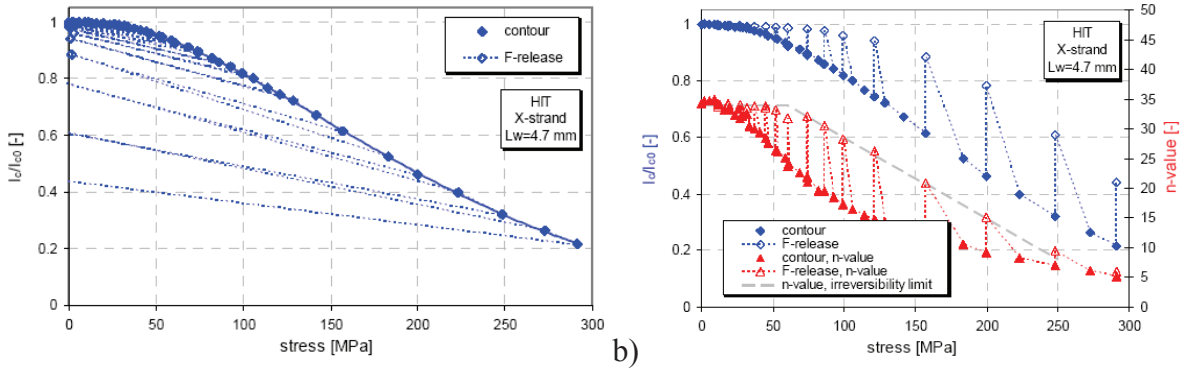

a) b)

Fig. 1.16. Reversible and irreversible impact of the contact stress on the critical current and the *n-index* at 4.2K (HIT strand) [Nijhuis 2009 a].

2.2 Assessment of the average strain developing in the strands of CICC

Supported by extended studies of the single strand properties, an important work has been done to characterize full size cable-in-conduit conductors. For the characterization of the critical current and the current sharing temperature, the strain locally sustained by the Nb_3Sn strands has to be estimated. Unlike the test of single strand, no direct measurement is possible in *CICCs*. However, from the thermo-electric measurements, the average axial strain in the Nb_3Sn filaments can indirectly be assessed. The assessments rely on the so-called smeared model briefly presented here. For more details, one can refer to [Mitchell 2003 a b], [Mitchell 2004-05-08], [Ciazynski 2000-07-08], [Martovetsky 2005 a], [Bruzzone 2009 a b], [Zanino 2003 a b c].

2.2.1 Presentation of the smeared model

The *smeared model* considers an average strand in the cable with respect to Nb_3Sn strain state, effective superconducting area and *n-index*. The average electric field along the conductor is then computed by averaging the electric field in a conductor cross-section, taking into account the background magnetic field and the temperature profile. The critical current of the *CICC* and its current sharing temperature can then be computed relative to the expected average strain. The open parameters are the average strain and *n-index* of the strands. In common interpretation of model coil experimental results, the effective average strain in the Nb_3Sn filaments is separated in three components that have respectively thermal, mechanical and electromagnetic origins:

$$\varepsilon_{eff} = \varepsilon_{th} + \varepsilon_{op} + \varepsilon_{BI} \qquad \textbf{eqn. 1.15}$$

In 2005, Zanino, Ciazynski and Mitchell have published a paper that present an advanced numerical method that attempts to take into account the mechanical, electromagnetic and thermal–hydraulic considerations of the *CICC* problems. The loading related to the structural aspect of the problem is simulated by the ANSYS Finite Element code that give ε_{op}. The Multiconductor Mithrandir (M&M) code deals with the thermo-hydraulic part of the problem [Zanino 2000-08] and provides for the temperature profile of the conductor, see also [Bottura 1995]. The ENSIC code treated the electromagnetic part of the problem introducing for instance the scaling law J_c (B, T, ε_{eff}) [Zanino 2005]. The value of ε_{th} and ε_{BI} have to be assessed so as to best fit the measured *V-I* and *V-T* curves. Moreover the value of the *n-index* of the strand should also be assessed.

More recently, important works have been done by Van Lanen and Nijhuis on the modelling of the transient electromagnetic behavior of conductors due to the presence the joints or other heterogeneities [van Lanen 2010]. The question of the redistribution of the current between the strands is as important of the transfer between the filaments down the microscopic scale [Mitchell 2000 a b], [Ilyin 2007 b], [Bruzzone 2006].

2.2.2 Indirect assessment of the average strain in CICC from thermo-electric experiment results

In 2003, Mitchell published the fitting of the experimental T_{cs} measurements using the smeared model for both the CSMC and the TFMC – see Fig. 1.17 [Mitchell 2003 a]. In this first approach, the current is assumed uniformly distributed among the strands. Fig. 1.17 b)

also shows the result for different set of parameters. In order to fit the *V-T* curves, the author estimates the *n-index* equal to 7 and the following thermal strains:

$$\varepsilon_{th}^{CSMC} = - 0.32\%$$

$$\varepsilon_{th}^{TFMC} = - 0.66\%$$

The difference comes from the different shape and the different material of the jacket of the *CICC* of the two coils (round-in-square INCOLOY for CSMC and circular Stainless Steel for TFMC) that lead to two different induced thermal strain. For the operating strain, Mitchell estimates the following values:

$$\varepsilon_{op}^{CSMC} = + 0.2\%$$

$$\varepsilon_{op}^{TFMC} = + 0.1\%$$

The strain due to local electromagnetic effects is expressed by a compressive strain that depends on the magnitude of the Lorentz force *BI* sustained by the strands but also change with the jacket material:

$$\varepsilon_{BI}^{CSMC} = - 0.0004*BI = - 0.275\ \%\ \text{(low CTE jacket)}$$

$$\varepsilon_{BI}^{TFMC} = - 0.00023*BI = -0.12\ \ \%\ \ \text{(high CTE jacket).}$$

The approach proposed by Mitchell in 2003 seems to give a relevant reproduction of the T_{cs} test curve but is not able to *a priori* predict the amplitude of the strain. However, the interpretation gives indications on the average value for the strains and the *n-index* of the strands.

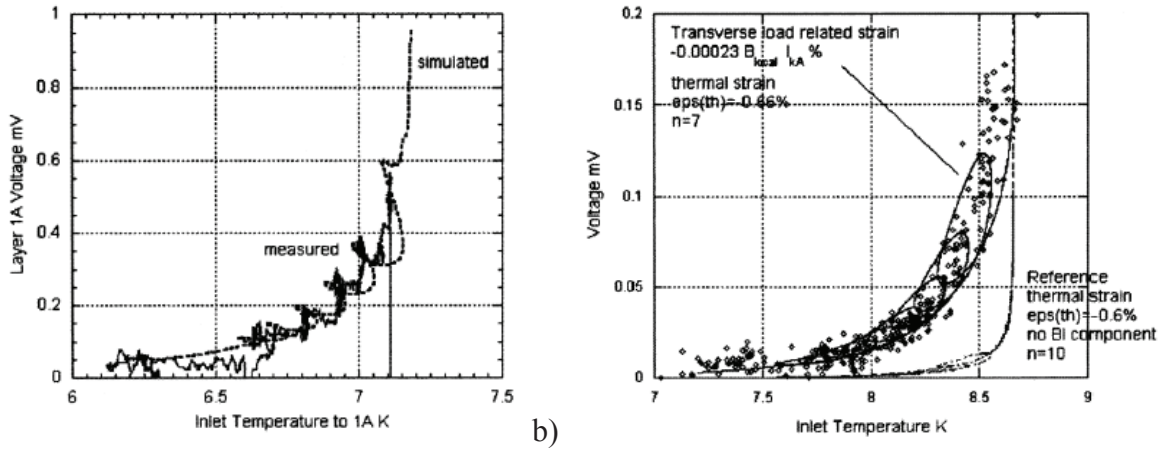

Fig. 1.17. Example of the current sharing temperature T_{cs} test results of the ITER model coils conductor. a) CSMC and b) TFMC. The plots show the identification of T_{cs} test using the strand scaling law and the smeared model, [Mitchell 2003 b].

2.2.3 Degradations induced by the Lorentz force loading

The extra strain introduce in the smeared model attempts to depict the effect of the Lorentz loading on the conductor behavior. In Fig. 1.18, the assessment of the average strain is plotted against the applied Lorentz loading for the CSMC [Zanino 2003 c] and the TFMC [Zanino 2005]. The results of two full size conductors, the TFMC-FSJS samples tested at the SULTAN facilities, are also shown. The analyses confirm that the strain is related to the electromagnetic loading, the *BI* (kAT) product and the average linearly scale with it. For these results, the *n-index* of the cable is between 5 and 8 to be compared with the 15-20 measured for LMI strands.

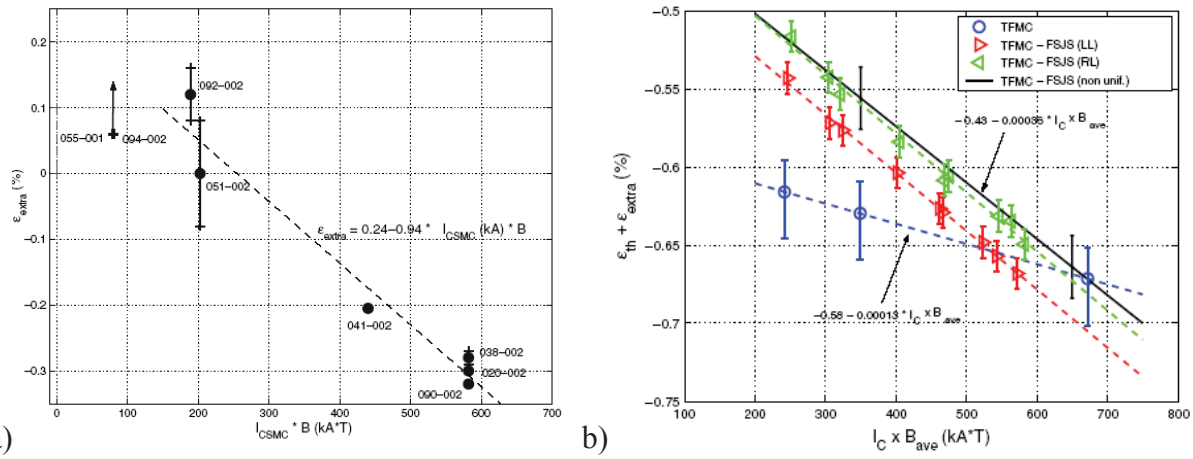

Fig. 1.18. Interpretation by the smear model of the degradation of the T_{cs} and I_c with the Lorentz loading by the mean of the compressive strains ε_{BI} (here ε_{extra}). The estimations of the average strain are done for, a) the CSMC and b) the TFMC conductors, [Zanino 2003 c -05].

2.3 The influence of the conductor design on the performances

2.3.1 New design for the ITER TF conductor

In order to overcome these degradations, ITER TF conductors have been redesigned and new *CICCs* samples have been tested at SULTAN. In 2008, Ciazynski published the test results of the six *CICCs* that use advanced strands (EAS bronze route or OST internal tin) [Ciazynski 2008].The design of the six conductors differ in their cable layout, void fraction, twist pitches with or without the inclusion of segregated copper strands. Table 1.2 summarizes the design parameters of the conductors. The jacket thickness is always 1.6mm.

Sample	TFAS1		TFPRO1		TFPRO2	
Conductor	EAS0	OST0	EAS1	EAS2	OST1	OST2
Strand diameter [mm]	0.81					
Cu: non- Cu in strand	0.91	1.0	0.91		1.0	
Strand manufacture	bronze	internal tin	bronze		internal tin	
Jc @4.2 K,12 T [A/mm^2][a]	710	1020	710		1150	1020
Cable layout	3[b] × 3 × 5 × 4 × 6		((2s/c+1Cu) × 3 × 5 × 5 + 3 × 4Cu) × 6			
Nr. of s/s strands	1080	720	900			
Nr. of Cu strands	0	360	522			
Twist pitch sequence [mm]	45 - 87 - 126 - 166 - 415		45 - 87.5 - 126.5 - 245 - 460			116 – 182 - 245 – 415 - 440
Petal void fraction [%]	34.0	33.3	33.8	29.3	29.1	27.7
Central spiral id × od [mm]	10 × 12		7 × 9			
Outer diameter [mm]	40.4		43.45	42.05	42.05	41.45

[a] As measured by CRPP.
[b] (2 s/c + 1 Cu) in OST0, 3 s/c in EAS0.

Table 1.2. Design parameters of the SULTAN tested advanced conductor. Between the various samples, the cabling pattern may change (blue border), the twist pitches (red border) and the void fraction (green border). The main variation in the design is for the TFPRO2 OST2 (pink border) with longer twist pitches and reduced void fraction. [Ciazynski 2008].

2.3.2 Improvement of performances with the new designs

Ciazynski published the interpretation and assessment of the average strain sustained by the stands for six cable-in-conduit samples tested at the SULTAN facility.

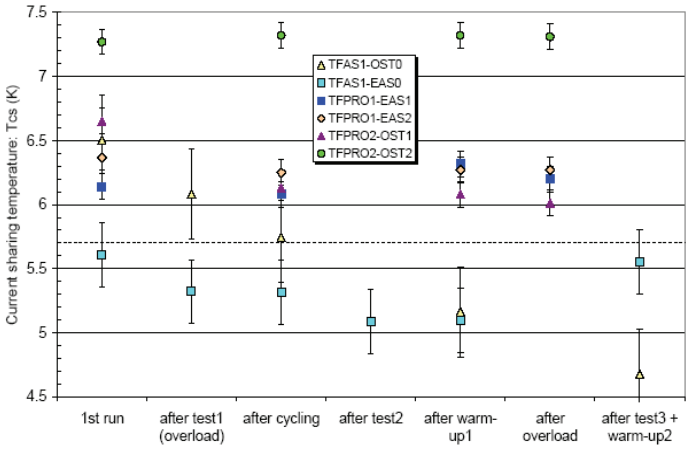

Fig. 1.19. Current sharing temperature for six different cable-in-conduit conductors. Only the TFAS1-EAS0 stays below the ITER specification. The T_{cs} degrades with the loading cycles (thousand Lorentz loading cycles) for all conductors but the TFPRO2 OST2 [Ciazynski 2008].

According to Ciazynski, the new four European TF conductors for ITER tested in 2007 have shown much better performance than the previous conductors tested in 2005-2006, see Fig. 1.11, particularly with a current sharing temperature T_{cs} above the ITER specification. Since the same Nb_3Sn strands were used in the old and the new conductors this improvement of performance has to be related only to the change in the cable structure. The main variation is related to the inclusion of copper core in the cable layout (blue border) a reduction of the void fraction (green border) and an increase of the last cable stage twist pitches (red border) in Table 1.1. The best conductor in term of T_{cs} values and degradation with cycles is the TFPRO2-OST2 which globally gets twice longer twist pitches and lowest void fraction. It is to be mentioned that this high performance was predicted by Nijhuis from the Twente University before the SULTAN testing of the *CICC* [Nijhuis 2005 b-06 c-08 b].

2.3.3 Assessments of the average strains from the smeared model

Table 1.3 exposes the assessment of the thermal strain ε_{th} and the extra strain $\varepsilon_{BI} = \gamma BI$ needed to describe the *V-T* and *V-I* curves for the six conductors [Ciazynski 2008]. This is the first model (m1) in the table. A second model (m2) uses a reduction of the effective superconducting area (α_{eff}) representative of the possible filament cracking instead of the extra strain. In SULTAN test, the conductors are straight and the hoop stress is null, thus ε_{op} is equal zero. The data in Table 1.3 provide valuable information on the average strains sustained by the strands in well characterized cable-in-conduit conductors.

Model	Conductor	TFAS1		TFPRO1		TFPRO2	
		EAS0	OST0	EAS1	EAS2	OST1	OST2
m1	ε_{th} (%)	-0.605	-0.505	-0.592	-0.595	-0.540	-0.477
	γ (%.kA^{-1}T^{-1})	2.4×10^{-4}	4.4×10^{-4}	9.5×10^{-5}	7.5×10^{-5}	3.1×10^{-4}	0
m2	ε_{th} (%)	-0.558	-0.370	-0.560	-0.570	-0.460	-0.477
	α_{eff}	0.614	0.400	0.800	0.840	0.470	1

Table 1.3. Assessment of the strain parameters from the smeared model for six *CICCs* tested at the SULTAN facilities [Ciazynski 2008].

2.3.4 Concluding remark on the uncertainties of the smeared model

The various authors mentioned that the use of the smeared model is a way to fit the experimental *V-I* and *V-T* curves but is not a predictive model. The mechanical phenomenon expected to degrade the superconducting performance is the local bending of the strands. In that sense, the use of an extra compressive strain to describe the occurrence of bending due to the Lorentz loading might be misleading. In addition, the account of the complex situation of the strands in cable by a single value of *effective* strain is not sufficient. As the model (m2) tends to show, the bending is likely responsible for the cracking of the Nb_3Sn filaments. The low n-value of the strands also points at some possible damages [Bruzzone 2003], [Ciazynski 2007]. Advanced electrical models that use networks of contact resistance and superconducting relation would now need a more precise description of the trajectories of the strands and ideally the axial strains along and across the strands everywhere in the cable [Zani 2009], [van Lanen 2010], [Torre 2010].

3 The mechanical models related to cable-in-conduit conductor

3.1 The models of single strands

3.1.1 Simulation of axial loading

a. Finite element simulations of elasto-plastic processes in Nb_3Sn strands

In 2003 and 2005, Mitchell proposed a standard finite element simulation of composite Nb3Sn-based strands. The numerical model is able to reproduce the effect of both the heat treatment and the cool down through a thermo-mechanical approach. The model is based on ANSYS FE code and considers the different components of the strands using 3D spar elements with three degrees of freedom at each node: translations in the nodal x, y, and z directions (LINK8). The material properties needed to describe the ITER strand are given in this paper. The axial stress-strain curves and the coefficients of thermal expansion are reported for the copper, tantalum, bronze, tin, niobium, Nb_3Sn and steel over a temperature range from 4 K to 900 K. The copper and the bronze are described by an elasto-plastic model with multilinear isotropic hardening model whereas the other materials (Tantalum barrier and filaments) are considered aspurely elastic. The model includes the temperature dependent stress-strain curves. The material properties of the filaments are switched from Nb to Nb_3Sn for the filament during the heat treatment to depict the alloying, [Mitchell 2003-2005 a b].

The internal stresses relative to each component of the strand are computed for different temperature variations. The calculated thermal shrinkage of the strand from 900K to 4K is -0.47% for Bronze route and -0.61% for Internal Tin. The Nb_3Sn intrinsic strain after cool down is found to vary from -0.25% to -0.38%. A tensile test of the strand has been simulated that shows small impact of the temperature on the axial stress-strain curve. This interesting result is also experimentally observed for strand tested at room, nitrogen and helium temperature as presented in [van den Eijnden 2005]. It is also reported that the mixture law is sufficient to describe the stress-strain curve of composite strands as long as appropriate volume fractions and relevant material properties are used for the materials.

b. Homogenization techniques

In 2005 and 2009, D. Boso *et al*. have proposed two approaches to model the thermo-mechanical problem of the composite strands. One uses a *hierarchical homogenization method* [Boso 2005 a b], the other the *generalized self-consistent-like homogenization method* [Boso 2009]. The models consider separately the different sub-elements of the strands with simplified geometry and solve the equation of the thermo-mechanics by homogenization techniques. The models are able to simulate the thermal pre-stresses induced by the matrix to the Nb_3Sn filaments due to the cool down with plasticity consideration. The approach remains limited to the strands level of the conductor problem.

3.1.2 Bending strain simulation

Mitchell has proposed an analytical model based on the beam theory to describe the bending of the strands inside a loaded cable [Mitchell 2002], [Mitchell 2003 a b]. The model considers the axial loading and the bending of a curved beam (sinusoid of length L) fully clamped at each end, except in the longitudinal direction for the axial loading. The beam is subjected on the one hand to Lorentz force or longitudinal compression, and on the other hand to contact reactions due to the neighbouring beams. The author gives the equation relative to the theory of straight indeterminate beams which is solved to calculate the deflection. The estimations of the maximum axial strains predicted by these models suffer from the lack of knowledge regarding the loads to apply and are limited by their simplicity. However, the analytical model points at the occurrence of important bending due to the application of the axial and transverse loading.

To complete the analytical approach, Mitchell also presents the results of a finite element code regarding the bending of composite strands. The strand is modelled using 3D solid elements. Three materials are represented (copper, bronze, Nb_3Sn) with isotropic elasto-plastic properties. The various elements are twisted around the axis to reproduce the twist of the filaments. The twist pitch is 10 mm and 10 mm of strand is modelled. The strand can be curved so as to reflect its situation in cable and two different axial compressions (-0.3 % and -0.7 %) are applied that would correspond to the effect of Stainless Steel or Incoloy jacket. The strand is then bent by a load applied to the middle of the strand. Assessments of the axial strain in the filament are proposed. The model shows that the expected loadings of cable-in-conduit conductors are able to produce sufficient tensile strain to suppose filament damages during the bending of the strands inside loaded conductor. In 2004, the modelling of bending was carried on with the derivation of the electrical performance of the strand [Mitchell 2004].

3.1.3 Transverse loading simulation

In 2005, J.L. Schultz & al. have proposed a finite element simulation of the pinching of a strand between two 1mm² rigid plates. The copper shell and the filaments are modelled – see Fig. 1.20 from [Schultz 2005]. However, neither the number of filaments nor the material properties are given in the paper. The model predicts that an applied transverse load of 121N can cause tensile strain up to +0.6 % on the filaments. It also states that an axial precompression of the filaments prevent the occurrence of high tensile strain – see Fig. 1.20.

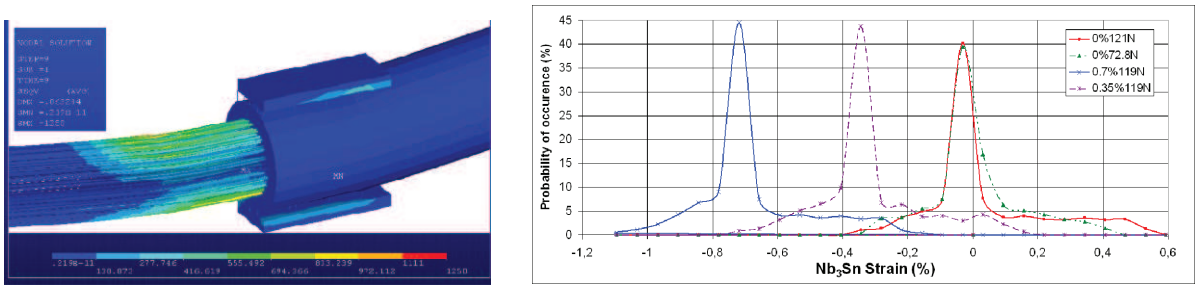

a) b)

Fig. 1.20. a) Finite element simulation of the transverse contact stress (Von Mises stress). b) Equivalent strain distributions among the filaments when different thermal compressions and contact loads are applied, [Schultz 2005].

3.2 The simulation of cable mechanical behavior using semi-analytical model

The simulations of the single strands have emphasized the need to know what are the amplitudes of the loadings effectively applied to the strand in *CICC*. In 2005, Mitchell proposed a simple approach to describe the mechanical behavior of cable [Mitchell 2005 c] that has been later completed Nijhuis with the Transverse Electro-Magnetic Load Optimisation (TEMLOP) model [Nijhuis 2006 c], [Nijhuis 2008 b]. The purpose of the TEMLOP model is to derive the bending strain due to the transverse Lorentz force along every strands of conductors using a simplified model of cable that use the standard beam equation.

First of all, the geometry of the cable is simplified considering arrays of beam sections uniformly distributed with regular spacing inside a square section that represents the conductor cross-section. The cable is then depicted by rows of beam sections that can move in the vertical direction – see Fig. 1.21. The initial size of the square, i.e. its edge, is defined as follows:

$$D = \left(\frac{N_s \pi d_s^2}{4(1 - vf)\cos\theta} \right)^{0.5} \qquad [m] \qquad \textbf{eqn. 1.16}$$

where, N_s is the number of beams, d_s their diameter, vf the cable void fraction and (cos θ) the average twist pitch angle. The beams of each layer are assumed to be supported by lower layers, through contact points distant from each other by a length L_w, depending on the considered layer. Secondly, for the Lorentz force loading, the model consists to apply a load F to the first layer of this geometry and to compute the induced deflection. Increasing F, this deflection will reach the maximum space for bending (f_{sb}) defined by the distance with the second layer. Once the contact is made between the two layers due to the deflection, the load supported by the first beam is partially transmitted through this new contact, and partially through the pillars already considered between the two layers. For the new layer, the distance between the pillars is half the distance relative to the above layer and the applied load is also half the previous values – see Fig. 1.21 b). The bending deflection of this second layer is then computed. The process is repeated for the successive layers to depict the accumulation of the Lorentz force. The bending for each layer of the cable is finally computed. To complete the model, the deformation of the pillars is considered using specific assumptions exposed in the various papers.

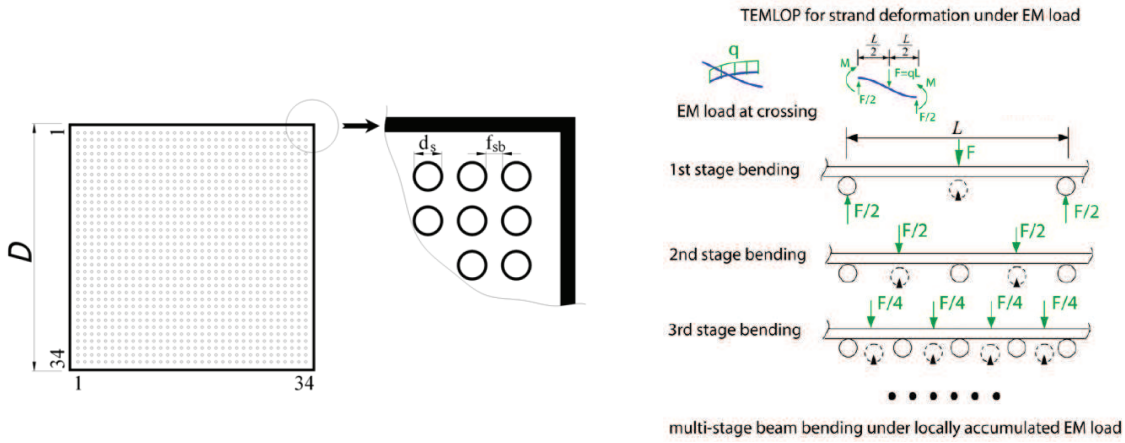

a) b)

Fig. 1.21. a) Simplified geometry of cable using a square cross-section containing array of beams sections. The geometry is used to derive the initial free deflection of the beam before reaching the row below, [Nijhuis 2006 c]. b) Corresponding model of indeterminate beam submitted to periodic bending. The Lorentz force load F is transmitted from layer to layer, [Zhai 2008 a].

To solve the problem, the equation of a circular beam submitted to periodic bending is used. The distance between the pillars is referred to as the "bending wave length" L_w of the model. The equations for the bending are solved for a load F imposed at the middle of the pillars. The deflection f_{sb} and the corresponding bending strain ε_b reads:

$$f_{sb} = \frac{F\,L_W^3}{192 E_{//} I_a} \qquad [m] \qquad \textbf{eqn. 1.17}$$

$$\varepsilon_b = \frac{F\,L_W}{8 E_{//} W_b} \qquad [-], \qquad \textbf{eqn. 1.18}$$

where, $E_{//}$ is the Young modulus, I_a is the moment of inertia and $W_b = \pi\, r_s^3/4$ is the section factor. In TEMLOP, the load F comes from the following estimation using the square root of the total number of strands, N_s:

$$F = I_s\, B\, N_s^{0.5} \qquad [N/m], \qquad \textbf{eqn. 1.19}$$

where I_s is the current per strand, B the magnetic field.

The main issue of the model is first to properly set the maximum deflection that defines the maximum bending for the layers and second the bending wavelength L_W that should be relative to the twist pitches of the cable. In TEMLOP, L_W is empirically estimated according to observation of real un-jacketed conductor and is about 6 mm for classical conductor design.

The TEMLOP semi-empirical model takes advantage of the TARSIS measurements to define the Young's modulus and the transverse modulus of the strands and to derive an estimation of the conductor electrical performances. Parametric study of the influence of L_w and f_{sb} on the bending strain predicted the beneficial effects of the increase of the twist pitches of the cable stages and the lowering of the void fraction, [Nijhuis 2008 b], [Nijhuis 2009 a].

In 2008 and 2010, Zhai has improved the TEMLOP model including the effect of the axial compression to the periodic bending beam model. The model refers now as the FEMCAM model. An axial displacement is applied to the curved beam and the deflection is derived using the Timoshenko beam–column theory for a given applied axial strain. Regarding the model of cable, it is assumed that all strands experience the same thermal bending effects. With the TEMLOP approach for the effect of Lorentz force loading, the effective axial strain in the Nb_3Sn strands can be estimated. The FEMCAM model, predicts for L_W=6mm, axial strain ranging from -1.7% to +1% and contact stress up to 50 MPa. The critical current of various conductors have then be derived [Zhai 2008 a b]. However, the analysis of the numerous cable-in-conduit conductors has proved that the model was not able to predict the observed degradation of the critical current.

3.3 Finite element approaches with general purpose codes

In 2009, A.S. Nemov *et al.* exposed their approach to simulate the mechanical behavior of cable using standard finite element codes [Nemov 2010]. The study focuses on sub-cables, from triplet to 3x3, 3x3x5 and the last cable stage of ITER conductor: the petal (3x3x5x5+3x4). This paragraph is devoted to introduce and discuss this approach.

3.3.1 Presentation of the different models

a. Different numerical codes

The authors mention the numerical issues usually faced up by the different codes to consider the contact interactions between a great number of beams. For this reason, three different finite element codes are used so as to cross check their results. These are: LS-DYNA, ABAQUS/Explicit and MSC.Marc. Three types of finite element are used by the model to represent the wires and the contacts between them:

- *3D linear solid elements* (eight nodes per element, four element per strand radius) and *contact elements* (surface-surface, the contact is checked pointwise, at the positions of the nodes),
- *beam elements* (two nodes per beam and 6 degrees of freedom per node) and *gap contact elements* (situated on the nodal positions),
- *beam elements* surrounded by *shell elements* representing the surface of the strands, and dedicated to support contact interactions, where connections between beam and shell nodes are modelled by so-called "*tie constrained*" elements in Abaqus.

The models take into account large strains and large displacements. The material properties correspond to the isotropic case with elastic or elasto-plastic material constitutive law.

b. Two different integration schemes to solve the problem

The codes may use two kinds of time integration schemes to solve the mechanical problem: the *explicit* or the *implicit* scheme. MSC. Abaqus can use either implicit or explicit solver, while LS-Dyna has only explicit solver and Marc is based on implicit solver.

3.3.2 Numerical issues with standard finite element method

a. Convergence problem of the code

On the one hand, the low computational cost of explicit time integration approach allows the use of a great number of solid elements – few hundred thousands. The explicit integration scheme does not automatically insure the convergence to the equilibrated solution in case of non linear problem e.g. contact problem or non linear constitutive law. The optimal speed of loading during the tensile test has to be found out. The loading speed should be slow enough not to produce unexpected dynamic effects but fast enough to limit the number of time integration steps and the error accumulation. On the other hand, the implicit algorithm guarantees the mechanical equilibrium is satisfied but results in a rapid increase in both computation power and memory requirements as the number of degrees of freedom increases. Besides, regarding the beam – gap element approach, implicit solvers are found to often face convergence problems when used in the large displacement framework, with a high number of contacts. The implicit approach was limited to the triplet and the 3x3 sub-cable. For larger cables, the use of the beam-shell elements is needed because it requires less computational time than the solid elements approach. However, the beam and shell model cannot take into account the transverse deformation of the strand cross-section during cable loading.

b. The issues with boundary conditions of the cable

The boundary conditions applied at the ends of the strands are presented. Along the axial direction, the strands are fully bounded at one side and free at the other. A tensile force can be applied to one side of the strands. In that case, the strand ends are free to move along the radial direction so as to allow the compaction but are locked along the circumferential direction in order to avoid the detwisting effect.

c. The issues of the initial geometry

Since the trajectories of the strands inside a tight cable are *a priori* not known, the model should compute it at first. The difficulties come from the high degree of compaction of the cable that should be considered (void fraction of ~32%). Regarding triplet and 3x3 cable, analytical formulations describe the initial geometry. But for larger cable, the theoretical configuration leads to work with highly loose structures that are not representative of cable inside the conduit. To compute the initial tight geometry, a tensile force is applied to the strand ends. After the tensile loading, the cable compacts itself in its radial direction. The compacted cable defines the new initial cable geometry for a second tensile test.

3.3.3 The numerical results

Regarding the axial behavior of the triplet, the results of the models correspond to the expectation from analytical formulation (elastic, without friction consideration). For the triplet, the different models and integration schemes are producing very similar results. For the test of the 3x3, the results start to differ from one method to another. Eventually for larger cable, there is no more analytical formulation and there is large discrepancy between the axial force-displacement curves of the open and tighter cable. The authors emphasize the large effect of the initial compaction of the cable on the tensile test result. The tensile test of 3x3x4 cable is performed using beam and gap model with good agreement with experimental data. However, only monotonic loading is performed.

3.3.4 Main problems of the simulation

For cables composed of more than 3 stages, the result of the tensile test largely depends on the initial compaction of the cable. The models of cable presented here control the void fraction until a certain point but do not reach the required void fraction. All approaches face issues regarding the modelling of the contact interactions.

3.4 Finite element approach with Multifil code

Another approach for the simulation of the mechanical behavior of cabled structures by means of finite element simulation has been proposed with Multifil software. Initially developed for simulating the mechanical behaviour of metallic wire ropes, the software has been extended to consider different kinds of entangled media. Using an implicit solver, Multifil models each fibre or wire in the studied structure by means of a kinematically enriched beam model. The methods and algorithms which have been developed to account for contact-friction interactions between wires allow assemblies of wires made of few hundred fibres to be handled, [Durville 2004-05]. Preliminary studies demonstrated Multifil's ability to deal with the assessment of local strains in ITER conductors subjected to different loading cases. The work of the present thesis is aimed at developing new features to improve the capabilities of the code to simulate more realistic cases and to help to better understand and optimize the performances of the ITER conductors.

Chapter II: Multifil modelling of Cable-in-Conduit Conductor

This chapter aims at introducing the main features of the Multifil code as well as its application to the modelling of cable-in-conduit conductors. The different steps of the modelling, from the shaping of the cable to the simulation of the operating conditions of the conductor are here presented. The work done in this thesis to develop the transverse boundary conditions dedicated to the conductor modelling are also described, supported by the analysis of their effects on the results of the cable shaping.

1 Introduction to the Multifil code

1.1 Introduction to the mechanical problem

Multifil code solves the mechanical equilibrium of assemblies of fibers submitted to large transformations, modelling each individual fiber. The code can handle up to few hundreds of fibers that interact with each other by contact and friction interactions. The behavior of the fibers and their contact/friction relations rely on mechanical models and related material constitutive laws. The assembly of beams is loaded by means of proper boundary conditions applied to each strand end or by moving rigid tools interacting by contact with the strands. The application of body force is also available to simulate the magnetic loading. The mechanical problem is formalized using the Virtual Work Principle in the framework of the large transformations and solved using the finite element method with an implicit resolution scheme [Durville 2003], [Durville 2004], [Durville 2005].

1.2 Formalisms of the mechanical problem

1.2.1 Beams domain

The assembly of beams that is concerned by the modelling is composed of N beams. In the reference configuration, the domain $\Omega_R^{(i)}$ of a beam i is characterized by its radius r and its length L. A material particle $\boldsymbol{\xi}$ in this domain is defined by its coordinates (ξ_1, ξ_2, ξ_3) in a direct orthogonal basis (0, $\mathbf{e_1}$, $\mathbf{e_2}$, $\mathbf{e_3}$):

$$\Omega_R^{(i)} = \left\{ \boldsymbol{\xi} = \xi_1 \mathbf{e_1} + \xi_2 \mathbf{e_2} + \xi_3 \mathbf{e_3} \quad , \quad {\xi_1}^2 + {\xi_2}^2 \le r^2 \, , 0 < \xi_3 < L^{(i)} \right\} \qquad \textbf{eqn. 2.1}$$

At each time t, this configuration is transferred by bijection toward a current configuration $\Omega_t^{(i)}$. The boundary of the beam's domain is divided into three parts: $\Gamma_u^{(i)}$ and $\Gamma_f^{(i)}$ are respectively the boundary surfaces for which the displacements are blocked and the forces are applied, whereas the surface $\Gamma_{c,j}^{(i)}$ is the part of the beam i that is possibly in contact with the beam j.

$$\partial\Omega_t^{(i)} = \Gamma_u^{(i)} \cup \Gamma_f^{(i)} \cup \Gamma_{c,j}^{(i)} \qquad \textbf{eqn. 2.2}$$

The contact domain $\Gamma_{c,j}^{(i)}$ is the union of two parts of beams about to interact. For a beam i and j for instance such domain is noted:

$$\Gamma_c^{(i,j)} = \Gamma_{c,j}^{(i)} \cup \Gamma_{c,i}^{(j)} \qquad \textbf{eqn. 2.3}$$

In this domain $\Gamma_c^{(i,j)}$, the contact-friction interaction that occurs between two material particles $\xi^{(i)}$ and $\xi^{(j)}$ of the beams *i* and *j* is assumed to result into two opposite forces:

$$\mathbf{R_{j\to i}}\left(\xi^{(i)},t\right) = -\mathbf{R_{i\to j}}\left(\xi^{(j)},t\right) \qquad \textbf{eqn. 2.4}$$

1.2.2 Virtual work principle

For each beam *i* of the assembly, the classical strong formulation of the mechanical equilibrium in the deformed configuration is expressed using the Cauchy stress tensor **σ** and the external unit normal **n** as follows:

$$\begin{cases} -div\,\boldsymbol{\sigma} = 0 & \text{on} \quad \Omega_t^{(i)} \\ \boldsymbol{\sigma}.\mathbf{n} = \mathbf{R_{j\to i}}\left(\xi^{(i)},t\right) & \text{on} \quad \Gamma_{c,t}^{(i,j)} \\ \boldsymbol{\sigma}.\mathbf{n} = \mathbf{f} & \text{on} \quad \Gamma_{f,t}^{(i)} \end{cases} \qquad \textbf{eqn. 2.5}$$

The variational formulation applied to the first equation leads to the Virtual Work Principle expressed in the current configurations with **v** a virtual displacement.

$$-div\,\boldsymbol{\sigma} = 0 \;\Leftrightarrow\; -\int_{\Omega_t^{(i)}} div\,\boldsymbol{\sigma}\cdot\mathbf{v}\,d\Omega_t^{(i)} = 0 \qquad \textbf{eqn. 2.6}$$

The application of the Green theorem on this relation makes appear the contributions of the different parts of the domain. After arrangement, it comes:

$$\int_{\Omega_t^{(i)}} \boldsymbol{\sigma} : \frac{D\mathbf{v}}{D\mathbf{u}}\,d\Omega_t^{(i)} - \int_{\Gamma_{c,t}^{(i,j)}} \mathbf{R_{j\to i}}\left(\xi^{(i)},t\right)\cdot\mathbf{v}\,d\Gamma_t^{(i)} = \int_{\Gamma_{f,t}^{(i,j)}} \mathbf{f}\cdot\mathbf{v}\;\; d\Gamma_t^{(i)} \qquad \textbf{eqn. 2.7}$$

From this relation, the problem is then to find the kinematically admissible displacement **u** so that for all corresponding virtual displacement **v**, the virtual work of the internal forces balances the virtual work of the external forces.

In the large transformation framework, the internal forces are described according to the deformation gradient tensor **F**, the Green-Lagrange strain tensor **E**, the second Piola-Kirchhoff stress tensor **s** and the Jacobian determinant *J* of **F** that read:

$$\begin{cases} \mathbf{F}\left(\mathbf{u}\right) = \mathbf{I} - \nabla\mathbf{u} \\ \mathbf{E}\left(\mathbf{u}\right) = \dfrac{1}{2}\left(\mathbf{F}^T\cdot\mathbf{F} - \mathbf{I}\right) \\ \mathbf{s}\left(\mathbf{u}\right) = J\,\mathbf{F}^{-1}\cdot\boldsymbol{\sigma}\cdot\mathbf{F}^{-T} \\ J = \det\mathbf{F} \end{cases} \qquad \textbf{eqn. 2.8}$$

The relation between the tensors *s* and *E* is described by the Lamé equation that involves the Lamé coefficients μ and λ relative to the material properties:

$$\mathbf{s} = 2\mu\mathbf{E} + \lambda Tr(\mathbf{E})\mathbf{I} \qquad \text{eqn. 2.9}$$

It can also be expressed using the so-called stiffness tensor C as follows:

$$\mathbf{s}(\mathbf{u}) = \mathbf{C}(\mathbf{u}) : \mathbf{E}(\mathbf{u}) \qquad \text{eqn. 2.10}$$

The stiffness tensor can be written using the Lamé coefficients with the Kronecker delta:

$$\mathbf{C}_{ijkl} = 2\mu\delta_{ik}\delta_{jl} + \lambda\delta_{ij}\delta_{kl} \qquad \text{eqn. 2.11}$$

Modifying the first term of the eqn 2.7 in order to make appear the tensor **s** and **E** and express it in the initial configuration yields:

$$\int_{\Omega_0^{(i)}} Tr\left(\mathbf{s}(\mathbf{u})\frac{D\mathbf{E}}{D\mathbf{u}}\cdot\mathbf{v}\right)d\Omega_0^{(i)} - \int_{\substack{\Gamma^{(i,j)}\\ c,t}} \mathbf{R}_{\mathbf{j}\to\mathbf{i}}\left(\xi^{(i)},t\right)\cdot\mathbf{v}\, d\Gamma_t^{(i)} = \int_{\substack{\Gamma^{(i,j)}\\ f,t}} \mathbf{f}\cdot\mathbf{v}\, d\Gamma_t^{(i)} \qquad \text{eqn. 2.12}$$

This equation in the variational formulation of one beam *i*. The global formulation for the assembly consists of a summation over every beam as follows:

$$\sum_{i=1}^{N}\int_{\Omega_0^{(i)}} Tr\left(\mathbf{s}(\mathbf{u})\frac{D\mathbf{E}}{D\mathbf{u}}\cdot\mathbf{v}\right)d\Omega_0^{(i)} = \sum_{i=1}^{N}\sum_{j=i+1}^{N}\int_{\substack{\Gamma^{(i,j)}\\ c,t}} \mathbf{R}_{\mathbf{j}\to\mathbf{i}}\left(\xi^{(i)},t\right)\cdot\mathbf{v}\, d\Gamma_t^{(i)} + \sum_{i=1}^{N}\int_{\substack{\Gamma^{(i,j)}\\ f,t}} \mathbf{f}\cdot\mathbf{v}\, d\Gamma_t^{(i)} \qquad \text{eqn. 2.13}$$

The non-linear eqn. 2.13 is numerically solved using the finite element method with an implicit scheme of resolution (Newton-Raphson) to approach the solution.

1.3 Enriched kinematic beam model

In Multifil, a fiber is represented by a specific beam model that makes use of enriched kinematics. In the domain defined by eqn. 2.1, the placement $\mathbf{x}(\boldsymbol{\xi})$ of any material particles $\boldsymbol{\xi}$ identified by its curvilinear abscissa along the beam axis ξ_3 and its transverse coordinates (ξ_1 and ξ_2) in the cross-section is expressed as a first order Taylor expansion with respect to transverse coordinates and reads:

$$\begin{aligned}\mathbf{x}(\xi,t) &= \mathbf{x}\left((0,0,\xi_3),t\right) + \xi_\alpha\frac{\partial\mathbf{x}\left((0,0,\xi_3),t\right)}{\partial\xi_\alpha} + o(\xi_\alpha) \quad , \quad \alpha = 1,2 \\ \mathbf{x}(\xi,t) &= \mathbf{x_0}\left(\xi_3,t\right) + \xi_\alpha\mathbf{g}_\alpha\left(\xi_3,t\right)\end{aligned} \qquad \text{eqn. 2.14}$$

In this expression, $\mathbf{x_0}(\xi_3,t)$ is the placement of the centroid of the cross-section and $\boldsymbol{g}_\alpha$ are the directors of the cross-section. The displacement of a material particle $\boldsymbol{\xi}$ is defined by:

$$\begin{aligned}\mathbf{u}(\xi,t) &= \mathbf{x}(\boldsymbol{\xi},t) - \mathbf{x}(\boldsymbol{\xi},0) \\ &= \mathbf{x_0}\left(\xi_3,t\right) - \mathbf{x_0}\left(\xi_3,0\right) + \xi_\alpha\left(\mathbf{g}_\alpha\left(\xi_3,t\right) - \mathbf{g}_\alpha\left(\xi_3,0\right)\right) \\ &= \mathbf{u_0}\left(\xi_3,t\right) + \xi_\alpha\mathbf{h}_\alpha\left(\xi_3,t\right)\end{aligned} \qquad \text{eqn. 2.15}$$

The kinematics of each cross section is described by the means of three vectors (nine degrees of freedom): the translation vector $\mathbf{u_0}$ and the vectors $\mathbf{h_1}$ and $\mathbf{h_2}$ standing for the variations of the two cross section directors. This kinematic is used for the determination of the Green-Lagrange strain tensor.

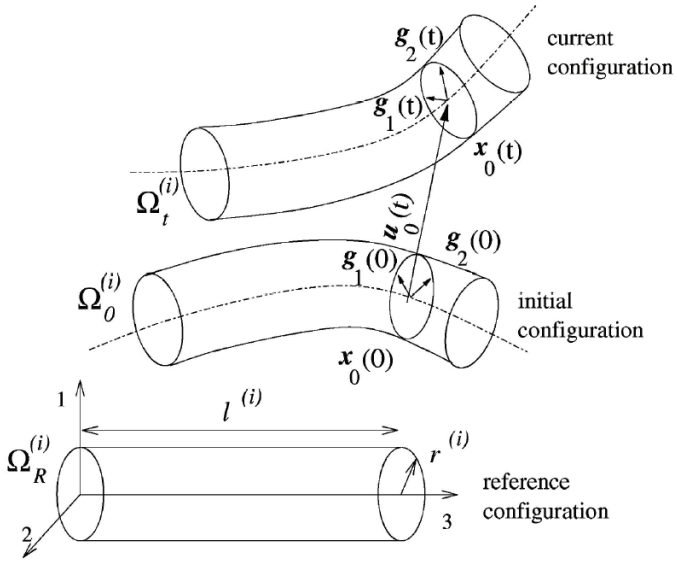

Fig. 2.1. Enriched beam model, [Durville 2005].

This enriched kinematical beam model allows considering a full three dimensional strain tensor at any point of the fibers. The standard beam deformations, namely the axial, bending and shear strains are accounted for by the beam model. The enriched kinematic also allows to take into account plane transverse deformations of the beam cross-section. Under contact loads, an initially circular beam cross-section can deform into an ellipse, while remaining plane. Several types of constitutive laws can be used with this beam model. As far as the elastic behavior is concerned, either an isotropic or a transverse isotropic constitutive law, with two different Young's moduli in longitudinal and transverse directions, can be considered. For the consideration of plasticity, due to the limits of the kinematical beam model, it has been chosen to restrict the modelling of plastic effects to longitudinal components of strain and stress tensors. The reason is that, accordingly to the kinematical beam model, all components of the strain tensor do not have the same polynomial degree with respect to transverse coordinates. In particular, transverse strains $E_{\alpha\beta}$ $((\alpha,\beta) \in \{1,2\})$ are assumed to be constant throughout the cross-sections, whereas longitudinal strains E_{33} express quadratically as function of transverse coordinates. The taking into account the incompressibility of plastic flow, which involves these components of different orders with respect to transverse coordinates, would lead to a locking that would drastically limit the axial strains.

1.4 Contact modelling

1.4.1 The contact detection

As exposed in the 1.1.2, there are specific issues in modelling contact between a large number of beams. Modelling contact is a twofold problem. First the positions of the contacts have to be detected and then the interaction forces developed at these locations have to be computed through appropriate models. Regarding contact detection, the Multifil original method is presented hereafter.

1.4.2 Definition of a proximity zone

The proximity zones of the contact model aim at defining intermediate geometries in the regions where contact is likely to occur. A proximity zone is made of a pair of parts of beam centerlines that are stated to be close enough to each other. The proximity zones are determined by the computation of the distance between beams. For each pair of beams (*i*,*j*), the neutral axis of the first beam *I*, taken under its interpolated form by finite element shape functions, is first coarsely discretized to define control points from which the distance between beams is next calculated. For each of these control points, the distance to the closest point on the opposite beam is computed; the closest point being either an extreme node of a finite element or an orthogonal projection of the initial control point onto a finite element. A proximity zone is then defined by two intervals on beams *i* and *j* bordered by successive pairs of close points. Once all pairs of beams have been treated, one gets a set proximity zones *PZ* delimited by their extreme points *a* and *b* relative to each pair of beams parts:

$$PZ^{(k)} = \left[a^{(i)}, b^{(i)}\right] \times \left[a^{(j)}, b^{(j)}\right] \qquad \textbf{eqn. 2.16}$$

Where, $[a^{(i)},b^{(i)}]$ and $[a^{(j)},b^{(j)}]$ are two intervals of curvilinear abscissa defined on beams *i* and *j* that are close enough.

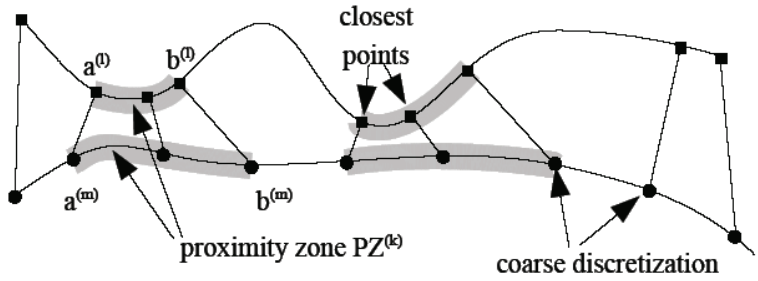

Fig. 2.2. Definition of the proximity zones [Durville 2005].

1.4.3 Definition of the intermediate geometry

Once the proximity zones have been generated, intermediate geometries that aim at approximating the unknown actual geometry of contact are created. For a proximity zone an intermediate geometry Γ_g is defined as the average of the centerlines of two close parts of beam $[a^{(i)},b^{(i)}]$ and $[a^{(j)},b^{(j)}]$ associated in the proximity zone – see Fig. 2.3. The position $\mathbf{c}(s)$ of any point on Γ_g identified by its relative curvilinear abscissa *s,* is defined as the middle point between the two points at the same relative abscissa on both parts of beams:

$$\mathbf{c}(s) = \frac{1}{2}\left[\mathbf{x}_0^{(i)}\left(\left(1-s\right)a^{(i)} + s\,b^{(i)}\right) + \mathbf{x}_0^{(j)}\left(\left(1-s\right)a^{(j)} + s\,b^{(j)}\right)\right] \qquad \textbf{eqn. 2.17}$$

The tangent to the intermediate geometry at the relative abscissa *s*, $\mathbf{T}_c(s)$, is obtained by derivating the above expression.

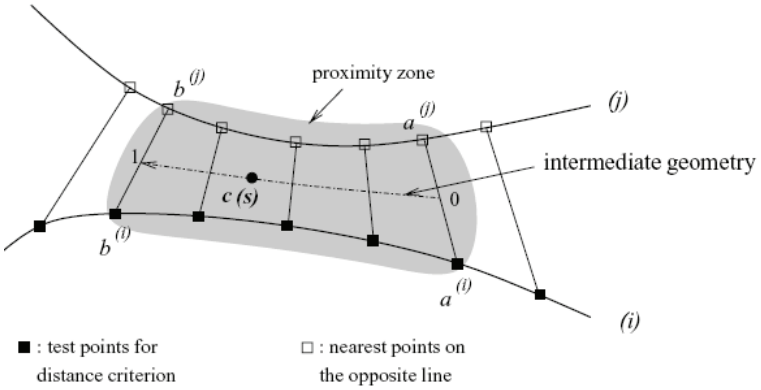

Fig. 2.3. Definition of the intermediate geometry. [Durville 2005]

1.4.4 Beam sections candidates to contact

The contact elements are created with respect to the intermediate geometries. The contact is chosen to be checked at some discrete points distributed on the intermediate geometry. If quadratic elements are used for the beams, the discretisation size between two contact elements is taken equal to the half of the smaller element size on both beams. Each check point denoted $\boldsymbol{x}_c$ is defined by its relative abscissa s_c on the intermediate geometry relative to a contact zone:

$$s_c = \frac{(1-k)}{(N_c - 1)} \qquad \textbf{eqn. 2.18}$$

Where k is the number of the point within the zone and N_c the total number of contact elements to be generated for this zone. The question is to find out the particles, i.e. the locations of the contact points that may be predicted to come to contact at the check points $\boldsymbol{x}_c$. These particles are situated at the border of two sections of contacting beams that should be determined now. The pairs of cross-sections are assumed located at the intersections between the normal plane at the point $\boldsymbol{x}_c$ to the intermediate geometry and the beam centerlines. These intersections define the two centroids of the beam cross-sections candidate to contact – see Fig. 2.4. The next issue is now to determine where the particles of the contact elements are situated on these sections.

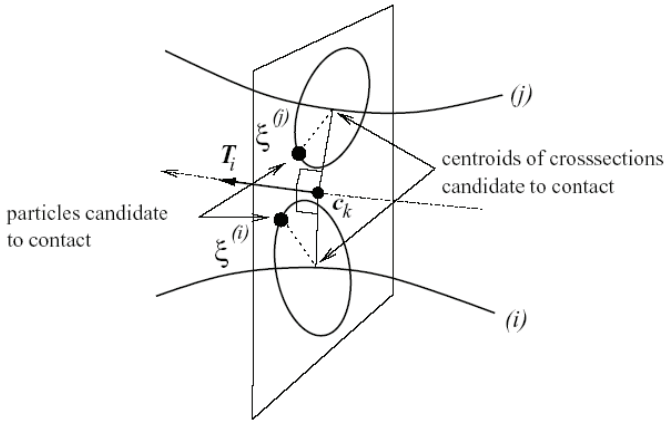

Fig. 2.4. Cross-sections candidate to contact [Durville 2005].

1.4.5 Contact particles determination

The contact elements are dedicated to point out the two particles of interacting beams that are predicted to come into contact at a given point of the intermediate geometry. The contact particles ξ_1 and ξ_2 are situated on the border of the beam cross-sections – see Fig. 2.4 and Fig. 2.5. In an equilibrium configuration, contact particles should have the same position on the intermediate geometry.

$$x(\xi_1) = x(\xi_2) = x_c \qquad \textbf{eqn. 2.19}$$

However, as contact elements have to be defined in out-of-equilibrium configurations, the positions of the contact particles can no longer be characterized by their identical positions, but must be predicted through appropriate geometric constructions. In the model, the particles of contact elements are chosen to be located on the contour of each cross-section candidate to contact, at the intersection with the projection of the direction between the two centroids on the cross-section, as shown in Fig. 2.5.

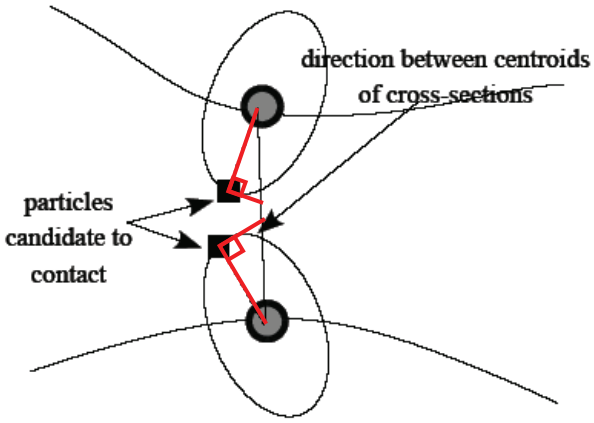

Fig. 2.5. Particle candidates to contact. [Durville 2004]

1.4.6 Normal contact direction and kinematical contact condition

A normal contact direction, denoted $\mathbf{N}_{12}$, standing for the direction along which the distance between particles will be measured, has to be defined and attached to each contact element. The role of this normal direction is to prevent beams to cross through each other. If the local angle between beams is large enough, the cross product between the tangent vectors to the centerlines of beams provides with a good normal contact direction. As the angle between beams gets smaller, the cross product between tangent vectors is less relevant, and the direction between the centroids of cross-sections candidate to contact can be used instead. The normal contact direction is used to set the kinematical contact condition to be prescribed to contact elements. This condition requires that the gap between contact particles, defined as the distance between these particles measured along the normal contact direction $\mathbf{N}_{12}$ must remain positive. This condition is expressed as follows:

$$g(x_c) = \left(\mathbf{x}(\xi_2) - \mathbf{x}(\xi_1), \mathbf{N_{12}}(x_c)\right) \geq 0 \qquad \textbf{eqn. 2.20}$$

According to this condition, contact particles are not allowed to cross a plane orthogonal to the direction $\mathbf{N}_{12}$.

1.4.7 The mechanical models for contact and friction

a. Regularized penalization with contact stiffness adaptation for the normal direction of the contact

A mechanical model is required to transform the kinematical contact conditions into interaction forces whose role is prevent interpenetration between beams when contact conditions are violated. A penalty method is used in Multifil to model contact interactions. Two improvements are made to the standard penalty method: a regularization at the origin by a quadratic function, and an adaptation of the penalty coefficient. In standard penalty methods, the contact reaction is taken proportional to the normal gap, with a penalty coefficient k. But the transition between contact and non contact status induces a discontinuity in the normal contact stiffness that may deteriorate the convergence of contact algorithms. The solution is brought by the introduction of a regularization of the linear contact reaction for small penetrations. For the penetrations of magnitude lower than a regularization depth g_{rg} , the contact reaction is taken quadratic with respect to the gap. The amplitude of the normal reaction is calculated as follows using the contact stiffness coefficient k – see Fig. 2.6.

$$g \geq 0 \Rightarrow F_N = 0$$

$$g_{rg} \leq g < 0 \Rightarrow F_N = \frac{k}{2g_{rg}} g^2$$

$$g < g_{rg} \Rightarrow F_N = -k(g + \frac{g_{rg}}{2})$$

eqn. 2.21

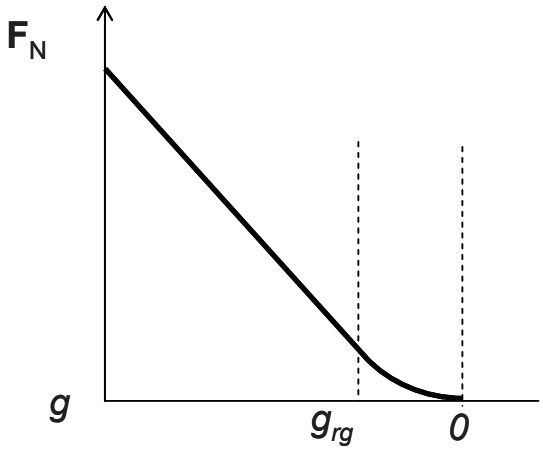

Fig. 2.6 . Regularized penalization model for the normal direction of the contact to prevent the beams to interpenetrate.

This regularization ensures a continuity of the derivative of the normal reaction at the origin. Despite of the expected variation of the contact loads magnitude, a stability of the penetrations is sought. For this reason, instead of a contact model where the penalty coefficient would be fixed, a control of the maximum penetration within each proximity zone is chosen. The idea is to adapt the penalty coefficient k so as to control the maximum penetration registered on each proximity zone. For each proximity zone, the maximum penetration measured by the contact elements should not exceed a given penetration defined by the maximal allowable penetration g_{max} of the model. The value of g_{max} should be sufficiently small compared to the radius of the beam so that the errors made on the contact geometry do not impact the global behavior of the system. For a given zone, the adaptation of

k relies on the maximum penetration measured by the contact elements. The procedure is first to measure the maximum penetration, denoted g_m , for each proximity zone. The coefficient k is then adapted so that g_m tends toward g_{max} as follows:

$$k^{n+1} = \frac{g_m}{g_{\max}} k^n \qquad \textbf{eqn. 2.22}$$

For g_{max}, a value of 5 times the regularization depth g_{rg} seems to be relevant value when g_{rg} is set below 1% of the beam radius. The adaptation of the local contact penalty coefficient is performed regularly at the end of each loop on the determination of the normal contact directions.

b. Regularized Coulomb model for the tangential direction of the contact

The tangential behavior of contact depends on the tangential relative displacements between the two particles. This displacement is defined according to the contact normal as follows:

$$\mathbf{u}^T(x_c) = \left[\mathbf{I} - \mathbf{N_{12}}(\mathbf{x_c}) \otimes \mathbf{N_{12}}(\mathbf{x_c})\right]\left(\mathbf{u}(\xi_2) - \mathbf{u}(\xi_1)\right) \qquad \textbf{eqn. 2.23}$$

Where, $\mathbf{u}$ (ξ_1) and $\mathbf{u}$ (ξ_2) are the displacements of the contact particles. A regularized Coulomb model is used to simulate the stick and slip behavior: a short reversible elastic displacement (few microns) is considered before gross slipping occurs. The friction model involves two parameters, the maximum allowed reversible tangential displacement and the coefficient of friction – see Fig. 2.7.

$$\begin{cases} \left\|\mathbf{u}^T(x_c)\right\| \le u_{rev}^T \Rightarrow \mathbf{F_T} = \dfrac{\mu\left\|\mathbf{N_{12}}\right\|}{u_{rev}^T}\mathbf{u}^T(\mathbf{x_c}) \\ \left\|\mathbf{u}^T(x_c)\right\| > u_{rev}^T \Rightarrow \mathbf{F_T} = \dfrac{\mu\left\|\mathbf{N_{12}}\right\|}{\left\|\mathbf{u}^T(\mathbf{x_c})\right\|}\mathbf{u}^T(\mathbf{x_c}) \end{cases} \qquad \textbf{eqn. 2.24}$$

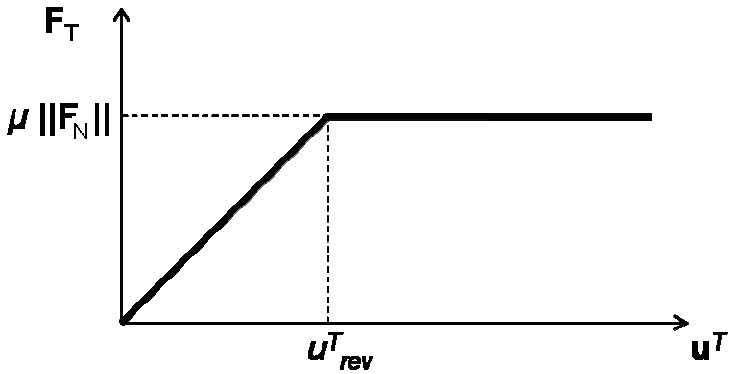

Fig. 2.7 . Regularized Coulomb model for the tangential direction to simulate the friction effects.

1.4.8 Consideration of contact with rigid tools

Multifil code offers the possibility to model rigid surfaces that can interact by contact with the beams. These surfaces are referred as the tools of the model. The tools are defined as plane or cylindrical analytical surfaces. Unlike the contact determination between beams, the contacts with the tools are here taken into account at the nodes of the beam elements. The contact

reaction between beams and tools follow the regularized penalty method in the normal direction, with an adaptation of the penalty coefficient for each proximity zone. Because the surface of analytical tools may change from one step to the next, it is not possible to keep track of the material particle of the tool in contact with a given node of a beam. For this reason the increment of relative tangential displacement between a beam node and a tool cannot be computed, and friction effects cannot be directly considered. Instead of that, to limit tangential displacements at the interface with the tools, it has been chosen to implement a tangential stiffness acting on increments of tangential displacements. $\mathbf{t_1}$ and $\mathbf{t_2}$ being two unit tangent vectors to the tool surface at the location of contact, a tangential reaction force $\boldsymbol{F}_{T,tool}$ is computed as follows:

$$F_{T,tool} = -k_T\left((\Delta\mathbf{u}^n \cdot \mathbf{t_1})\mathbf{t_1} + (\Delta\mathbf{u}^n \cdot \mathbf{t}_2)\mathbf{t}_2\right) \qquad \textbf{eqn. 2.25}$$

Where, $\Delta\mathbf{u}^n$ is the increment of displacement of the node and k_T is the tangential stiffness. This tangential stiffness is taken to half the normal contact stiffness.

1.5 Algorithm

The major issue is to find out an algorithm that allows converging toward the solution. The computation algorithm is composed of three nested loops that are respectively dedicated to the determination of contact elements, then the determination of contact normal directions and finally to the solving of the nonlinear problem with fixed contact conditions:

1. Contact positions determination
2. Contact normal determination
3. Newton-Raphson solving

This iterative process is used to approximate, step by step, the mechanical equilibrium of the whole structure for a given loading step until the solution converges. The number of loops for the three parts of the resolution may vary from one structure to another and depends on the loading increment size.

2 Multifil simulation of superconducting cable-in-conduit conductors

2.1 The different phases to be simulated with Multifil

2.1.1 The initial configuration of cables inside the conduit

The trajectories of the strands inside cable-in-conduits cannot be known *a priori* and thus need to be calculated in a way. The first part of the modelling is then dedicated to the computation of a *geometry of cable* relevant to ITER conductor design. In the real process, the different stages sub-cables are produced by successive cabling machines. The triplets are first cabled and then spooled. The same procedure is used for the next stages: the triplet strands form the second stages and so on. The final assembly is inserted inside the jacket by pulling the cable inside. Eventually the cable-in-conduit is compacted to its final cable void fraction by passing through a die. Since it is not conceivable to reproduce with the code the whole cabling, jacketing and hammering processes, an equivalent route is proposed to shape a cable. This shaping part of the simulation is presented in 2.2.1.

2.1.2 The effect of the heat treatment

The real manufacturing process induces important deformation of the cabled strands with the occurrence of permanent pinching at the contacts and plastic strains. During the heat treatment, the temperature is sufficient to cause the annealing of the different materials. The annealing implies the relief of the internal stresses accumulated in the various materials (mainly copper and bronze) during the manufacturing. The heat treatment aims at creating the Nb_3Sn superconducting phase in the filaments of the strands. The alloying reaction and the annealing of the material imply a change of the properties of the materials, from unreacted to reacted strands and from copper to *Oxygen-free high thermal conductivity,* OFHC copper wires. After the heat treatment and before the cool-down, all stresses in the strands of the conductor are assumed to be zero. In Multifil, a part of the modelling aims at setting such virgin state to a shaped cable as explained in 2.2.2.

2.1.3 The different loadings of conductors along its service life

a. The thermal compression

During the cool-down of the conductor, from the heat treatment temperature of 900 K to operating temperature of 5 K, the differential of thermal shrinkage between the jacket and the cable is assumed to result in a compression applied to the cable. The simulation of the cable axial compression is developed in 2.2.3.

b. The cyclic magnetic loading

In ITER conductors, the current that flows in the superconducting strands combined with the presence of an external magnetic field produces a Lorentz force that acts orthogonally to the strands. The Lorentz forces are classically calculated by the cross product of the field B by the current I_s along the strands, e.g. with a current of I_s = 100 A per strands in the B = 11 T background magnetic field, the local Lorentz F_L is 1.1 N/mm. During their service life, the conductors are submitted to several thousand Lorentz loading cycles. The simulation of the magnetic effect by Multifil is exposed in 2.2.4.

2.2 The different steps of the simulation

2.2.1 The shaping

a. Definition of the initial beam assembly

The first part of ITER conductor modelling is about the definition of an initial configuration for the beam assembly. The idea is to have a geometrical description of an assembly that fulfills the arrangement according to successive stages with different twist pitches. In the proposed model of cable, the initial configuration is theoretically described by helices recursively defined on helices to represent the different cabling stages. A standard helix is parameterized by its curvilinear abscissa s, and defined by its radius r_h and its twist pitch p_h. The recursive formulation for the successive stages of a cable made of N stages can be parameterized as follows:

$$\mathbf{x}(s) = \sum_{i=1}^{N} \left\{ r_h^i \left[cos\left(2\pi \frac{s}{p_h^i} + \varphi_0^i \Big|_{random} \right) \mathbf{e_1} + sin\left(2\pi \frac{s}{p_h^i} + \varphi_0^i \Big|_{random} \right) \mathbf{e}_2 \right] \right\} + s\,\mathbf{e}_3 \qquad \textbf{eqn. 2.26}$$

The variable r_h^i ϕ_0^i stands for the helix radius and initial angle for the helices of each stage. As an example, Fig. 2.8 illustrates the result obtained for a 100 mm long sample containing three stages with a 3x3x5 cabling pattern and the following twist pitche sequence {45x85x125x180} (mm).

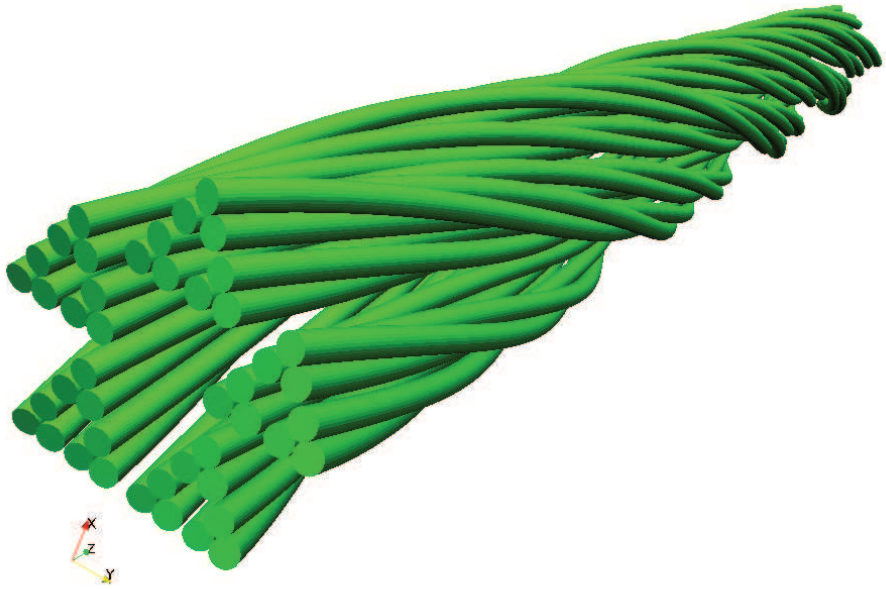

Fig. 2.8. Theoretical initial configuration of a 3x3x5 cable 100mm long.

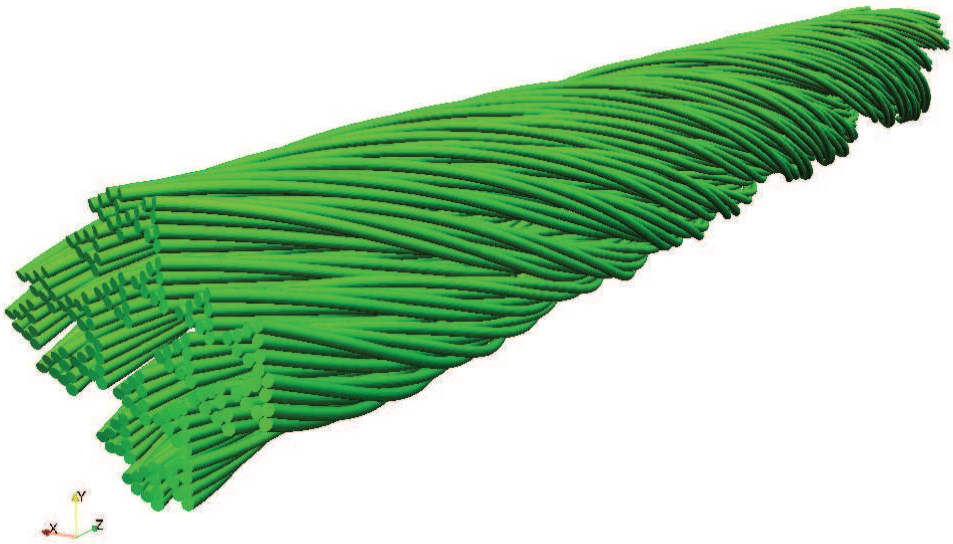

Fig. 2.9 . Theoretical initial configuration of a 3x3x5x4 cable 150mm long.

b. Use of rigid tool to shape the initial assembly

The available tools of Multifil can be used in order to shape the assembly of beams and to model the presence of the outer conductor's jacket. The driving of the tools motion allows deforming the assembly through the contact conditions. Regarding cable-in-conduit modelling, the idea is to deform the theoretical initial configuration of the cable by the means of cylindrical and plane tools. In order to get a round cable, the tool can be a cylinder around the assembly. The loading of the structure then consists in the decreasing of the diameter of this cylinder. The induced displacement aims at compacting the assembly until a given void fraction.

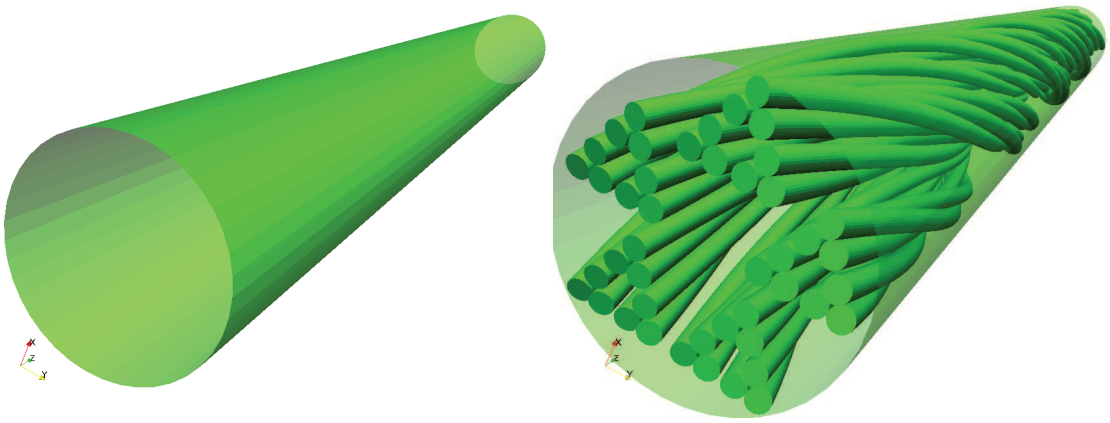

Fig. 2.10 . Illustration of cylindrical tool around initial strand assembly (3x3x5).

In the same way, a square cable can be obtained using four plane tools as the four faces of a parallelepiped. The lateral displacements of the tools deform the structure.

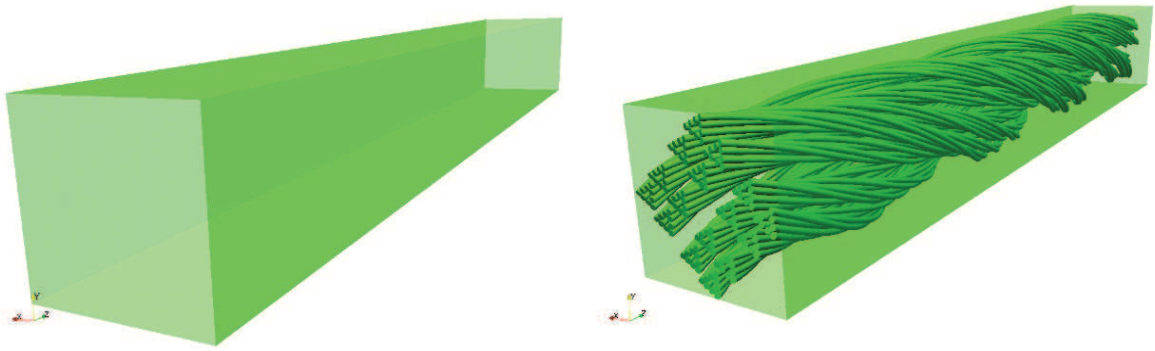

Fig. 2.11 . Illustration of square tool around initial strand assembly (3x3x4x4).

The combination of cylindrical and plane tools allows deforming the structure into a petal-like shape.

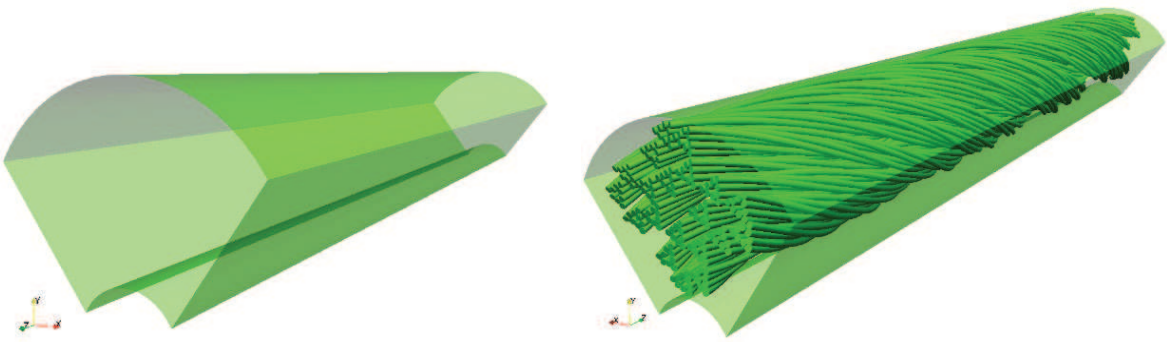

Fig. 2.12 . Illustration of petal tool around initial strand assembly (3x3x5x4).

c. *Gradual compaction of the initial assembly*

The Multifil procedure, referred to as the shaping process, performs the compaction of the initial cable configuration by the means of rigid tools and proper boundary conditions. The transverse stiffness of the assembly increases as the cable gets more compact. Constant increments of displacement for the tools during the compaction do not seem convenient, because the convergence deteriorates as the compaction progresses. To have a more constant evolution of internal stresses in the cable, it has been chosen to decrease the increment of displacement applied to the tool according to a geometric progression. Starting from an initial increment Δu_r^0, the increment Δu_r^n for the step n is calculated as:

$$\Delta u_r^n = w^n \Delta u_r^0 \qquad \textbf{eqn. 2.27}$$

Where w is taken lower than 1. As an example, for initial and final radius R_i = 5.2mm, R_f = 3.0mm, w = 0.97 and Δu_r^0 = 0.04 mm, the evolution of the tool's radius is illustrated in Fig. 2.13.

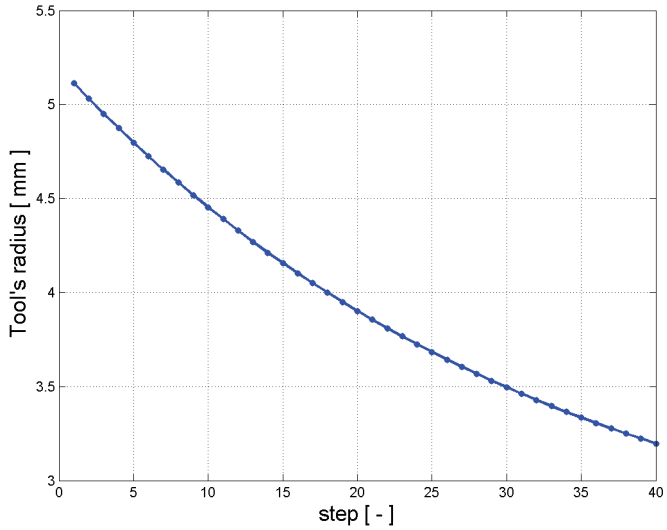

Fig. 2.13. Driving of the tool's radius during the shaping.

The void fraction VF of the cable can simply be derived with the tool's radius R_t, the radius of the strands r_s , the number of strand N.

$$VF_1 = \frac{R_t^2 - N \cdot r_s^2}{R_t^2} \cos(\theta) \qquad \textbf{eqn. 2.28}$$

where $cos(\theta)$ is the average angle between the axis of the beams with the cable axis $\mathbf{e_3}$.

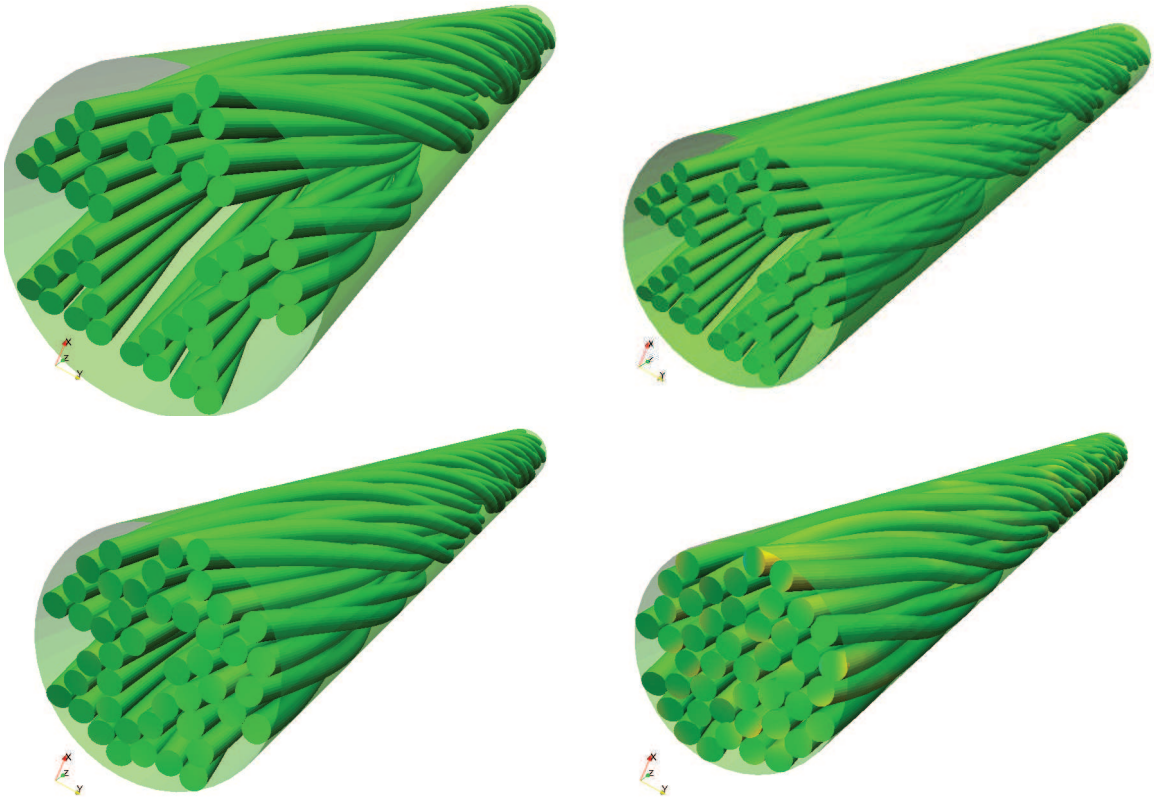

Fig. 2.14 . Example of the shaping of a round cable (3x3x5) up to VF=32%.

For simplicity, during the compaction, the material constitutive law corresponds to the elastic case (but rigorously, it should be plastic) with the Young's modulus equal to 100 GPa without considering the transverse deformation of the beams. The friction coefficient is taken equal to 0.05.

2.2.2 The stress reset

In the model, the material annealing effect is simulated by a reset of the local stresses that have been generated during the shaping process. The procedure consists in considering the last configuration at the end of the shaping as the new initial configuration at rest. Doing so, all stresses are reset to zero. After the reset of internal stresses, normal contact reactions vanish. Even if small penetrations induced by the efforts during the shaping process still exist, the adaptation of the contact stiffness is no longer relevant. The values of these contact stiffnesses, stored for each proximity zone, need however to be changed, since they correspond to the high interaction efforts exerted between beams at the end of the shaping. Going on with these values after the stress reset makes the contact algorithm very unstable. To solve this problem, at the same time of the stress reset, the contact stiffnesses are reset for all proximity zones to uniform value which should be low enough not to introduce artificial contact stiffness (induced by the remaining small penetration) but high enough to prevent large penetrations that would not be counteracted by the adaptation of the coefficients. The coefficients of the zones would not converge if the algorithm starts from too low value. The initial value of the coefficients after the reset is set to a few tens N/mm. At this stage of the modeling, the material properties are switched. Whereas the constitutive law for the strands was elastic during the shaping part of the modelling, the plastic behavior is introduced for the

rest of the modelling. The constitutive laws used for the superconducting strand and the pure copper wire are described in the Chapter 3.

2.2.3 Application of the axial loadings

Multifil can not address for the moment the thermo-mechanical problem of the determination of the thermal compression, since it does not take into account either the thermal expansion of the strands or the presence of a deformable jacket. In the model, the thermal effects are simply simulated by the application of an axial compression to the cable inside its conduit. More generally, the axial loading of cable is simulated imposing some axial displacements to the ends of the strands via the axial boundary conditions of the model. The tools simulate the presence of the jacket around the conductor. In real conductor, the cable and the jacket are assumed to be fully bonded during the cool down. For this reason, the tangential displacements of the nodes contacting the tools are penalized.– see 2.3. The amplitude of the compression that is used for the simulation of the ITER conductor comes from admitted results published in various papers [Mitchell 2003 a b], [Ciazynski 2007]. The conductor is loaded up to about -0.6~0.7% axial strain. The main advantage of the simulation is that it allows the effect of various applied compressions to be quickly checked.

2.2.4 Application of the Lorentz forces

The Lorentz loading is simulated by the application of loads along the strands. These loads point at one of the transverse directions ($\mathbf{e_1}$ or $\mathbf{e_2}$). In the model, an increment of force ΔF_L is applied at each step of the computation and is about 0.01 N/mm. The assumptions made by the simulation are here discussed. First, the model assumes uniformly distributed current among the strands of the conductors: the local forces are taken to be equal everywhere in the cable. But non-uniform currents may exist due to the presence of the joints that induce a transient zone before the currents balance between the strands. The variations of strain along the strands are also responsible for some current non-uniformity [Mitchell 2000 a], [Mitchell 2003 b]. In the SULTAN test facility, the magnetic field is not uniform, either along or across the conductors [Ilyin 2007 b]. In that sense, the model simplifies the problem by taking a constant Lorentz force everywhere in the cable. At last, the Lorentz forces are applied in a single direction, whereas they should theoretically act orthogonally to the strand axis, which is another simplification of the model. However, the approximation should be proportional to $(1-\cos\theta)$ which should not bring much difference. During the application of the Lorentz force loading, the thermal compression is maintained to its reference value. In that sense, the axial displacements of the strands are locked in the axial direction by the boundary conditions while the Lorentz forces are applied.

2.3 Issues related to the boundary conditions of the model

This paragraph presents the issues related to the modelling of the boundary conditions of the model. The main concepts relative to the boundary conditions are first illustrated for what regards the shaping part of the modelling. These concepts can then be extended to the other loading cases (axial and transverse).

2.3.1 Introduction of the boundary condition issues

In the proposed model of cable, Multifil considers samples of limited size due to the computation time. The model focuses on cables of few tens centimeters length using relevant kinematical conditions at the boundaries. The boundary conditions are needed so that the problem is well posed. The issue is then to define proper conditions that would simulate the effect of the non modelled parts at both sides of the cable model. The idea is that the strands at the ends behave as if the cable was running further. The boundary conditions aim to control the displacements of the nodes situated at the ends of the strands, in regards with the transverse ($\mathbf{e_1}$, $\mathbf{e_2}$) and the axial ($\mathbf{e_3}$) directions. The formalism relative to the boundary conditions of the Multifil cable model is exposed hereafter.

2.3.2 First approach of the boundary conditions

a. Along the longitudinal direction

Along the axial direction, the extreme nodes can be fully bonded, free or submitted to a displacement. To prescribe a given displacement δ along the axial direction 3 to a node *N,* the following kinematical condition is set:

$$\mathbf{u}_N^n \cdot \mathbf{e}_3 = \delta\,, \qquad \textbf{eqn. 2.29}$$

where $\boldsymbol{u}^n{}_N$ is the displacement of node *N*. In the following, for simplicity, the reference to the node *N* is assumed implicit and it is now omitted. Prescribing the value of the increment of displacement instead of the displacement itself comes to set the following condition:

$$\begin{aligned} &\Delta\mathbf{u}^n \cdot \mathbf{e}_3 = \delta \\ &(\mathbf{u}^n - \mathbf{u}^{n-1}) \cdot \mathbf{e}_3 = \delta \\ &\mathbf{u}^n \cdot \mathbf{e}_3 = \mathbf{u}^{n-1} \cdot \mathbf{e}_3 + \delta \end{aligned} \qquad \textbf{eqn. 2.30}$$

which is equivalent to the eq 2.26. replacing δ by $(\mathbf{u}^{n-1},\mathbf{e}_3) + \delta$. This condition is accounted for using a standard penalty method, consisting in adding to the energy of the system a binding energy *W* expressed as:

$$W = \frac{k}{2}(\mathbf{u}^n \cdot \mathbf{e}_3 - \delta)^2 \qquad \textbf{eqn. 2.31}$$

The corresponding virtual work writes:

$$\frac{dW}{d\mathbf{u}} \cdot \mathbf{v} = k(\mathbf{u}^n \cdot \mathbf{e}_3 - \delta)(\mathbf{v} \cdot \mathbf{e}_3) \qquad \textbf{eqn. 2.32}$$

And the corresponding axial reaction force acting on the node is expressed as:

$$\mathbf{F_{ax}} = -k(\mathbf{u}^n \cdot \mathbf{e}_3 - \delta)\mathbf{e}_3 \qquad \textbf{eqn. 2.33}$$

During the shaping, the strand ends are locked along the axial direction at one side of the cable whereas the other extremities are free along this direction. One of the cable sides is let free to prevent the buckling of the structure as the radial compaction is performed. A tensile loading could also be applied during the shaping even though this possibility has not been

explored during this thesis. This could help to reproduce the pulling of the cable during the manufacturing.

b. Along the transverse directions

The displacement of the strand ends are also controlled along the transverse direction ($\mathbf{e}_1$, $\mathbf{e}_2$). But it is obviously not possible to either fully lock extremities or let them completely free as it is for the axial direction. On the one hand, since the cable is compacted by the tool during the shaping, it would be meaningless to block the displacements in the transverse directions. On the other hand, if the extremities are let free then the cable tends to unwind itself during the shaping, and the initial coherence of the cable stages tends to be lost as the cable is compacted. This de-twisting effect is natural since the configuration of minimal energy corresponds to the case where the strands are straight and parallel. The strands tend to align to each other while the assembly is compacted if the transverse displacements are not constrained. To stop the unwinding, a first approach for the transverse boundary condition is to penalize the radial and the orthoradial displacements with the same method as for the axial direction. First, the radial and orthoradial directions, $\mathbf{e_r}$ and $\mathbf{e_\theta}$, relative to the node N are defined. Assuming the axis of the cable is identical to the third global axis, the unit radial vector $\mathbf{e}_r$ and the unit orthoradial vector $\mathbf{e}_\theta$ are calculated as:

$$\begin{cases} \mathbf{e}_r = \dfrac{(\mathbf{x}^n \cdot \mathbf{e}_1)\mathbf{e}_1 + (\mathbf{x}^n \cdot \mathbf{e}_2)\mathbf{e}_2}{\left\| (\mathbf{x}^n \cdot \mathbf{e}_1)\mathbf{e}_1 + (\mathbf{x}^n \cdot \mathbf{e}_2)\mathbf{e}_2 \right\|} \\ \mathbf{e}_\theta = \mathbf{e}_3 \times \mathbf{e}_r \end{cases} \qquad \textbf{eqn. 2.34}$$

Penalizing the increments of displacements along these two directions amounts to apply the following forces with two different penalty stiffnesses k_r and k_θ:

$$\begin{aligned} \mathbf{F_r} &= -k_r \cdot (\mathbf{\Delta u}^n \cdot \mathbf{e_r})\mathbf{e_r} \\ \mathbf{F_\theta} &= -k_\theta \cdot (\mathbf{\Delta u}^n \cdot \mathbf{e_\theta})\mathbf{e_\theta} \quad , \end{aligned} \qquad \textbf{eqn. 2.35}$$

The coefficients of penalization for the two directions need to be adjusted, as they define the stiffness with which the nodes are maintained. The main drawback of the method is that the induced stiffness counteracts the displacement induced by the shaping. For this reason, the coefficient relative to the orthoradial direction is set higher than the coefficient for the radial direction. At the beginning of the thesis, the transverse boundary conditions were proved to cause a peripheral densification of the strands during the shaping. Moreover the results of the shaping were highly dependent on the value set for the penalty coefficient. For these reasons, an important part of this thesis was dedicated to the development and the implementation in the code of a new kind of boundary conditions for the transverse direction.

c. Penalization of the increment of displacement or the total displacement

Regarding the boundary conditions, either increment of displacements or total displacements have been introduced so far. Since the penalization of the boundary conditions allows a small gap to the exact condition, considering the total displacement or the increment of displacement does not lead exactly to the same solution. The interest of the penalization is precisely to allow this gap to the exact condition, and to enable the strand ends to move a little to rearrange, even if the kinematical condition would aim at prescribing zero displacements. As a drawback, if boundary conditions are applied to increments of displacement, if an

approximately constant resultant force acts on an end node, it would induce roughly the same increment of displacement for each loading step, which means the total displacement for this node would depend on the number of loading steps used to simulate a given stage. Applying boundary conditions to the increments of displacements introduces consequently a dependence on the followed path, and especially on the number of loading steps. Along the shaping of the cable, the current positions of the strands ends notably differ from their initial position. For this reason, a penalization relative to the increments of displacement is preferred, despite the dependence on the increment. For the other loadings applied to shaped the cable, the penalizations are relative to the total displacements, so that the result does not depend on the increments of loading.

3 Development of transverse pseudo-periodic boundary conditions

3.1 Pseudo-periodicity or the notion of longitudinal invariance

In order to simulate the continuity of the cable beyond its ends, an invariance of the phenomena is assumed along its axial direction. This assumption supposes that the displacements in all sections of the cable are globally identical in the transverse directions. Since the cable model is not a periodic structure, there is no direct correspondence between the positions of the nodes from opposite sections. As a result, it is not possible to exactly prescribe any equality between the displacements of the extreme nodes. This is the reason why the boundary conditions are described as pseudo-periodic.

3.2 Implementation of the boundary conditions in the code

3.2.1 Specific coupling of the extreme nodes

The question is now to define a criterion to determine which nodes are coupled. It is chosen to link the node from one side of the cable to the two nodes on the opposite side which are the closest according to transverse directions. This coupling is done as follows:

– The extreme nodes at the right and left hand sides of the strands are denoted N_i^L and N_j^R

– The distances between the nodes N_i^R and N_j^L along the transverse directions $\mathbf{e_1}$ and $\mathbf{e_2}$ are defined by:

$$d(N_i^L \to N_j^R) = \left\| \left(\left(x(N_i^L) - x(N_j^R) \right) \cdot \mathbf{e_1} \right) \mathbf{e_1} + \left(\left(x(N_i^L) - x(N_j^R) \right) \cdot \mathbf{e_2} \right) \mathbf{e_2} \right\| \qquad \textbf{eqn. 2.36}$$

– Each node Ni L is associated with two nodes Nj,1 R and Nj,2 R that are the closest along the transverse directions.

3.2.2 Bounding condition between the coupled nodes

In order to bind the coupled nodes, the kinematical condition is expressed as follows:

$$\begin{aligned} \left(\mathbf{u}(N_i^L) - \mathbf{u}(N_{j,1}^R) \right) \cdot \mathbf{e}_1 = 0 \\ \left(\mathbf{u}(N_i^L) - \mathbf{u}(N_{j,1}^R) \right) \cdot \mathbf{e}_2 = 0 \end{aligned} \qquad \textbf{eqn. 2.37}$$

The penalization term that sets the transverse binding of the coupled nodes corresponds to the energy W_{bind}:

$$W = \frac{k_{bind}}{2}\left[\left(\left(\mathbf{u}(N_i^L) - \mathbf{u}(N_{j,1}^R)\right)\cdot \mathbf{e}_1\right)^2 + \left(\left(\mathbf{u}(N_i^L) - \mathbf{u}(N_{j,1}^R)\right)\cdot \mathbf{e}_2\right)^2\right] \qquad \textbf{eqn. 2.38}$$

The minimization of W yields the term that should be added to the virtual work:

$$\frac{dW}{d\mathbf{u}}\cdot \mathbf{v} = k_{bind}\left(\left(\mathbf{u}(N_i^L) - \mathbf{u}(N_{j,1}^R)\right)\cdot \mathbf{e}_1\right)\left(\left(\mathbf{v}(N_i^L) - \mathbf{v}(N_{j,1}^R)\right)\cdot \mathbf{e}_1\right) + \left(\left(\mathbf{u}(N_i^L) - \mathbf{u}(N_{j,1}^R)\right)\cdot \mathbf{e}_2\right)\left(\left(\mathbf{v}(N_i^L) - \mathbf{v}(N_{j,1}^R)\right)\cdot \mathbf{e}_2\right) \qquad \textbf{eqn. 2.39}$$

It comes to apply to the nodes N_i^L and $N_{j,1}^R$ the opposite interaction forces F_{bind} and $-F_{bind}$ defined by:

$$F_{bind} = k_{bind}\left(\left(\mathbf{u}(N_i^L) - \mathbf{u}(N_{j,1}^R)\right)\cdot \mathbf{e}_1\right)\mathbf{e}_1 + \left(\left(\mathbf{u}(N_i^L) - \mathbf{u}(N_{j,1}^R)\right)\cdot \mathbf{e}_2\right)\mathbf{e}_2 \qquad \textbf{eqn. 2.40}$$

The binding condition can be applied either according to the total displacement or to the increment of displacement of the current step. For the same reasons as developed in 2.3.2.c, the pseudo-periodic conditions are relative to the increments of displacements for the shaping part of the modelling and to the total displacements for the other loadings (which guarantees by the way the reversibility in case of cycling loading).

3.2.3 Artefacts induced by the pseudo-periodic boundary conditions

The non-periodicity of the cable does not allow Multifil to fully respect the kinematical condition. For this reason, the coefficient k_{bind} that sets the intensity of the interactions cannot be arbitraryly high. It needs to be adjusted in order to tolerate some deviations. Besides, the various couplings established between the nodes are not independent, since one node can be involved in several interactions. As a result, an interacting network is produced between all nodes of each extreme section of the cable, which introduces a transversal stiffness for these sections. The stiffness of this framework depends on the values of k_{bind} which is the topic of the paragraph 5.2.

4 Adaptation of the initial lengths of the strands to insure plane sections of cable

4.1 Issue

Initially the strand ends have the same axial coordinates $z=L_m$, with L_m the length of the sample. But after the shaping, the free section of the cable is not flat anymore because the trajectories of the strands have extended during the compaction. This effect may cause problems during the application of the Lorentz Loading. In fact, if some strands are longer than others, the parts of strands that exceed the average length of the cable are not supported. The effect is reported in Fig. 2.15 where the strands at the periphery are longer than at the core of the cable. The application of a magnetic force to these unsupported parts will cause a local high bending having no physical sense, which may deteriorate the convergence of the solution algorithm and induce an overestimation of damage.

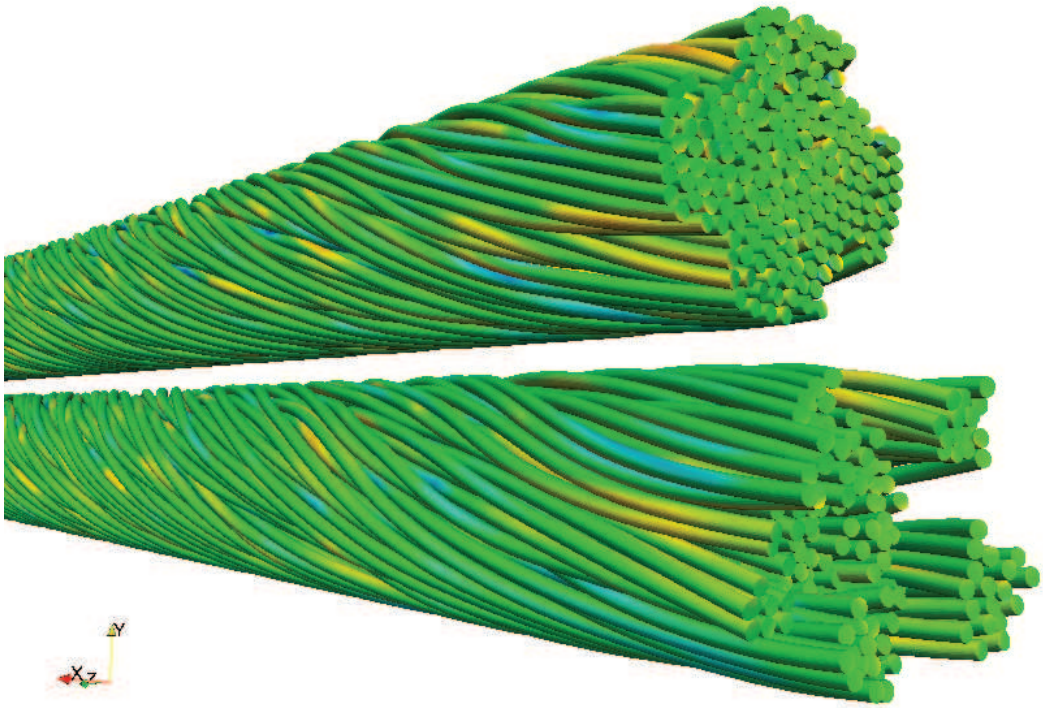

Fig. 2.15 . Result of the first shaping of the 3x3x5x4 cable. The free section is not flat because during the shaping, some strands have stretched more than others.

4.2 Proposed solution

The method is simple. A first shaping is performed. The initial and final lengths of the strands are then measured. A second shaping is realized, but now the initial configuration is adapted according to the result of the first shaping. For the second shaping, the initial lengths *Li* are increased by the amount *ΔLi* needed to get flat cable sections aligned with the maximum length measured during the first shaping:

$$\Delta L_i = \max(L_j^{ini}) - L_i \qquad \textbf{eqn. 2.41}$$

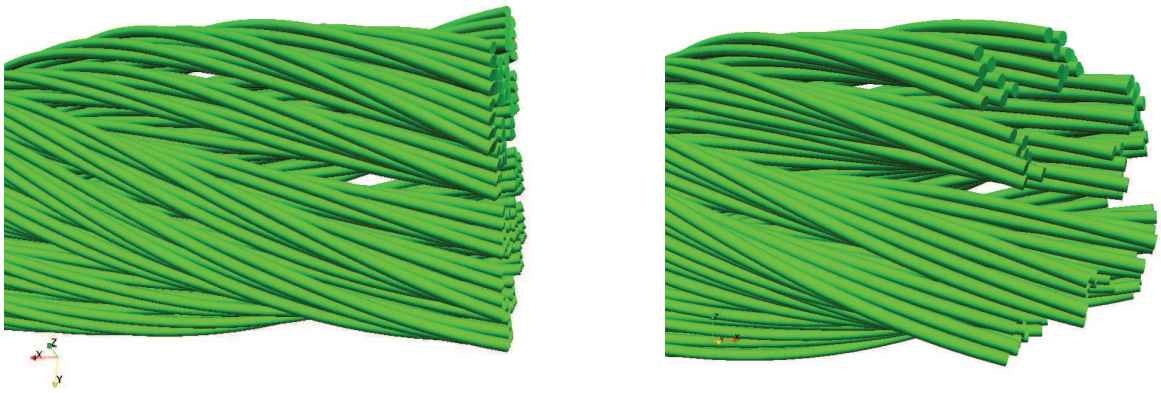

a) b)

Fig. 2.16. Illustration of the adaptation of the strand initial lengths. a) Initial and b) modified right hand sides of the cable. According to the result of the first shaping, the strands for the second shaping are now longer at the core of the cable.

4.3 Verification of the method

In this paragraph, the method developed to get plane extreme sections at both cable sides is checked. The result of the first shaping of a 3x3x5x4 cable is shown in Fig. 2.15. From this result, the initial lengths of the strands are adapted. The new strand geometry is shown in Fig. 2.16. Finally, the result of the second shaping is presented in Fig. 2.17. It can be concluded that the shaping result is in agreement with the objective of having plane extreme sections. The main drawback is the need to perform two successive shapings, which is time consuming.

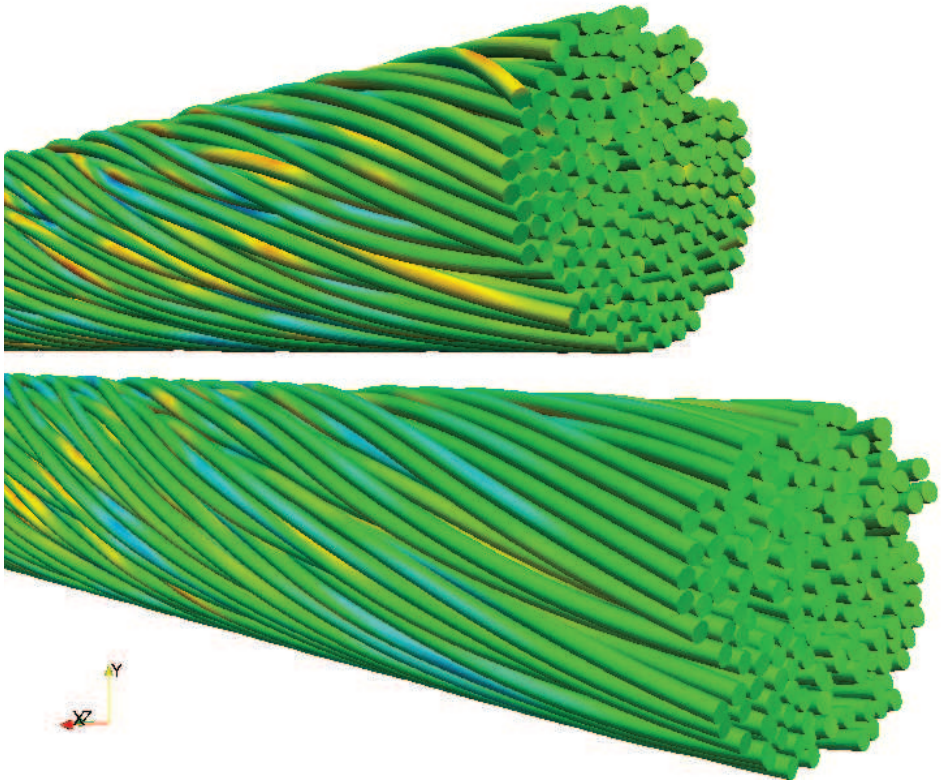

Fig. 2.17. Cable extreme sections after second shaping: both free and constrained sections are now flat. It shows that the adaptation of the initial length is a relevant method to obtain flat sections.

5 Parametric study of the influence of the pseudo-periodic boundary conditions

5.1 Verification of the longitudinal invariance

The assumption on which the transverse pseudo-periodic conditions relies presumes the invariance of the displacement along the cable axis. The detwisting effect is expected to induce orthoradial displacements at the strand ends. In order to validate the assumption of invariance and to observe a possible detwisting effect, the average of the norm of orthoradial displacement calculated within some sections of cable is plotted against the cable axis. The results for four different steps (32, 34, 36, 38, 40) of the shaping of a 100 mm and 200mm long cable are presented in Fig. 2.18. The curves present some oscillations extending over few tens millimeters but their amplitudes do not much differ. The orthoradial behavior is not truly invariant but the variations are of comparable orders, both all along each of the two samples, and compared from one sample to the other. Moreover, on these curves, no peculiar end effect is noticeable. From this study it can be concluded that the application of pseudo-periodic boundary conditions does not seem to induce noticeable end effects.

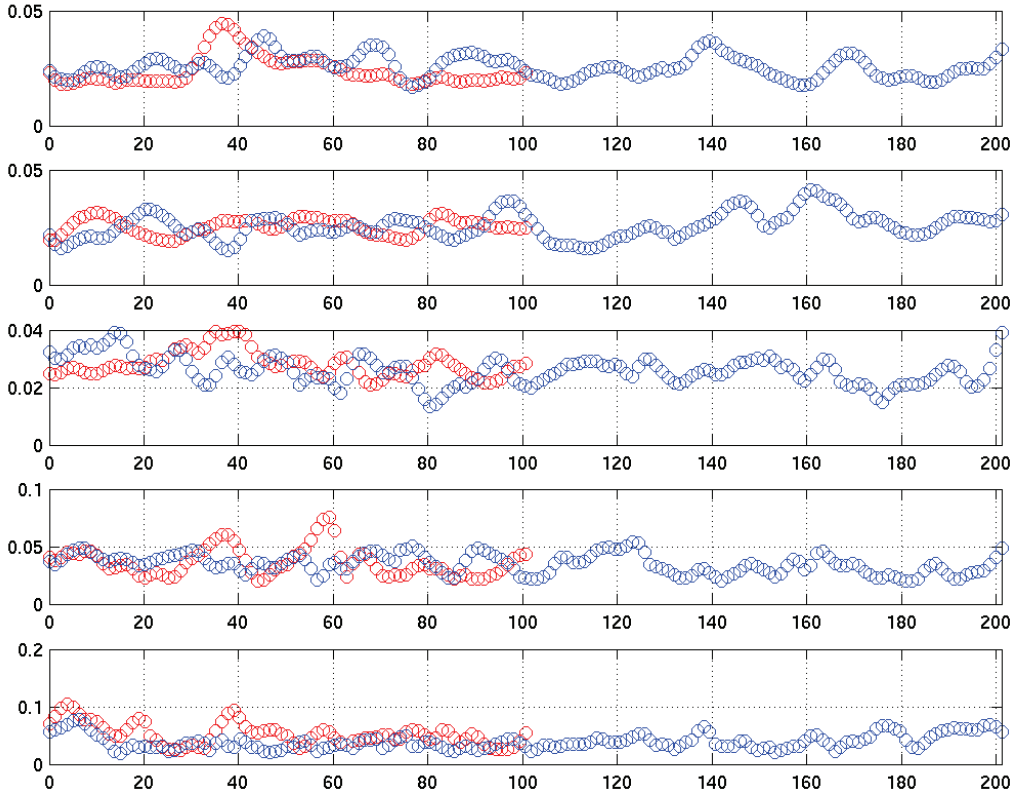

Fig. 2.18. Plot of the mean orthoradial displacements of the nodes along the cable axis. The invariance of the behavior along the cable axis is checked.

5.2 Parametric study of the length of the modelled sample

5.2.1 Effect of large variation of the length

After having shown the absence of noticeable end effects induced by the pseudo-periodic conditions, it is interesting to study the influence of the length of the modelled sample. For this purpose, the same plot is presented in Fig. 2.19. for 25, 50, 75 and 150mm long samples compared with the reference 200mm long cable. For the shortest samples (25 & 50mm), the behavior substantially differs from the reference, whereas longer samples better match it.

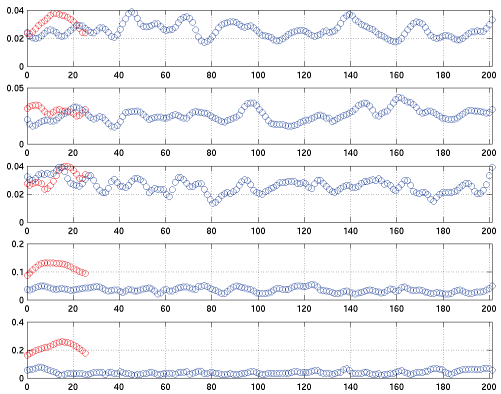

a) 25 mm

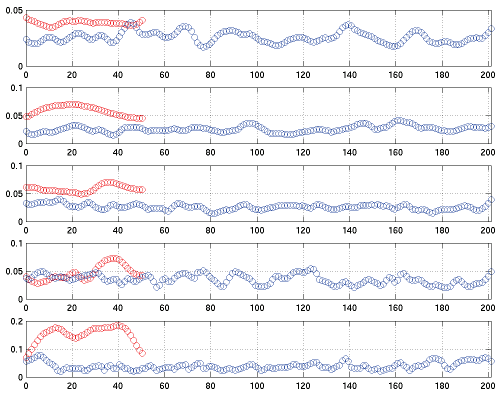

b) 50 mm

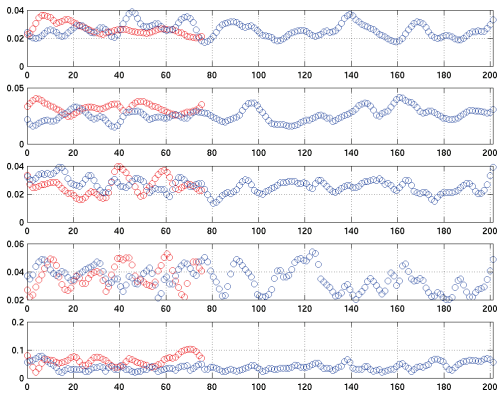

c) 75 mm

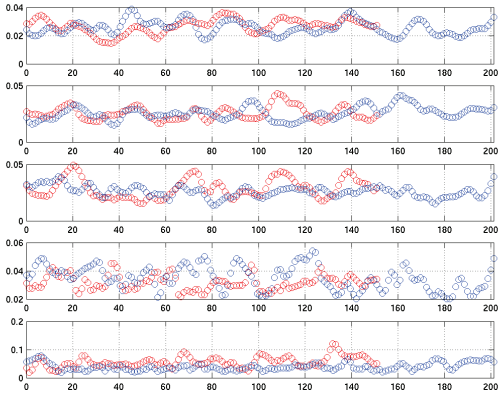

d) 150 mm

Fig. 2.19. Plot of the mean orthoradial displacements of the nodes along the cable axis. Different cable lengths are: 25, 50, 75 and 150mm long. The boundary conditions seem not well adapted to short samples, say smaller that 75mm.

Other quantities can be analyzed to study the influence of the length of the modelled sample. We choose to study here the evolution of mean curvature with the compaction of the assembly (void fraction). Samples of different sizes have been shaped. The different cable lengths are respectively 25, 50, 75, 100, 150, 200 and 400 mm. In Fig. 2.20, the results are compared to each other in terms of their distribution, mean and standard deviation calculated for the local curvatures. These graphics are plotted for the different steps of the compaction.

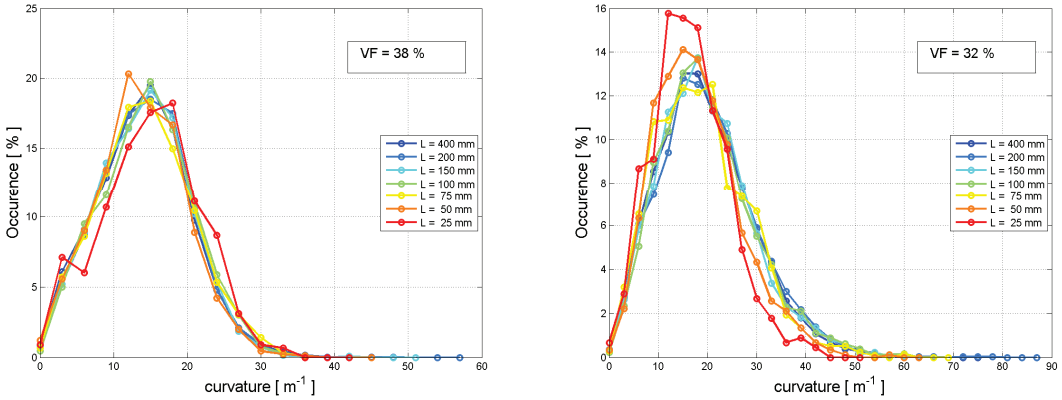

Fig. 2.20. Comparison of the curvature distribution for three steps of the compaction and different cable length.

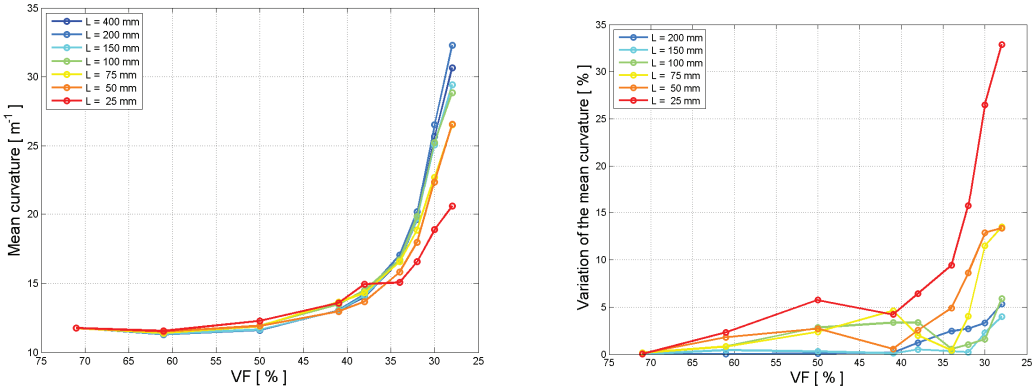

Fig. 2.21. Evolution of the mean curvature along the compaction and error made compared with the reference sample 400mm long.

Compared with the reference sample, the discrepancy of the mean curvature is above 30% for the shortest sample and below 5% for the longest. The distributions of the different samples get closer to each other when the length of the sample is greater than 75mm. From these results it seems that beyond a value of 75mm, the length of the sample does not influence the obtained results.

5.2.2 Effect of small variation of the length

The boundary conditions set a coupling between the closest extreme nodes according to the transverse directions. If the length of the cable slightly increases, the positions of the extreme nodes change. As a result the coupling network relative to the transverse boundary conditions varies as well – see Fig. 2.22. The boundary conditions may then produce in turn different effects and the result may change when the modelled length varies.

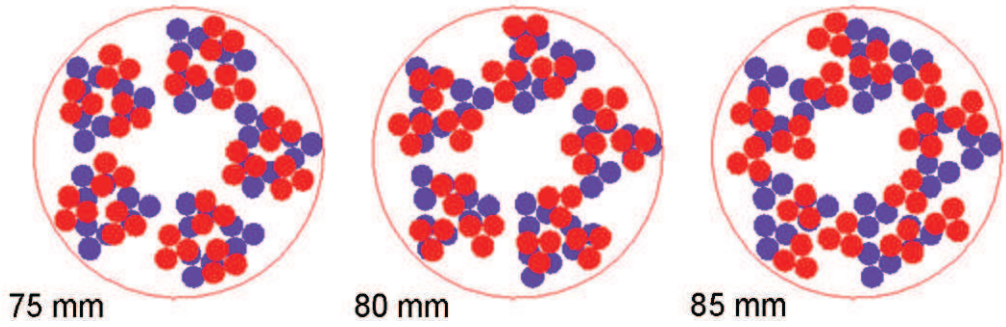

Fig. 2.22. Extreme sections for three different modelled lengths. According to the cable length, the strand ends are coupled in a different way by the boundary condition.

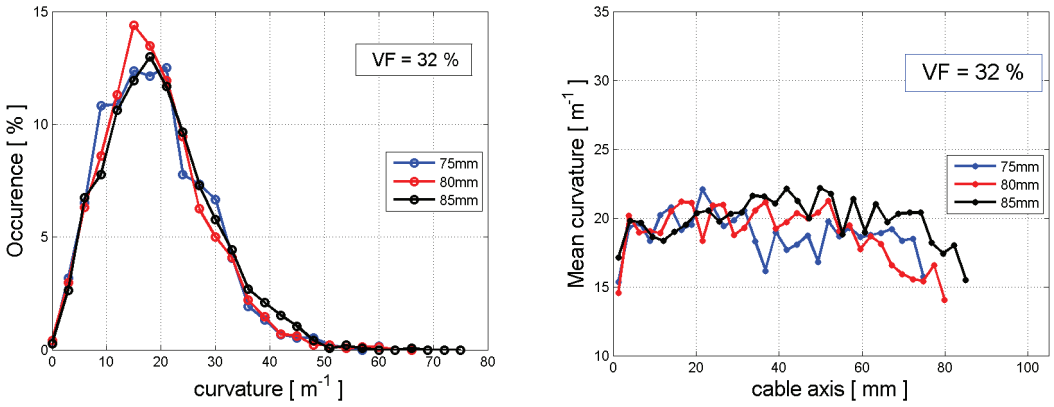

Fig. 2.23. Distribution of the local curvatures for the three different lengths.

Curves in Fig. 2.23 show that the results are not significantly influenced by the changes in the couplings between extreme nodes induced by small variations of the length.

5.3 Parametric study of the penalty coefficient

In order to check the influence of the binding coefficient k_{bind} on the results of the shaping, different values are assigned to 100mm long samples. The tested values range over four orders of magnitude: 0.1, 1, 10, 50, 100, 500, 1000 and 5000 N/mm. Fig. 2.24 shows the evolution of the mean curvature along the step of the shaping for the different samples. These curves are compared with a reference behavior. The reference corresponds to the 200mm long sample assumed long enough to be independent of any end effects. Its shaping is performed

using k_{bind} =200 N/mm. Compared to the reference, low values of k_{bind} (< 50N/mm) produces underestimations of the curvatures whereas high values of k_{bind} (< 100N/mm) overestimate them. The case k_{bind} =100N/mm gives the closest result: the mean and the distribution match the reference behavior. Are these discrepancies in the results due to peculiar behavior at the cable ends that eventually perturb the statistic?

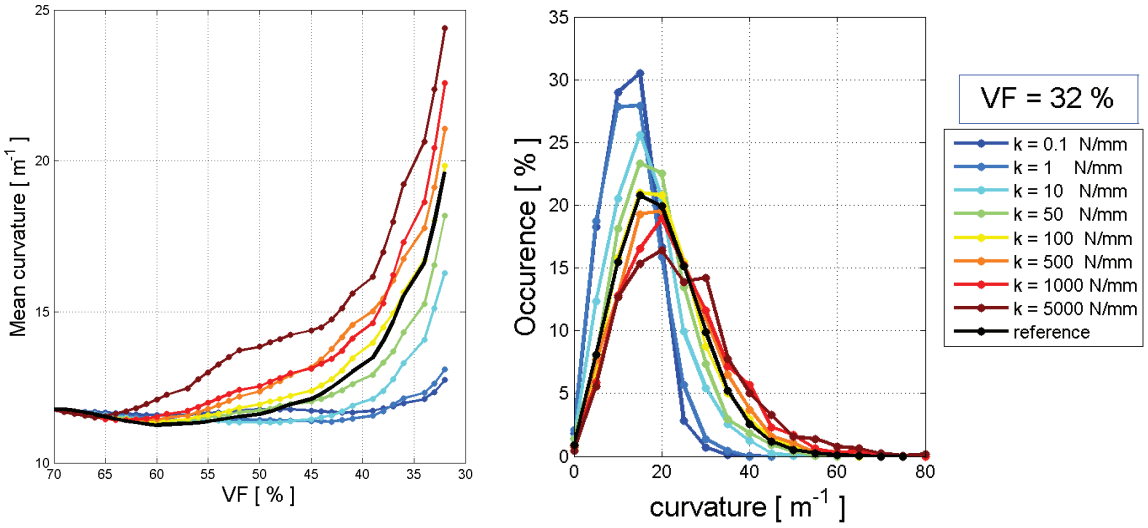

a) b)

Fig. 2.24. Observation of the effect of the penalty coefficient. a) Evolution of the mean curvatures along the steps of the shaping. b) Distribution of the curvatures for a given step of the shaping.

The local curvature of the beams, along the cable axis can be illustrated by the detwisting of the sub-bundles along the compaction or other ends effect. The next set of graphics in Fig. 2.25 shows the evolution of the mean curvature per cable sections for the different step of the compaction for the different values of k_{bind}. Low values of k_{bind} (< 50 N/mm) may be not sufficient to produce the desired coupling of the extreme nodes. It seems that for low value of k_{bind} the cable unwinds itself. The detwisting is illustrated by low curvature at the strand ends. High values of k (> 500 N/mm) are expected to cause the stiffening of the cable extreme sections because of the artificial transverse rigidity introduced by the pseudo-periodic boundary conditions. It appears that the curvatures are too high at the extremities of the cable – see last graphics in Fig. 2.25. The end effects extend over 10mm at both cable sides. For average values of k (between 50 and 500N/mm) there are limited end effects with low discrepancy between the behavior at ends and the rest of the cable.

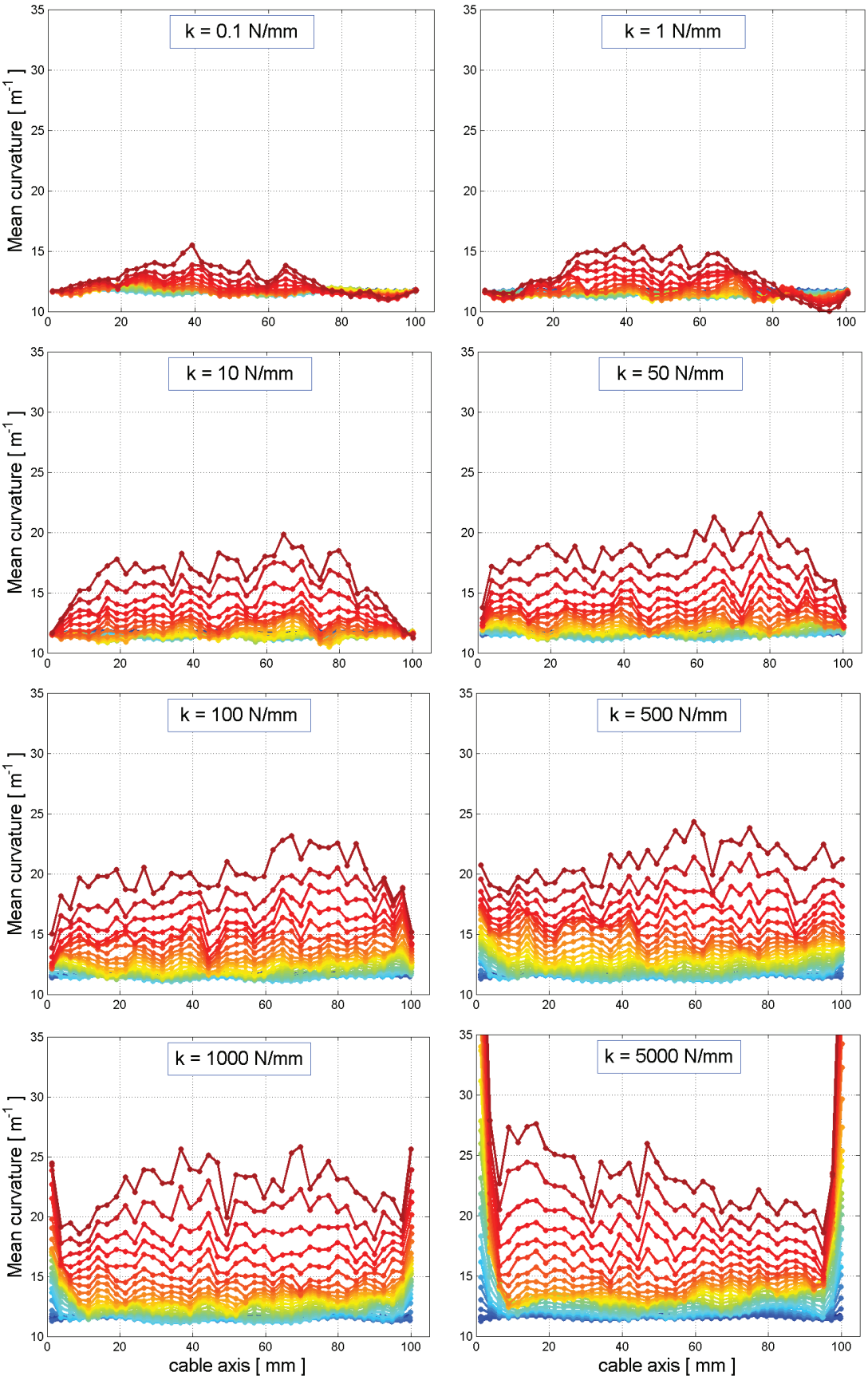

Fig. 2.25. Illustration of the effect of the binding intensity relative to the pseudo-periodic condition on the average behavior relative to the curvatures.

For a given void fraction of 32%, the mean curvatures along the cable axis are compared with the reference behavior. Fig. 2.26 and Fig. 2.27 show the comparison for the different k_{bind}. It seems that to reproduce the result of the reference sample for a void fraction of 32%, the value of k should range between 50 and 500N/mm.

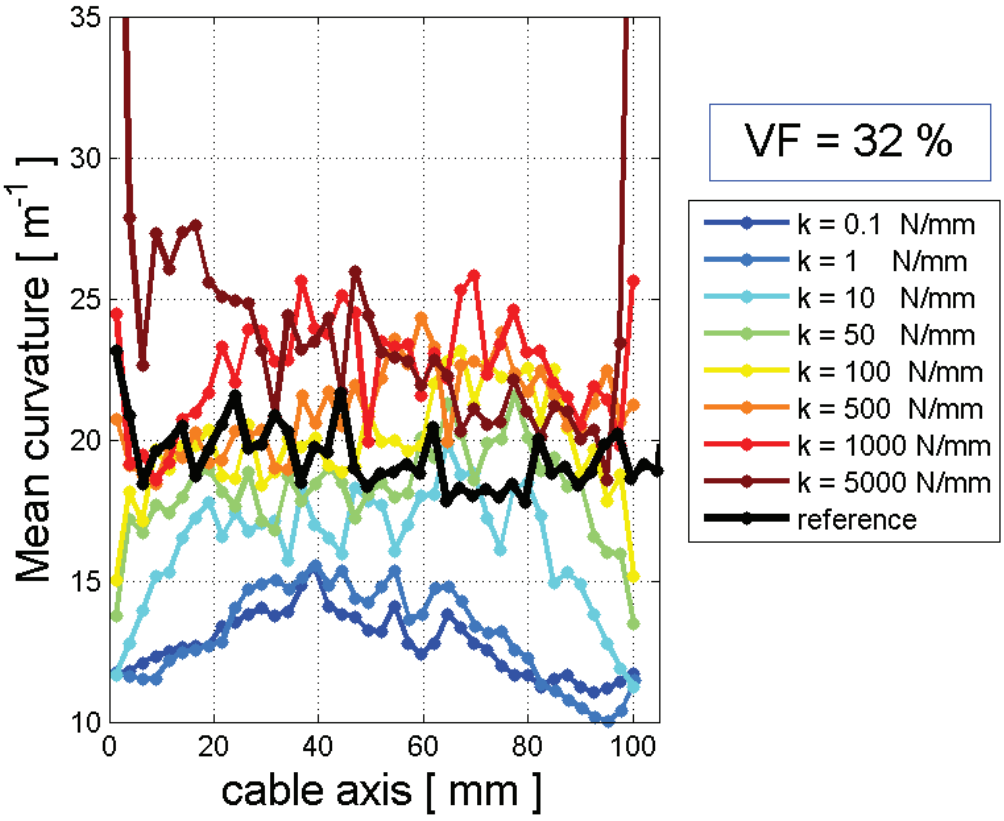

Fig. 2.26. Influence of the parameter k on the mean curvature per section and comparison with the reference sample.

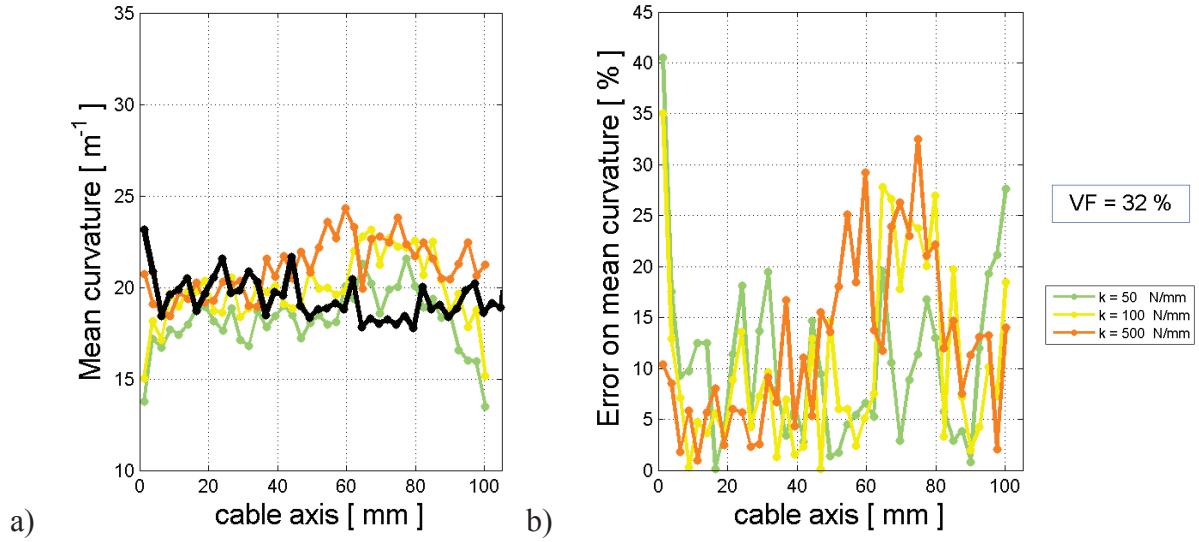

Fig. 2.27. Mean curvature per cable section compared with the reference behavior and estimation of the discrepancy.

5.4 Final result regarding the shaping of four cable stage conductor

This last paragraph concludes the work done on the boundary conditions and their influence during the shaping by presenting the results obtained regarding sub-size conductors. The models presented in Fig. 2.28 are composed of either one hundred and forty four or one hundred and eighty strands built upon four cabling stages. The different designs have been chosen in accordance with existing conductors that have been experimentally tested at SULTAN or FBI facilities under ITER relevant operating temperature and field conditions. The design parameters of the four conductors are listed in the Table 2.1. They all get the same twist pitch sequence TP {51-79-136-166} and the same length L=160 mm. Except for the petal, the void fraction of the cable inside its conduit is chosen equal to 33% (41.4% for the petal). The dimensions of the cross-sections correspond to the cable radius for the round cable, the edges for the square and the outer diameter of the central spiral and inner diameter of the jacket for the petal.

Cabling pattern	Number of strands	Shape & Dimension [mm]			Void Fraction [%]	Twist Pitches [mm]	L [mm]
		Round	square	petal		51-79-136-166	160
3x3x**4**x4	144	**6.01**	**10.7**	**x**	33	51-79-136-166	160
3x3x**5**x4	180	**6.72**	**x**	**6-18.6**	33 – 41.4	51-79-136-166	160

Table 2.1. The design parameters of the four-stage cable-in-conduit conductor simulated by Multifil.

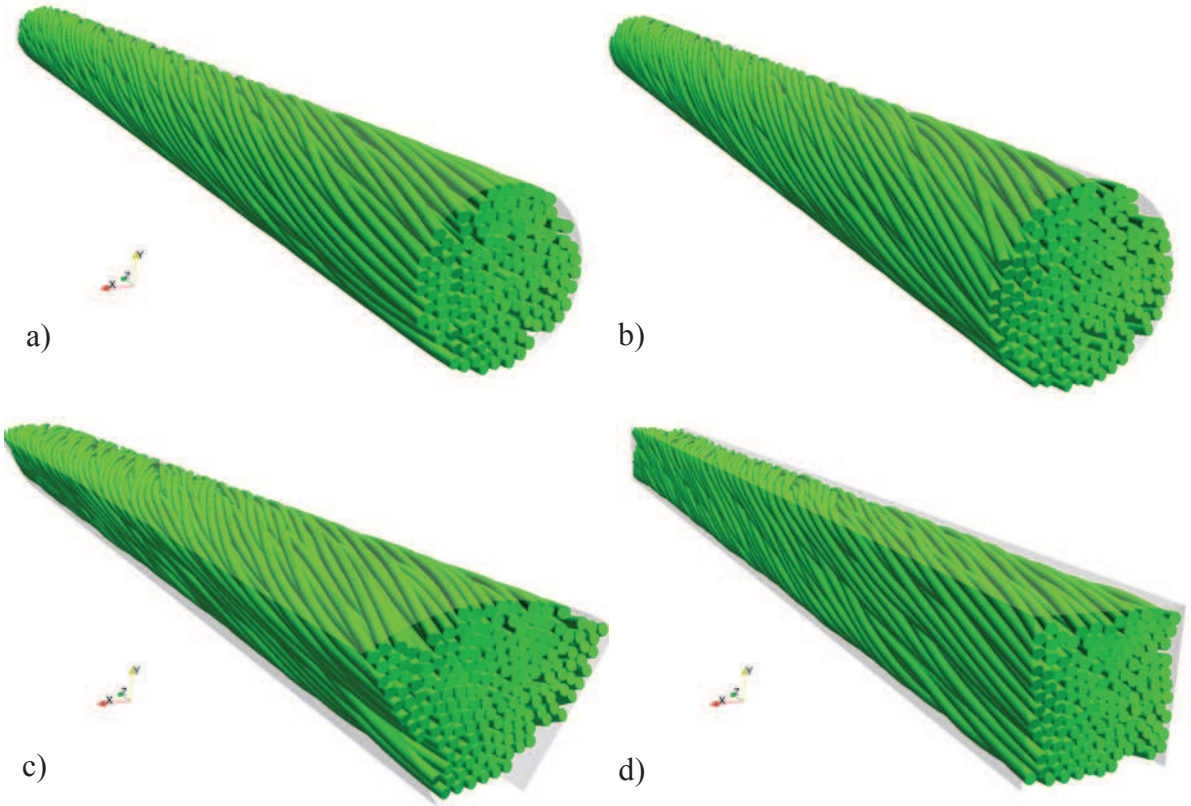

Fig. 2.28. Final result of the shaping down to a void fraction of VF=32%. a) Circular 3x3x4x4. b) Circular 3x3x5x4. c) Petal 3x3x5x4. d) Square 3x3x4x4.

Chapter III: Validations of the model for the axial loading

The goal of this chapter is to validate the Multifil model of cable for the axial loading tests with comparison with available experimental data. For this purpose, the material constitutive laws of the cable components, the copper wires and the composite strands, have been experimentally identified, by carrying out uniaxial cyclic tensile tests on individual wires. In the first part of this chapter, the experimental method that allows the axial loading curves of wires to be obtained is introduced. The results of the tensile tests, performed at room temperature, are here presented and discussed. In addition to this macroscopic approach, Scanning Electron Microscopy observations of the tested strands complete the strand characterization. These microscopic observations aim at identifying a *strain criterion* for the initiation of micro-cracks in Nb_3Sn filaments. In the second part of this chapter, the model for longitudinal elasto-plastic behavior used Multifil code is introduced. Different functions are fitted to reproduce the evolution of hardening observed on the experimentally obtained stress-strain curves. The results of the simulation of low cyclic tensile on single wires are compared with experimental curves. In the last part, the model of axial plasticity is put to good use in the simulation of the tensile test of a 36 strand cable. The cable stress-strain curve that is calculated is directly compared with the experimental results obtained at the Twente University [Ilyin 2006]. The agreement between experimental data and simulation results provides a first validation of the model for a tensile test performed on a real cable, with no other free parameters than the fitting of the constitutive behavior of individual wires.

1 Tensile test of strands at room temperature

1.1 Experimental procedure

1.1.1 Presentation of the materials

The strands provided by CEA were from the *EAS Bronze route* and the *Alstom Internal Tin process* production, whereas the OFHC copper strands were extracted from conductor. Fig. 3.1 illustrates the different samples, typically 100 mm long, that have been tested. These samples have been mechanically tested to derive their axial stress-strain characteristics.

a) 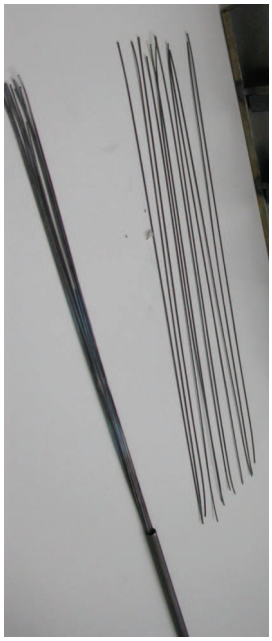 b) 

Fig. 3.1. a) Straight reacted Nb_3Sn-based strands and OFHC copper wires and b) mounted samples to be used with the capstan device. All materials were delivered after heat treatment by CEA.

1.1.2 Measurement process

The axial stress-strain curves of the wires are measured using a standard tensile machine equipped with a *load cell* that measures the force applied to the sample (maximum loading of the cell is 5kN). The axial deformation of the sample is probed by *clip-on extensometer* – see Fig. 3.2. The distance between the two blades of the extensometer is 12.5mm and the length of the samples is 100mm. The test is performed at room temperature with a rate of applied displacement of 0.5mm/min. The unloading/loading of the sample can be performed to produce cyclic loading. Regarding the stress-strain loading curve, the stress σ is defined by the force F divided by the cross section of the strand and the strain ε by the displacement ΔL measured by the extensometer divided by its gauge length L_g.

$$\sigma = \frac{F}{\pi r_s^2} \text{ and } \varepsilon = \frac{\Delta L}{L_g} \qquad \textbf{eqn. 3.1}$$

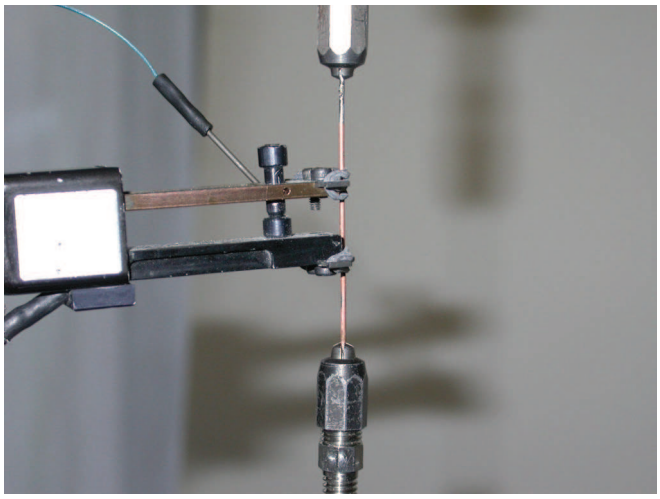

Fig. 3.2. View of the two blades clip-on extensometer mounted of strand sample.

1.1.3 The issue of the wire tightening

The main issue of the tensile test experiment is to grip the sample at its ends in a way that would not cause damage or stress concentration that would lead to the early breakage of the sample. Different devices have been tried to get the most accurate and reproducible results.

The first attempt was to use classic jaw - Fig. 3.3 a) to hold the sample. But the samples systematically broke inside the jaws even when the samples were put inside thin copper sleeves at their ends to protect them against the pressure of the jaws. The device was then discarded. The second attempt was to grip the sample using four jaws mandrel - Fig. 3.3 b). In order to withstand the tightening at their extremities, the samples were plated with silver over one centimetre. It appeared that the samples were eventually sliding out of the mandrel and the device was discarded.

a) 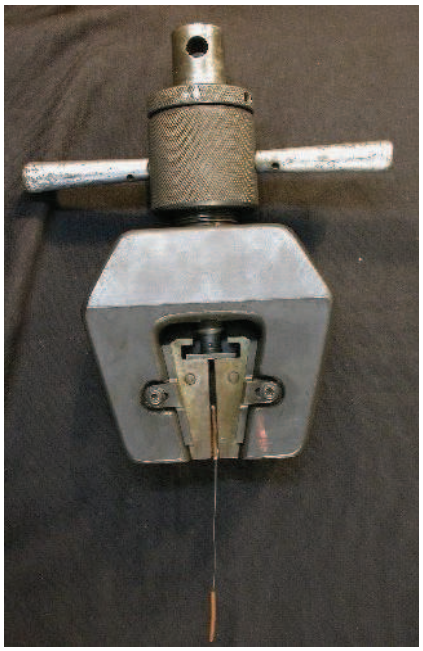 b) 

Fig. 3.3. a) First attempt to grip the strand inserted in copper sleeve at the extremities. b) Second attempt with four jaws mandrel with silver plated extremities.

Facing these difficulties, a third device was specifically designed so as to introduce no pinching of the strand at their ends by the use of two capstans – see Fig. 3.5 a). For this new montage, the Nb_3Sn strands should have been reacted on a Titanium stand in the desired shape – see Fig. 3.1 a). This montage however has proved to produce unexpected result when the sample was cyclically loaded. The interpretation was that the strand slides against the capstans when the load is released. Nonetheless, for monotonic loading the result were correct. Fig. 3.4 illustrates as an example the reason why the capstan device has been discarded. When the strain is released, the stress abruptly drops. The same phenomenon appears when the strain increases again. This was interpreted as stick-slip behavior of the strand against the capstan.

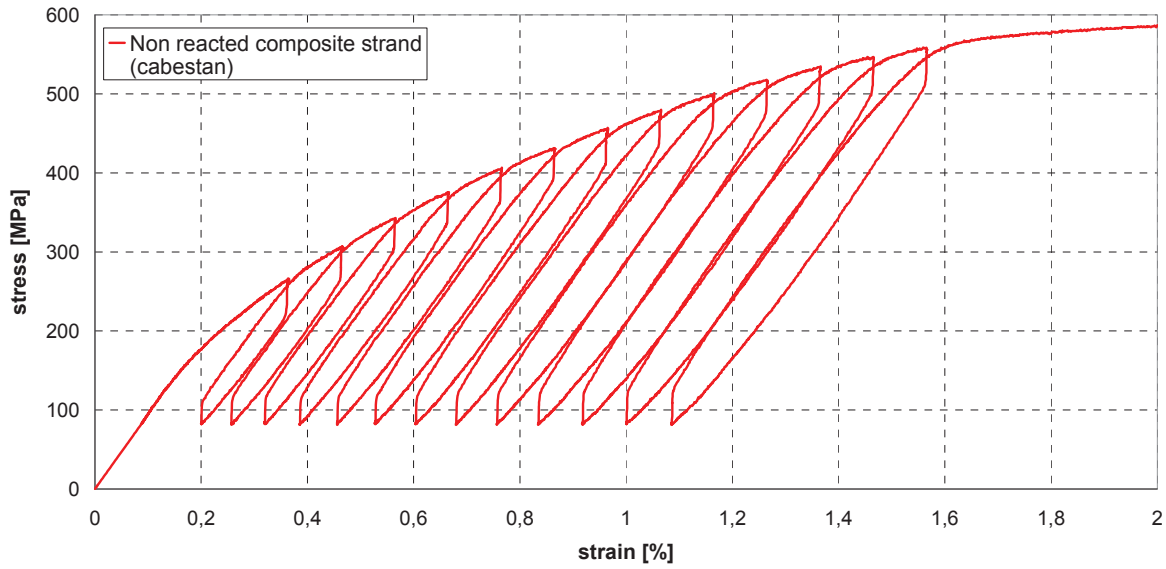

Fig. 3.4. Illustration of the issue related to the capstan device regarding the unloading and loading of non reacted strand.

The fourth and last device uses gripping jaws especially dedicated to test small diameter wires – see Fig. 3.5 b). The jaws maintain tightening of the sample by a gripping force that automatically increases with the applied load (so-called key-less clamp). Using this device, the tests have produced reproducible results where the sample always breaks at its middle (far from the clamps) which proved that no detrimental effects (slipping or pinching) were caused by the jaws. This device was finally chosen for it to avoid the issue induced by the capstan– see Fig. 3.6.

a) b)

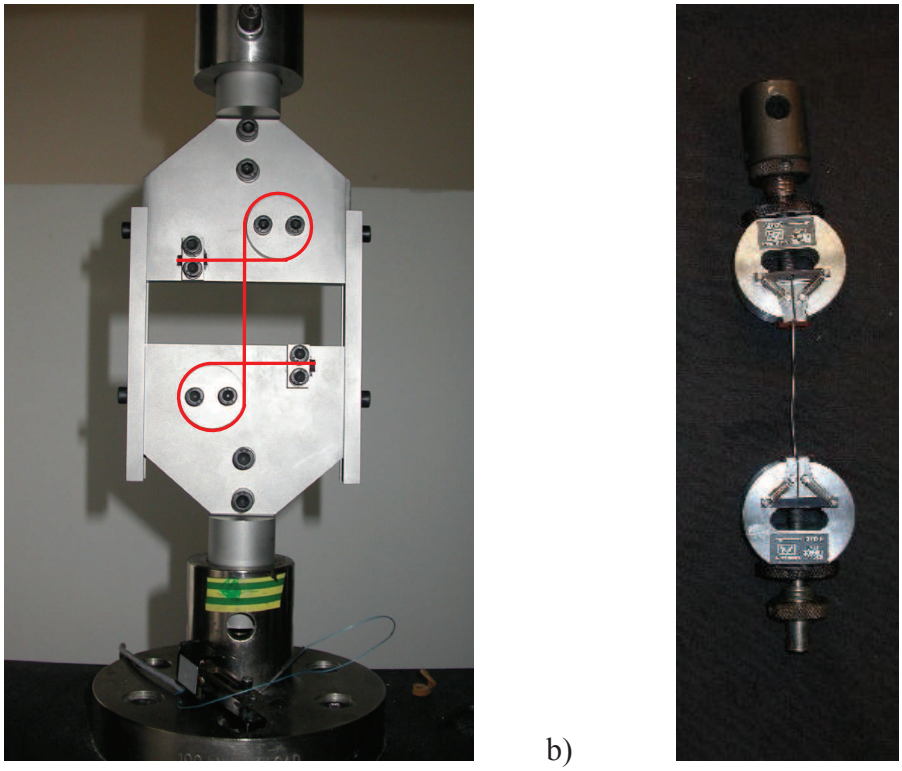

Fig. 3.5. a) Third attempt with double capstan device. b) Fourth attempt using keyless clamp specially dedicated to millimetre size wires.

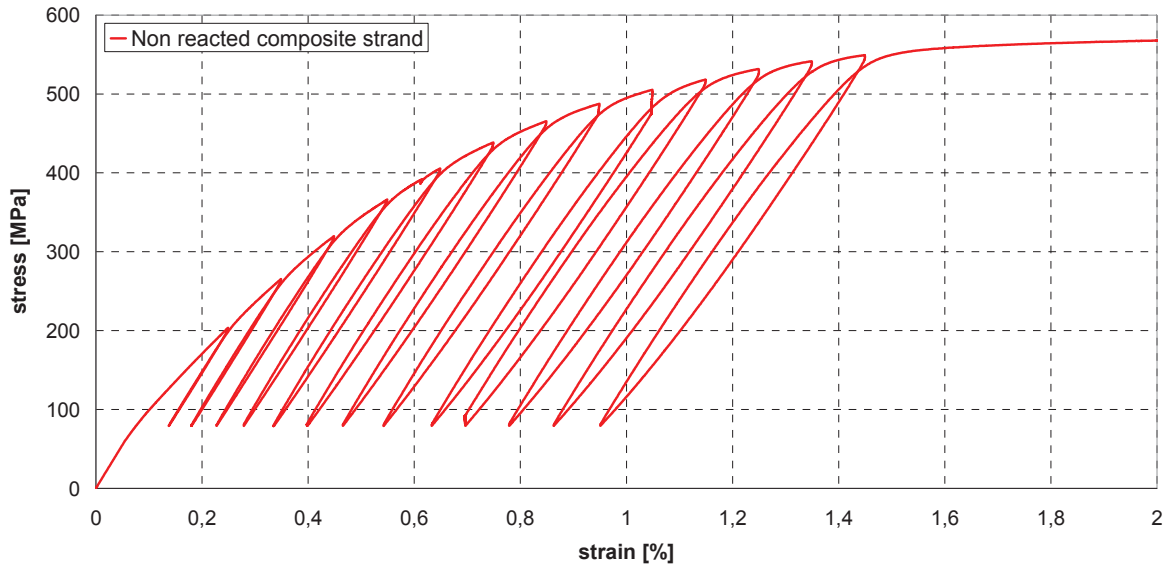

Fig. 3.6. Validation of the wire testing dedicated keyless clamp device for the investigation of the axial stress-strain behavior.

To conclude, the issues faced to obtain relevant and reproducible results have been overcome and an experimental procedure has been found out. In the next part the results of the measurements are presented.

1.2 Analysis of the uniaxial loading curves

1.2.1 Monotonic loading

For the OFHC copper wires and the EAS reacted strands the results of the most representative measurements are exposed in Fig. 3.7 and Fig. 3.8. The measurements between the three samples are well reproduced. The unloading-loading of the samples are done to measure their effective axial stiffnesses defined as the slope of the curves for the unloading. These are 80 GPa for the copper and 115 GPa for the composite. The tests are run until the rupture of the sample that occurs for strains beyond 2% for the copper and around 0.7 ~ 0.8% for the composite. The measurements are in agreement with expectation from the literature [van den Eijnden 2005], [Mitchell 2005 a b]. The stress-strain curves exhibit non-linear behavior typical of plasticity. The annealing of the copper in both pure and composite wires that occurs during the heat treatment is the cause of the small elastic domain of the samples. The OFHC wires have almost no elastic domain whereas the yield stress and strain for EAS reads σ_y = 50MPa and ε_y = 0.045% which are quite low. The slope of the stress-strain curve in the plastic domain of the Nb_3Sn composite strand is quasi-linear.

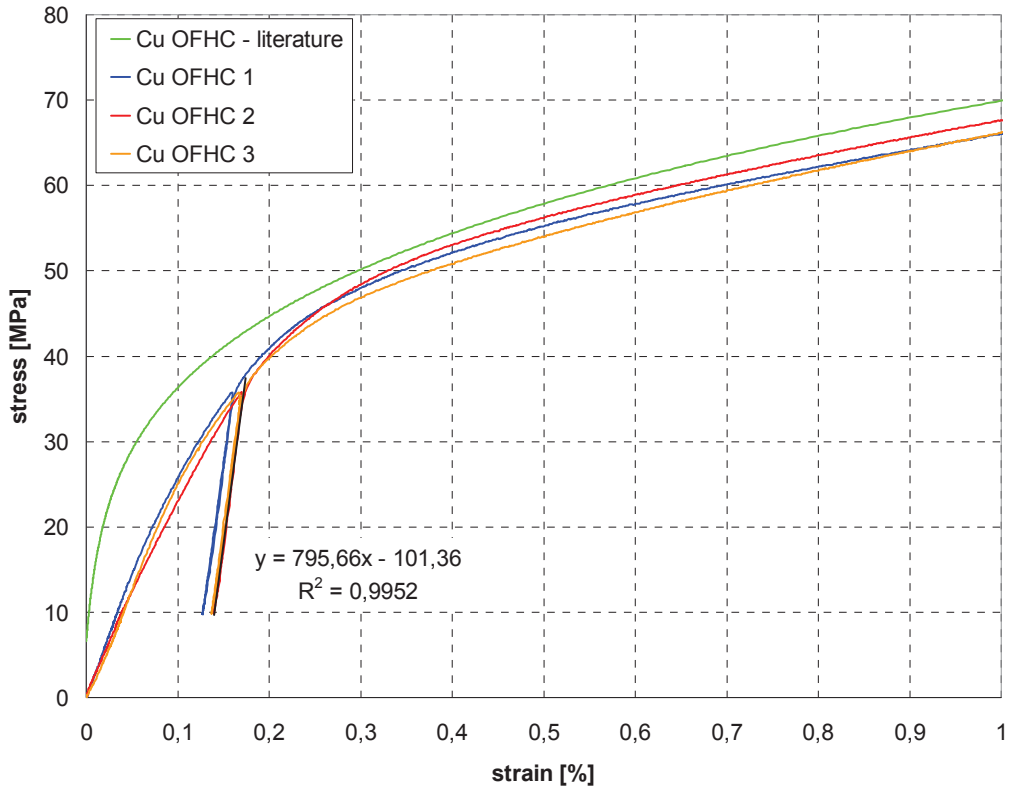

Fig. 3.7. Measurement of the axial stress-strain curves of OFHC copper wire. The first unloading allows the axial stiffness to be retrieved.

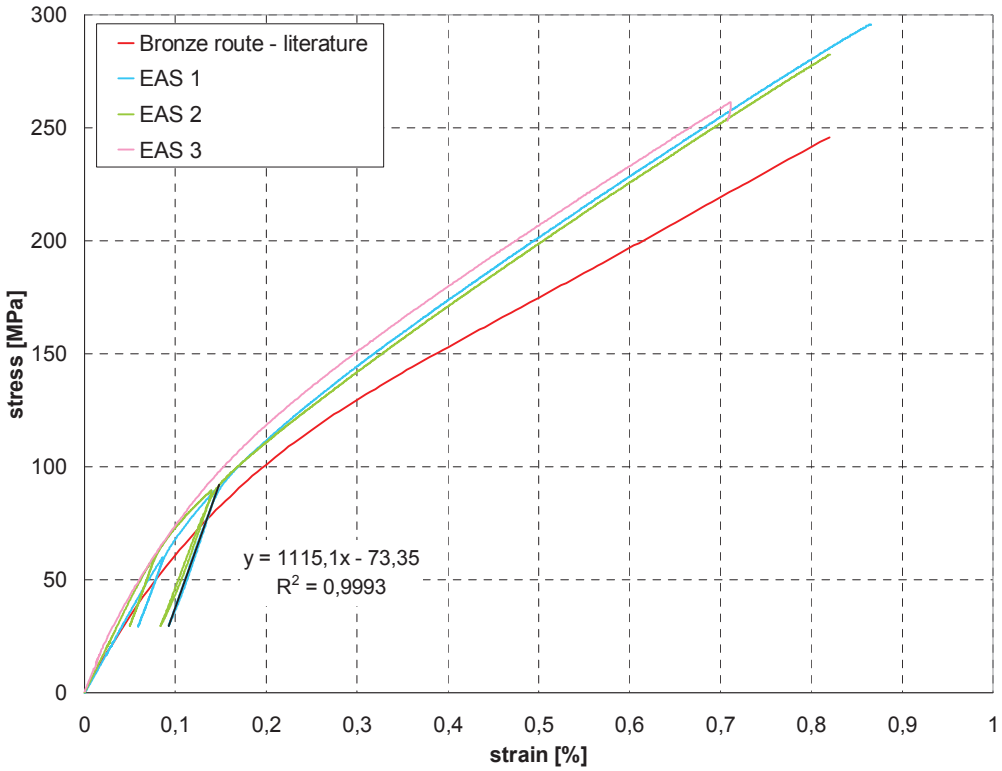

Fig. 3.8. Measurement of the axial stress-strain curves of EAS reacted strands and comparison with result from [van den Eijnden 2005].

1.2.2 Application of the law of mixtures

In order to better understand the stress-strain characteristic of the composite strand, it is proposed to apply the *law of mixtures* to derive a *homogenized* stress-strain curve.

The law of mixtures states that the stiffness of the composite is the sum of the contribution of the different materials which are the Tantalum, the Bronze, the Nb_3Sn and the OFHC copper. The law of mixtures simply reads for the total stress:

$$\sigma_T(\varepsilon) = \nu_{Ta} \cdot \sigma_{Ta}(\varepsilon) + \nu_{CuSn} \cdot \sigma_{CuSn}(\varepsilon) + \nu_{Nb_3Sn} \cdot \sigma_{Nb_3Sn}(\varepsilon) + \nu_{Cu} \cdot \sigma_{Cu}(\varepsilon) \quad \textbf{eqn. 3.2}$$

Where the terms ν stand for the volume ratio of the different materials, from [van den Eijnden *2005*]:

	Ta	Nb_3Sn	CuSn	Cu
ν [%]	4	14.8	21.2	60

Table 3.1. Volume ratios of the various components present in composite superconducting strand

The elasto-plastic characteristics of the different materials at room temperature come from [Mitchell 2005 a]. Fig. 3.9 presents the stress-strain curves for the different materials, the result of the mixture law and the experimental result. The behavior of the composite strand is correctly modelled by the law of mixtures even though the volume ratios could be more accurately measured to get more accurate model.

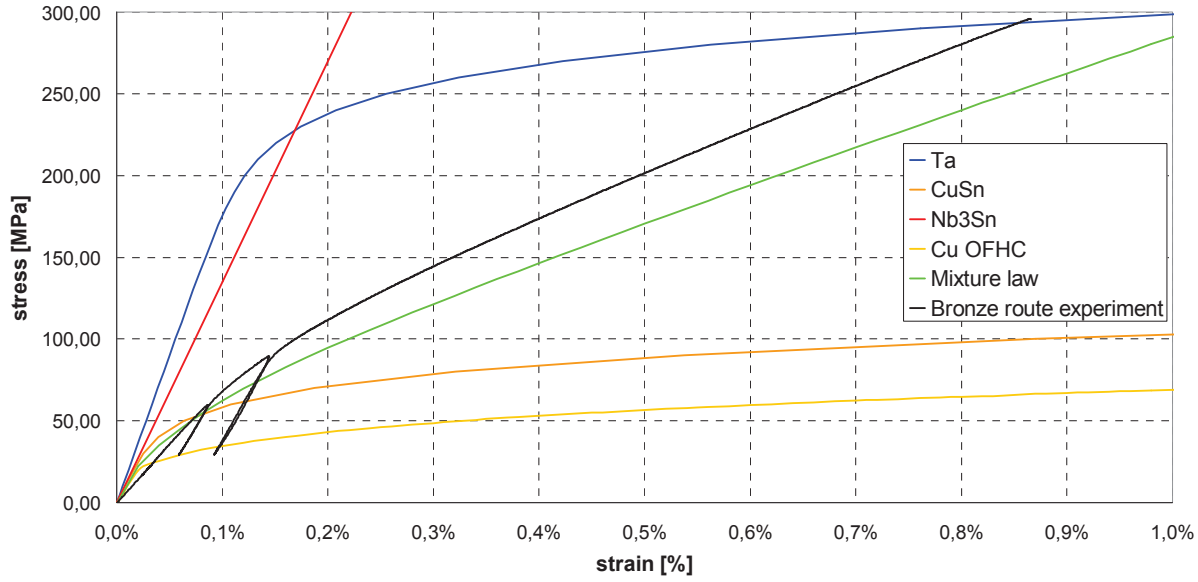

Fig. 3.9. Illustration of the use of the law of mixtures to model the behavior of composite material.

Now that the monotonic stress-strain curve is analysed, some cyclic loading can be performed.

1.2.3 Plastic cyclic loading

The strands in operating conductor are cyclically loaded, it then appeared important to perform plastic cyclic loadings of the materials. Two kinds of Nb_3Sn strand have been tested:

the bronze route from EAS and the internal tin from Alstom. The obtained stress-strain curves from the tests are presented in Fig. 3.10.

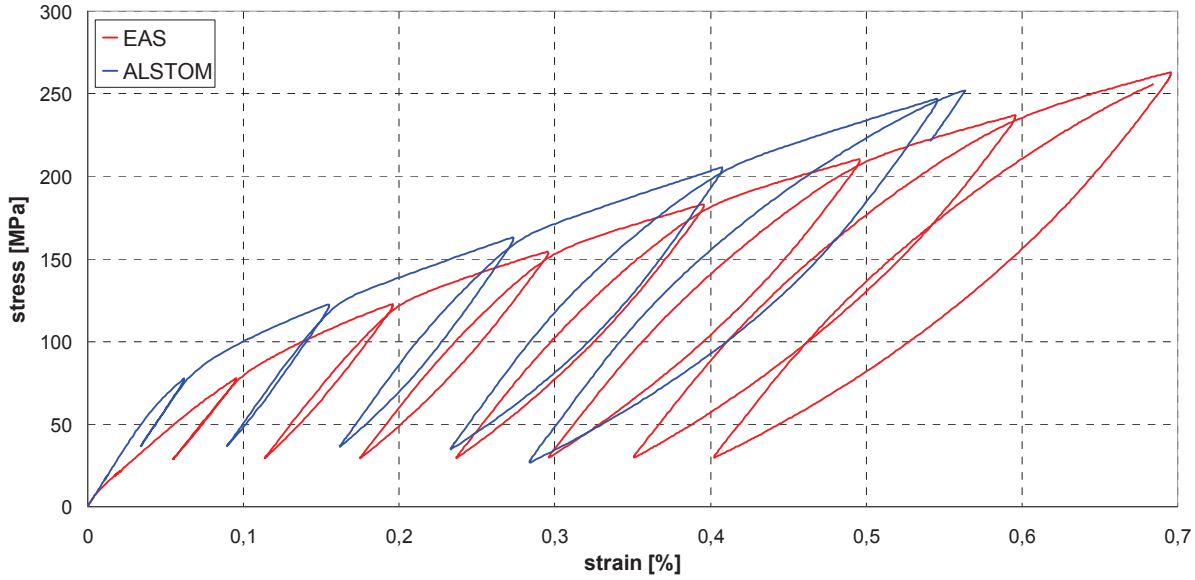

Fig. 3.10. Tensile cyclic loading stress-strain curves of two kinds of Nb_3Sn reacted strand, EAS Bronze Route and Alstom Internal Tin.

The results indicate similar behavior for both kinds of strands. The most striking feature of these curves is the non-linear behavior when the stress is released which is characteristic of the *Bauschinger effect* where the yield strength decreases when the direction of the strain is changed [Lemaître Chaboche 1988].

1.2.4 Evolution of the Young's modulus with the strain

An additional question has risen from the cyclic curves. It is wondering if gradual damage of the Nb_3Sn filaments might occurs during the tensile test which could be measured through the gradual decrease of the axial stiffness of the strands with loading. As earlier mentioned, the stiffness is measured by the slope of the linear part of the unloading curve. The linear fits of these are illustrated in Fig. 3.11.

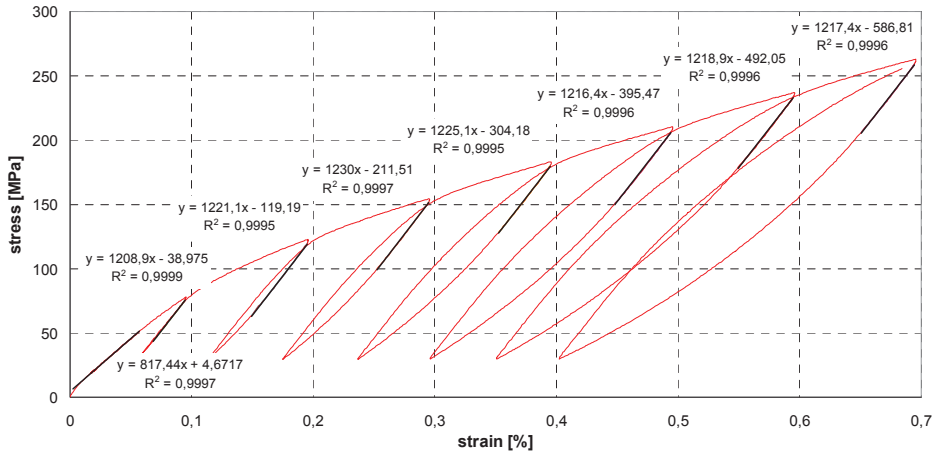

a)

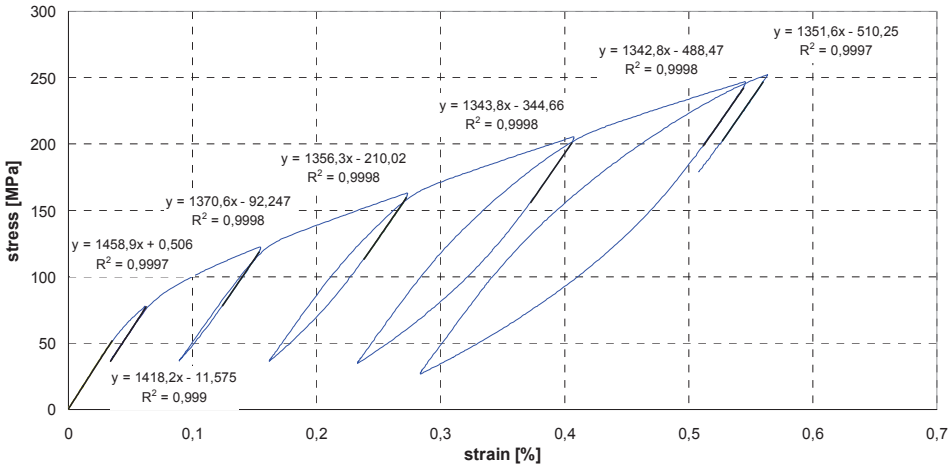

b)

Fig. 3.11. Measurement of the axial stiffness by the slope of the unloading curve. a) EAS Bronze Route strand. b) Alstom Internal Tin strand.

The plot of the stiffness against the applied strain is then shown in Fig. 3.12. The variation at the beginning of the curves is likely due to the settlement of the machine. Then a slight decrease is measured that does not exceed 3%. It would be adventurous to draw a conclusion about any correlation with filament breakage.

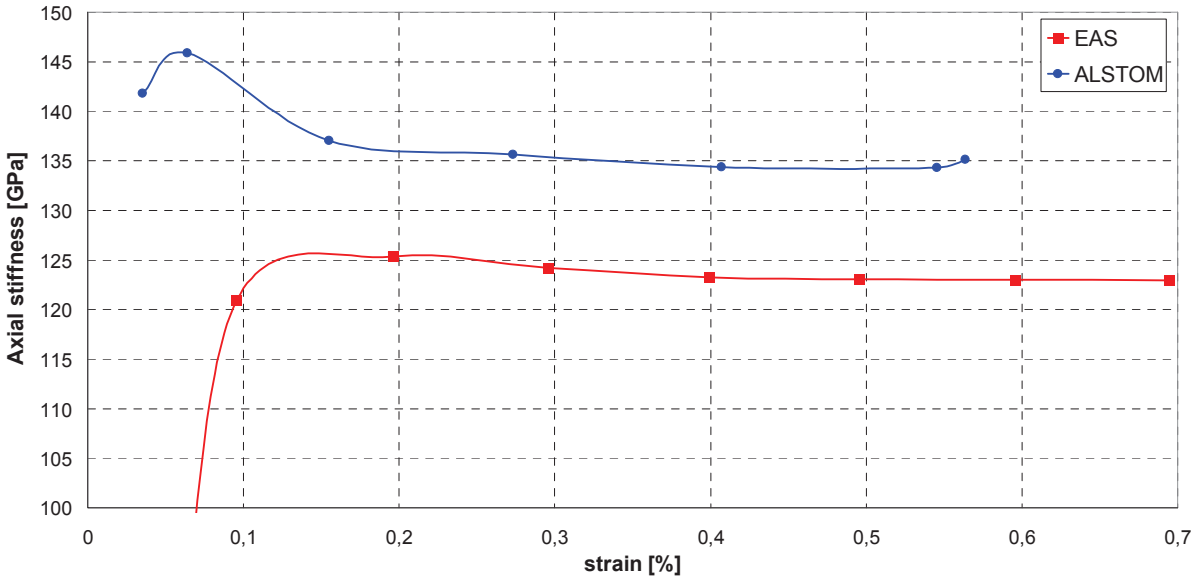

Fig. 3.12. Illustration of the evolution of the axial stiffness of the strands with the strain.

1.2.5 Isotropic and kinematic hardening measurement

At this stage, it is interesting to determine the isotropic and the kinematic hardenings of the material. They respectively stand for the evolution with the strain of the radius of the elastic domain and of the position of its centre. They are commonly written R and X [Lemaître Chaboche 1988]. In uniaxial loading, these are calculated as:

$$R = \frac{\sigma_a - \sigma_b}{2} \quad \text{and} \quad X = \frac{\sigma_a + \sigma_b}{2}, \qquad \textbf{eqn. 3.3}$$

where σ_a is the envelope of the curve and σ_b is the limit of the linear part of the unloading path as it is illustrated on Fig. 3.13, the initial the elastic domain is defined by the yield stress σ_0 and strain ε_0.

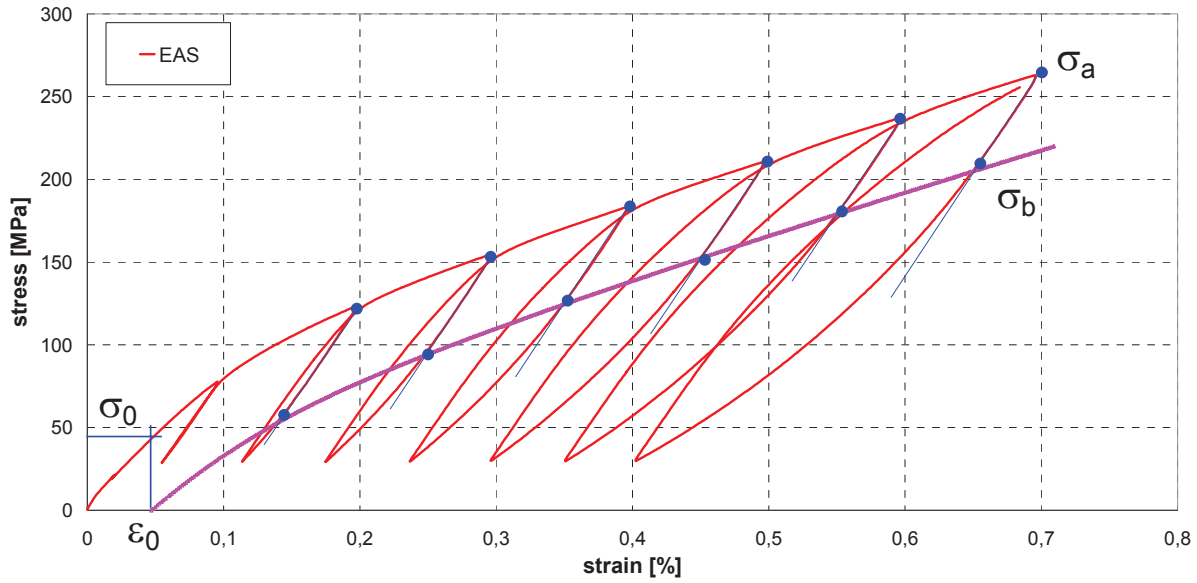

Fig. 3.13. Determination of the elastic domain and the stresses needed to derive the hardening variables.

The hardening variables can then be plotted as illustrated in Fig. 3.14 that shows the evolution of R and X with the strain (ε - ε_0). The measurement shows that there is no isotropic hardening, whereas the displacement of the yield surface is significant. These curves will be useful for the next paragraph that deals with the modelling of the elasto-plastic behavior.

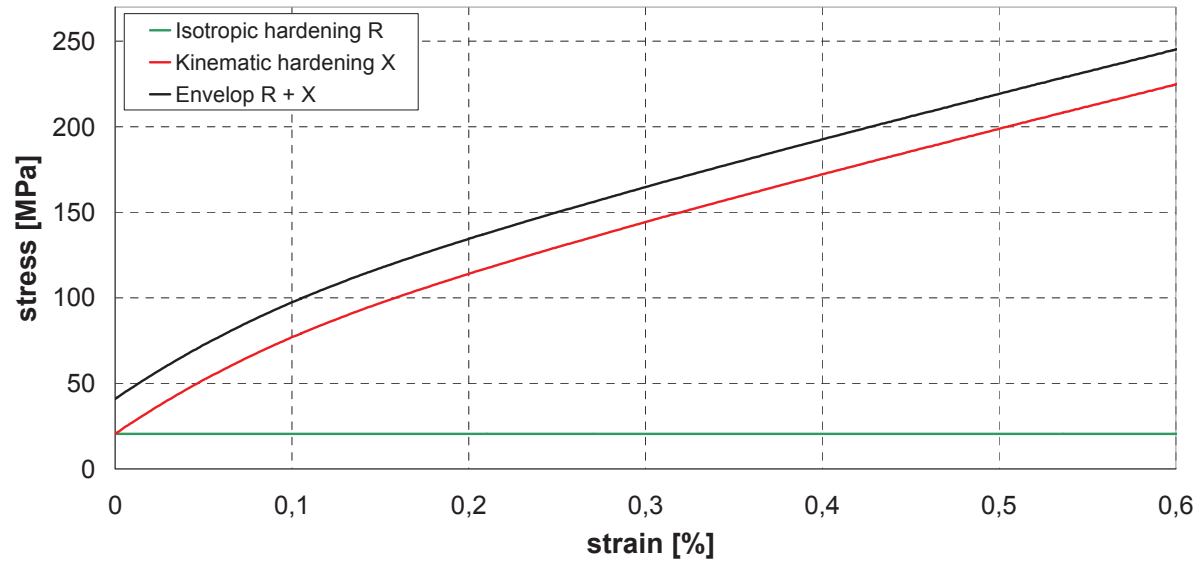

Fig. 3.14. Plot of the evolution of the isotropic hardening and the kinematic hardening as function of the plastic strain.

1.2.6 Evidence of a racheting effect after few loading cycles

The Racheting effect is a phenomenon that occurs as materials are cyclically loaded between constant stresses with a non-zero mean stress for a certain number of cycles. It reflects the accumulation of plastic deformation with cycling. Only fifteen loading cycles have been

performed on the bronze route and on the internal tin. The results are shown in Fig. 3.15 with a zoom on the strain accumulation in Fig. 3.16. The plots clearly show the occurrence of a ratcheting effect that causes additional irreversible deformation that mounts up to 0.017% after 15 cycles for the EAS strand. It seems that there is a stabilisation of the maximum strain after 15 cycles. A better way to show the ratcheting effect would be to perform hundred cycles and plot the maximum strain versus the number of cycles and see if there is stabilisation at a limit, as it seems in figure 3.16.

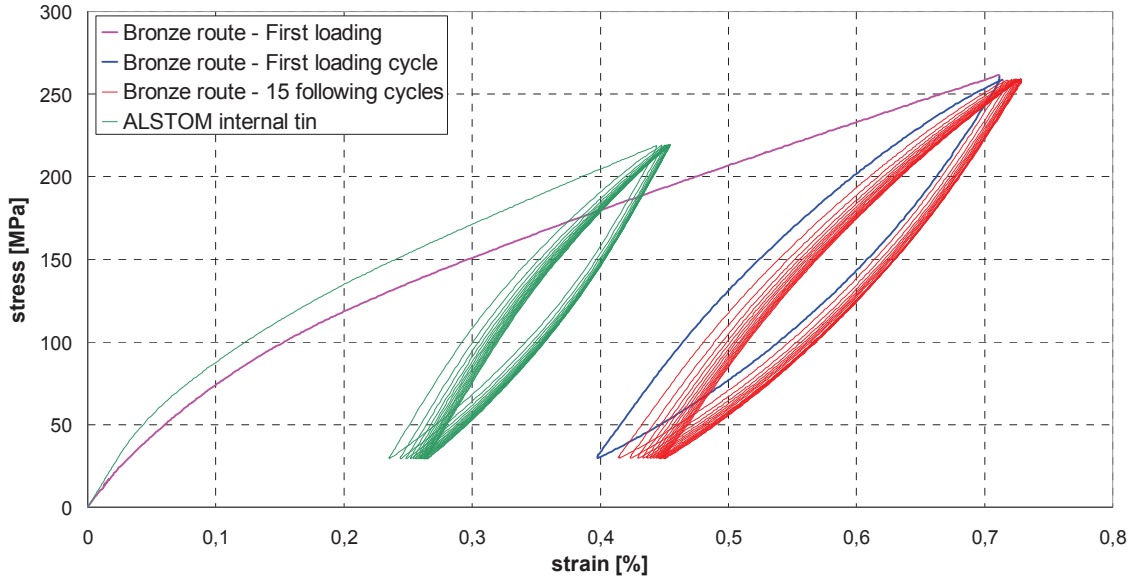

Fig. 3.15. Investigation of the Ratcheting effect for Bronze route and Internal tin Nb_3Sn strands. 15 cyclic loadings are performed.

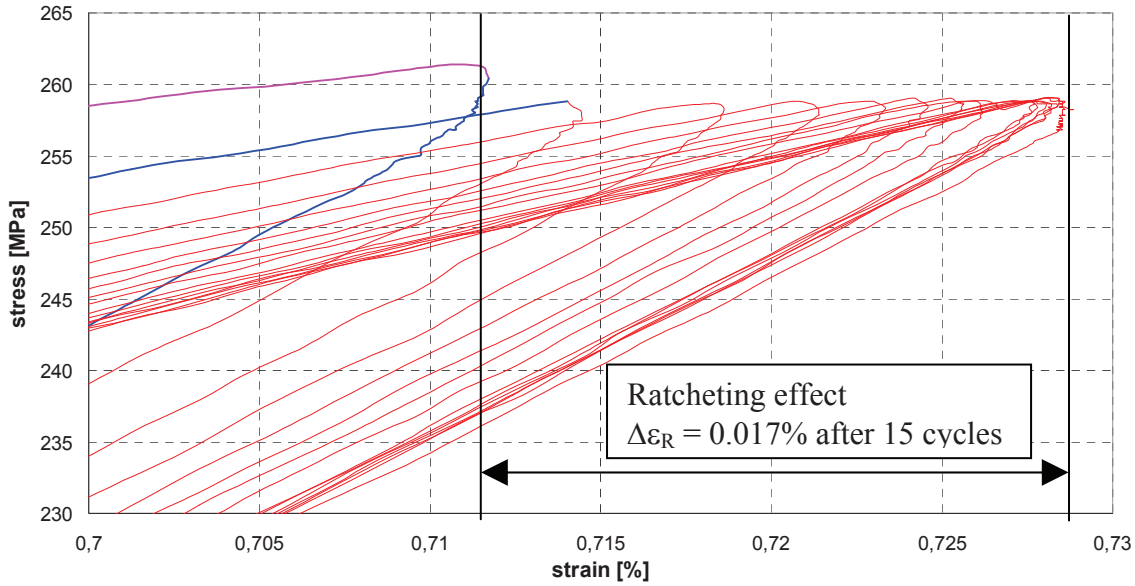

Fig. 3.16. Zoom on the accumulation of plastic deformation with the number of cyclic loading.

One remaining question is to determine whether the cyclic behavior stabilizes or not ($\Delta\varepsilon_R$ does not evolve anymore). In order to conclude on the influence of the Racheting effect produced by the cyclic Lorentz loadings during the ITER conductors' service life, it would be interesting to perform several hundred cycles on the strands.

1.3 Microscopic observation of the determination of crack occurrences

The application of the mixture law suggests that the mechanical behavior of composite strand could be better understood looking at the details of the composite structure of strands. Moreover, the question of the presence of micro-cracks in the Nb_3Sn filaments after the tensile tests of the strands is still to be answered. In this purpose, microscopic observations have been carried out down the scale of the microfilament. The Scanning Electron Microscopy technique has been used to determine the composition of the strand and to measure the dimensions of the different components. SEM method asks to work on highly clean surface in order to get the most detailed microscopic depiction. In the next paragraph, the specific procedure that is needed to prepare samples is briefly reminded (for more details, one should refer to the work of [Jewell 2008]). The observations of reacted internal tin and bronze route strands that have revealed some interesting features are presented. The author wishes to deeply thank the members of the ASC laboratory of NHMFL that welcome him for internship, especially Peter Lee for his great advices in sample preparation for SEM observation.

1.3.1 Sample preparation for SEM observation

The samples to be observed should be prepared by careful polishing so as to get good SEM images. The first step of the procedure is about the impregnation of the sample into a cylindrical puck made of EPOXY. The impregnated material is then gradually ground on successive polishing papers of decreasing size of grain (from 40 to 8µm ,Grit P320, P3500) during few minutes and then by diamond suspension paste (grain of 3 or 1µm) on a soft cloth for few tens of minutes. The final polishing step is performed using the automatic *Vibromet* polisher that reduces the depth of the polishing scratches below 0.06µm (the size of the grain in the SiO_2 colloidal liquid) after twenty four hours of its use. The polishing quality brought by the *Vibromet* is mandatory to avoid generating any cracks of the filaments in samples virgin of any loading. By the way, it produces highly clean surface as presented in the following.

1.3.2 Validation of the polishing techniques

In order to determine the presence of cracks in the strands after their tensile test, the first step is to be sure that the polishing procedure did not cause any breakage of the initially crack-free filaments. The results of the SEM observation of the polished samples are presented hereafter.

a. Internal Tin strand observation

Fig. 3.17 a) & b) and Fig. 3.18 a) & b) present what could be a damaged and a clean strand after polishing when the longitudinal and transverse cross-sections are observed.

a) 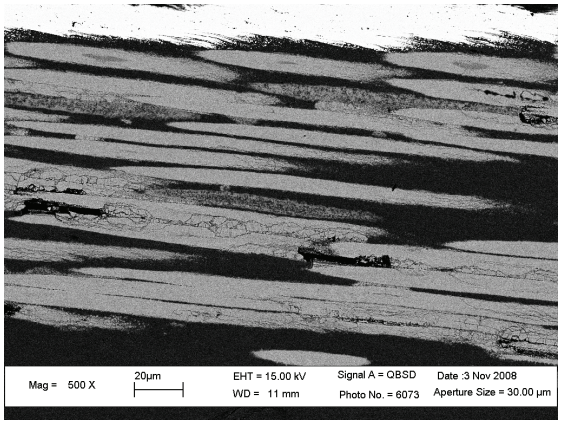

b) 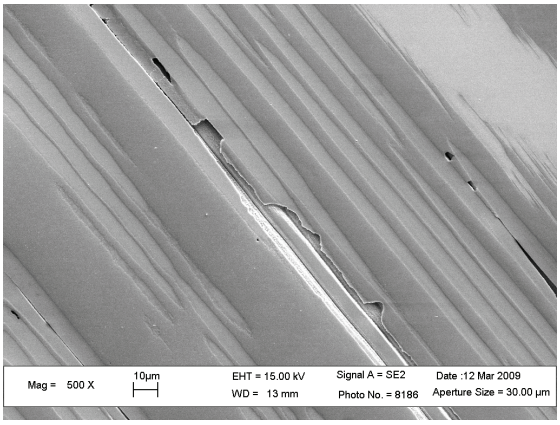

Fig. 3.17. a) Longitudinal cross-section of the internal tin strand. Observation of the damages due to bad polishing. b) Example of clean polishing with filaments free of cracks. The filament (diameter: 8µm) of the row is seen through a Kirkendall void.

a) 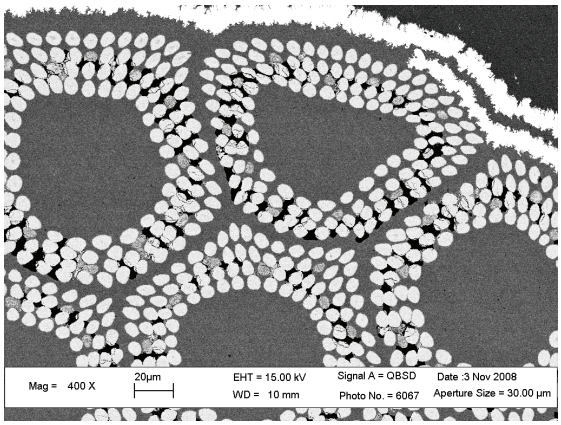

b) 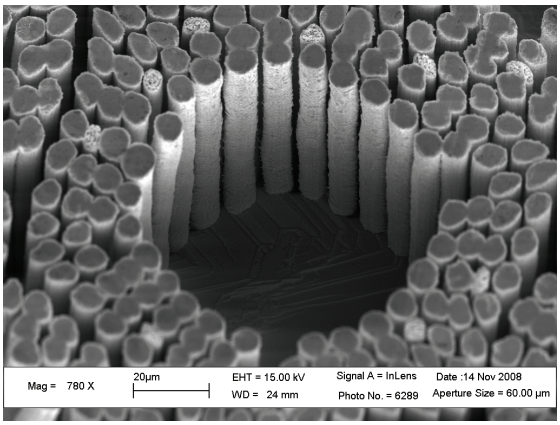

Fig. 3.18. a) Transverse cross-section of the internal tin strand. Illustration of the filament bundles and the overlap of Tantalum diffusion barrier. Observation of damage due to polishing greater near the voids in-between the filaments where these are not supported. b) Example of etched zone where the Nb_3Sn filaments and Nb_3Sn -Ti enriched filaments are crack-free over tens of micrometers after good polishing.

It has also been observed that ALSTOM reacted strands shows some microfilament with a high Titanium content – see Fig. 3.18 b). Their aspects are quite specific. For this thesis, it has been asked to measure the Nb_3Sn area of strands in order to better characterise their critical current. The analysis gives:

- Number of filament bundles: 19
- Number of filaments per bundle: 140
- Total number of filaments: 2660
- Mean filament diameter: ~6µm

For one filament bundle, roughly 10 {Nb_3Sn+Ti} filaments over 140 filaments are observed. If the filaments sections are assumed to be circular, the total cross-sectional area is:

S_{Nb_3Sn}= 75200 µm²

b. Bronze route strand observation

Fig. 3.19 a) & b) show that the polishing method is now well carried out. In Fig. 3.20 a) & b) the different materials are depicted. In particular, it has been asked during this thesis to

measure the width of the Chromium coating for quality control. The measurement is in agreement with procurement.

$e_{coating} \approx 2\mu m$

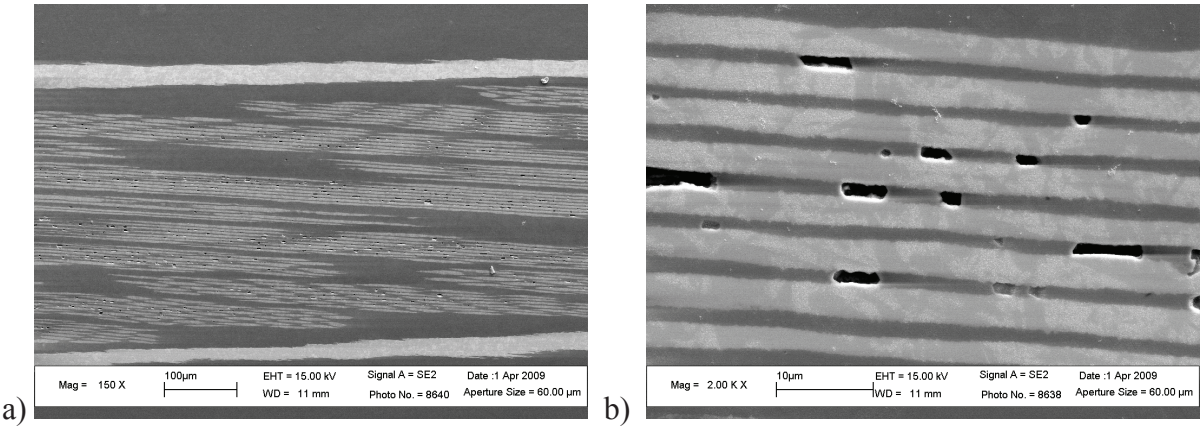

Fig. 3.19. a) Longitudinal cross-section of the bronze route strand. The Tantalum diffusion barrier and the twisted filament bundles are visible. b) Zoom in the filament with evidence of voids of few microns between the filaments (diameter: 4µm).

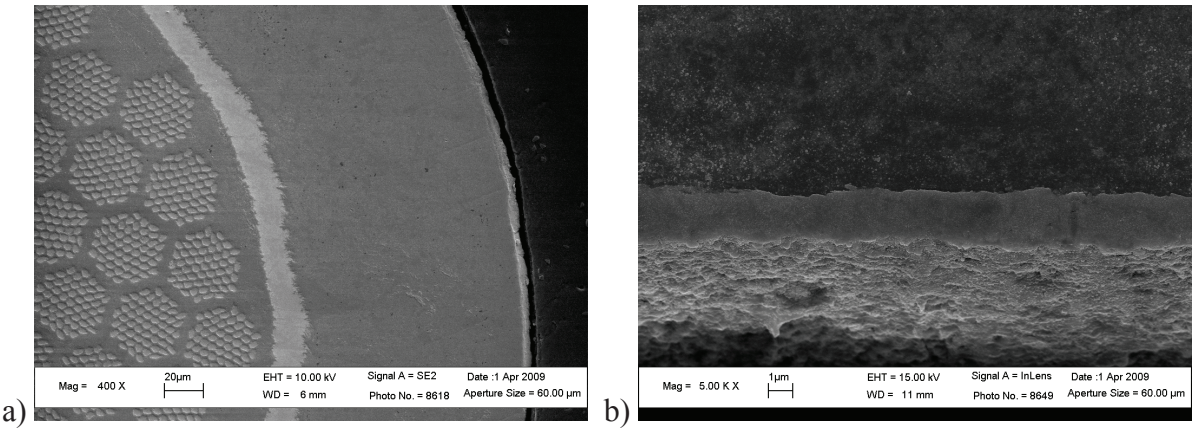

Fig. 3.20. a) Transverse cross-section of the bronze route strand. The filament architecture is shown as well as the Ta barrier, the OFHC copper ring and the Chromium coating. b) Zoom on the 2 micron Cr coating with asperities at its outer surface.

1.3.3 Micro-crack observations of tensile tested strands

Now that the polishing techniques are validated, the next step of the microscopic analysis was about the observation of micro-cracks at the scale of the filaments. Two different samples have been strained up to 0.7% and up to the global failure at 0.8%, their longitudinal and their transverse cross-sections have been observed. The main result is that the sample is essentially crack-free after a tensile loading of 0.7% - see Fig. 3.21. However, when cracks are observed they can lie either along the longitudinal or the transverse direction (regarding the current transverse crack are more detrimental than longitudinal) – see Fig. 3.22. The radial cracks are arising from voids in Fig. 3.22 b). As far as transverse cross-section is concerned, it seems that the cracks propagate from the non-reacted cores to the outside of the filaments – see Fig. 3.23. Finally, when the same analysis is performed on the second sample, cracks are found for almost all filaments – see Fig. 3.24. The rupture modes are not unique and cracks propagate in different directions – see Fig. 3.25. Finally, too few samples have been tested (at different loading) to conclude about an accurate determination of a crack initiation criterion but the presented result seems to point toa an axial strain greater than 0.7%. The main issue relative

to SEM observation of the strands comes from the twisting of the filament (going in and out the surface) and the small area that is covered by the observation. Besides it clearly appears that the size of the crack opening is about a few hundred nanometres, which is small enough that is also reduces the ability to detect or count the number of cracks.

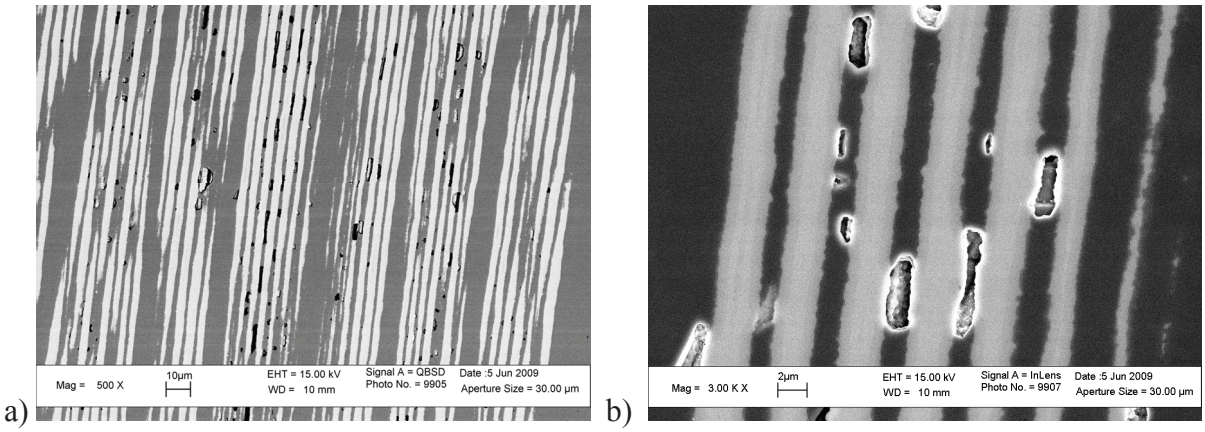

a) b)

Fig. 3.21. After a tensile loading up to 0.7%, the sample is essentially crack-free.

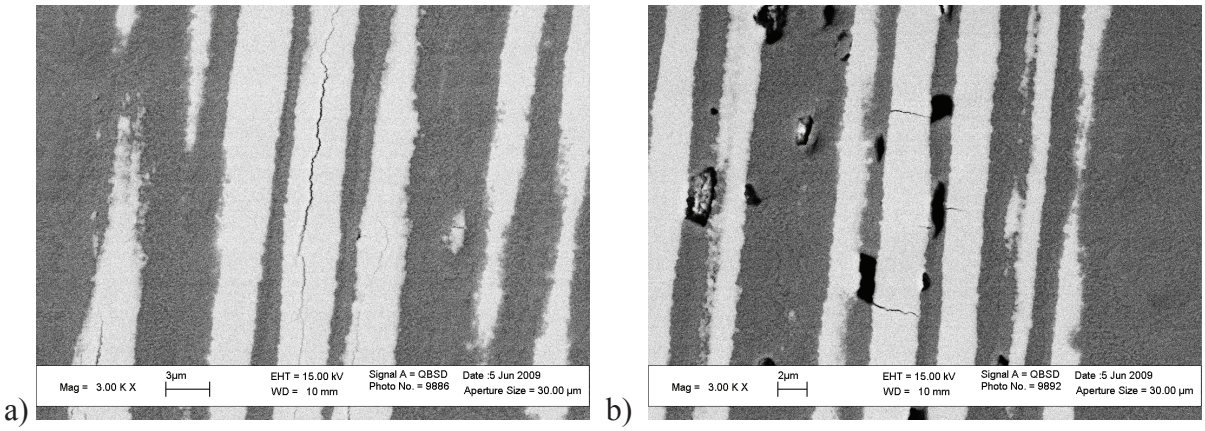

a) b)

Fig. 3.22. After a tensile loading up to 0.7%, few cracks have been observed in both the filaments longitudinal a) and the transverse directions b).

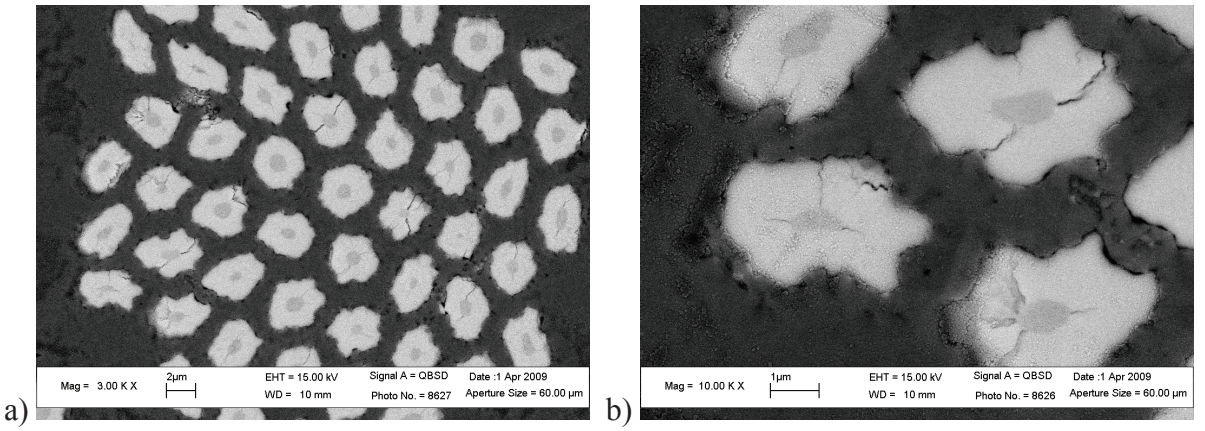

a) b)

Fig. 3.23. a) After a tensile loading up to 0.7%. Detailed view of a filament bundles with presence of radial cracks. b) Zoom of the Nb_3Sn filaments with non-reacted core from which cracks are coming out.

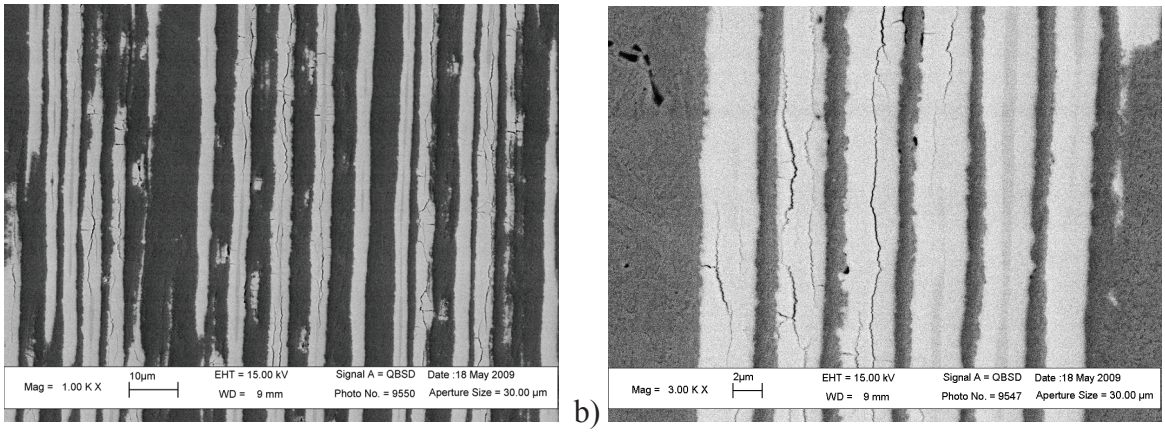

a) b)

Fig. 3.24. After a tensile loading up to the global failure, most of the filaments are now damaged.

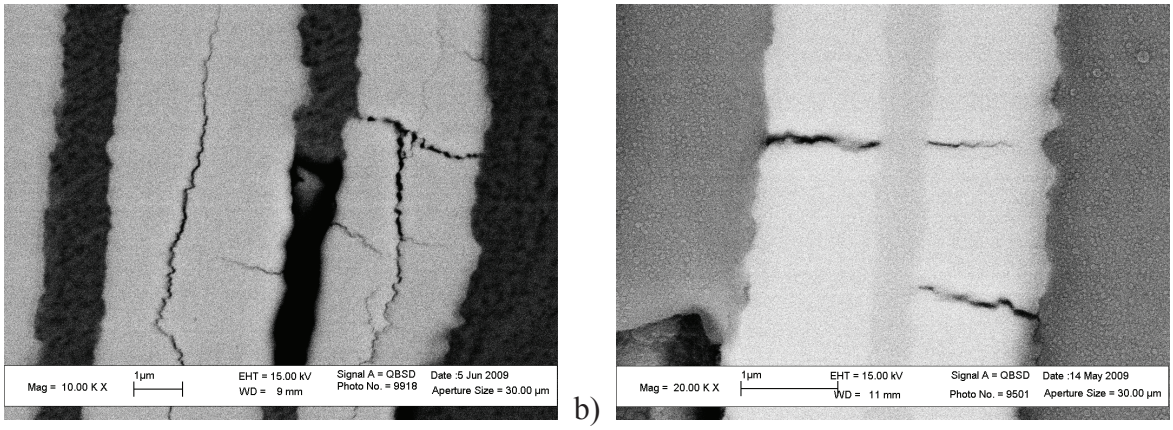

a) b)

Fig. 3.25. After a tensile loading up to the global failure, a great number of damaged filaments are found in the sample.

2 Multifil axial material constitutive law

2.1 The axial elasto-plastic model

2.1.1 Assumptions of the model

In the light of the experimental results, it appears mandatory to be able to simulate plastic behavior in Multifil. An important task during this thesis has been dedicated to the modification of the Multifil material constitutive law for axial plasticity to take into account the experimentally characterized behavior. Modelling the axial plastic behavior asks to be able to reproduce the non-linearities of the stress-strain curves with the induced irreversible deformations. However, the kinematical beam model does not pretend to depict the complex three dimensional phenomenon of plasticity. Whereas plastic deformations could be very localized within a strand, particularly in case of deformations induced by a pinching contact, the beam model in Multifil is not rich enough to represent the three-dimensional aspect of such localized plastic deformations. Considering the components of the Green-Lagrange strain tensor derived from the employed kinematical beam model, and expressed in a local framework relative to the beam (the third axis standing for the longitudinal direction) one can remark that all components of this tensor do not evolve the same way through the beam cross-section as function of the transverse coordinates. In particular the components $E_{\alpha\beta}$ are constant through the section, the components $E_{\alpha 3}$ are linear and the components E_{33} evolve

quadratically with respect to the transverse coordinates. Therefore, it is considered that only the axial components E_{33} of the strain tensor are described with sufficient fineness to be consistent with a localization of plasticity in the cross-section of a strand. For this reason, it is assumed that the plastic behavior affects only the longitudinal components of the strain and stress tensors. The second Piola-Kirchhoff stress tensor **s** is expressed **s** as follows in function of the Green-Lagrange strain tensor **E**:

$$\mathbf{s} = \mathbf{C}^* : \mathbf{E} + s_{33}(E_{33})\, \mathbf{e_3} \otimes \mathbf{e_3} \ , \qquad \textbf{eqn. 3.4}$$

where the components of adapted stiffness tensor **C*** are calculated as follows in function of the standard elasticity stiffness tensor **C**:

$$C^*_{ijkl} = C_{ijkl} \text{ for } (i,j) \neq (3,3) \qquad \textbf{eqn. 3.4}$$
$$C^*_{33kl} = 0$$

This expression means that the consideration of the elastoplastic behavior is limited to the relation between the longitudinal stress s_{33} and the longitudinal strain E_{33}. This limitation of the consideration of plastic effect to the axial components is also related to the difficulty to identify and describe the actual behavior of strands in transverse directions. Indeed, since strands are constituted of a complex assembly of twisted Nb_3Sn filaments within a copper matrix, plastic deformations occurring in the transverse directions involve phenomena taking place at the microscopic scale of filaments which would be very hard to homogenize at the scale of the strands. As measurements coming from traction experiments are usually the only available data concerning the strains, it appeared consistent in a first stage to limit the accounting of plastic effects only to longitudinal components.

2.1.2 Model of hardening

The elastoplastic model finally leads to consider a mono-dimensional model which can be written with the stress σ, the strain ε and f a non linear function:

$$\sigma = f(\varepsilon), \qquad \textbf{eqn. 3.5}$$

where $f(\varepsilon)$ is a unique function that fits the experimental curves.

In order to model irreversible deformation, the axial stress should depend on two other scalar variables. Their introduction aims at reproducing the different loading paths while unloading-loading (cycle) and the accumulation of plastic deformation with the loadings. In classical elasto-plastic formulation, these two variables are referred to the isotropic and the kinematical hardening of the material (R and X). Their evolution with the strains depicts the hardening of the material. The evolution of R reflects the increase of the yield strength with strain. The evolution of X is associated with the *Bauschinger effect*. With the initial elastic limit k, both the isotropic and kinematic hardenings define the domain of plasticity of the material. In a monodimentional model, the criterion of plasticity simply reads (limit of the plastic domain):

$$\left|\sigma - X\right| - R \leq 0 \qquad \textbf{eqn. 3.6}$$

The variables R and X evolves with the strain according to the following relation:

$$R = f_R(\varepsilon_h)$$
$$X = \alpha \cdot f_X(\varepsilon_h) \qquad \textbf{eqn. 3.7}$$

where ε_0 is the yield strength, E is the Young modulus, ε_h is the strain hardening since the last yielding, f_R and f_X are non linear functions of ε_h representative of the hardenings and α indicates the direction of the loading, tensile or compressive (1 or -1). Chaboche's proposal is to use exponential functions for the hardening functions so as to be valid over a broad range of strain and to be continuously differentiable. However, other functions can be used depending on the experimental stress-strain properties. The issue is to find out the proper law.

2.1.3 Numerical integration through beam cross-sections

Since the terms coming from the expression of virtual works are not linear with respect to transverse coordinates (due to the presence of quadratic terms in the strain tensor, and especially to the nonlinearities introduced by the plastic behavior), the integration of these terms cannot be performed analytically. The integration is thus performed numerically, using a grid of 24 integration points distributed on the cross-sections of beams which are located at Gauss integration points of the centroid line of the beam elements. The history variables that are required to describe the plastic behavior are stored at each of these integration points.

2.1.4 Identification of the longitudinal plastic behavior for the different components of the cable

For the simulation of superconducting conductors, at least three kinds of material behavior should be considered: the copper wires and the composite strands (reacted or unreacted). The issue is now about the determination of the hardening functions f_R and f_X to be used in the model. As exposed in 1.2.5, the functions are determined by the proper fit of both the envelope and the cyclic curves. Three kinds of function are used to fit the stress-strain characteristic of the OFHC copper wire, the non reacted strand and the reacted strand. The functions are based on polynomial function or a combination of exponential and affine functions identified on experimental result. It is also shown that the axial behavior of copper wire and unreacted composite wires can be described using a unique function to represent the hardening which is not possible for the reacted strand.

a. Unreacted strand

The experimental stress-strain of unreacted strand measured at 4.2K is presented in Fig. 3.26 from [Ilyin 2006]. The function used to fit the curve is a fifth order polynomial function. For the identification of the coefficients, the elastic domain is removed out of the curve (offset defined by $\{\sigma_0, \varepsilon_0\}$) – see Fig. 3.27. The identification is:

Unreacted strand @4.2K	$\sigma_0 = 200\ MPa$ $\varepsilon_0 = 0.2\ \%$ $E = 92\ GPa$	$\sigma(\varepsilon) = a_1 \cdot \varepsilon^5 + a_2 \cdot \varepsilon^4 + a_3 \cdot \varepsilon^3 + a_4 \cdot \varepsilon^2 + a_5 \cdot \varepsilon$ a_1= 1.13 e^{11}, a_2= -6.55 e^9, a_3= 1.87 e^8, a_4= -4.45 e^6, a_5= 7.77 e^4,

Table 3.2. Identification of the parameters for the unreacted strand.

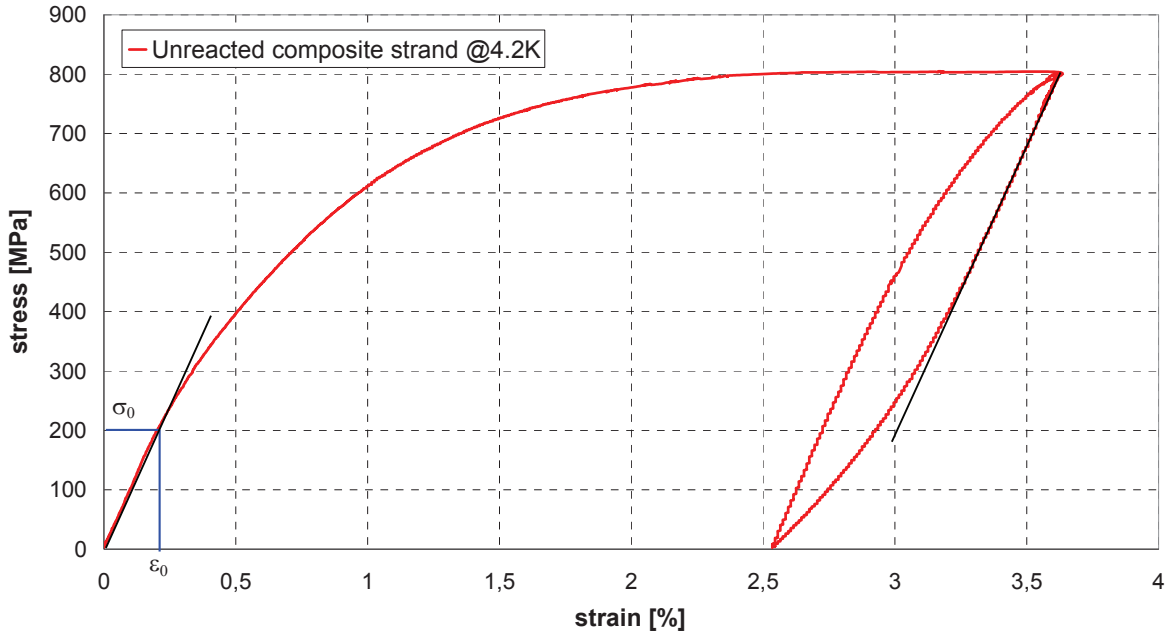

Fig. 3.26. Stress-strain characteristic of the unreacted wire measured at 4.2K.

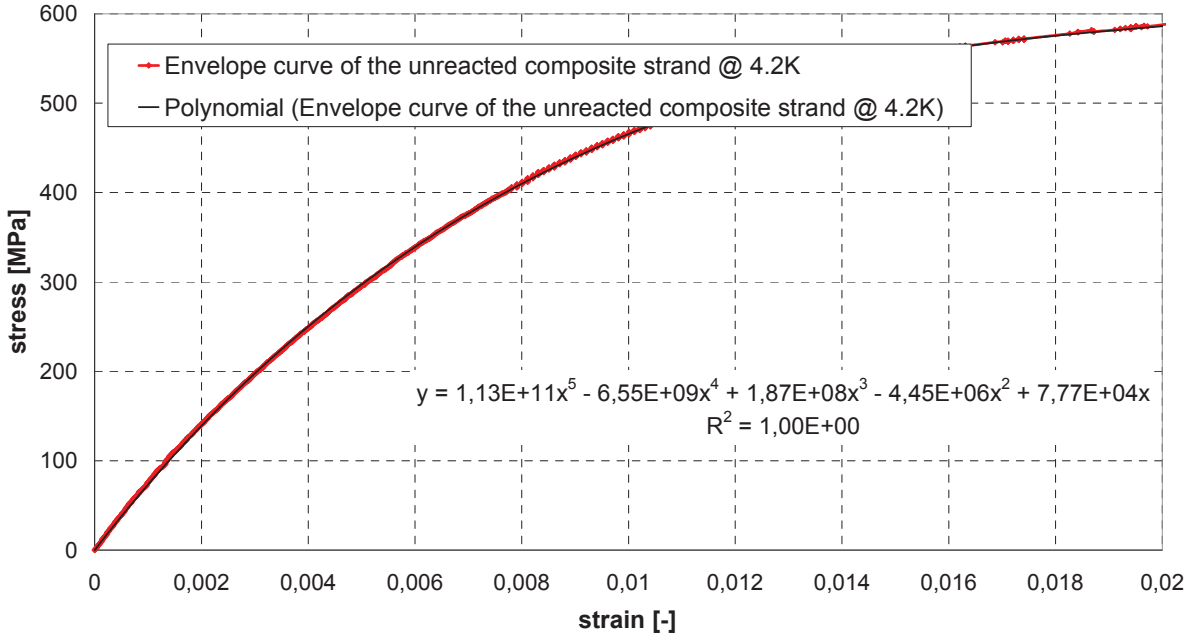

Fig. 3.27. Identification of the envelope curve (plastic domain) of the unreacted wire measured at 4.2K. A polynomial function is sufficient to fit the curve up to 2%.

b. Copper OFHC

Regarding the identification of OFHC copper wires, polynomial functions are not able to reproduce the envelope of the curve (green curve in Fig. 3.28). A sum of exponentials with offset is then preferred. The identification is:

OFHC copper @4.2K	$\sigma_0 = 20\ MPa$ $\varepsilon_0 = 0.02\ \%$ $E = 80\ GPa$	$\sigma(\varepsilon) = a \cdot \exp(-b \cdot \varepsilon) + c \cdot \exp(-d \cdot \varepsilon) + e \cdot \exp(-f \cdot \varepsilon) + g$ $a = -35; b = 671; c = -24; d = 4126; e = -94; f = 66; g = 153$

Table 3.3. Identification of the parameters for the OFHC copper

Using this relation and the proper coefficient, it is possible to fit the experimental stress-strain curve and so for two different temperatures: 300K and 4.2K – see Fig. 3.28. The experimental data are from [Mitchell 2005].

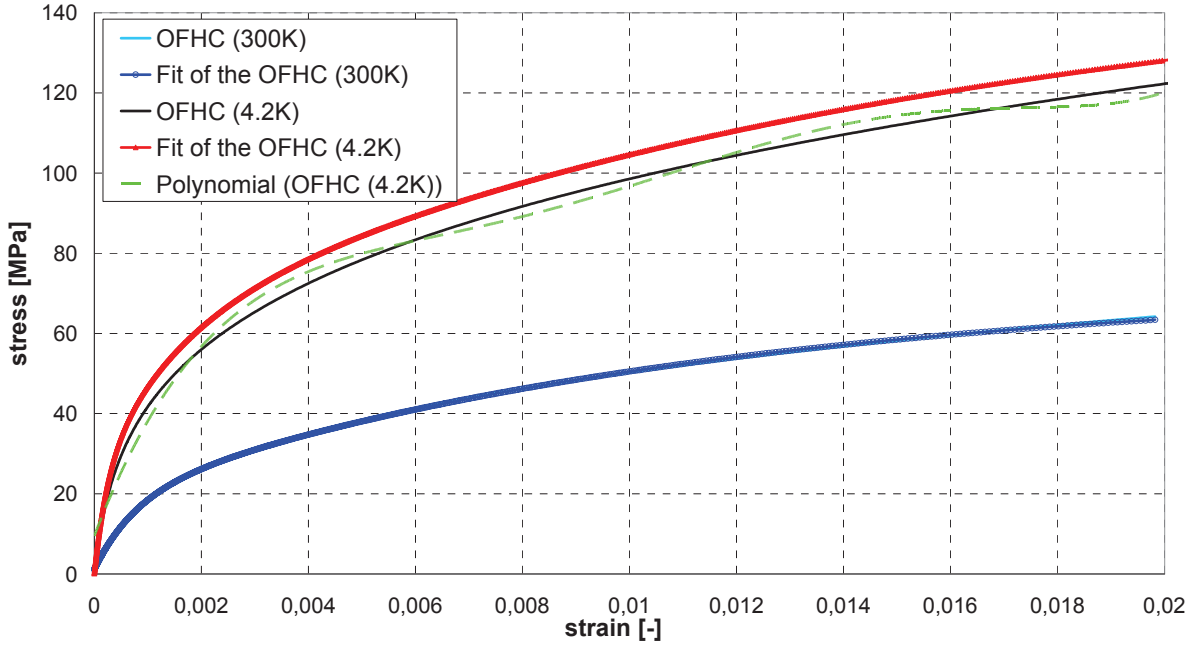

Fig. 3.28. Stress-strain characteristic (without the elastic domain) of the OFHC copper wire measured at room temperature and 4.2K [Mitchell 2005]. The curves are fitted using exponential functions.

c. Reacted wire

For the reacted strands, investigations have failed to find a unique hardening function able to reproduce both the behavior of the envelope curve and the behavior of unloading/loading cycles. The Nb_3Sn filaments in the reacted composite strand have an elastic behavior until breakage – see Fig. 3.9. However, even subtracting this linear part from the stress/strain curve, the method fails to identify the function. Therefore, it was decided to describe the behavior using two different functions. The first represent the kinematic hardening related to the envelope curve f_{env} and the second the unloading/loading cycles f_{cyc}. The use of two different hardening functions should be considered only as a means to reproduce the experimental curve rather than as a rendering of the real mechanisms inherent to the composite nature of the strand. The identification starts with the determination of the elastic domain. Then, the envelope and the cyclic curves are selected – see Fig. 3.29. The slope of the linear part of the envelope is determined (here 27 GPa). The linear contribution is removed from the envelope and from the cyclic curve – see Fig. 3.30. Two noteworthy points here are that the unloading and the loading curves all match but the envelope curve differs – see Fig. 3.31, Fig. 3.32 and Fig. 3.33. As a result, a single relation can be used for every loading cycles and a second for the envelope. Chaboche's formulation plus the linear function is used for the envelope. For the cyclic curves, Chaboche's model is multiply by an exponential. The identifications are:

Reacted strand @300K	$\sigma_0 = 50\ MPa$ $\varepsilon_0 = 0.04\ \%$ $E = 125\ GPa$	$\sigma_{env}(\varepsilon) = a \cdot (1 - \exp(-b \cdot \varepsilon) + c \cdot \varepsilon$ $a = 38\ ;\ b = 1466\ ;\ c = 27157$ $\sigma_{cyc}(\varepsilon) = i \cdot \left(1 - \exp(-j \cdot \varepsilon)\right) \cdot k \cdot \exp(\varepsilon) + c \cdot \varepsilon$ $i = 99\ ;\ j = 592\ ;\ k = 1.45$

Table 3.4. Identification of the parameters for the reacted strand.

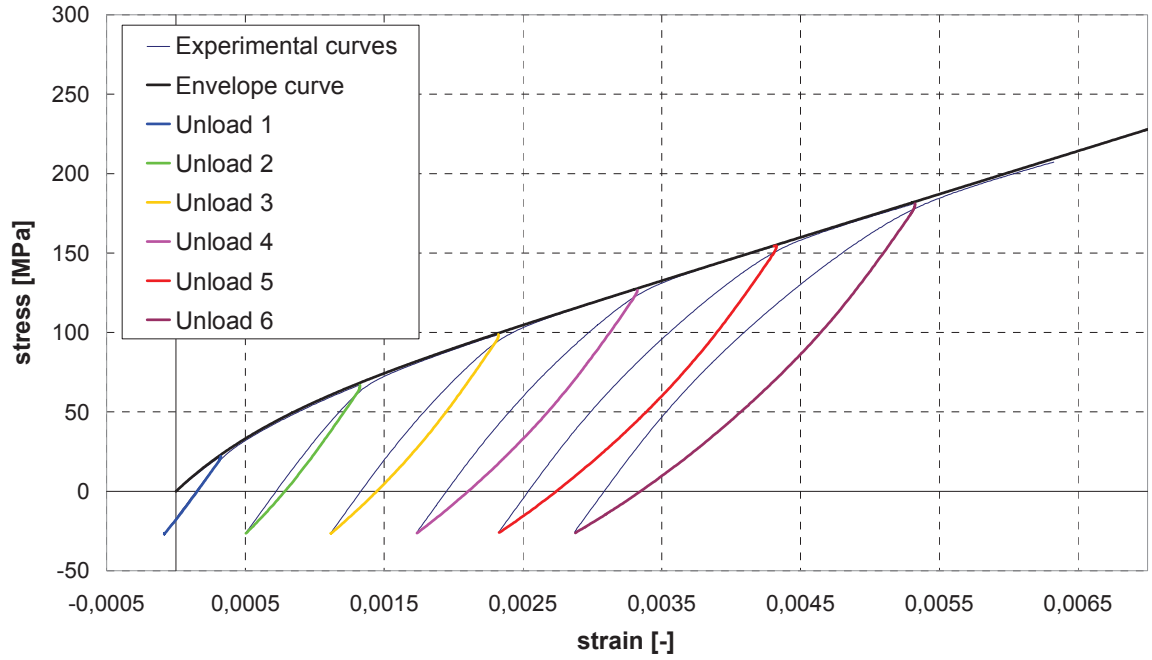

Fig. 3.29. Selection of the parts of the curve to be identified, the envelope and the cyclic curves. The elastic domain of the envelope has been removed.

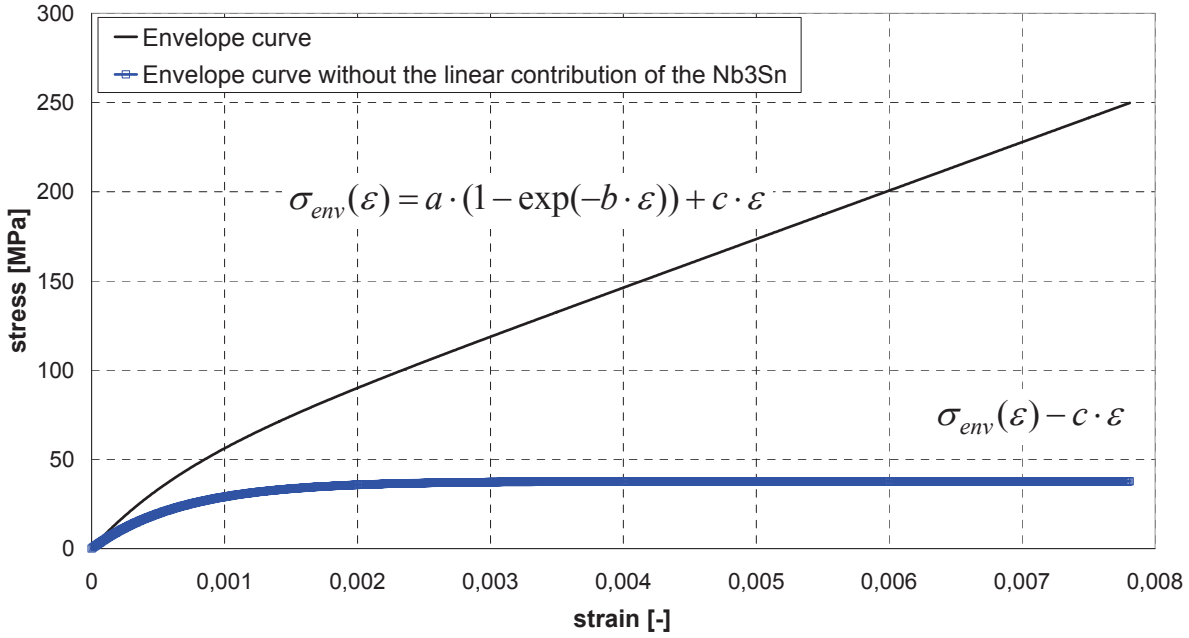

Fig. 3.30. Illustration of the envelope curve from which the elastic domain has been removed. The two curves are for the cases with or without the linear contribution of the Nb_3Sn.

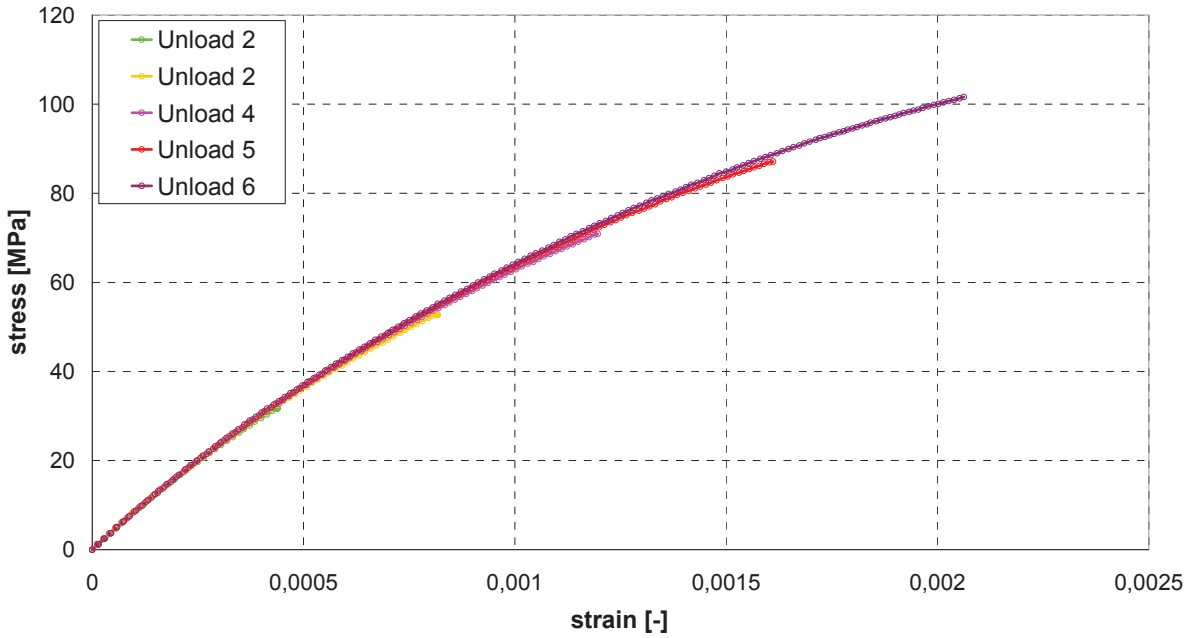

Fig. 3.31. Illustration of the overlapping of the five unloading curves from which the elastic part and the linear contribution of Nb_3Sn have been removed.

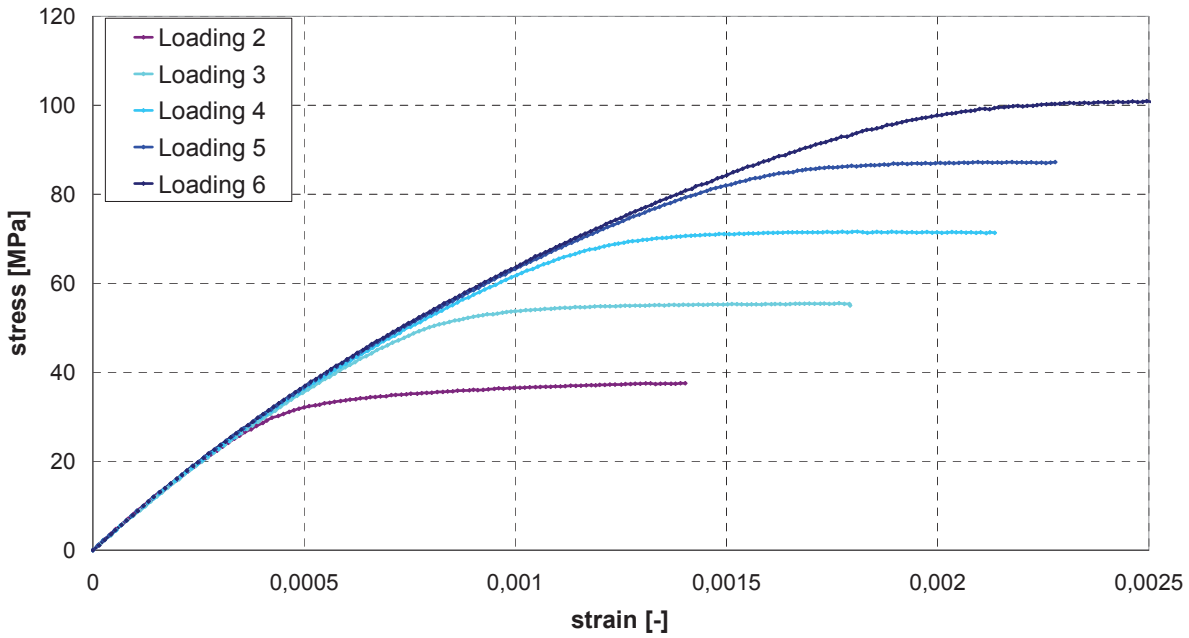

Fig. 3.32. The five loading curves match (the Nb_3Sn linear contribution has been removed). The parts of the curves that differ from the main part are corresponding to the return to the envelope after cycling.

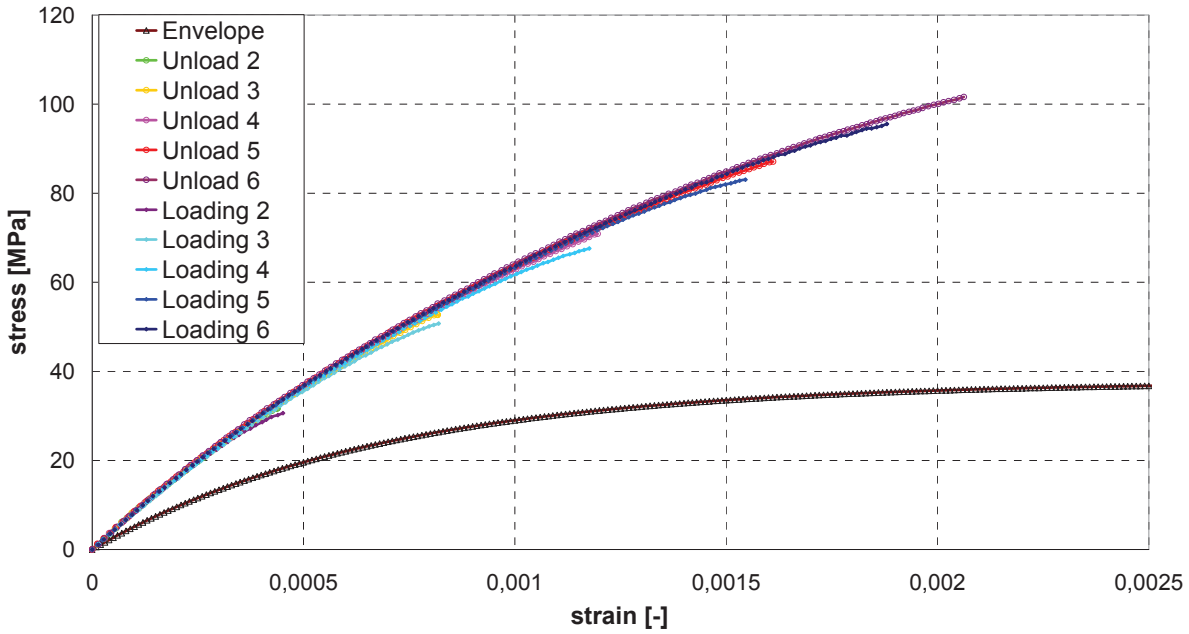

Fig. 3.33. Illustration of the overlapping of the cyclic curves (unloading and loading). The envelope curve is different from the cyclic curves.

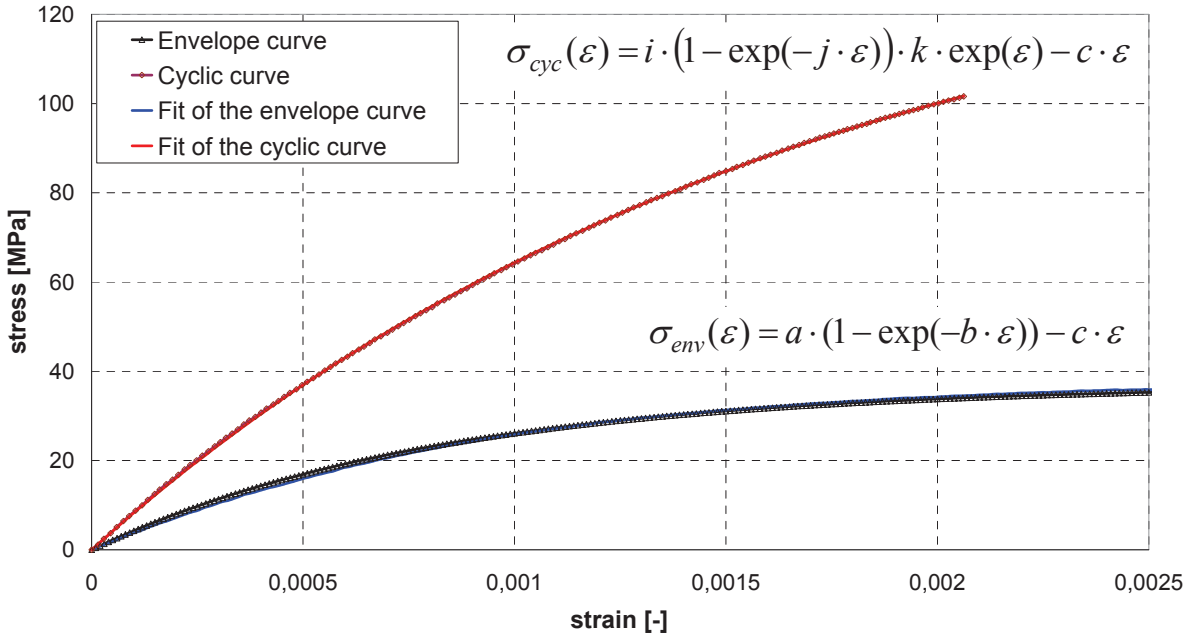

Fig. 3.34. Identification of the envelope curve and the cyclic curve for the reacted wire at room temperature. The functions are based on exponentials so as to properly fit the curves.

2.2 Elasto-plastic simulation of the axial behavior

The elastoplastic model is now applied to describe the cyclic behavior of the three kinds of wires. The hardening functions f_R and f_X to be used in the model are set according to the fitting function earlier defined. According to the material that is considered, one or two of the hardenings (R or X) are used. For the unreacted strand, R is constant and X evolves according to the fitting function. For the copper wire, both hardening function are activated. Their respective contributions are taken proportional to half on the fitting function. At last, for the reacted strands, the isotropic hardening is constant and two kinematical hardening functions

are used for the envelope and the cyclic curve. This method requires storing the maximum strain that have been ever reached during the loading history and determining whether the loading path is the envelope or the cycles. The issue regarding the ending of the cycles is only partially solved. The loading path effectively goes back to the envelope as sought but still in a discontinuous way. Fig. 3.35 presents the result obtained by the developed model of axial plasticity that show the relevance of the approach.

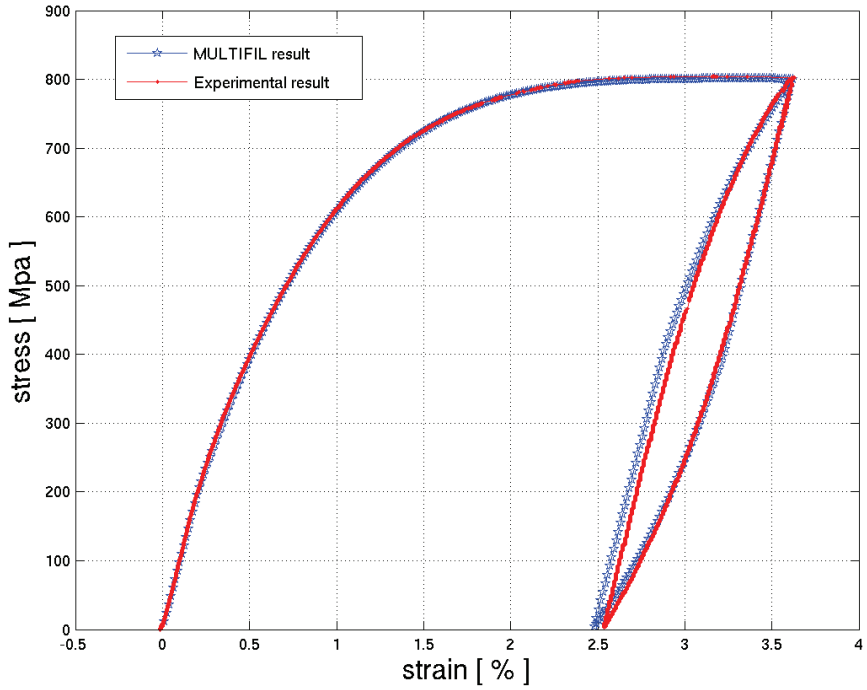

a)

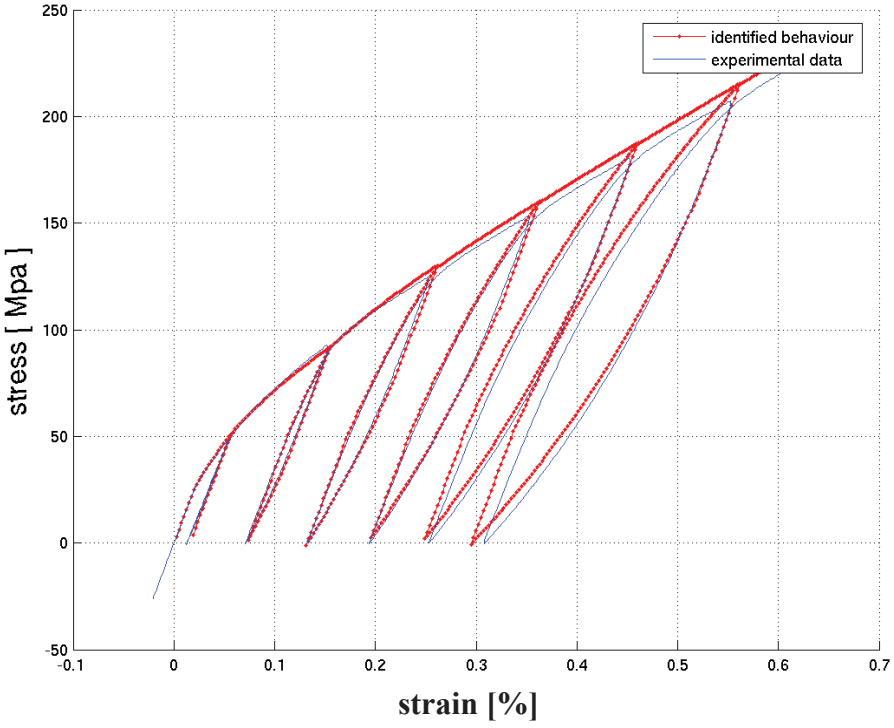

b)

Fig. 3.35. Axial stress-strain curve relative to non reacted and reacted strand calculated with the axial plastic model from the fit of the experimental data.

The next figure presents the result for OFHC wire and reacted strand when the loading starts either with compression or with tension. It is important that the model is valid for any direction in order to properly describe the bending solicitation as it is found in the cable. The behavior in Fig. 3.36 b), relative to the reacted wire, is not symmetric, as it is for the copper. It indicates the remaining issues relative to the reacted strand behavior and the difficulties to get homogenized behavior [Mitchell 2005 b], [Boso 2005 a], [Boso 2009].

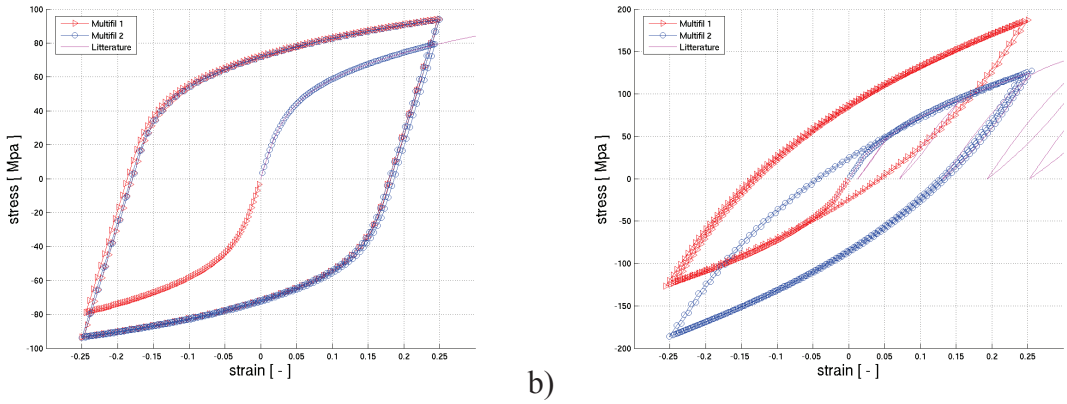

a) b)

Fig. 3.36. Axial stress-strain curve relative to OFHC wire and reacted strand calculated with the axial plastic model. The model remains valid for both the compressive and the tensile part.

3 Validation of the cable model for the axial loading

3.1 Tensile test of 36 strand cable

3.1.1 Procedure of the test

The axial elastoplastic model is now defined and will be used for the simulation of the uniaxial tensile test of a 36 unreacted strand cable. The strand mechanical properties are identified from data reported in Fig. 3.35 a). The cable design is 3x3x4 with the twist pitches of 26-70-110 mm and a void fraction of 32% [Ilyin 2006]. The global axial stress-strain curve of the cable is derived as follows:

$$\varepsilon_C = \frac{L - L_0}{L_0}, \qquad \textbf{eqn. 3.8}$$

with, L and L_0 the length of the cable calculated by the difference of the axial position of the extreme nodes N_r and N_l at the left and right end sides of one of the stand:

$$\begin{aligned} L &= (\mathbf{x}_{Nr}^{n} - \mathbf{x}_{Nl}^{n}) \cdot \mathbf{e_3} \\ L_0 &= (\mathbf{x}_{Nr}^{0} - \mathbf{x}_{Nl}^{0}) \cdot \mathbf{e_3} \end{aligned} \qquad \textbf{eqn. 3.9}$$

The global stress is defined as the sum of the reaction forces F measured by the nodes N_r from one side of the cable divided by the cross-sections of the strands. With N_b the number of strand and r_b the strand radius, it reads:

$$\sigma_c = \frac{\sum_{N_r} F}{N_b \cdot \pi \cdot r_b^2} \qquad \text{eqn. 3.10}$$

Before presenting the final result of the cable tensile test, the effects of the boundary condition are presented.

3.1.2 Boundary condition effects

Regarding the transverse boundary condition, the issues with the axial loading are less severe than for the shaping part of the modeling, when large transverse displacements are involved – see Chapter II 3.2. However, two important points must be mentioned. First, the transverse displacements cannot be penalized according to the increment of displacement anymore but according to the increment of displacement instead. In the second case, the result depends in deed on the loading increment. Second, the transverse stiffness of the cable, i.e. the ability of the strand to move along the transverse direction during the tensile test is ruled by the penalty coefficient, k_{bind}. Its impact must be checked.

a. Dependence on the loading increment

A tensile test is performed on a 50mm long sample using either the increment of displacement or the total displacement. In both cases, the penalty coefficient k_{bind} is 200N/mm. For both cases, the test consists to apply various increments of displacement (δU = 0.1, 0.05, 0.02, 0.01, 0.007 and 0.005 mm) and to observe the stress-strain curve – see Fig. 3.37 a) & b). It clearly appears that when the increment of displacement is used, the results vary. But this is no more the case when the boundary conditions are relative to the total displacement. For this reason, the second approach will be used now each time the simulation concerns shaped cable.

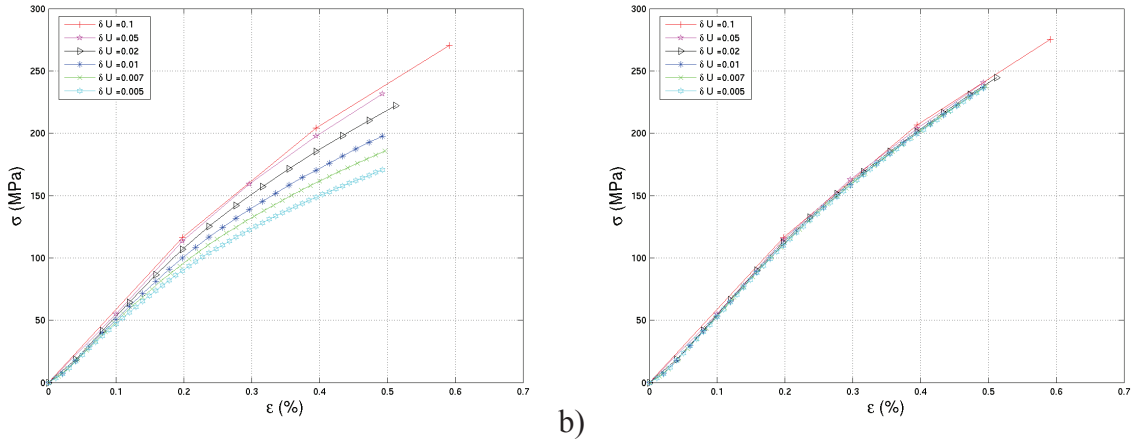

a) b)

Fig. 3.37. Influence of the pseudo-periodic boundary conditions is case of a) condition relative to the increment of displacement and b) relative to the total displacement.

b. Dependence on the penalty coefficient

The test consists to perform the tensile loading on the 50mm and 200mm long samples using different values of k_{bind} that range over three orders of magnitude. In Fig. 3.38, the various results are compared to each other. The experimental curve is also reported on the graphic. It

can be concluded that the influence of the penalty coefficient is rather limited and the curves are close. The dependence is more pronounced for the shortest 50mm long sample with larger dependence on the value of k_{bind}. The effect of the boundary conditions is stronger for short samples. For the following, the coefficient k_{bind} will be 50N/mm.

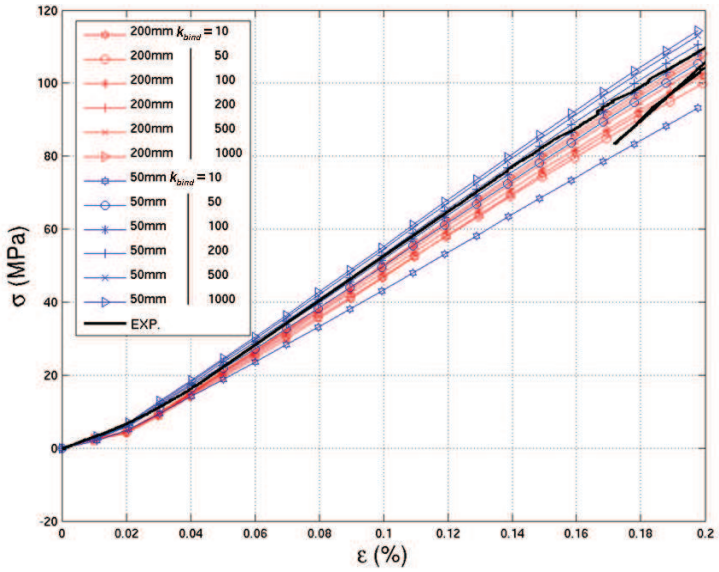

Fig. 3.38. Check of the effect of the penalty coefficient k_{bind} used in the transverse pseudo-periodic boundary conditions. Two different cable lengths are considered. The influence of k_{bind} is light with stiffer cable corresponding to higher k_{bind}. The result is more sensitive to the value of k_{bind} for the shortest sample.

3.1.3 Comparison with experimental results

Now that the boundary condition issues are solved, the final simulation is on a sample 100mm long with k_{bind} = 50N/mm. The numerical stress-strain curve is shown in Fig. 3.39 and is compared with the experimental result from [Ilyin 2006]. Just as the experiment, some unloading/loadings of the sample are realized at different applied strains. The non linearities of the curve are well represented. Both the computation of the initial geometry of the cable and the consideration of an elasto-plastic model for strands may explain the agreement observed between experimental and numerical results. This result partially validates the relevance of the proposed cable model regarding the axial loading.

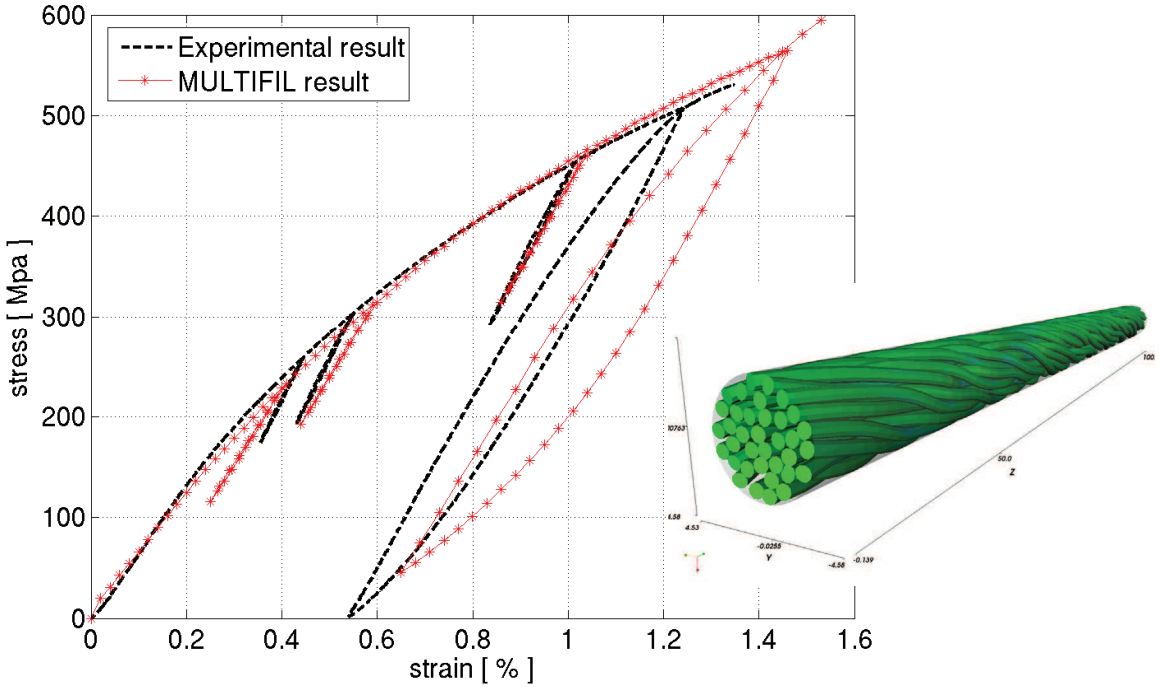

Fig. 3.39. Multifil 36 strand cable model on which the axial tensile test is performed. The calculated and experimental axial stress-strain characteristics are plotted together [Bajas 2010].

3.2 Axial compression/tension low cyclic loading

This paragraph presents the results predicted by the model regarding the *axial compressive* and *tensile loading* of 45 reacted strand cable with or without inclusion of copper wire in the triplet. For this test, the material constitutive laws are relative to the reacted strand and the copper wire at 4.2K. The purpose of the computation is to prove that the inclusion of copper does not cause any new issues. Moreover, the successive axial compression and tension is representative of the loading endured by the conductor during the SAMAN experiment [Weiss 2007], [Bajas 2010].

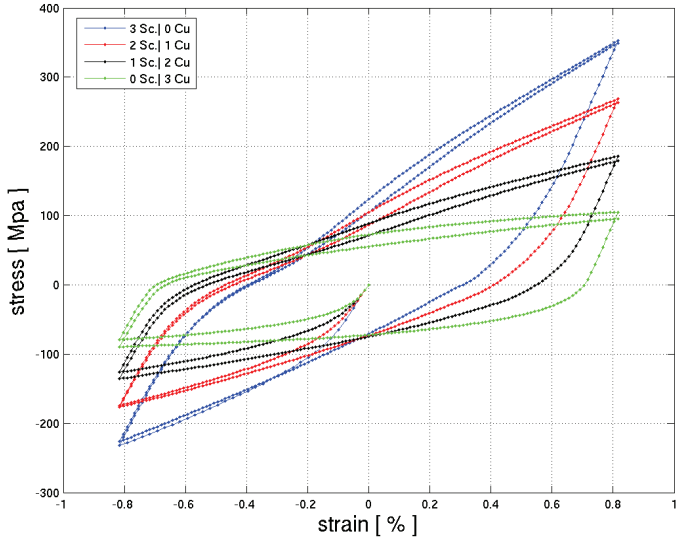

Fig. 3.40. Stress-strain characteristics of 45 reacted strand cable with or without the inclusion of copper wires. The loading path would reproduce the cool down and the consecutive tensile strain endured by the conductors during the SAMAN experiment [Weiss 2007].

Chapter IV: Validation of the model for transverse loadings

This chapter is devoted to the modeling of the transverse behavior of conductors, which corresponds to the loading induced by the magnetic Lorentz forces. Dealing with loadings in transverse directions introduces a new difficulty, since we are faced with the limits of the current beam model used in Multifil. This beam model is indeed well suited as long as transverse loadings applied to the conductors result mainly in bending deformations at the scale of strands. Nevertheless, the adopted kinematical beam model appears inconsistent to reproduce significant transverse deformations of cross-sections, since it can only account for a uniform transverse strain for each cross-section, and since plastic effects are considered only in the longitudinal direction. Some means are yet carried out to circumvent this difficulty. By chance, as shown by experiments of transverse compression performed on two crossing wires, the force-displacement curve corresponding to the plastic pinching of wires turns out to be almost linear. This quasi-linear stress-strain relation can be approximated for monotonic loadings with a transverse isotropic elastic model. The first part of this chapter presents the transverse compression experiments performed at CEA and their results. Complementary experiments have then been carried out to study the pinching between two crossing wires with various angles, in order to identify the mechanical response in transverse directions. Simulations using Multifil are then proposed to try to reproduce these experiments between crossing wires, and to fit the transverse stiffness for the transverse isotropic model. The relatively good agreement that is obtained allows this identified apparent transverse stiffness to be used to account for transverse deformations of cross-sections. The simulation of the transverse compression experiment for a 45 strand conductor is then addressed. The influence of various parameters is tested. It is shown that it appears necessary to take into account an initial pinching of wires induced by the forming process to get results consistent with experimental data. This initial pinching of wires is simulated using an appropriate transverse stiffness. Eventually, the cyclic transverse compression experiment is reproduced by Multifil with a rather good agreement.

1 The cable transverse press experiment for conductors

1.1 Description of the experiment

The transverse compressive loading of two different cables has been performed at CEA Cadarache during this thesis. The press experiment consists in compressing a cable in its transverse direction between two jaws (half cylinders). The force is applied to the jaws by a hydraulic actuator and measured by the load cell. The displacement is measured by four sensors placed in-between the jaws. The force-displacement curve can then be drawn. The pictures in Fig. 4.1 present the CEA transverse press devices.

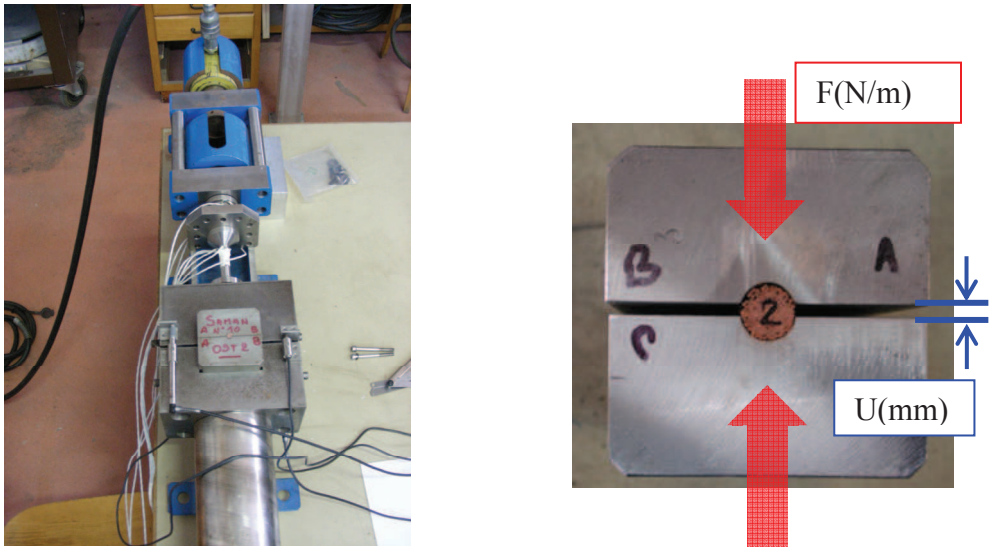

Fig. 4.1. Experimental set up for the transverse compressive tests

For both cables (initially virgin from mechanical loading), the applied transverse loading corresponds to what could have been the total Lorentz force on a conductor under operating condition. For instance, in an external field of 12 T and for a current of 50 A flowing in the strand, the Lorentz force per strand is about 600 N/m. For the 180 strand cable, the total line force would then be about 100 kN/m. The first experiment has been carried out by P.Decool & al. in December 2007 on a 180 strand cable. The cable was 150mm long with 3x3x4x5 cabling scheme and was composed of one third of superconducting strand (reacted Internal Tin LMI) strands and two thirds of OFHC copper wires. The twist pitch sequence of this sample is: {48-100-150-165} mm. The sample was cyclically loaded up to the ITER nominal peak loading (3 cycles at 100 kN/m), then up to twice this loading (3 cycles at 200 kN/m) and finally up to 2.7 times this loading (3 cycles at 270 kN/m). The second experiment has been performed by M.Nannini & al. in May 2009 on a 45 strand reacted cable. The cable was 150mm long with 3x3x5 cabling scheme and only composed of superconducting strands (reacted Internal Tin OST2). The twist pitch sequence of this sample is: {45-85-125} mm. The sample was cyclically loaded up to 25 kN/m (20 cycles) then up to 50 kN/m (10 cycles) and finally up to 100 kN/m (10 cycles). For both experiments, the results are presented in Fig. 4.2 and Fig. 4.3 in term of their force-displacement characteristic with the force expressed in kN/m and the displacement in mm. The diagram in the bottom left corner presents the chronology of the loading paths.

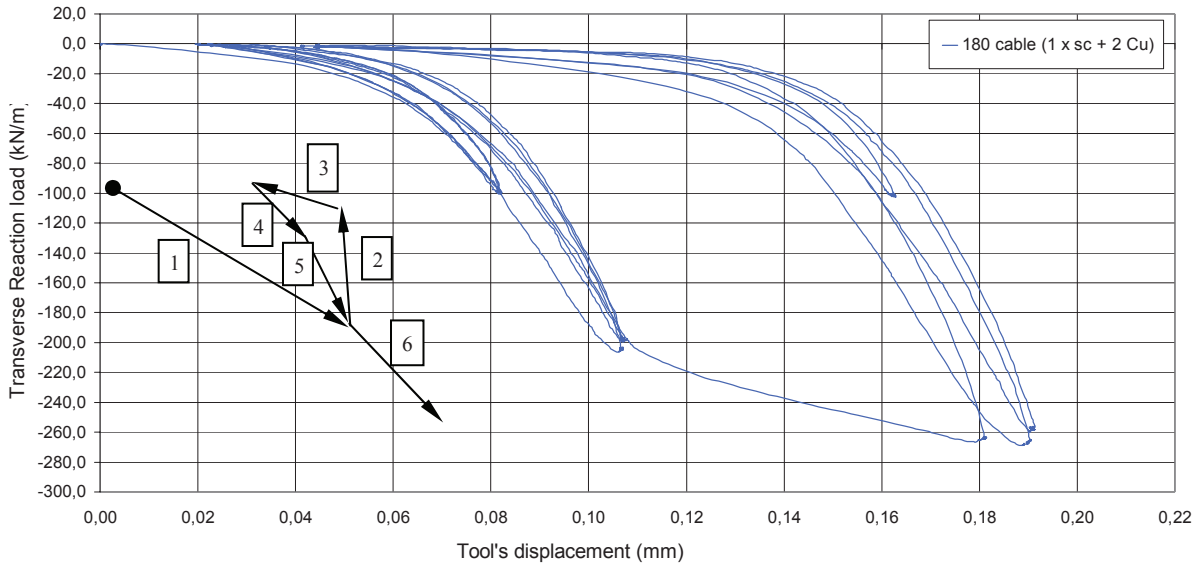

Fig. 4.2. Transverse compression of a 180 strand cable (1 sc + 2 Cu)x3x4x5 | {48-100-150-165}mm | 150mm.

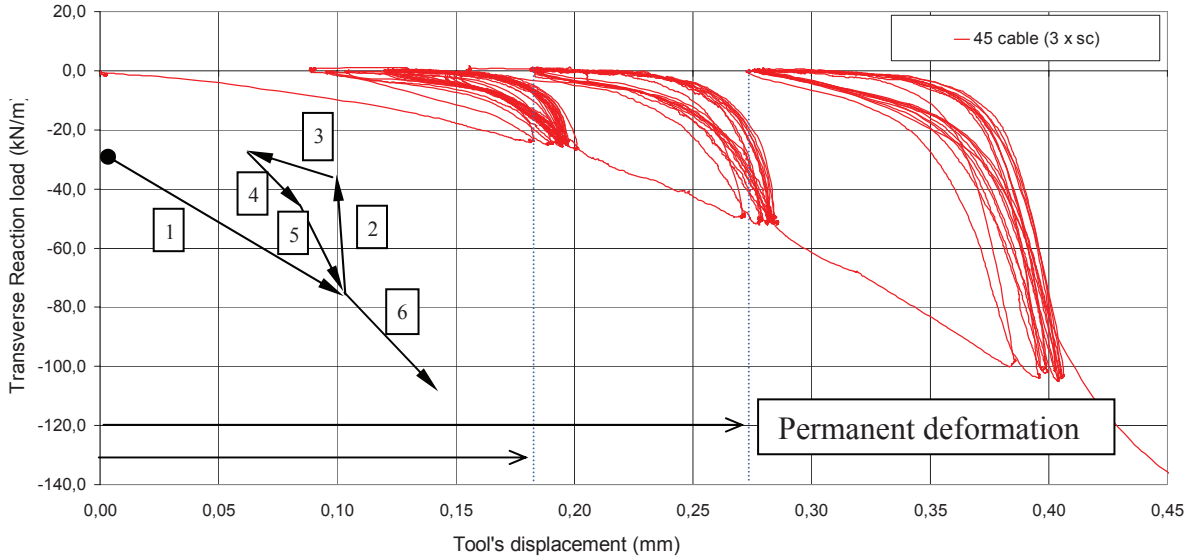

Fig. 4.3. Transverse compression of a 45 strand cable (3 sc + 0 Cu)x3x5 | {45-85-125} mm | 150 mm.

When inserted in the jacket both cables have an estimated void fraction of 32%. This void fraction corresponds to diameters of respectively 13.18mm and 6.6mm for the 180 and 45 strand samples. But after the jacket removal, the diameters are respectively 13.2mm and 6.7mm. The void fractions then increase up to 32.2% for the 180 strand cable and 34.2% for the 45 strand cable. It means that a possible radial springback effect is occurring after jacket removal that is more important for the 45 strand cable than for the 180 strand cable. The interpretation could be that the presence of pure copper wire influences the effect compared with superconductors only because of the low yield strain of annealed copper. In Fig. 4.4, the comparison of the 180 and 45 strand cables is shown. To be compared, the 180's curve is scaled by a factor 2 since the diameter of the cable is twice the 45 strand cables. Under this scaling assumption, a clear difference appears between both behaviors. The 180 strand cable seems to be stiffer than the 45 strand cable since, for the same force, the displacement is 4 times lower in the 180 than in the 45 cable. The slopes of the linear part (unloading) may give the apparent transverse stiffness of the cables and are respectively 7.7GPa for the 180 cable and 4.7 GPa for the 45 cable.

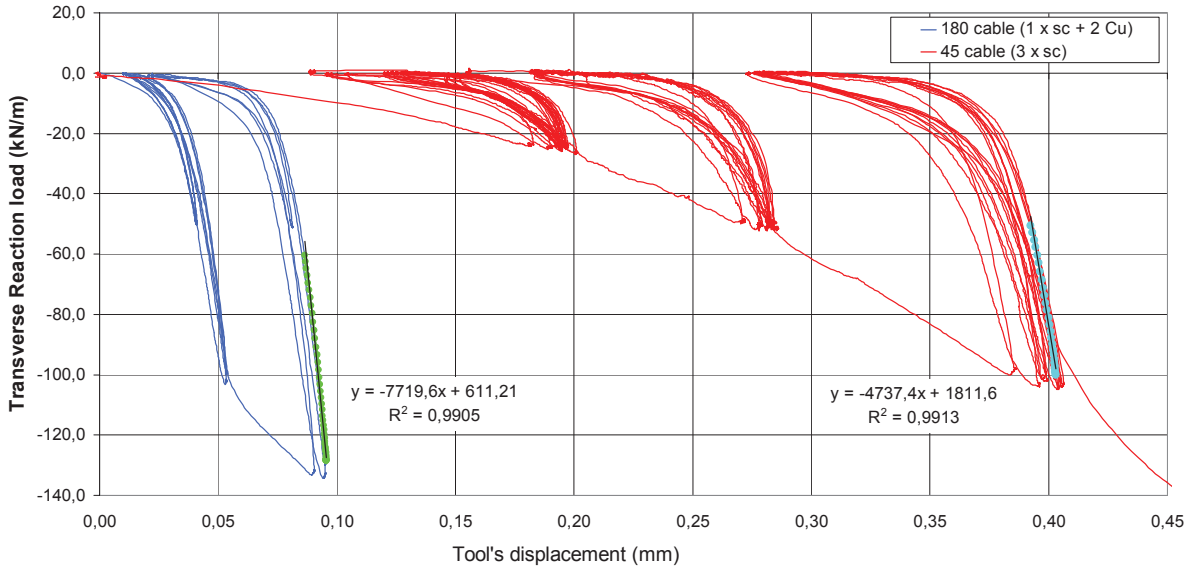

Fig. 4.4. Transverse compression: 45 strand cable vs. scaled 180 strand cable

The uncertainty in the effective initial cable diameter due to possible springback effect, the inclusion of copper wires and the difference in the cabling scheme (and twist pitches) make difficult the comparison between both samples. Nevertheless, the discrepancy in the results is quite important. It seems to indicate that the way the experiment is carried out is crucial, especially in term of initial cable diameter definition.

1.2 Discussion of the force-displacement curve

The transverse characteristics exhibit several specific features that are here described. The curves are highly non-linear and basically present *cyclic behaviors* (points 2-3-4-5 of the diagram) situated along *an envelope* curve (1-6). The cycles present a hysteretic pattern defined by the surface between loading and unloading paths. After few loading cycles, the behavior of the cycles is not stabilized. The slope of the envelope is not constant as the tool's displacement increases and significantly differs from the slope of the cycles with a factor of 10. The transitions between the cycle and the envelope show discontinuities quite similar with what is observed in the axial stress-strain characteristic in Chapter III. The tool does not go back to its initial position at the zero applied load which indicates a permanent deformation of the cable in its transverse direction due to the loading. The permanent deformation is more pronounced for the 45 strand cable than the 180 strand cable. After the third peak load (100kN/m), the irreversible displacement is about 0.18mm (dashed blue line) for the 45 strand cable (4% of the cable diameter), whereas it is only 0.05mm (0.38% of the cable diameter) for the 180 strand cable.

The permanent deformation (between two peak loads) and the hysteretic behavior (cycles) are likely due to both *plastic behavior* and *friction effects* between strands. Plasticity could have two different origins: *transverse* and *axial plasticity* due to either *pinching* or *bending strains* of the strands. The transverse cable loading behavior may then be driven by the respective contributions of friction, pinching and bending effects at the scale of the strands with expected plastic behavior. Nevertheless the competition between these effects is not clear. The simulation of these experiments could help to understand the mechanisms which drive the transverse cable behavior by testing the different mechanical effects separately. The cables tested in the experiment are made of reacted strands that are assumed to behave as the internal tin strand earlier presented (ALSTOM). In order to reproduce the cable transverse behavior

with Multifil, the axial plastic model developed in Chapter II will be used. The transverse compression is expected to cause transverse deformation of the strand due to pinching. An attempt to model this plastic effect with the Multifil beam model is proposed.

2 *Experimental approach to the transverse compression between two crossing wires*

Since the transverse compression experiment involves local phenomena between wires, it has been chosen to try to identify the mechanical behavior of two crossing wires subjected to a transverse compression. The goal of these experiments is first to identify the apparent transverse stiffness of wires, in order to set this parameter for Multifil simulations. The second objective of this study is to better understand phenomena taking place at the crossing between wires and their influence on the possible breakages of Nb_3Sn filaments, in order to try to determine a damage criterion depending on the local transverse loading.

2.1 Transverse compression experiment of two crossing strands

2.1.1 Experimental process

The following analysis exposes the method to identify the transverse stiffness E_t to be used in the orthotropic model of Multifil. This stiffness is defined by the relation between the applied contact force and the induced transverse deformation. The transverse force-displacement curves of OFHC copper wire and Nb_3Sn-based strand have been measured during this thesis. The basic experiment consists in placing two wires, three centimeter long, that cross each other with a given angle. The standard tensile testing machine is used to apply a compressive loading to a steel cylinder (anvil head of one centimeter diameter) that compresses the samples at the contact– see Fig. 4.5. The force F(N) is measured by the load cell of the machine. Unlike the uni-axial test described in Chapter II, it appeared delicate to place any extensometer to measure the transverse displacement. The internal displacement sensor of the machine is used instead. The main difficulty was about the proper alignment of the system so as to apply a pure transverse loading at the contact. To prevent the samples from moving during the test, they are gently held by modelling clay.

a) 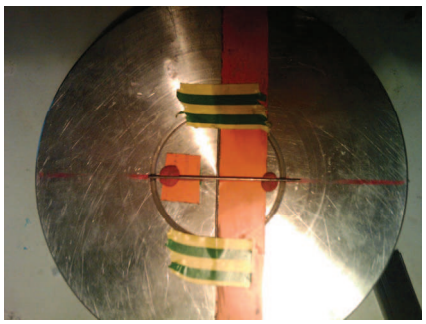 b) 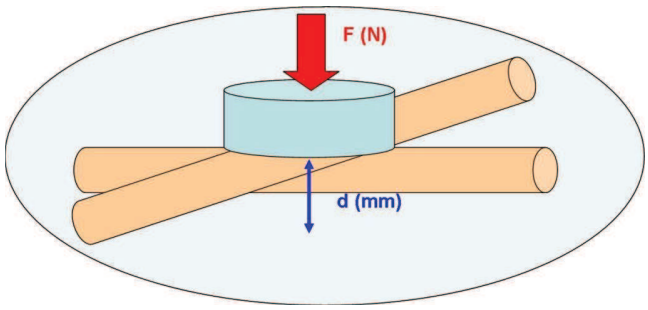

Fig. 4.5. a) View of two strands crossing at a 90 degree angle. The lower sample is held by adhesive tape and the upper sample lies on two soft supports made of modelling clay. b) Scheme of the transverse crossing strand experiment.

2.1.2 Transverse force-displacement curves of the OFHC copper wire and the reacted strand

In Fig. 4.6, the force-displacement curves of eight different runs are presented. These first results allow conclusions about the reproducibility of the method with a matching of the eight most representative tests. The main feature to notice here is the striking linearity of the force-displacement characteristics. However, this linear behavior corresponds to a plastic behavior as it will be shown by loading-unloading curves.

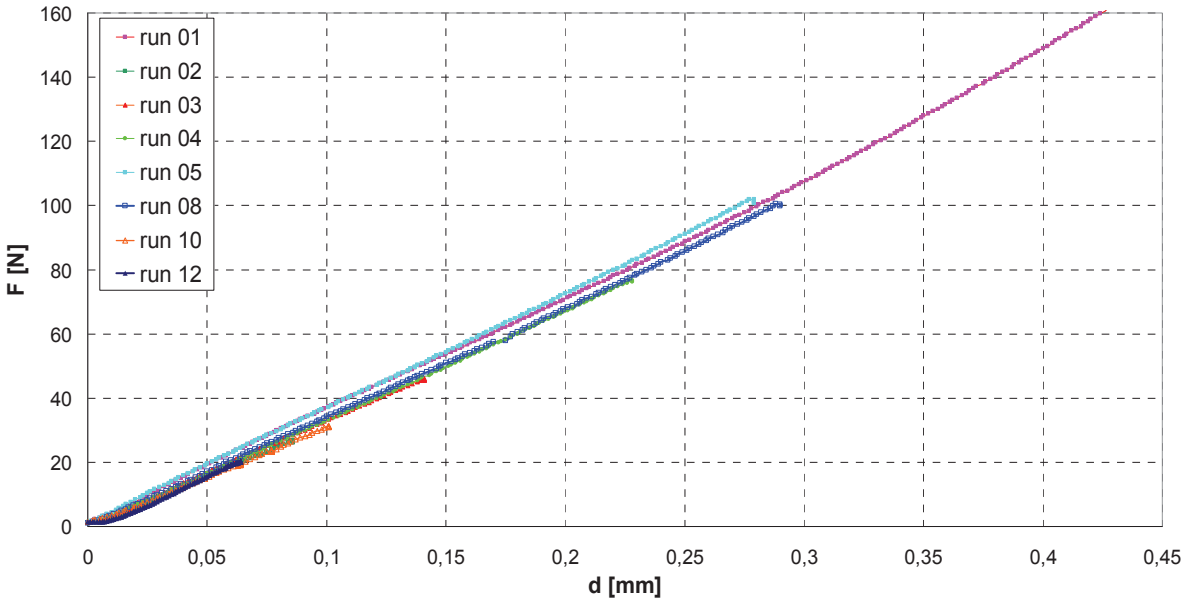

Fig. 4.6. Measurements of the transverse force-displacement characteristics of OFHC copper wires crossing at an angle of 90°.

It is assumed that the deformation of the two samples at the contact is equal. As a result, for the slopes of the force-displacement curves, half of the displacement is considered. The slope defines the apparent transverse stiffness of the wires. The mechanical response of some materials is known to be dependent on the rate of applied displacements due to visco-elastic effects. To test this effect, two different rates have been used: 0.5 mm/min and 0.1 mm/min. The values for the different runs are summarized in Fig. 4.7. The error bar corresponds to the standard deviation, whereas the dark blue line stands for the mean value. The visco-elastic effect exists but keeps limited to a variation of 10% on the mean value of the slopes, from 660 N/mm to 600 N/mm.

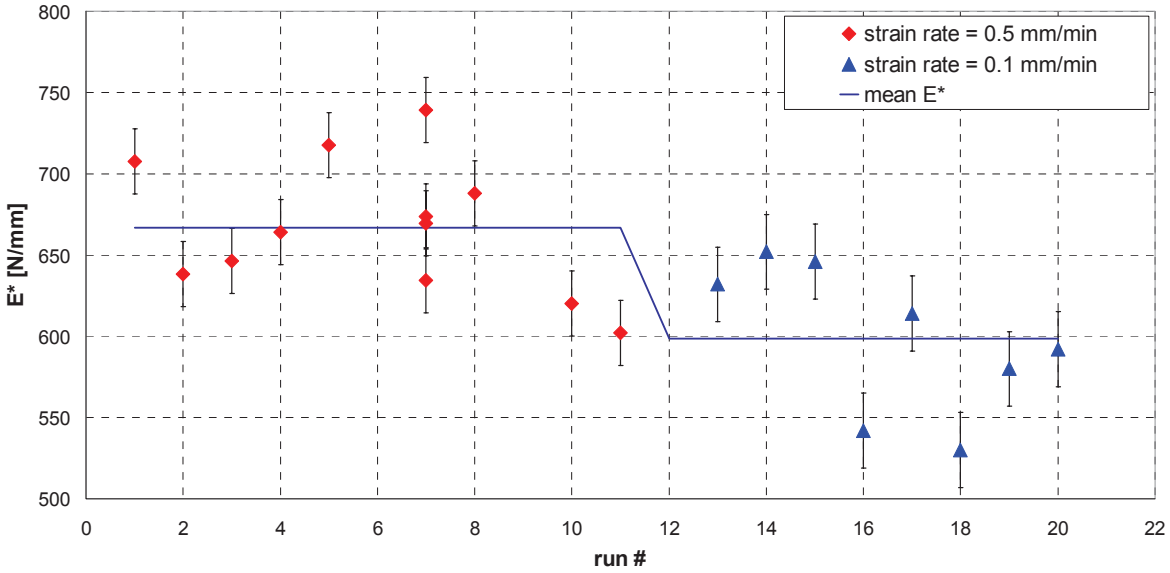

Fig. 4.7. Measurements for two rates of applied displacement of the apparent transverse stiffness E* of OFHC copper wires crossing with an angle of 90°.

As it was done during the uniaxial tensile test, some loading/unloading cycles have been performed on the sample. The result of this cyclic test is presented in Fig. 4.8. Five loading cycles are performed. When the load is released the loading path differs from what can be called an envelope curve (black line). When the load increases again up to the last peak loading, the path goes back to its envelope. The slope of the cycles is about ten times higher that the slope of the envelope from 650 N/mm to 7500 N/mm. These two apparent stiffnesses are now referred to E_t^1 and E_t^2. The interpretation of the result presented in Fig. 4.8 is that the behavior of the wire presents an elastoplastic behavior. The plastic response is quasi-linear (envelope curve), whereas unloadings are elastic. The initial elastic domain could be properly described by the Hertz analytical contact model of two crossing cylinders. However, since the yield stress of annealed copper is very low, plasticity occurs rapidly, and the Hertz model, only valid for elastic materials, can no longer be used.

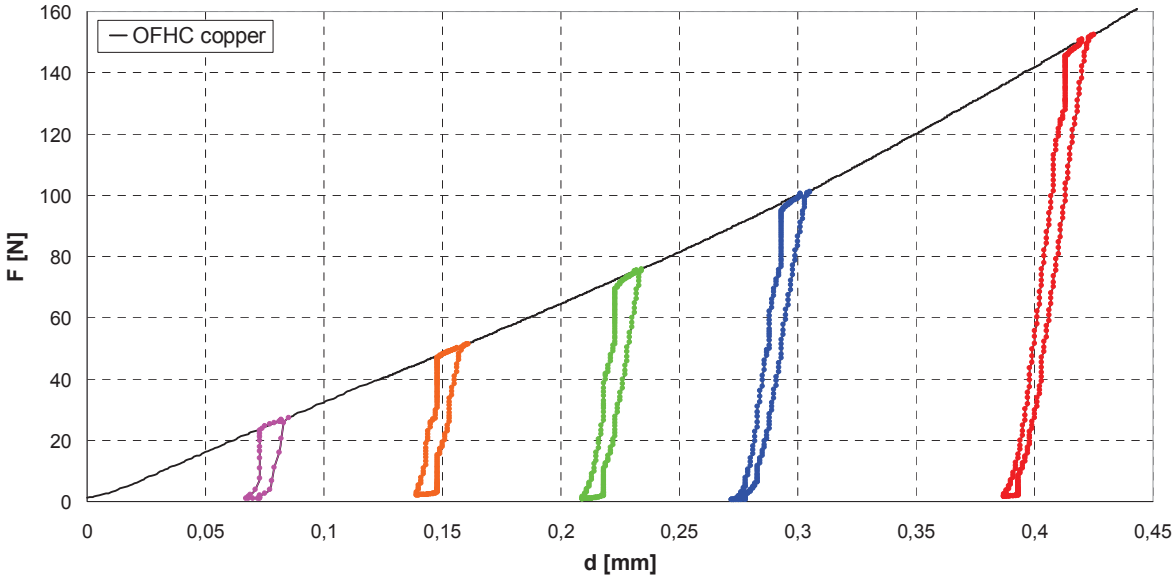

Fig. 4.8. Measurements of the transverse force-displacement characteristics for the low cyclic loading of OFHC copper wires crossing at an angle of 90°.

In a cable, various angles between contacting strands can be encountered. The transverse compression of wires crossing at different angles is presented in Fig. 4.9. The main result is an increase of the slope of the curve with the decrease of the angle. This effect is expected since the surface of contact increase with decreasing angle.

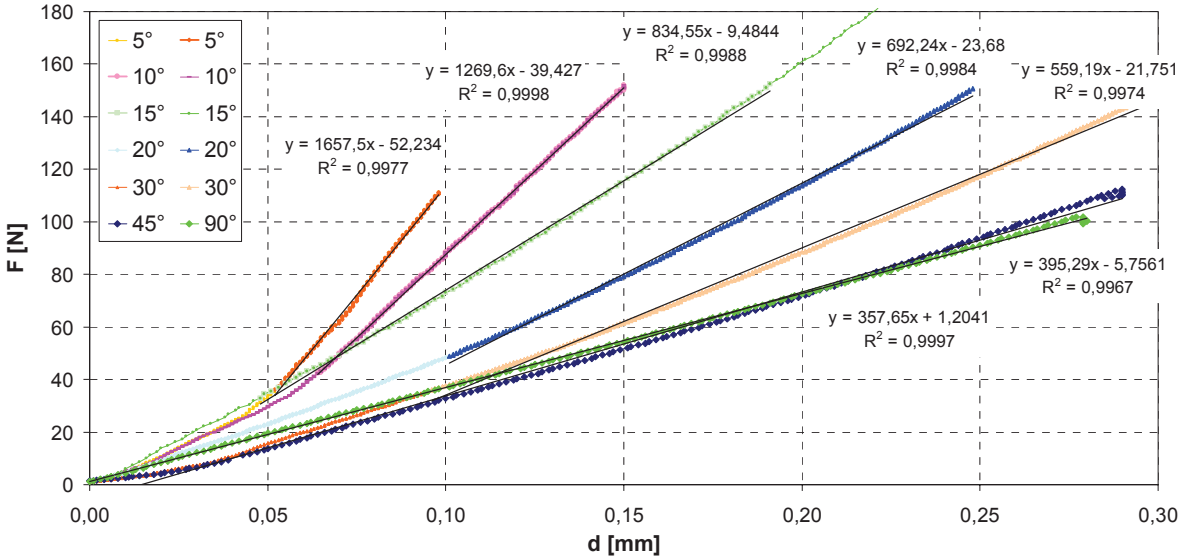

Fig. 4.9. Measurements of the transverse force-displacement characteristics of OFHC copper wires crossing at various angles.

The same work has been performed on nine samples of reacted Nb_3Sn strands from EAS. As shown in Fig. 4.10, the loading curve of composite strands present a double slope that copper wires do not exhibit. This double slope is interpreted as a consequence of the composite nature of the strand. The slope of the first part is similar to the one obtained for pure copper. The change of slope for the second part could correspond to the loading of Nb_3Sn filaments present in the composite. As an example, Fig. 4.11, shows the behavior during the unloading and loading cycles. The first linear part in Fig. 4.10 extends up to 25µm with a slope of 550 N/mm. The second part shows a slope of about 1650 N/mm – see Fig. 4.12 and Fig. 4.13.

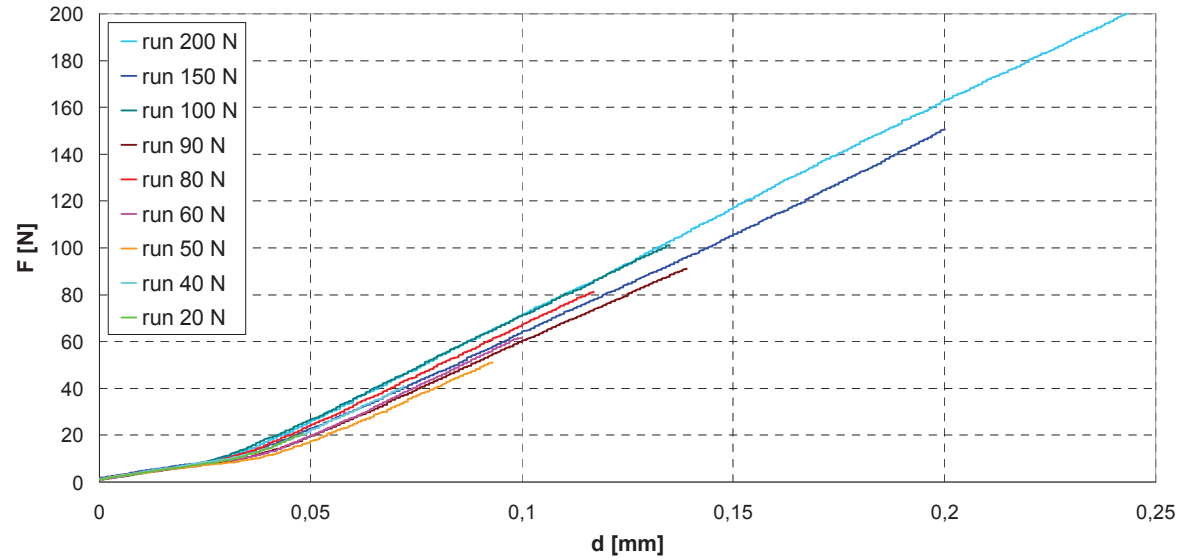

Fig. 4.10. Measurements of the transverse force-displacement characteristics of Nb_3Sn strands crossing at an angle of 90°.

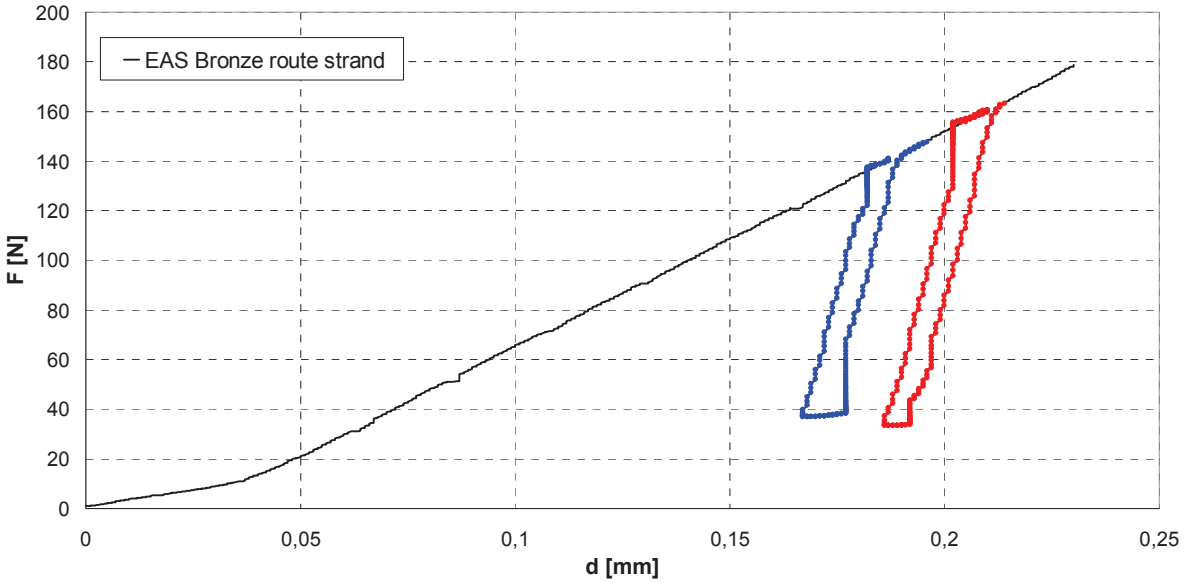

Fig. 4.11. Transverse low cyclic loading of Nb_3Sn strands crossing at an angle of 90°.

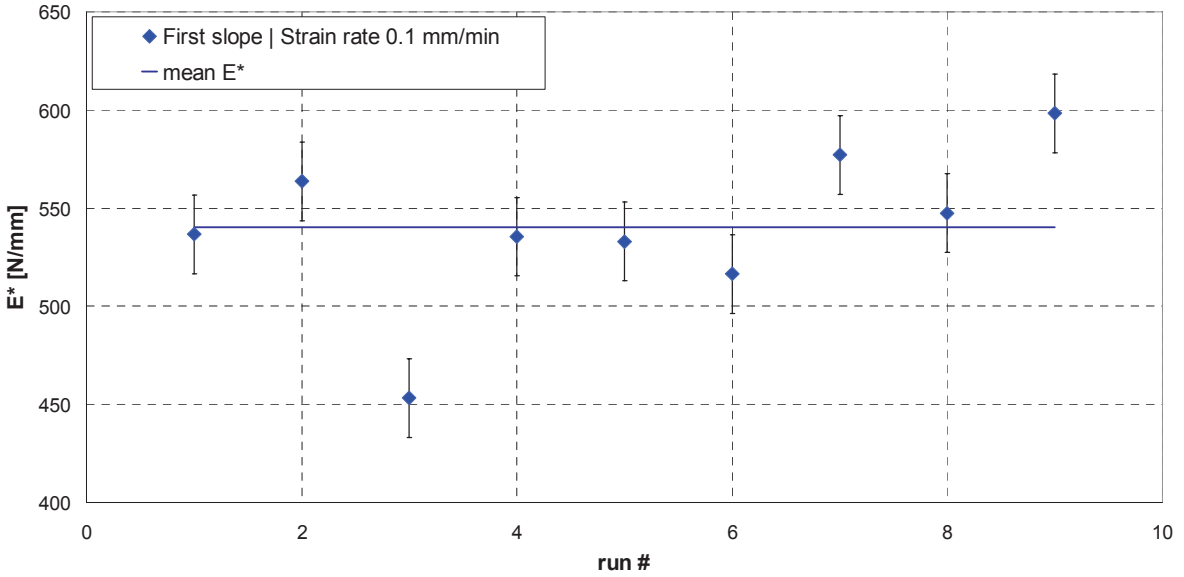

Fig. 4.12. Measurements of the apparent transverse stiffness E* for the first part of the curve of Nb_3Sn strands crossing at an angle of 90°.

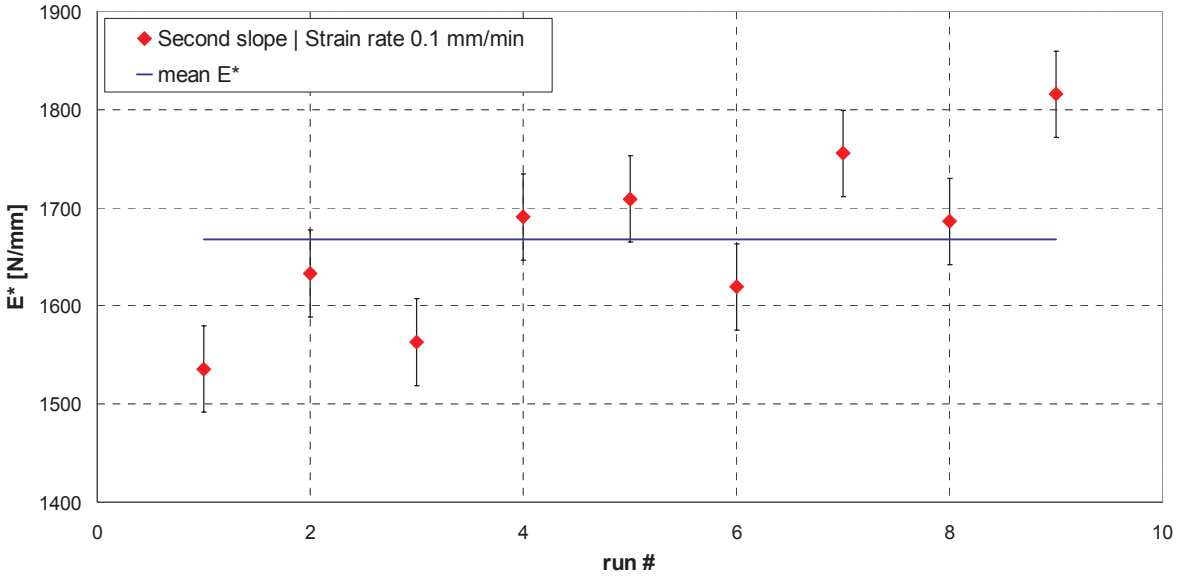

Fig. 4.13. Measurements of the apparent transverse stiffness E* for the second part of the curve of Nb_3Sn strands crossing at an angle of 90°.

The transverse compressions of the composite strand have been stopped at different peak loads – see Fig. 4.10 in order to investigate the damage that could be caused by the transverse loading to the brittle Nb_3Sn filaments.

2.1.3 Measurement of indentation depths using confocal microscopy

As earlier mentioned, no extensometer is used to measure the displacement. The intrinsic displacement sensor of the machine might be suffering of a lack of accuracy. In order to check the relevance of the measurements, the prints made on the sample after testing up to a given peak load have been observed. A confocal microscope was used which allows three-dimensional reconstructions to estimate depth and surface of the prints for the tested samples corresponding to Fig. 4.6. The various runs correspond to various peak loads, saying 15, 20, 25, 30, 40, 45, 60, 75 and 100 N at which the compression has been stopped. The different samples present prints of different depths that are calculated using the three dimensional reconstruction obtained by confocal microscopy, and compared to the displacements measured by the tensile machine. The next set of pictures in Fig. 4.14 shows the surface of the prints and their profile for the different peak loads. On each graphic the difference between the red and the green lines, i.e. the depth of the print, is written in the pink rectangle. In order to estimate the influence of the error made on the measurements of the transverse displacement on the calculation of the apparent transverse stiffness, the force/displacement and the force/measured depth are plotted on the same graphic in Fig. 4.15. It is to be noted that the possible elastic springback of the wires when the load is released is taken into account by the optical measurement. Despite a discrepancy between the measured displacement and the measured depth, the slopes of the two curves differ only by ~10% (variation of the slope calculated from linear regression). Calculating the apparent transverse stiffness using the transverse displacement measured by the tensile machine is therefore valid, even if a small error is committed on the displacement.

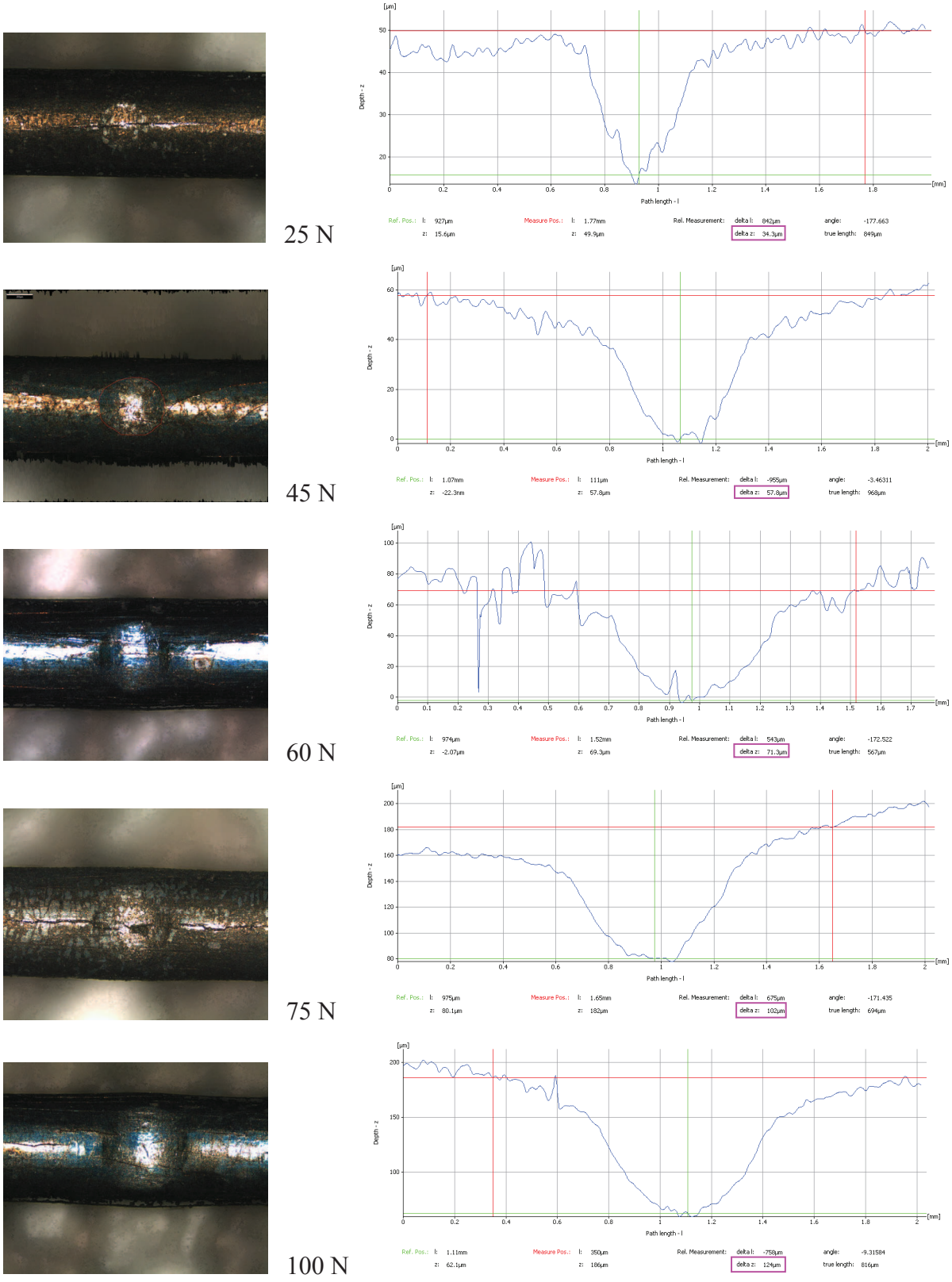

Fig. 4.14. Pictures of the plastic imprints due to the pinching of the strands at contact and measurement of the depth of the imprints using optical method.

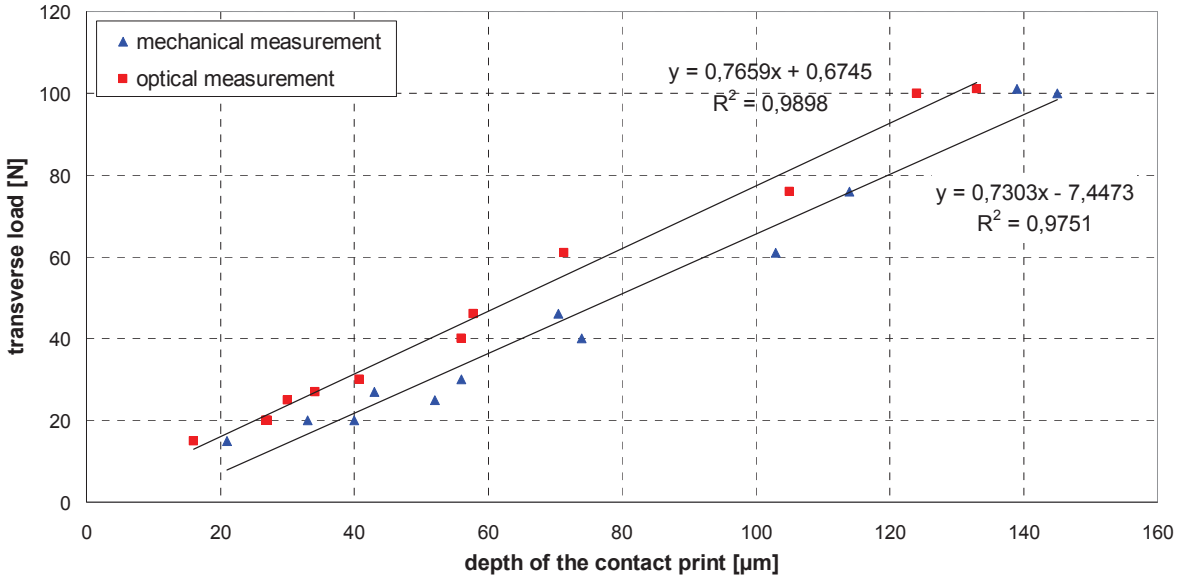

Fig. 4.15. Measurements of the depth of the imprints after different transverse peak loads using either mechanical or optical measurement. The linear regressions of the plots are also shown.

The new question that has risen from the tests is about the reason for the linearity observed in the transverse force-displacement characteristic. Since plastic deformations are involved, such linearity is intriguing. The surfaces of the contact prints can be estimated from the 3D reconstruction obtained by confocal microscopy. The method is simple: the contour of the print is drawn by hand, see Fig. 4.16 a) , the surface is automatically generated and its area is calculated, see Fig. 4.16 b).

a) 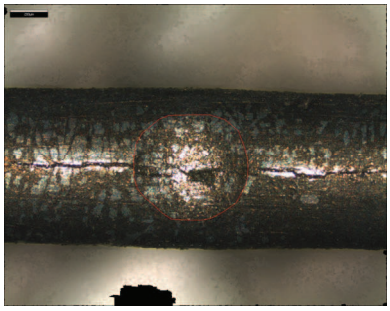 b) 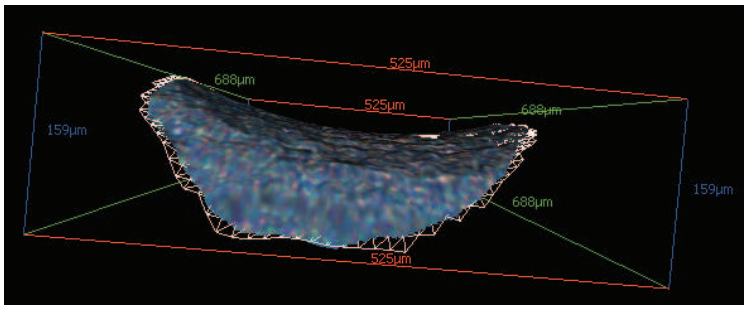

Fig. 4.16. Example of contact surface measurement using optical analysis.

For the various samples loaded up to different peak loads, the surfaces have been measured. In Fig. 4.17, the areas are plotted as function of the transverse load. The obtained curve appears to be rather linear.

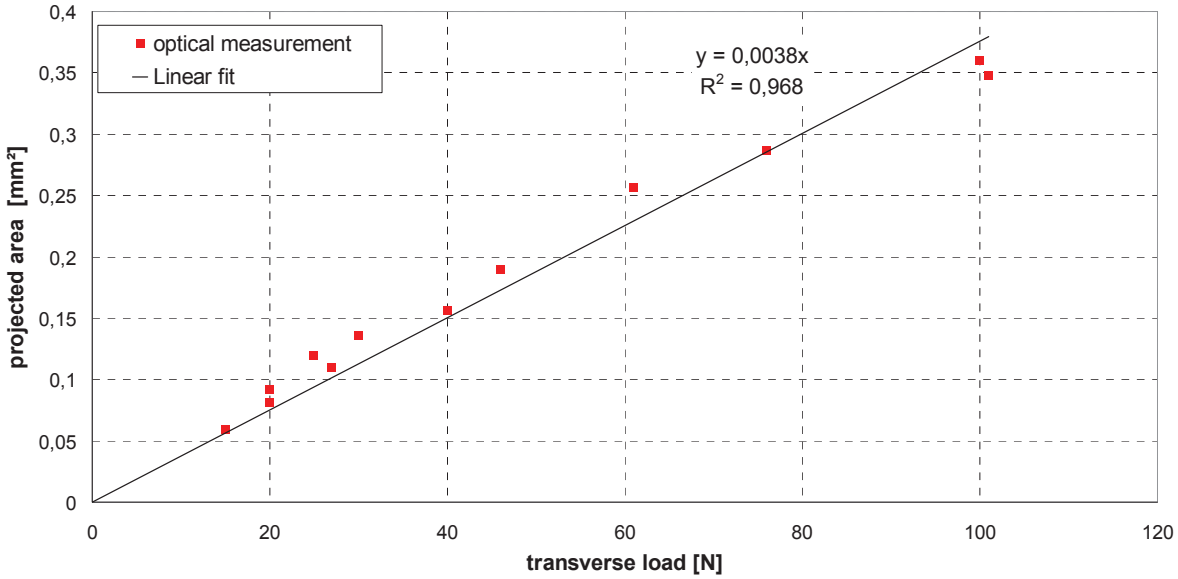

Fig. 4.17. Measurement of the evolution of the contact surface as function of the applied load. The surface is here defined by the projected area of the print.

2.2 Microscopic observation of cracks due to pinching

The samples of Nb_3Sn composite strands that have been beforehand transversally loaded are now analyzed at the microscopic scale. Using the polishing techniques developed in Chapter III, the samples have been polished in the longitudinal direction and the state of the filaments below the contact surface is observed by SEM method. The idea is to define a a breakage criterion for filaments as function of the transverse loading from 20 to 200 N. Unfortunately during this thesis only three samples have been observed using the SEM method: the samples loaded up to 80, 100 and 200 N. To save time regarding the polishing of the sample, these three loadings are applied at different locations on the same sample.

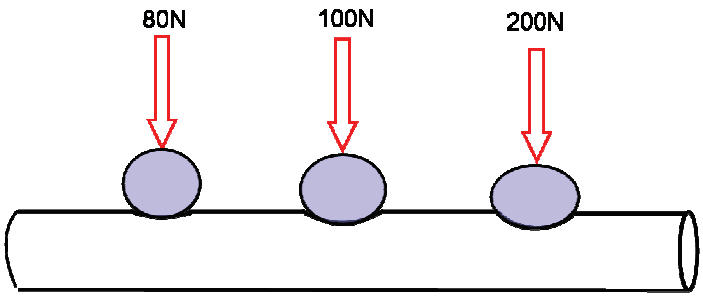

Fig. 4.18. Illustration of the sample that was transversally tested at three different peak loads for the determination of a crack onset criterion due to pinching.

After careful polishing, the print due to the loading in clearly visible – see Fig. 4.19. On the one hand, for the 100 N case, the filamentary region seems not impacted by the loading and only the copper matrix is deformed. On the other hand, for the 200 N case, the Tantalum tube and the filament inside get deformed by the loading. A global bending of the tube is visible on Fig. 4.19 b).

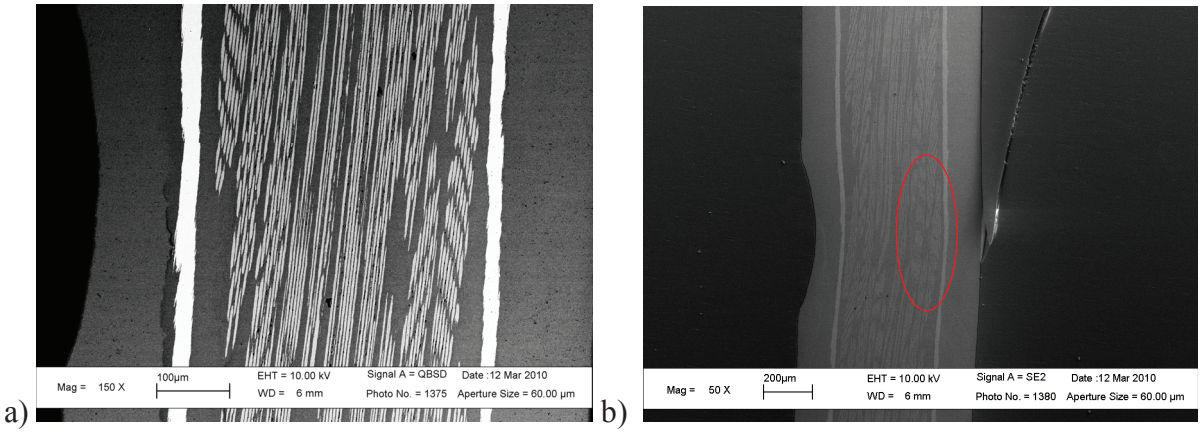

Fig. 4.19. SEM observations of polished longitudinal cross sections of Nb_3Sn sample submitted to transverse compression up to a) 100 N and b) 200 N.

A careful survey of the filaments situated below the contact shows no visible damage after both loadings (100 and 200 N). However, after 200 N, an interesting phenomenon is observed. The filaments appear not broken below the contact but at the opposite side (solid red circle in Fig. 4.19 b) and Fig. 4.20). For the first zone (dotted line), the filaments are not damaged. For the two others (dashed and solid lines), the filaments are cracked and so for the different layers. The origin of this phenomenon is not obvious. The pinching seems to induce a global bending of the strand and the tantalum tube. Due to this bending, tensile axial strains are induced in the filament situated at the stretched zone opposite to the contact surface. However a compressive loading up to 200 N seems to be significantly higher than what is expected in cable-in-conduit conductors [Nijhuis 2008 b].

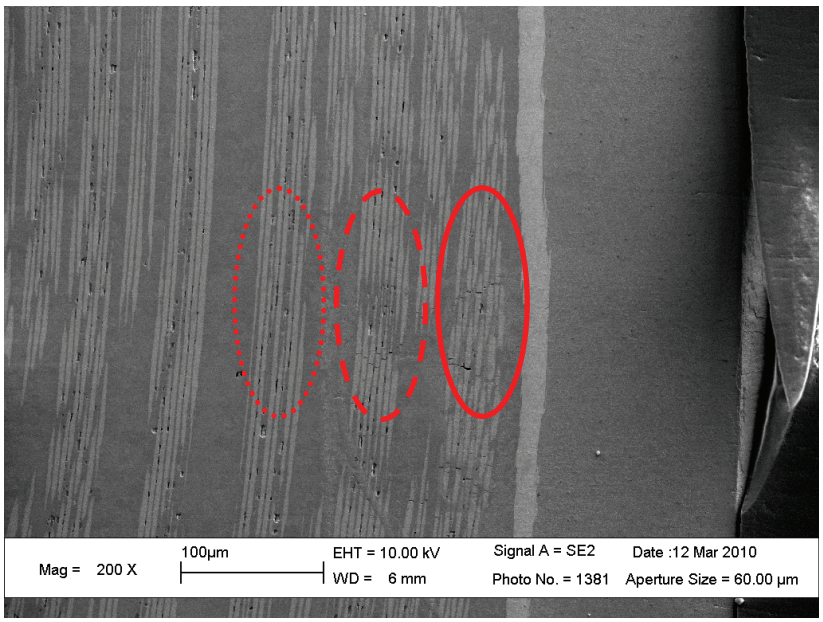

Fig. 4.20. Zoom in the filament bundles situated at the opposite side regarding the contact print after an applied transverse compression up to 200 N.

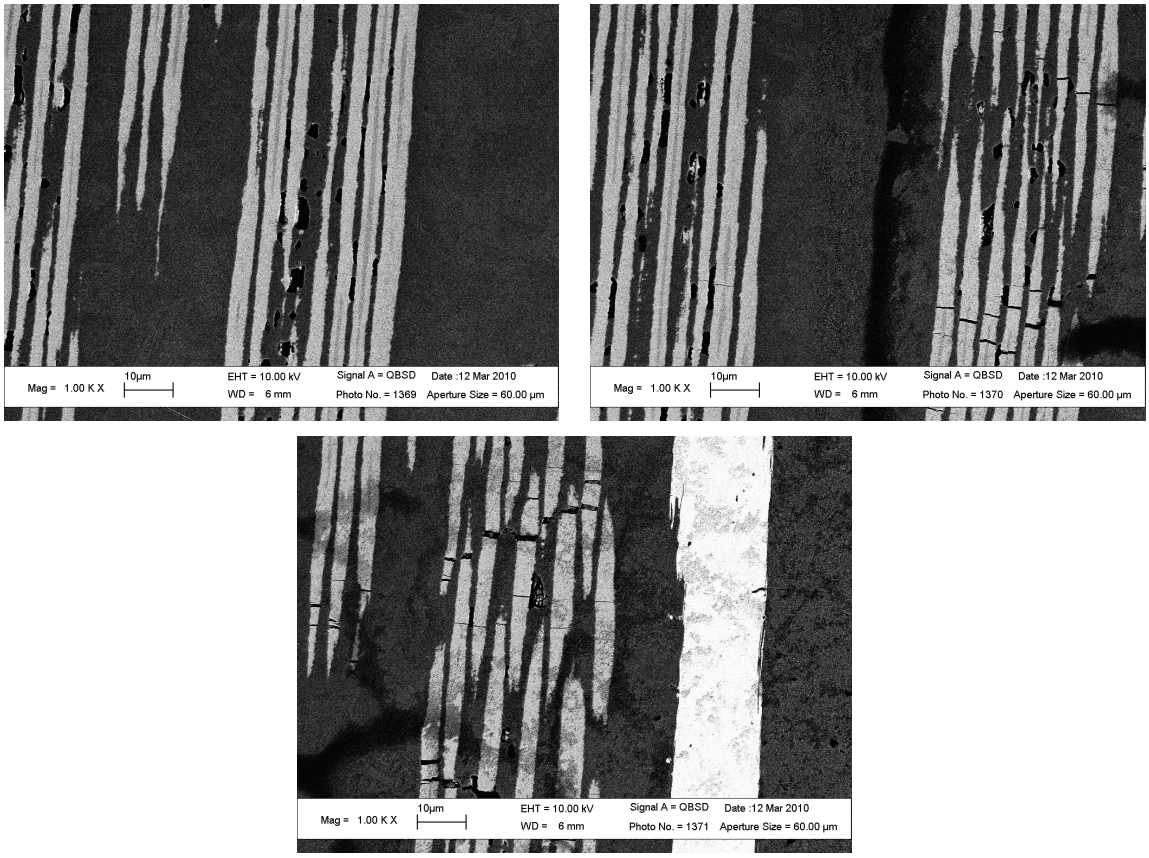

Fig. 4.21. Zoom in the filaments situated at the opposite side regarding the contact print after an applied transverse compression up to 200 N.

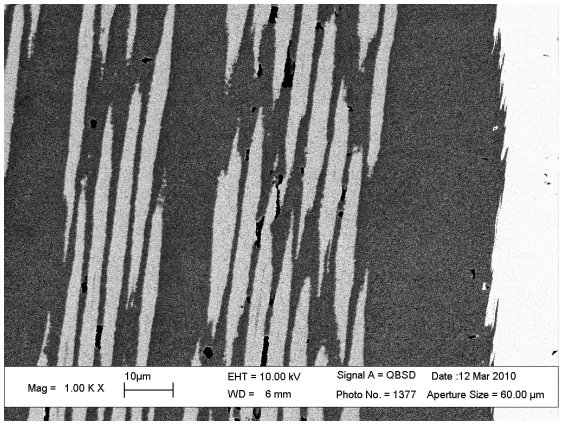

Fig. 4.22. Zoom in the filaments situated at the opposite side regarding the contact print after an applied transverse compression up to 100 N.

In conclusion, the occurrence of crack due to pinching starts for an applied load between 100 N and 200 N. Compressive loading lower that 100 N are not causing any damages of the filaments – see Fig. 4.22. At last, since these tests have been performed at an angle of 90° the results may be seen as the most pessimistic case regarding the contact loading.

2.3 Comparison with a volumetric finite element model

It has been proposed to simulate the transverse pinching experiment using Abaqus finite element code in order to better understand the experimental results. As shown in

Fig. 4.23, the model has been generated so as to be able to take into account three different materials (copper, tantalum and Nb_3Sn) in the strands. However, in a first approach all materials are set to OFHC copper. The transverse compression is simulated by taking into account contact with two moving rigid planes. The total reaction force is derived summing the amplitude of the local forces measured by the contact elements of one of the rigid planes. The calculated force-displacement curve is shown in Fig. 4.24, and can be compared to the experimental one (Fig. 4.6).

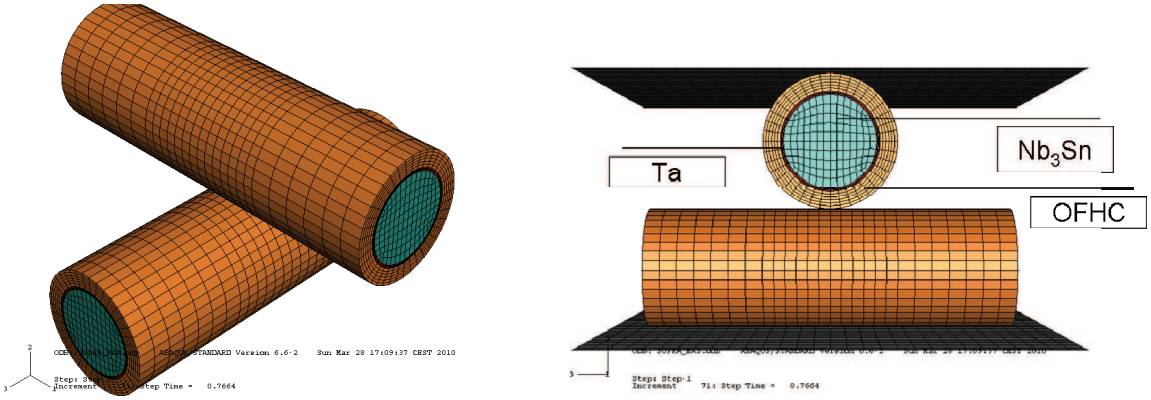

a) b)

Fig. 4.23. Illustration of the finite element simulation of the transverse compression of two composite strands crossing at an angle of 90°.

A quasi-linear global response is obtained, very similar to the one observed on the experimental curve. The apparent transverse stiffness is here 624 N/mm which is in agreement with the experimental result – see Fig. 4.7. For the composite model, the results are not yet relevant to be exposed. To conclude this model could be improved by considering separated bundles of filaments. The main motivation is to get deeper insight of the local strains on the scale of the filaments. Such an approach could complement the Multifil modelling that works at the scale of the strands.

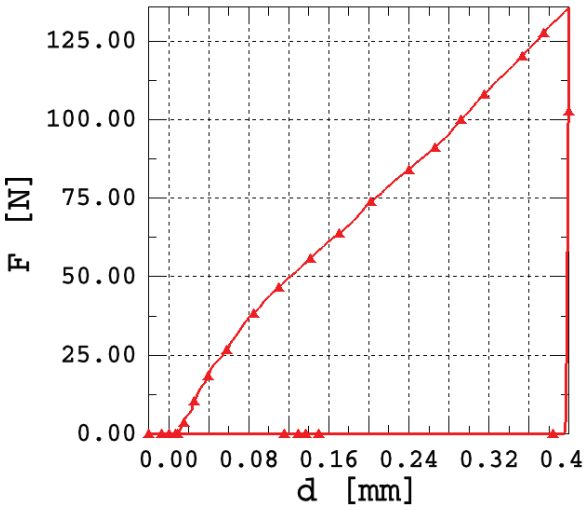

Fig. 4.24. a) Computed transverse force-displacement curve in case of pure copper. The linearity of the curve is depicted by the simulation.

3 Fitting of the transverse stiffness for the Multifil beam model

3.1 Multifil simulation of the pinching experiment

In Multifil, the transverse orthotropic behavior can be considered only elastically. The reason for this is that the kinematical beam model is not rich enough to be consistent with the consideration of real three-dimensional plastic deformations. Since transverse strains derived from this kinematical model are constant throughout the cross-section of the beam, taking into account the coupling between transverse strains (constant through the cross-section) and axial strains (quadratic through the cross-section) induced by the consideration of the incompressibility of the plastic flow would lead to a locking which would severely limit axial strains. It is however proposed to try to reproduce the pinching experiment running a simulation with Multifil. As the force-displacement curves from pinching experiments appeared to be linear, even reflecting a plastic behavior, it is possible to try to reproduce these experiments by considering an elastic orthotropic behavior with an elastic transverse stiffness fitted on the experimental data. This way of doing is nevertheless valid only for a monotonic loading, but not if any unloading or cycling is considered. The goal of the simulation of the pinching experiment by Multifil is to fit the transverse modulus to be used in the orthotropic model, by finding out which value of E_t should be set in Multifil to reproduce the force-displacement curve for the OFHC copper wire and the Nb_3Sn strand.

The pinching experiment is modelled by placing two beams that contact each other with a given angle and to use two plane rigid tools (above and below the beams) to apply a displacement to the beams. So that the beams do not slide away during the compression, two other beams are placed on each side of the tested beams. The transverse force is recovered by the summation of the local contact forces measured on the tool. The force-displacement curve can be plotted and compared with the experimental result. The orthotropic elastic model is used for the two tested beams whereas the other beams are in comparison non-deformable (setting high value to the Young's modulus). The single open parameter is here the transverse stiffness modulus E_T relative to the beam constitutive law that is wished to be identified. The axial stiffness is equal to 130 GPa – cf. Chapter III.

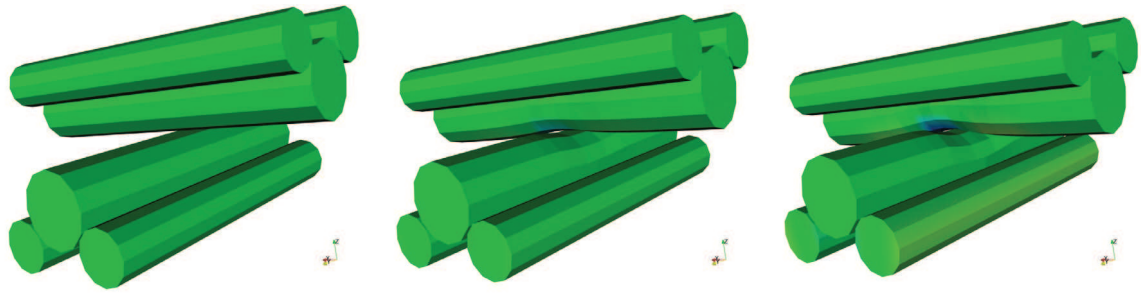

Fig. 4.25. Multifil simulation of the pinching experiment. The strands are crossing at 90°.

3.2 Fitting of the transverse stiffnesses of OFHC copper wire and Nb_3Sn strand

The transverse stiffness E_T is first fitted on a compression between two wires forming a 90° angle– see Fig. 4.26. The found value for the OFHC copper wire is :

E_t = 650 MPa

and for the Nb_3Sn strand, it is.

E_t = 1700 MPa

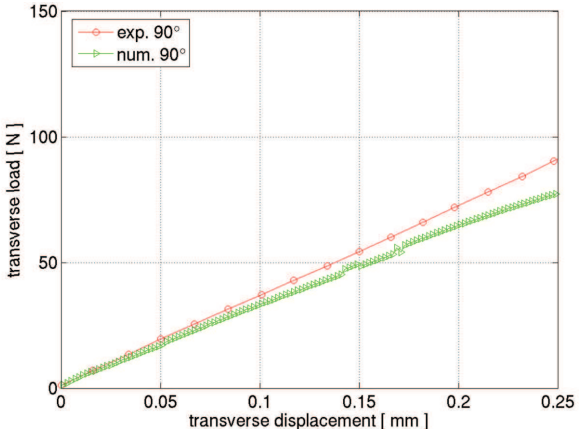

Fig. 4.26. Fitting of the transverse stiffness in Multifil in comparison with the experimental result

In a second stage, keeping the same value for the transverse stiffness, different values for the angle between the two wires are considered, in order to check if the fitted value still provides a good agreement for these different angles. On the graphics in Fig. 4.28, the angle between the beams is changing and the loading curves are compared to the experimental results from Fig. 4.9. The results are sufficiently close to the experimental results in regard with the different assumptions and uncertainties inherent to the method. The results of model are globally stiffer than the experiment.

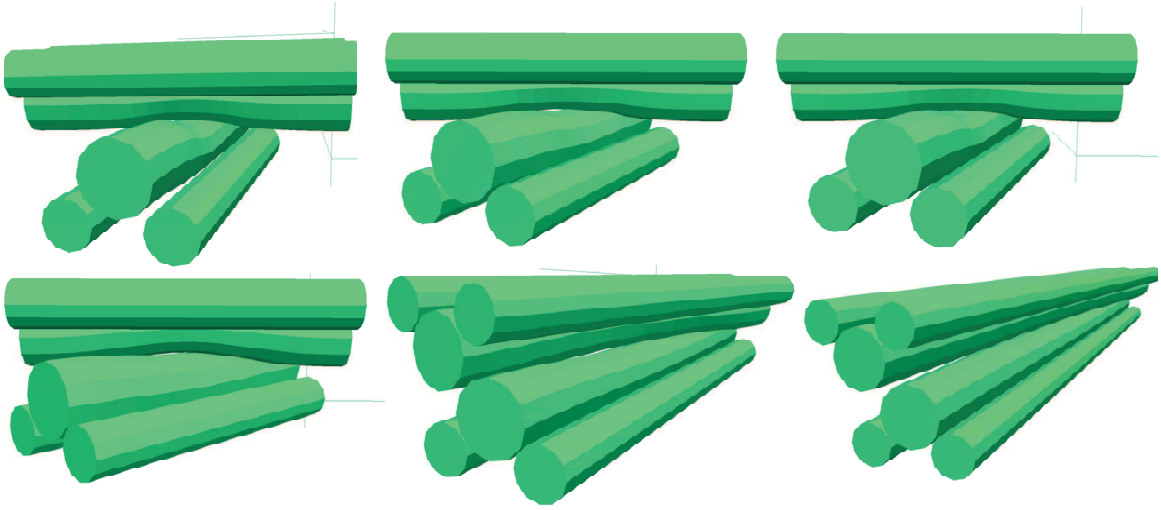

Fig. 4.27. Multifil simulation of the pinching experiment for strands crossing at different angles (45°, 30°, 20°, 15°, 10°, 5°).

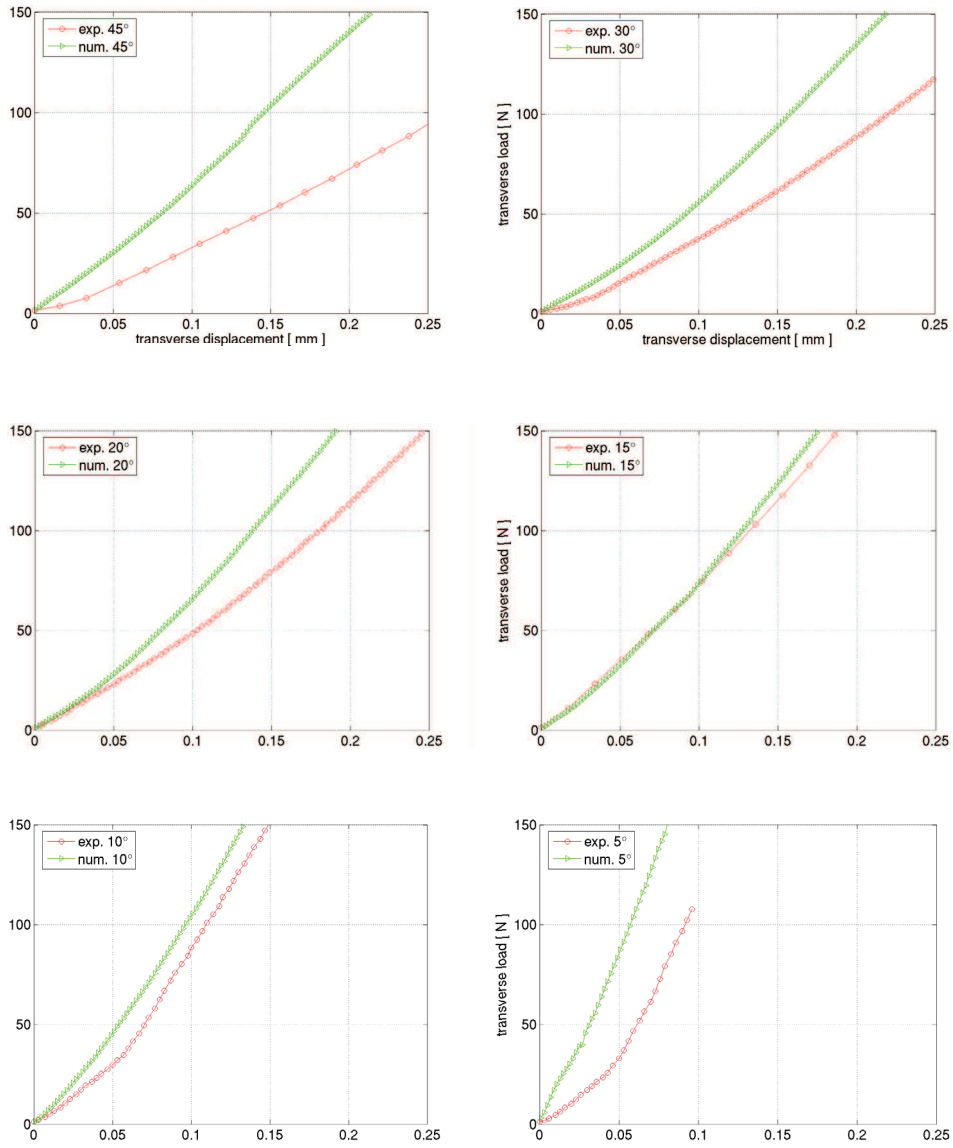

Fig. 4.28. Check of the validity of the identification when the angle between the wires varies. For these test, the transverse stiffness remains the one identified for an angle of 90°.

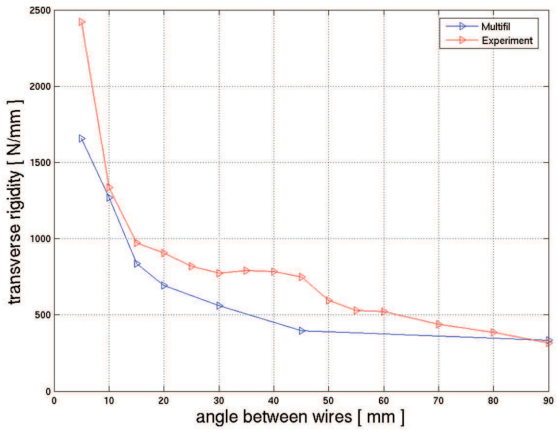

Fig. 4.29. Comparison between numerical and experimental results of the apparent transverse stiffness function of the angle between the wires.

The fitted value for the apparent transverse stiffness is valid only for the plastic domain on the loading path. In order to fit the curve for unloading (elastic), different values are found. For the OFHC copper wire, the fitted transverse stiffness for unloading is:

$E_t^2 =$ 7700 MPa ($E_t^1 =$ 650 MPa)

and for the Nb_3Sn strand,

$E_t^2 =$ 20000 MPa ($E_t^1 =$ 1700 MPa)

In conclusion, although Multifil cannot consider plasticity in transverse directions, two apparent elastic transverse stiffnesses can be fitted in order to reproduce the linear relations between the force and the displacement which characterize the pinching experiment between two crossing wires.

4 The issues related to the simulation of cable under transverse compression

4.1 Simulation of the press experiment

The method that has been implemented in the code in order to simulate the transverse press experiment is presented here. After its shaping, the cable is compressed between two cylindrical tools that gradually move in opposite directions – see Fig. 4.30. To simulate a transverse cyclic loading, the tools are moved in one direction until a given peak load is reached (expressed in kN/m) and are then moved in the other direction to unload the cable. For the following analysis of the transverse experiment, the study focuses on 3x3x5 cable, 75 mm long, with a void fraction of 38% and twist pitches {45-85-125} mm.

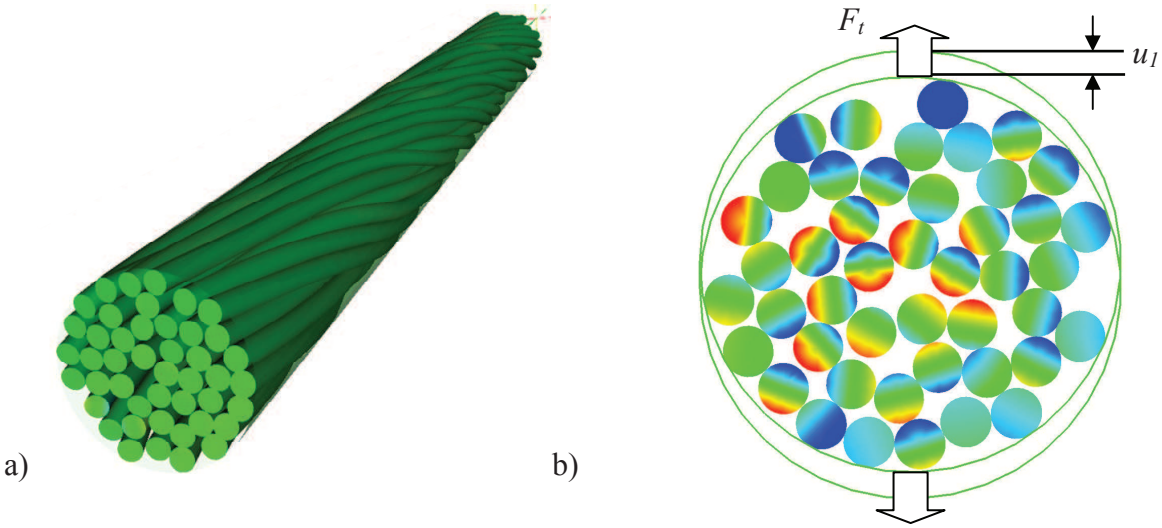

Fig. 4.30. a) View of the 3x3x5 shaped cable. b) Cross-section of the cable surrounded by two cylindrical tools used to compress the cable transversally.

Just as the experiment, the result of the test is represented by the plot of the global transverse reaction load F_t (kN/m) versus the transverse displacement U_t (mm) of the tools.

$$F_t = f(U_t) \qquad \text{eqn. 4. 1}$$

The total reaction load F_t is calculated summing the local vertical reaction forces at contacts with the tools. This reaction is then divided by the length of the cable to obtain lineic load. It reads:

$$F_t = \frac{1}{L_c} \cdot \sum_{\substack{\text{contact elements} \\ \text{beam / tool}}} f_c \qquad \textbf{eqn. 4. 2}$$

The transverse displacement U_t is the sum of the displacements of two tools u_1 and u_2. Since the tools move in opposite direction, U_t reads:

$$U_t = |u_1| + |u_2| \qquad \textbf{eqn. 4. 3}$$

The real transverse experiment is a force-driven test – see Fig. 4.4. But in Multifil, the rigid tools can only be driven by displacements. The numerical experiment is then a displacement-driven test. However, instead of prescribing constant increment of displacements to the tools until reaching a contact reaction force on the tools equivalent to the desired peak load, we want to adapt these increments of displacement so that the induced increments of reaction force are almost constant. To do this, the idea is to correct the increment of displacement to be applied to the tools for the next step depending on the increment of force obtained at the last step. For a given step n of the compaction, the increment of displacement ΔU_t^n is adjusted according to the previous increment of force ΔF_t^{n-1} so that the new increment of force ΔF_t^n has a value close to a given constant increment ΔF_0:

$$\Delta F_t^n = F_t^n - F_t^{n-1} \approx \Delta F_0 \text{ (kN/m)} \qquad \textbf{eqn. 4. 4}$$

The value of the increment of displacement ΔU_t^n for the next step is calculated in the following way, in function of the previous increment of displacement ΔU_t^{n-1} :

$$\Delta U_{t_i}^n = \frac{\Delta F_0}{\Delta F_t^{n-1}} \cdot \Delta U_{t_i}^{n-1} \qquad \textbf{eqn. 4. 5}$$

If $\Delta F_t^{n-1} > \Delta F_0$ then the next tool's increment is larger, otherwise it should be smaller. With the proper values for ΔF_0 and ΔU_t^0 set by the user, the approach leads to stable increments of force ΔF_t^n after few steps. The increment ΔF_0 may go up to few kN/m depending on the convergence.

4.2 Adjustment of the penalty coefficients for contact

Since the available space around wires is explicitly controlled by the displacements prescribed to the two rigid cylindrical tools, contact interactions are much more constrained in the simulation of the transverse compression than in the simulation of the axial loading. As a consequence, the adjustment of the penalty coefficient for contact to control the maximum penetration within each proximity zone may become unstable. As the displacements of wires are limited in transverse directions by the rigid tools, the adjustment of the contact stiffness for one contact zone, which changes the allowed gap between wires, may have an important influence on neighboring zones in transverse directions, even if the variation of the allowed gap remains very small compared with the wire radius. To improve the adjustment of the penalty coefficient for contact, an extra criterion is set on the average of the variations of penalty coefficients on all proximity zones, and extra iterations on the contact determination are performed until this average variation is below a given value. The initial values set for the

resetting of contact stiffnesses at the stress reset stage (for the modelling of the annealing of materials induced by the heat treatment), play an important role regarding the convergence of the adjustment of these stiffnesses at the beginning of the transverse compression. These values need to be reset as the reset of internal stresses in wires makes contact interaction forces go to zero. A good guess for new initial values assigned to the contact stiffnesses at this stage is important to help the convergence of the adjustment for the first steps of the transverse compression.

4.3 Setting of the maximum allowed penetration within proximity zones

For the contact model, the maximum allowable penetration, p_m must be defined. The maximum allowed penetration controls the regularization threshold for the penalty function which is fixed to one fifth of the maximum allowed penetration. The maximum allowed penetration is chosen as small as possible compared to the beam diameter. The influence of the parameter p_m is tested for the transverse compression of the earlier described 45 strand cable. In Fig. 4.31, the force-displacement curves obtained for seven values of p_m are presented. p_m ranges from 0.6% to 10% of the beam radius (410µm), i.e. p_m equal 2.5 to 40 µm. For this test, the parameter p_m significantly influences the behavior of the cable. However, with smaller and smaller p_m, the curves tend to converge. Moreover, it seems not possible to go below 0.6% of the beam radius because of convergence issues.

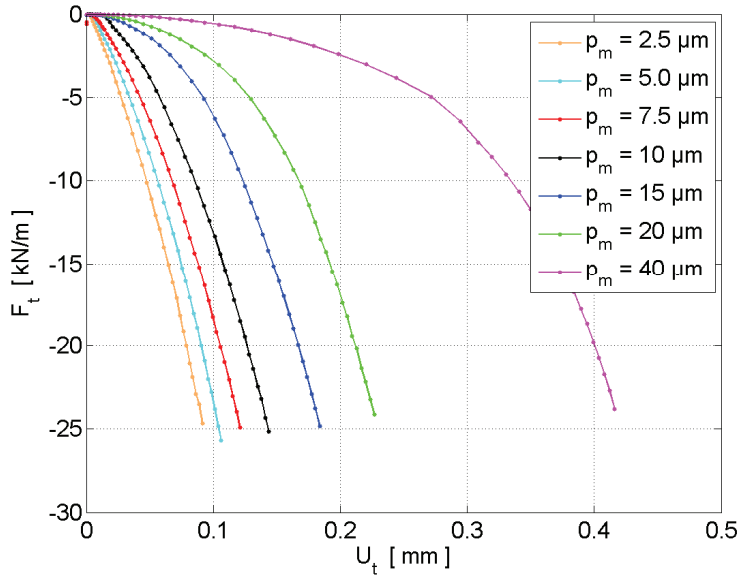

Fig. 4.31. Force-displacement curves for seven samples with different values for the maximum allowable penetration. The behavior seems to converge with smaller and smaller values.

5 Understanding of the mechanisms involved in the transverse compression of cable

5.1 Analysis of the different mechanical effects

In the following analysis, the basic mechanical effects likely involved in the transverse compression of cable are separately studied. The study consists in activating the different features of the code for different runs of transverse compression of a reference sample with a cable void fraction of 38 %. The transverse force-displacement curves of the samples for the

different runs are presented hereafter. The test is performed until a maximum load of either 25 kN/m or 50 kN/m. Two loading cycles are simulated for each run.

5.1.1 Isotropic elastic case

For the first case the isotropic elastic behavior is used without considering either the friction between the beams (setting the friction coefficient to 0) or the pseudo-friction with the tools. The Young's modulus is set to 100 GPa. The F_t (U_t) is presented in Fig. 4.32 a). The behavior of the cable is fully reversible after the loading cycles as it is expected. On the next run the pseudo-friction with the tools is introduced. The result of the loading curve is shown in Fig. 4.32 b). The behavior of the cable is no more reversible with slightly different path of the loading and the unloading. A resultant hysteresis appears on the loading curve.

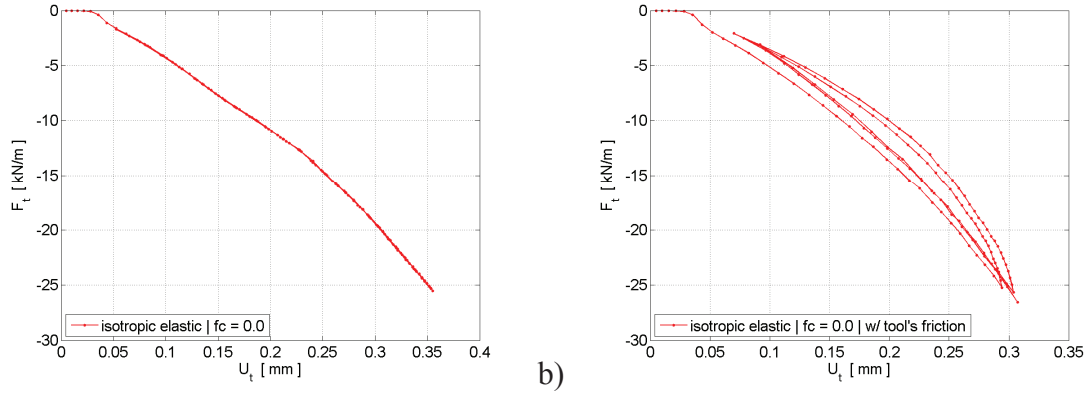

a) b)

Fig. 4.32. Transverse loading curves of the 3x3x5 reacted cable for the simplest case involving isotropic elastic model without friction consideration (a) and using the pseudo-friction between the tool and the beams (b).

5.1.2 Influence of friction

For the next case, a friction coefficient of 0.3 is chosen for the contact-friction model. The result presented in Fig. 4.33 shows a hysteretic behavior during cycles only due to friction. Two cycles are not enough to reach a stabilization of the cyclic curves, indicating strands still accommodate.

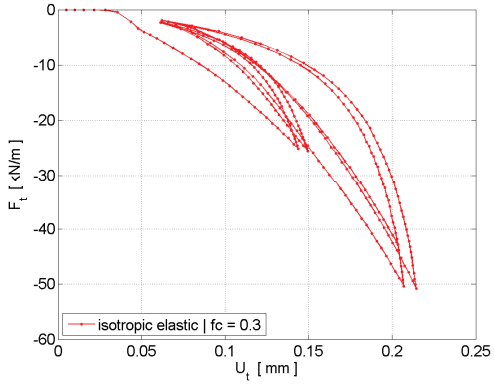

Fig. 4.33. Case involving isotropic elastic model with friction consideration.

5.1.3 Influence of the axial plasticity

The axial elasto-plastic model is now activated. The axial stress-strain behavior has been described in Chapter III. The loading curve is presented in Fig. 4.34 a). In order to test the effect of axial plasticity, the friction effects are removed. Compared with the elastic case – see Fig. 4.32 a), the cable does not exhibit fully reversible behavior: the loading and unloading paths do not overlap and a permanent deformation appears after the force is released to zero (about 0.3 mm after the two peak loadings). An envelope curve can be defined along with the loading cycles that present hysteresis. The modification of the loading curve is only due to the introduction of the axial plastic model. It indicates that the strands locally go to the axial plastic domain involving the hardening effects described in Chapter III.

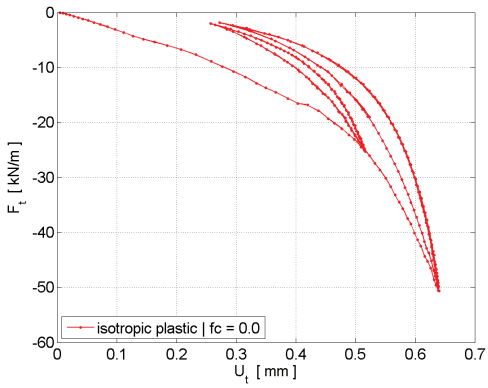

Fig. 4.34. Case involving isotropic and elasto-plastic model without friction consideration.

The next step implies the use of different friction coefficients in order to check its effect. In Fig. 4.35, the coefficient is set to 0.1, 0.25 and 0.3. The higher the friction coefficient the steeper is the slope of the curve.

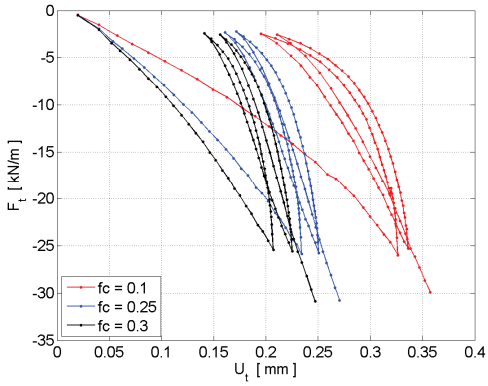

Fig. 4.35. a) Test of the effect of friction in the case of isotropic elasto-plastic model.

Fixing the friction coefficient to 0.25, different stiffnesses are now introduced for the axial and the transverse directions using the orthotropic model. The value of the transverse stiffness is the one earlier identified. The loading curve is presented in Fig. 4.36. The slopes of both the envelope and the cycles decrease due to the decrease of the transverse stiffness. The interpretation is that the applied transverse compression causes non negligible deformation of the cross-sections of the beams.

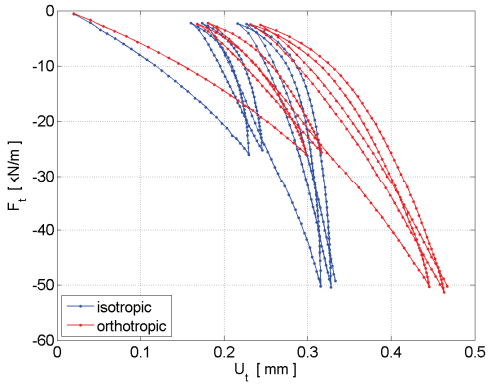

Fig. 4.36. Case involving the orthotropic model and the elasto-plastic model with friction consideration.

5.1.4 Influence of the penalty coefficient for the transverse boundary conditions

Here, the effect of the transverse boundary conditions is checked. A fairly different value is chosen for the penalty coefficient, 50 and 300 N/mm. The impact of an increase from 50 to 300 N/mm is not negligible on the force-displacement characteristic.

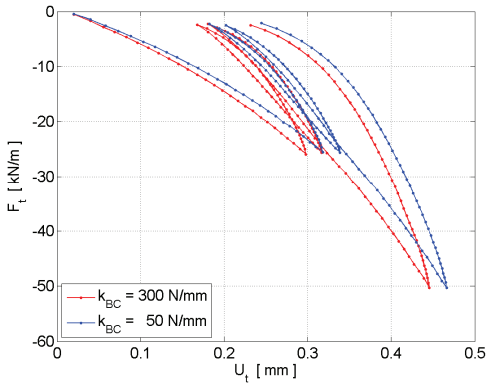

Fig. 4.37. Dependence on the boundary condition.

5.1.5 Influence of the initial void fraction

The last tested parameter is the initial void fraction of the cable sample which is decreased to 32%. The results in Fig. 4.38 a) show that a tighter cable exhibits a stiffer behavior. The slopes of the envelopes calculated between 30 and 50 kN/m are respectively 330 MPa and 220 MPa. At this stage the model seems realistic enough to attempt a comparison with experimental data for the first two transverse peak loads of 25 and 50kN/m. The curves in Fig. 4.38 b) show encouraging result but it seems that some new elements need to be introduced to come closer to the experimental behavior. The experiment is situated between the two calculated results. By the way, a void fraction of 38% seems to be overestimated compared with the real cable and 32% would not consider the opening of the cable after the removal of the jacket. But as described in the next paragraphs, adjusting the void fraction of the cable is still not sufficient to describe the experimental curve.

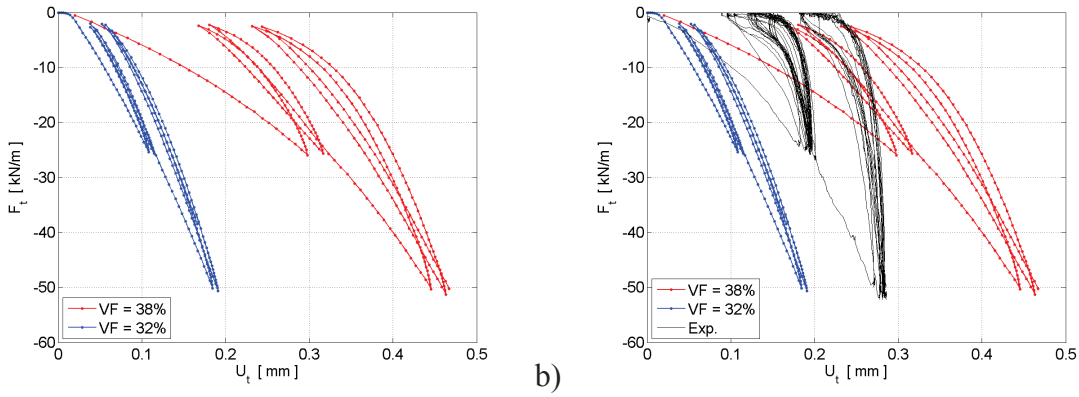

a) b)

Fig. 4.38: a) Variation of the void fraction from 38% to 32% in the case of orthotropic elasto-plastic model with friction consideration. b) Comparison of the result with the experimental data.

5.2 The introduction of an initial pinching

The large influence of the void fraction parameter on the force-displacement curves indicates that the space left between strands must be one of the main factors that rule the transverse behavior. From Fig. 4.38, it seems that the void fraction of the cable should be situated between 32 and 38%. A void fraction of 34.5% is now considered that seems to be more realistic compared with the diameter of the cable measured after the jacket removal. Looking at the cross-section of a conductor (Fig. 4.39 a), one can notice that some of the wires are severely pinched. Deforming by pinching, the cross-section of some of the wires increases locally their density, and consequently leaves more space elsewhere between strands. From this observation, simulating somehow the initial pinching between wires induced by the shaping process can be a way to get more room between wires, and to approach better the experimental curve for transverse compression. This *initial pinching* of the strands at the contacts is the phenomenon that is attempted to be modelled by Multifil. The idea is to use the contact forces generated during the *shaping part* of the modelling to deform the beam cross-sections. After the last step of the shaping, the tool is kept still and the transverse stiffness coefficient of the beam is gradually decreased. The cross-section progressively deform in return from circle to ellipse, as sketched in Fig. 4.39 b). The amplitude of the pinching is controlled by the value of the transverse stiffness, E_t. Moreover, the transverse deformations are made permanent during the *stress-strain reset part* of the modelling.

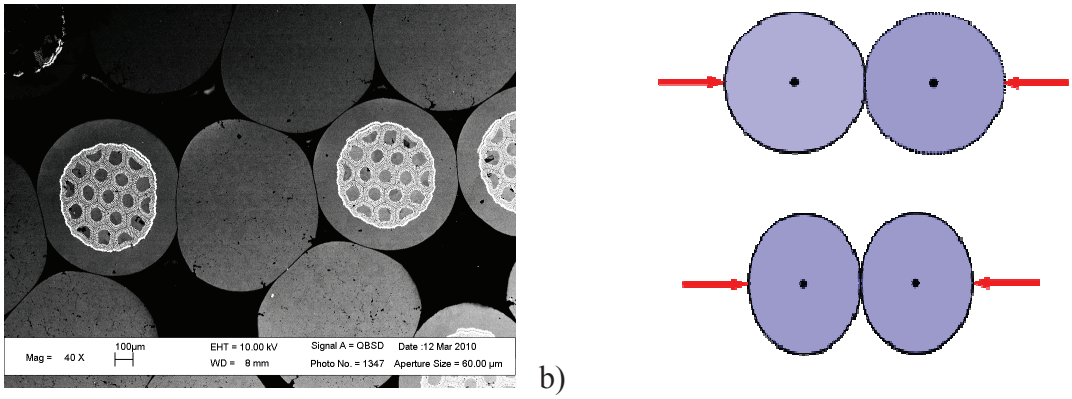

a) b)

Fig. 4.39. a) SEM observation of some transverse cross-sections found in cable-in-conduit conductor. There is strong plastic deformation. b) Modelling of the transverse deformation with Multifil. The cross-sections deform from circle to ellipse, the deformation is constant across the section.

In Fig. 4.40, the transverse force-displacement curves of samples shaped using four different amplitudes of initial pinching are plotted. These four different initial pinching have been simulated using four values of E_t, respectively 50, 10, 1 and 0.1 GPa (to be compared with the axial stiffness of 100GPa). From this result, it seems that fixing the transverse stiffness of the strands allows the non linear envelope of the experience to be reproduced. By the way, this approach has the advantage to keep a mechanical origin. Compared with the identified transverse stiffness of 1.7GPa, the modulus needed for the initial pinching is ten times lower. Since the real manufacturing process is not simulated, this difference is not unsettling.

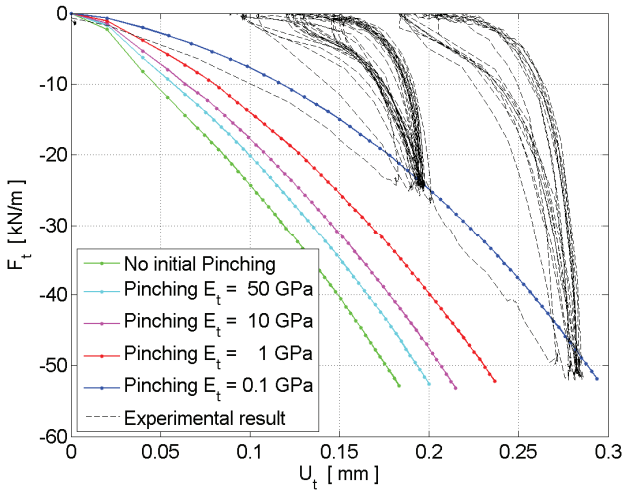

Fig. 4.40. Results for a void fraction of 34.5%, using the identified orthotropic model and axial elasto-plastic model of the strand and a friction coefficient of 0.25. The variation of the initial pinching influences the transverse behavior and help to come closer to the experimental curve.

Using this new sample that present initial pinching, two loading cycles are performed at 25kN/m and 50kN/m as it is done during the experiment. In Fig. 4.41, the loading curve shows that although the envelope is well described, the behavior of the cable when the force is released is too soft. The reason for this comes from a new issue that is so far partially solved.

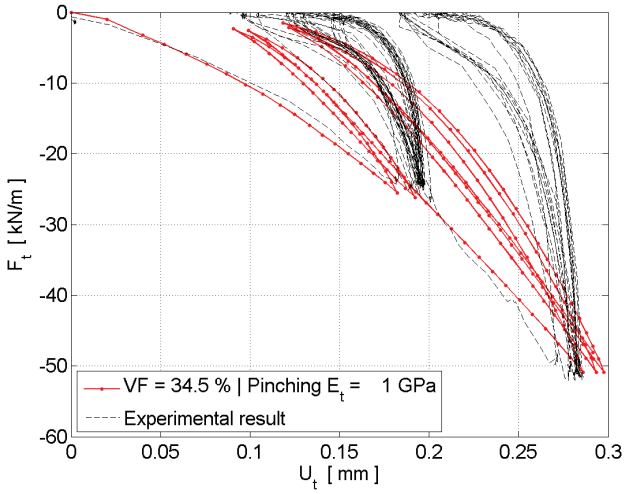

Fig. 4.41. Case using the identified initial pinching, the orthotropic model and the elasto-plastic model and a friction coefficient of 0.25.

5.3 Modification of the transverse stiffness while cycling

As exposed in the paragraph 3.2, the elastic orthotropic model is valid only for a monotonic loading. However, the pinching experiment showed that depending on the direction of the loading, the mechanical response of the strands is either plastic (on the main envelope loading) or elastic (for small unloadings) – see Fig. 4.8. The strand displays two different apparent stiffnesses: the real elastic stiffness for unloading, and an equivalent stiffness for the main loading path. The transverse stiffness identified for the elastic orthotropic models corresponds to the main loading path, and so to the plastic domain. When the cable is unloaded, the transverse response to the pinching of the strands is driven by elasticity, with a much higher stiffness. To try to reproduce this effect, the value of the transverse stiffness of the strands is switched to higher value from (1.7GPa to 20GPa) when the loading decreases. Due to this modification, the slope of the cycles gets steeper as described in Fig. 4.42. Such behavior seems more realistic compared with the experiment. However, this switch of the transverse stiffness is artificial. A possible solution would be to introduce a bi-dimensional plastic criterion on the transverse stresses of the beams.

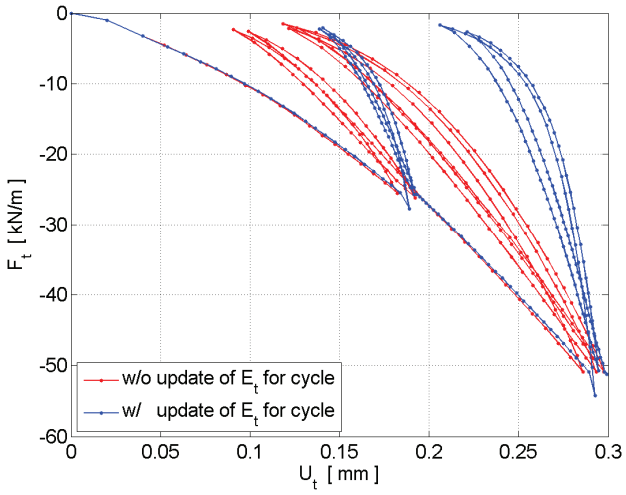

Fig. 4.42. The transverse stiffness of the strands is switched to higher value when the loading path leaves the envelope.

6 Validation of the model for transverse loadings

6.1 Comparison with experimental curve

This paragraph concludes the works done to identify the proper transverse stiffnesses, to understand the cable behavior submitted to transverse compression and to finally validate the model of cable with comparison to experimental force-displacement curves. The latest result including the different features developed so far is presented in Fig. 4.43. The open parameters of the simulation that can be seen as fitting parameters are the initial void fraction of the cable, the transverse stiffness used to simulate the initial pinching and the friction coefficient. The model remains valid up to 100kN/m which is expected to be in the range of the loading induced by the Lorentz forces in conductor. In order to illustrate the loading curve of Fig. 4.43, some pictures of the loaded cable are described in Fig. 4.44 for the three peak transverse loads: 25, 50 and 100 kN/m. The axial strains range for -1% to +1%, i.e. far beyond the yield strain. In Fig. 4.45, the cross-sections of the cable at its middle are shown. The

occurrence of plastic deformation when the transverse load is released is illustrated (existence of non zero strains when F_t goes back to 0).

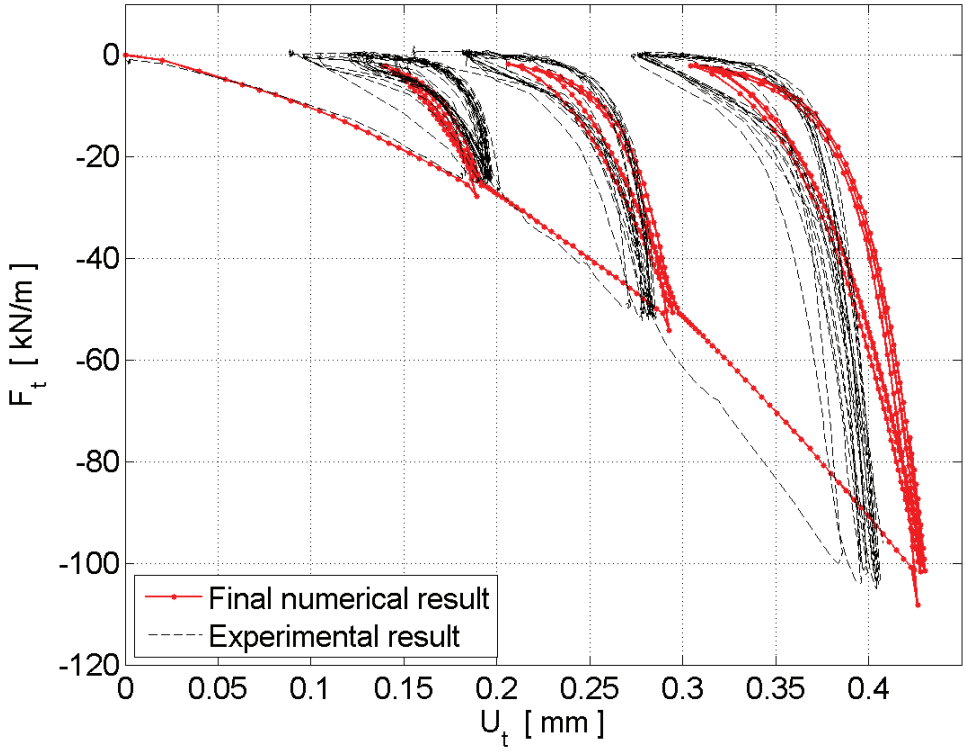

Fig. 4.43. Final result of the modelling of cable submitted to transverse compression. The numerical and experimental result regarding the force-displacement loading curves are here compared.

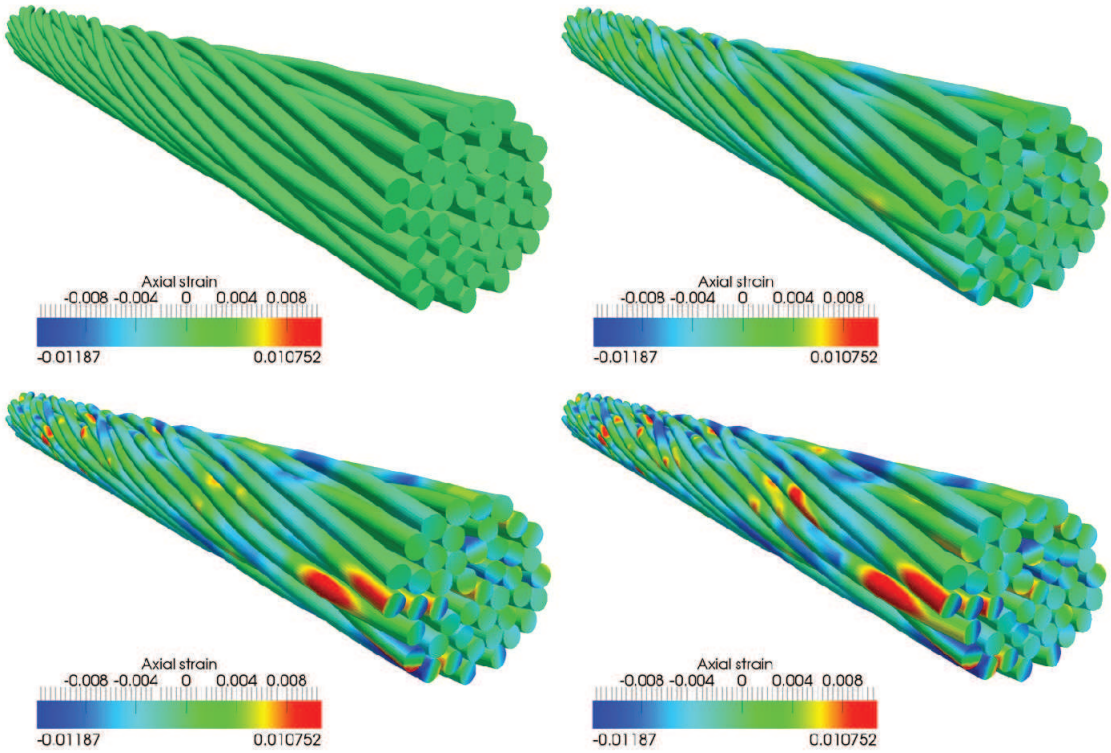

Fig. 4.44. Global view of the 3x3x5 cable submitted to transverse compression. The four pictures correspond to F_t= 0, 25, 50 and 100 kN/m.

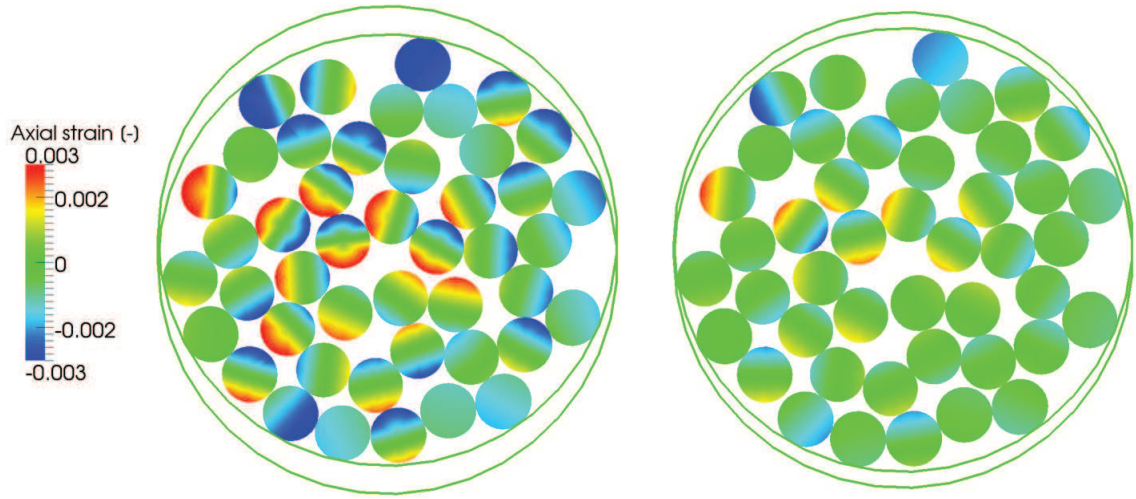

Fig. 4.45. Transverse cross-section of the 3x3x5 cable submitted to transverse compression. The peak load is here F_t =50 kN/m which is then released to 0. Some permanent plastic deformations remain after the force is released due to the plasticity of the strands.

In Fig. 4.46, the graphics shows that the transverse compression can still be carried on but the results starts to differ from the experiment. At such a loading, it is likely that the plastic deformation of the strands at contacts become a dominant phenomenon. The kinematic of the beam model is no more sufficient to completely describe realistic behavior.

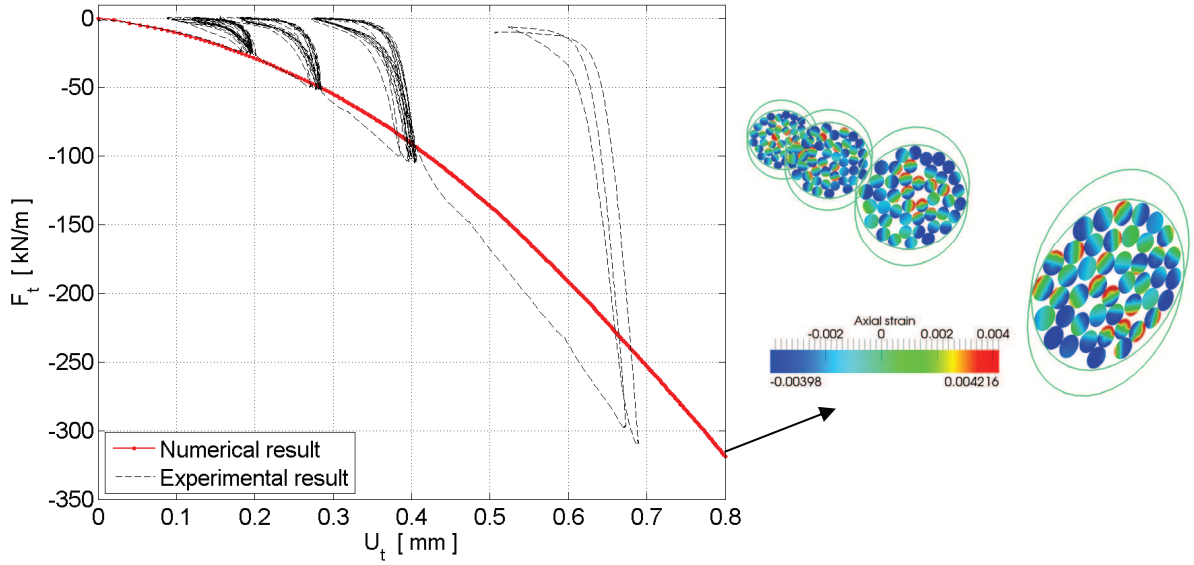

Fig. 4.46. Illustration of the extent of the domain of validity of the cable model submitted to transverse compression. As the picture on the right shows, the cable loaded at 200 kN/mm is severely deformed.

6.2 The effect of the inclusion of pure copper wires

To conclude with this chapter, the influence of the inclusion of copper has been checked. Four samples were transversally compressed using superconducting strands only, next one third, then two thirds of copper wires and eventually using copper wires only. Except for the wire materials, the cables are exactly the same. The global force-displacement curves are shown in Fig. 4.47. The transverse cross-sections (at the middle of the cable and at 60 mm) are shown in Fig. 4.48 when the applied loading is 100 kN/m. The same strands are loaded but with

different amplitude depending on the material of the wires. Increasing the number of copper wires leads to higher plastic strains.

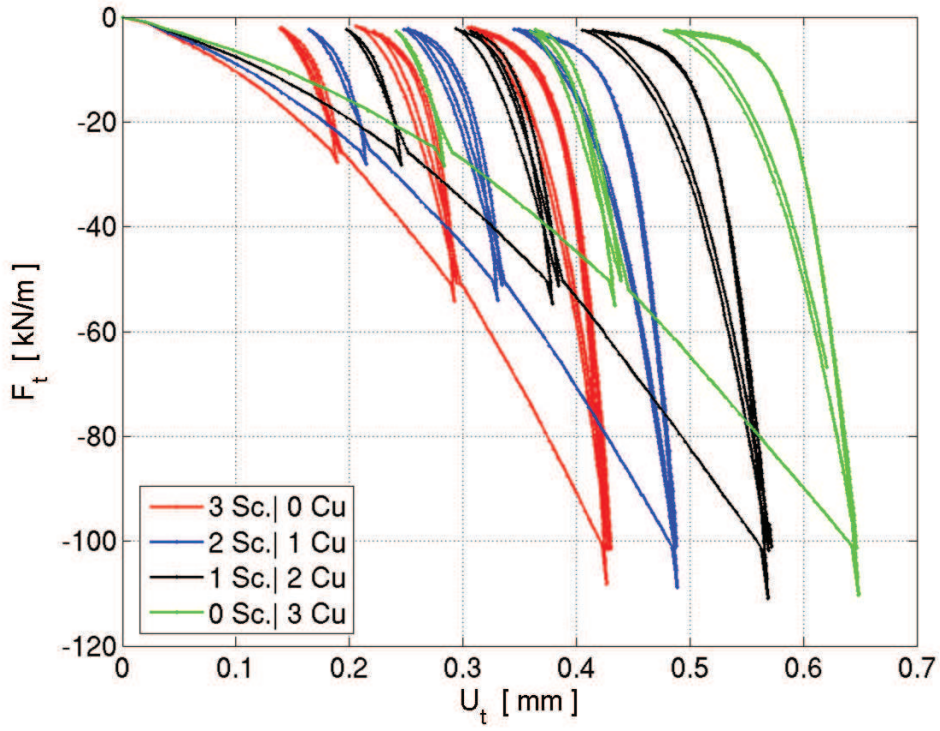

Fig. 4.47. Influence of the inclusion of copper wires inclusion on the transverse behavior of the conductor.

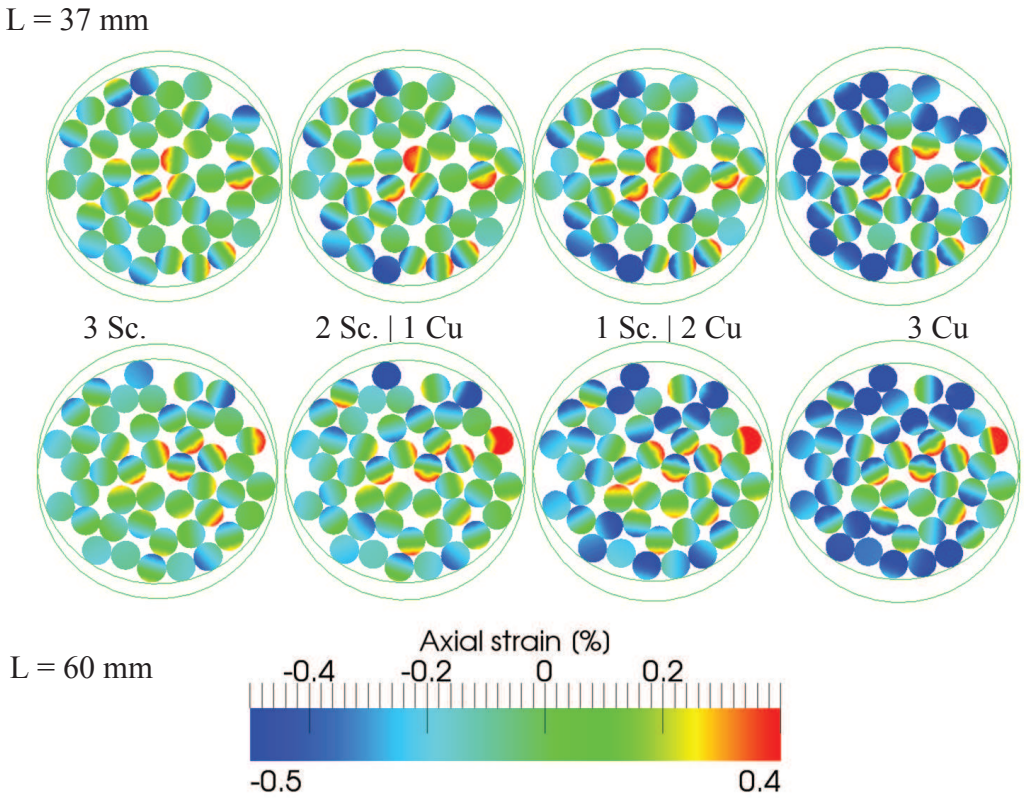

Fig. 4.48. Transverse cross-sections (at L = 37 & L = 60 mm) of the 3x3x5 cable with superconducting strand only, with one third, two thirds of copper wires and with copper wires only. The applied transverse loading is 100 kN/m.

Chapter V: Simulation of ITER Cable-In-Conduit Conductor under operating conditions

1 Main purposes of the simulations

1.1 Objectives of the simulation

As described in Chapter I, the degradation of superconducting performance in cable-in-conduit conductors comes from the local deformations of the strands that are axially and transversally loaded due to thermal and electromagnetic effects. These deformations induce some axial compression, bending or pinching to the strands which prevent good transport current down the level of the Nb_3Sn filament. Moreover, the tensile strain arising from the bending or even pinching can cause the microscopic breakages of the brittle filaments. In this chapter, the purpose of the work is to understand the mechanical effects involved in loaded cable-in-conduit conductor and the origin of the deformation by means of the simulation. Starting from a shaped conductor, the axial compression and the local Lorentz forces will be applied and the local axial strains that are created at the scale of the strands will be analyzed. The analysis of the simulation results has allowed some specific behaviors to be highlighted that seem to be typical of the mechanics of loaded cable-in-conduit conductor. In particular, the developed model tends to show that the local strains are highly non uniform along and across the conductor with a broad range of possible amplitudes. In addition, the proposed analysis aims to quantify and localize the critical axial strains within the conductor which provides an estimate of what could be the damaged areas relative to the Nb_3Sn filamentary region. The simulation also allows different conductor designs to be tested that will be compared one another. At last, the information relative to the local scale of the strands might be used to feed existing electrical codes. The presented work will focus on four stage cables, presented in Chapter II 5.3.2.

1.2 Complete simulation of conductors under operating conditions

1.2.1 The different tested conductors

The complete simulation has been performed on four stage cable, from the shaping to the Lorentz loading. In Chapter II 5.3.2, the designs of the four samples have been described. These are summarized in Table 5.1. The reasons for choosing these designs are explained presently.

Cabling pattern	Number of strands	Shape & Dimension [mm]			Void Fraction [%]	Twist Pitches [mm]	L [mm]
		Round	square	petal		51-79-136-166	160
3x3x**4**x4	144	**6.01**	**10.7**	**x**	33	51-79-136-166	160
3x3x**5**x4	180	**6.72**	**x**	**6-18.6**	33 – 41.4	51-79-136-166	160

Table 5.1. The different designs of conductors that have been simulated.

a. 144 strand round cable

In 2004, N. Martovetsky *et al.* published the SULTAN test results (I_c and T_{cs} measurements) of two *CICCs* composed of 144 superconducting strands (from the excess strand of the CSMC strand production) [Martovetsky 2004]. These two *CICCs* are identical except that the jacket (1.0 mm thick) is either made of titanium or stainless steel. The use of two different jacket materials on two identical conductors allows getting indication of the effects of two different applied thermal strains on the electrical behavior. The effect can be quickly tested by the simulation which is also the reason why these conductors have been chosen to be simulated. Their void fraction and the twist pitches are taken as the reference for the four simulated conductors.

b. 180 strand petal and round cable

In 2008, D. Ciazynski published the test results of the ITER-like *CICC*: the "TFAS1 EAS0" composed of 1080 strands in a 1.6mm thick stainless steel jacket. The cabling pattern of the conductor is 3x3x**5**x4 with a void fraction of 33% and the following twist pitches: {45-87-126-166} mm [Ciazynski 2008]. The void fraction and pitches are very similar to those of the earlier 144 strand *CICCs*. For this reason, the TFAS1 EAS0 conductor has been selected to be simulated. One petal of this conductor is simulated. In 2007, K.P. Weiss *et al.* have published the final results of the ITER sub-size conductors SAMAN task performed at the FBI facility [Weiss 2007]. Among the numerous tested *CICCs*, the simulation of the 180 round conductor could be put together with the SAMAN 8 (0.8mm thick SS jacket). The cabling scheme is the same: 3x3x5x4, the pitches and void fraction of the actual conductor faintly change (45-85-125-160 mm and 32%). No copper wire is introduced in the simulation (unlike the PITSAM 2 and the SAMAN 8 which include copper wires in their triplet, respectively 1/3 and 2/3).

c. 144 square cable

In 2008, P. Bruzzone presented the SULTAN test results of a 108 strand *CICC* enclosed inside a square jacket, the conductor PITSAM2 [Bruzzone 2008]. This *CICC* gets a 1.75mm thick SS jacket square jacket with a 30% void fraction. The cabling pattern differs from the model (3x3x4x4 against 3x3x**3**x4) but pitches are similar {58-95-139-213} mm. The design of the model is different because only the influence of the jacket shape is sought to be tested here. In the simulation, though the 144 round conductor can be directly compared with the square conductor.

To conclude, the models of conductor do not aim at exactly reproducing the actual conductors. The goal is rather to draw some tendencies regarding the mechanical behavior of the cables of different designs. For the sake of the parametric study, only one parameter varies from sample to sample. The main purpose of the following study is two-fold. First, the effect of a change in the cabling pattern from 3x3x**4**x4 to 3x3x**5**x4 is investigated. Second, the influence of the conductor's shape is examined with round, square and petal-like cross-sections.

1.2.2 Application of the loadings

a. Amplitude of the thermal strain

The amplitude of the axial compression to apply to the conductors comes from the assessment of the thermal strain ε_{th} of the smeared model – see Chapter I. In [Mitchell 2003], the author emphasizes that the true fully bonded model would give a strain of about -0.8 % to -0.85 %

with steel. But due to curvature of the strands, the strain would be relaxed by up to 0.2%. Regarding the 180 strand petal cable, D. Ciazynski [Ciazynski 2008] suggests from the smeared mode a value of -0.6% for TFAS1 EAS0 conductor or -0.558% using the reduced superconducting area model. Weiss and Duchateau [Weiss 2007] expect thermal strains between -0.55% and -0.6% from their analytical model of the 180 strand Saman conductor whereas for the square conductor, it is close to -0.62% [Bruzzone 2008]. Martovetsky [Martovetsky 2004] provided for values of two identical 144 strand cables inside either stainless steel or titanium jacket. Using the smeared model, the thermal strains for these two *CICCs* are respectively -0.458 % and -0.6 %. Regarding the titanium jacket, the assessed ε_{th} is higher than the expected value. The authors indicate that the thermal strain is expected to be around -0.2 ~ -0.3% for the titanium jacket so that the occurrence of cracks could explain the need of an arbitrary high thermal strain by the smear model to match the degradation of the critical current with Lorentz force cycling. Mitchell [Mitchell 2003 b] proposes a value of -0.38% for the thin jacket of TFI cable-in-conduits. For the Multifil computations, it has finally been decided to use two different thermal strains that range within expectations. The reference axial compressions that are applied to the conductors are:

ε_{th} = -0.38% or ε_{th} = -0.66%

b. Amplitude of the Lorentz force loading

For the determination of the Lorentz force loading to be applied in the Multifil model, the magnetic field B and the current I_s are assumed uniform across and along the conductor, and their respective values are directly taken from experimental measurements. In Fig. 5.1 for instance, the 144 strand SS round *CICC* is carrying a maximal current I_c =13.5 kA (~100 A per strands) in a background magnetic field B = 11 T at a temperature of T=4.5 K [Martovetsky 2004]. In that case, the Lorentz force loading that would be:

F_L = 13500*11/144 = 1031 N/m = 1.031 N/mm

For the conductor with the titanium jacket, with lower induced thermal strain, the critical current is higher, I_c =18.5 kA so that F_L would have been higher 1.375 N/mm. Regarding the Multifil simulation, the reference amplitude of the Lorentz force loading at which the different conductors would be compared is:

F_L = 1.35 N/mm

In the model, like in the experiment, the applied thermal strain is assumed to maintain its effect during the Lorentz force loading. Therefore, the axial displacements of the strands are fully locked by the boundary conditions of the model while the Lorentz forces are applied.

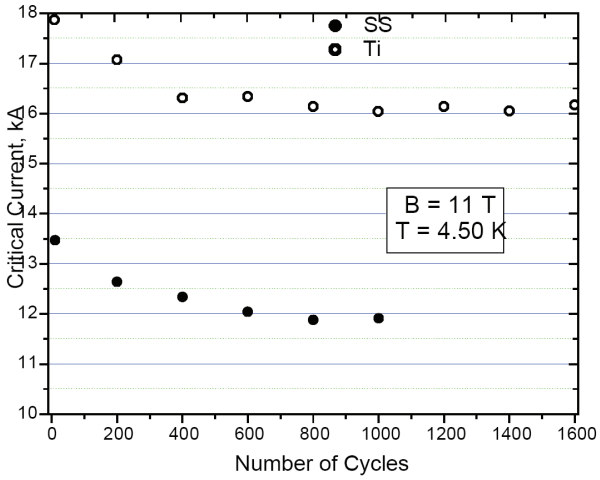

Fig. 5.1. Evolution of the critical current with the number of cyclic loadings (at constant operating condition B&T) of two 144 round *CICCs* that only differ by their jacket's materials, namely stainless steel (SS) and titanium (Ti). [Martovetsky *et al.* 2004].

c. Loading increments

In the Multifil model, both the final thermal strain ε_{th} and the final Lorentz loadings F_L are incrementally reached. The corresponding loading increments are, for the strain, $\Delta\varepsilon_{th}$ and for the Lorentz force, ΔF_L. Just as for the shaping part of the modelling, the idea is to use a large enough increment not to be over time-consuming but small enough to insure the convergence. Some rules of thumb are here presented regarding the amplitude of $\Delta\varepsilon_{th}$ and ΔF_L. As far as the cable model is only composed of superconducting strands, it is delineated that the simulation may start with $\Delta\varepsilon_{th}$ = -0.01 % which can be increased up to -0.025 % after ε_{th} ~ -0.2 %. As a matter of fact, the elastoplastic model induces some convergence issues that limit the size of the loading increment. Regarding the Lorentz loading, ΔF_L should be gradually decreased as the loading increases. The user should take care to control the size of ΔF_L as the cable gets compressed. For the various computations, it appeared that the loading may start with ΔF_L = 2.10^{-2} N/mm and ends with 3.10^{-3} N/mm. Yet, the size of the increment can likely be optimized.

1.2.3 Numerical parameters of the simulation

The loadings applied to shaped conductors are performed using the developed elasto-plastic behavior with transverse deformation of the beams and friction between the beams as presented in Chapter III and IV. For the rest of the study, the material properties are identified at room temperature and not at 4.2K. The effect of the change of material properties at low temperature is not tested here. The initial pinching has been realized as well. The penalty coefficient of the transverse boundary condition is k_{bind} = 300 N/mm, the maximum allowable penetration is $p_m = 2.10^{-3}$ mm and the reversible displacement is $\Delta u_{irr} = 7.10^{-3}$ mm.

1.3 Post-treatment of the axial strains

1.3.1 Axial strain across the beam section

Since the work focuses on the axial strain, this paragraph presents how the axial strains are defined. In the output of the model, the axial strains are given for each node, at the neutral

axis of the beams, ε_0 and at eight points distributed on the periphery of the cross-section at eight different angles, $\varepsilon_{peri}(\theta_i)$ where i=1,8. For the post-treatment, a linear variation of the axial strain is assumed through the beam cross-section. For each cross-section, knowing the axial strain $\varepsilon_{peri}(\theta)$ for a given angle θ at the periphery of the section, the axial strain ε_0 at the center of the cross-section, the axial strain is interpolated at a point of the cross-section identified by its relative radius ρ (varying from 0 to 1) and its angle θ in the following way:

$$\varepsilon(\rho,\theta) = \varepsilon_0 + \rho(\varepsilon_{peri}(\theta) - \varepsilon_0) \quad \textbf{eqn. 5.1}$$

The term $\rho(\varepsilon_{peri}(\theta) - \varepsilon_0)$ in this expression corresponds to the contribution due to the bending. For this reason, this term is defined as bending strain, denoted $\varepsilon_b(\rho,\theta)$:

$$\varepsilon_b(\rho,\theta) = \rho(\varepsilon_{peri}(\theta) - \varepsilon_0) \quad \textbf{eqn. 5.2}$$

Regarding the post-treatment, the strains are measured at the center of the section and at 24 points in each cross-section that correspond to three values of relative radius (ρ = {1/3, 2/3, 1}) and the same values of angle as those provided in outputs (θ_i with i = {1:8}). In Fig. 5.2, the beam's section is typical of a bent strand as found in cable. It shows the strain gradient across the section with compression in blue color and tension in red. However, the behavior in Fig. 5.2 is not pure bending since ε_0 is here -0.25 %, i.e. a larger area of the section is under compression.

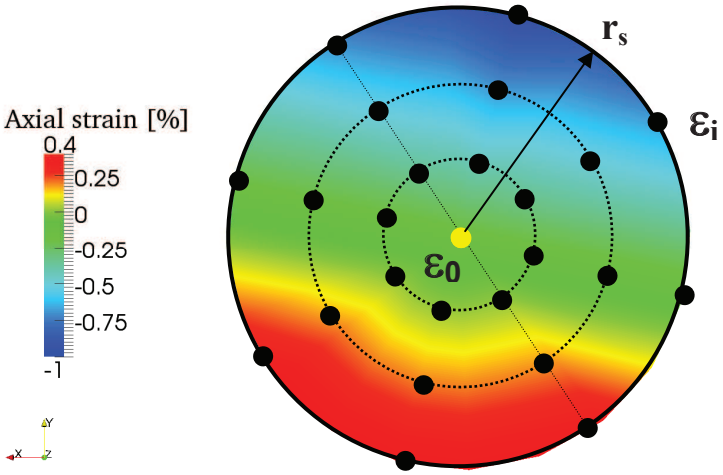

Fig. 5.2. The 25 discretisation points across the strand section where the axial strains are measured. The axial strain linearly varies across the section. On this example, the bending is illustrated by the strain gradient across the section. The colors depict the amplitudes of axial strain ε [%].

Only the filament region inside the strand is concerned by the degradation of conductivity properties. For this reason, the analysis focuses on the strains of this filament region, considering the maximum relative radius:

$$\rho_{max} = \frac{r_f}{r_s}, \quad \textbf{eqn. 5.3}$$

where r_f and r_s, are respectively the radius of the filament region and the radius of the strand with the typical following values:

r_f = 225 µm and r_s = 405 µm.

An interesting value to analyze is the maximum strain for the filament region, called the peak strain ε_p, defined as the maximal strain found around the perimeter of the filamentary region:

$$\varepsilon_p = \max\left(\varepsilon_0 + \frac{r_f}{r_s} \cdot (\varepsilon_{peri}(\theta_i) - \varepsilon_0) \right) \qquad \textbf{eqn. 5.4}$$

The peak strain ε_p appears to be a relevant figure to depict the critical tensile strain that would cause filament damage.

1.3.2 Statistical tools

Some statistics can be performed on the Multifil output data. In a first approach, the data can be represented by the distribution. A distribution represents the probability to locally measure a given strain somewhere in the conductor. It presents the advantage to show every value of strain with a single curve representative of the conductor strain state at a given step of the computation. The mean $<\varepsilon>$ and the standard deviation $std(\varepsilon)$ are also interesting data to be analyzed. In a second approach, the axial strains can be plotted for each strand along its length. Among the available quantities, ε_p is chosen, because it is representative of the most critical points. The various strands can be compared against one another. In a third approach, a method has been developed that helps in locating the zones in the conductor where the peak strains are statistically the greatest. The idea is to represent average or maximum strains along the cable axis in order to observe the variations of these quantities in the transverse directions of the conductor. The method aims to draw a map of the strain across a typical cable cross-section. The three statistical approaches are complementary and useful tools to analyze the Multifil output data.

2 The mechanisms involved in cable-in-conduit conductor

2.1 The cable effects during the loadings

2.1.1 General observations

Once the computation is over, the first step of the analysis is the visualization of the post-treated results. The pictures in Fig. 5.3 a) and b) present the results of the model for the 3x3x5x4 round conductor after the application of the reference thermal strain (ε_{th} = -0.66 %) and after the reference Lorentz force loading (F_L = 1.35 N/mm along the x direction). The colors stand for the axial strains locally sustained by the strands expressed in percent. These pictures indicate non-uniform deformation of the strand in the cable with some localized areas of high strain (red color). These red spots are in greater numbers after the Lorentz loading.

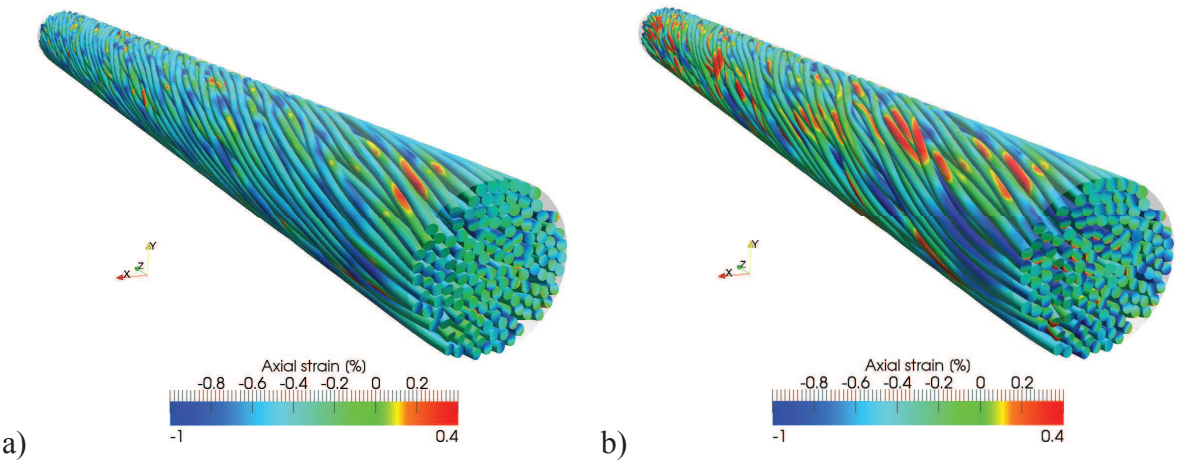

Fig. 5.3. Global view of the simulation results for 3x3x5x4 conductor, a) after the axial compression ε_{th} = -0.66% and b) after the Lorentz loading F_L = 1.35 N/mm.

In Fig. 5.4, the cross sections of the conductors at the middle (L=80mm) are shown before and after the Lorentz force loading. The axial strains are not uniform across the conductor section with clear occurrence of bending (non-uniformly deformed strand sections) but also almost some pure compression (uniformly blue sections) at the periphery of the cable. The Lorentz force loading impacts the amplitudes of the local strains and causes a migration of the strands towards the direction of the force. The model shows that there are many possible bending orientations which add to the complexity of the behavior.

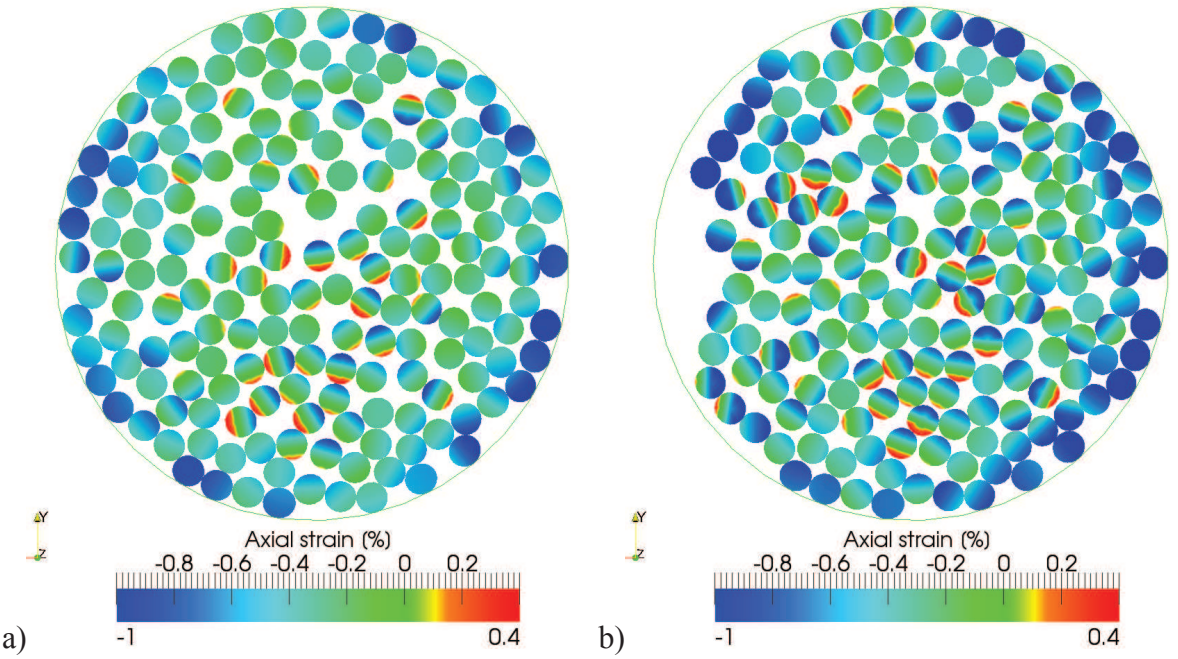

Fig. 5.4. Cut view at the middle of the 3x3x5x4 round conductor a) after axial compression ε_{th} = -0.66% and b) after the Lorentz loading F_L = 1.35 N/mm.

2.1.2 Peripheral densification of the strands during the axial compression

An interesting phenomenon has been highlighted by the simulation of the axial compression. It seems that some cable cross-sections 'open' in a significant way. These peculiar cross-sections are localized by the longitudinal cut view as exposed in a)

b) c)

Fig. 5.5.

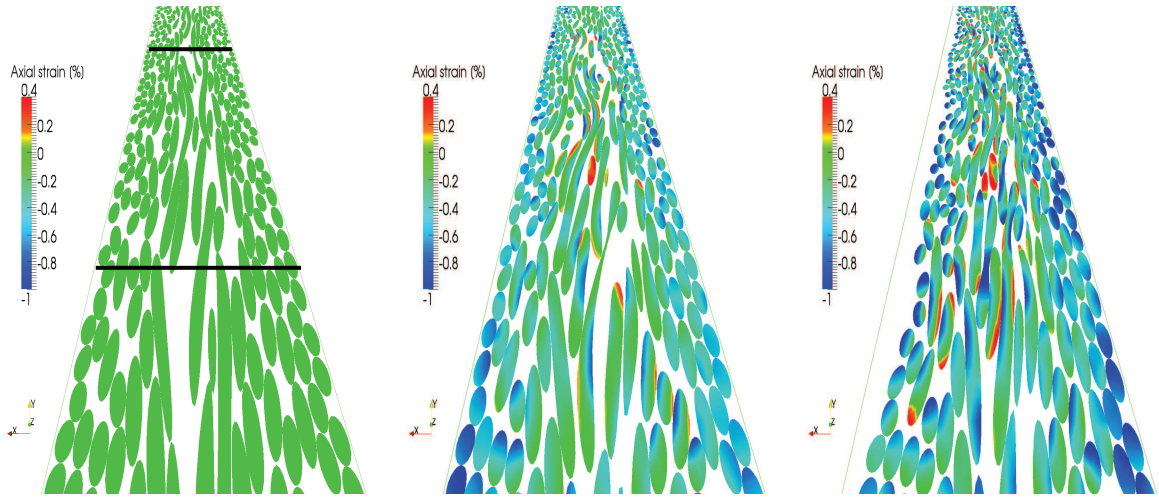

a) b) c)

Fig. 5.5. Longitudinal cut view (at the median plane) of the 3x3x5x4 round conductor a) after the shaping, b) after the axial compression ε_{th} = -0.66% and c) after the Lorentz loading F_L = 1.35 N/mm.

The black lines in the first picture point at these open cable sections. It is proposed to look at the conductor's sections at the precise abscissa of these sections, at z = 20mm and 145mm. The corresponding cross-sections are shown in Fig. 5.6. There is a clear migration of the strands towards the periphery of the cable that leaves voids at the centre of the structure and induces a consecutive peripheral densification of the strand. The density of strands increases from the centre to the outer surface of the cable where the displacements are stopped by the surrounding jacket. Consequently, the strands contacting the jacket get no chance to bend. In the core of the cable, the strands may take advantage of the available space to bend. At the core, the lower density of strands after the axial compression means more available room for the strands to move there. As a matter of fact, the strands that pass through the core of the conductor are showing more tensile strain than those passing by the periphery.

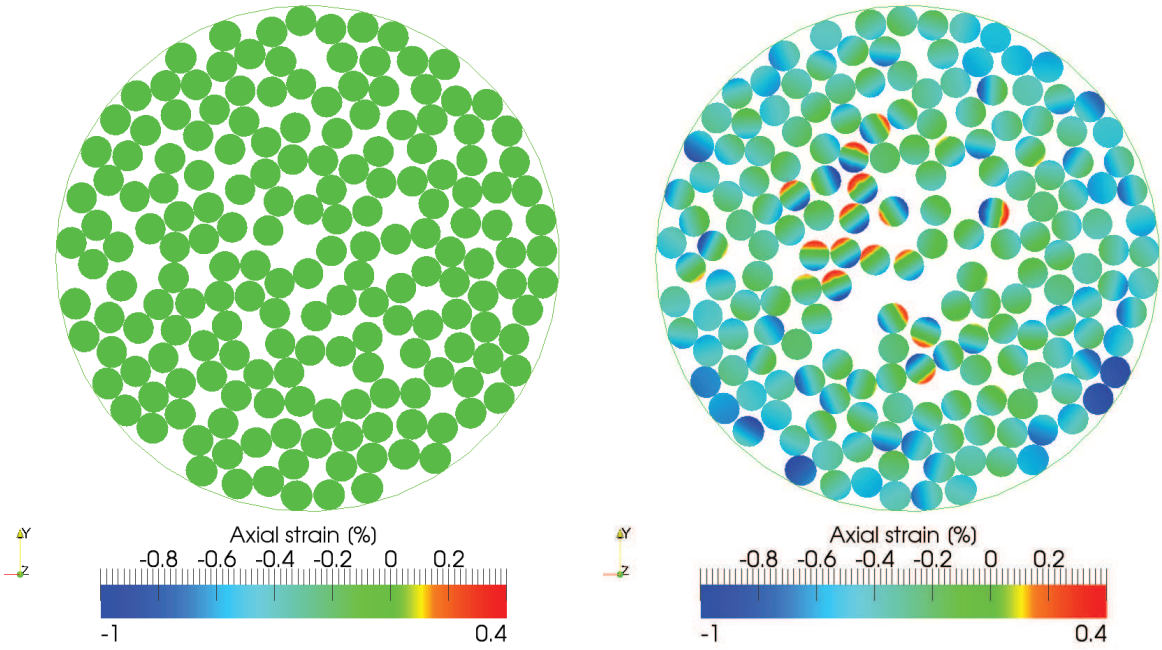

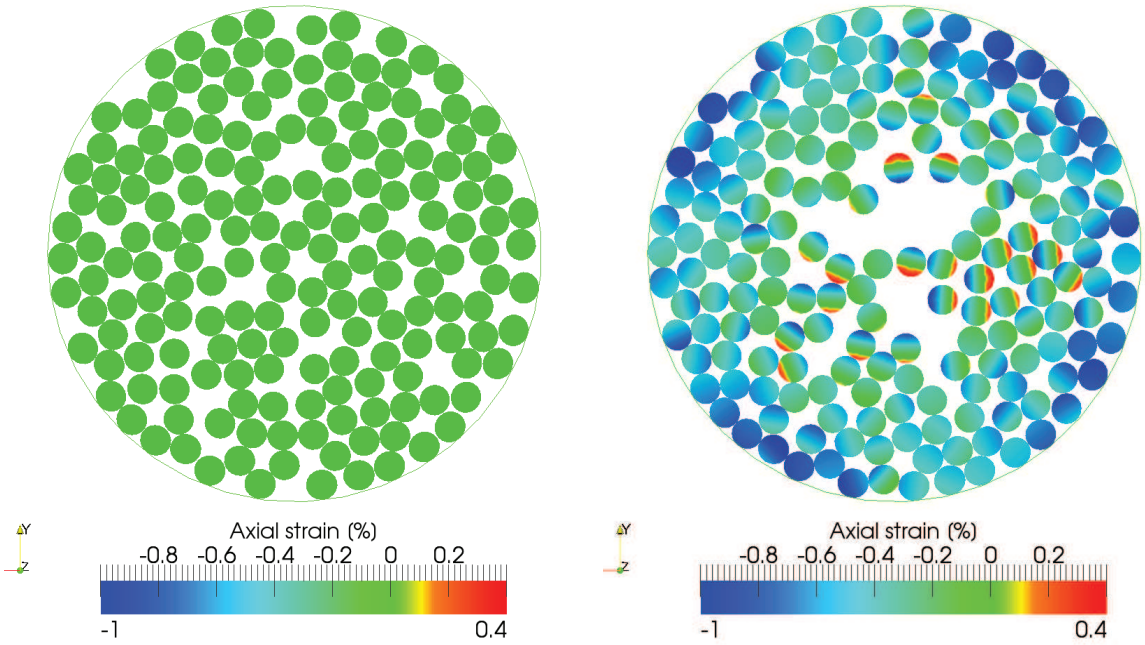

Fig. 5.6. Peculiar *open* cross-sections in the 3x3x5x4 round conductors after the shaping, after the axial compression ε_{th} = -0.66%.

2.1.3 Crush of the conductor due to the Lorentz forces

a. Formation of the gap between the cable and the jacket

During the Lorentz force loading, the cable is deformed in the direction of the forces. The top surface of the cable (with respect to the direction of the loading) tends to flatten in the direction of the forces – see Fig. 5.7. This effect is experimentally well known in cable-in-conduit conductor. In fact, the pressure drop in the Helium flow is observed as the Lorentz loading increases. The effect is usually explained by the creation of a 'channel' at the upper part of the *CICC* from which the strands have migrated. The Helium flows through the channel causing the pressure variation. The simulation allows this gap to be directly estimated at about 1mm in the 180 strand round conductor – see Fig. 5.8. Due to the flattening of the surface, some local bending appears at the borders of the flatten zone.

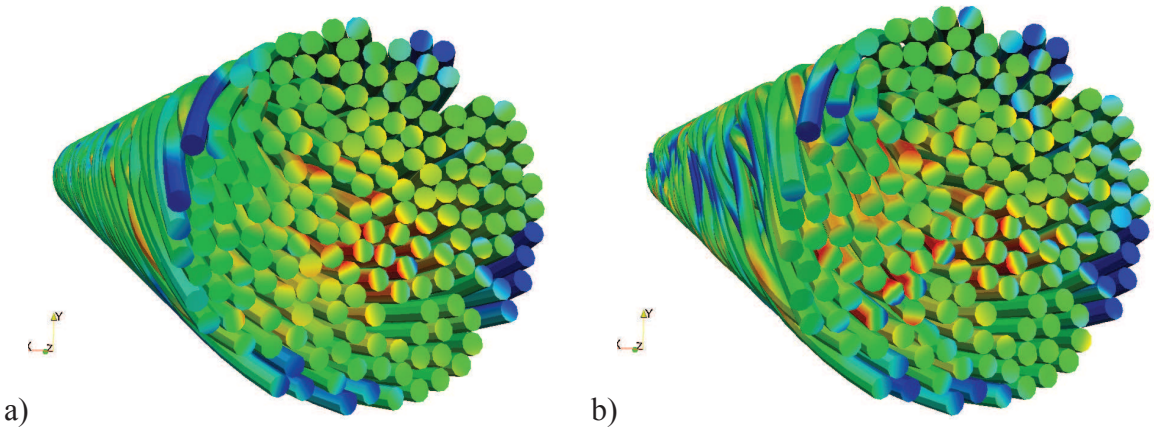

a) b)

Fig. 5.7. Evidence of the Lorentz loading impact on the geometry of the conductor with a flattening of the surface in the direction of the forces.

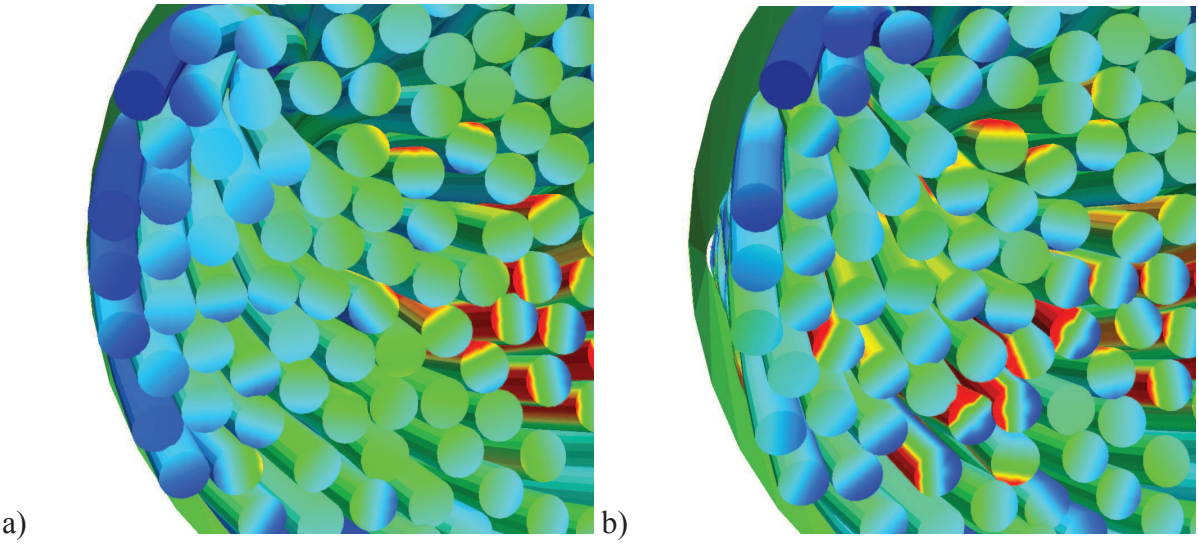

Fig. 5.8. Illustration of the creation of a *gap* of about one strand diameter (~1mm) between the cable and the jacket due to the Lorentz loading application.

b. Displacement of the strands due to the Lorentz forces

The effects of the Lorentz force loading on some conductor cross-section are presented in Fig. 5.9 and

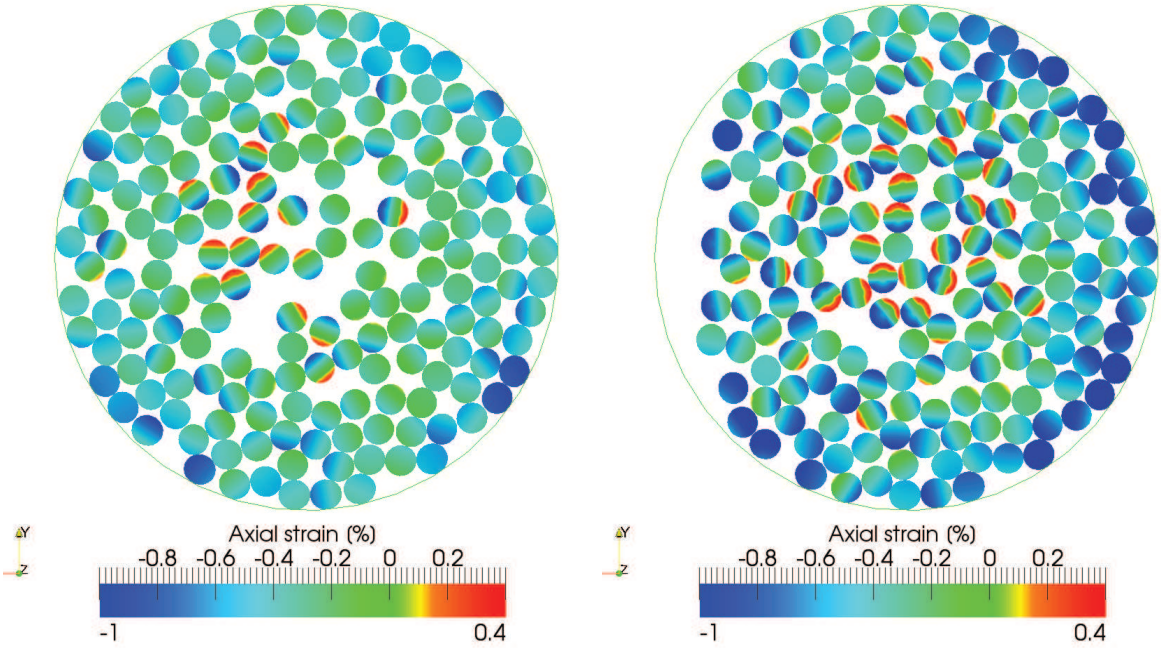

Fig. 5.10. Although the relation between displacement and bending of the strand inside the conductor is not obvious, it seems that the Lorentz force is effectively generating more bending. The strands situated at the center of the cable seem to be preferentially deformed by bending, whereas the strands at the periphery are rather purely compressed (uniform blue color).

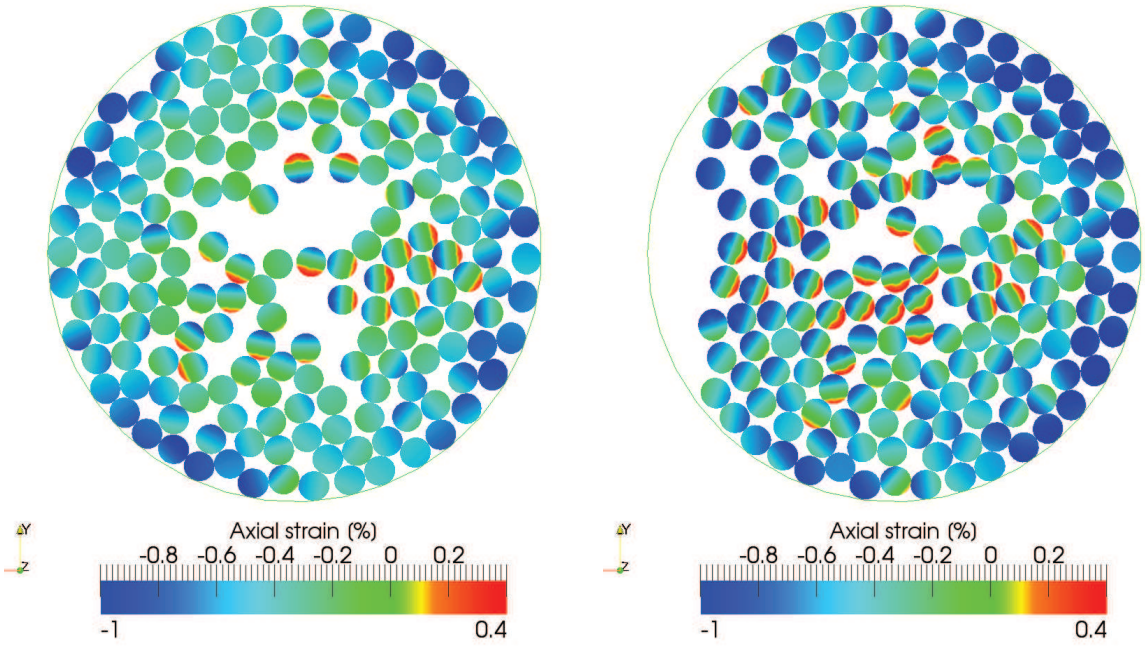

Fig. 5.9. Conductor cross-sections at L = 30 mm in the 3x3x5x4 round conductors after the axial compression ε_{th} = -0.66 % and after the Lorentz loading F_L = 1.35 N/mm.

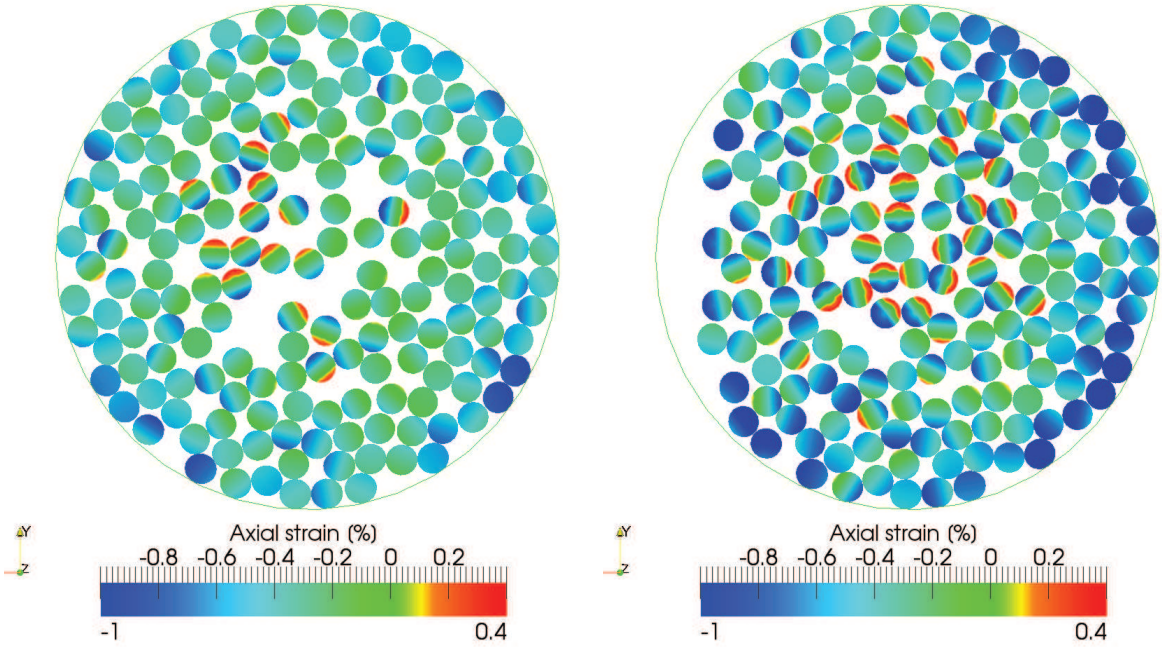

Fig. 5.10. Conductor cross-sections at L = 140 mm in the 3x3x5x4 round conductors after the axial compression ε_{th} = -0.66% and after the Lorentz loading F_L = 1.35 N/mm.

2.1.4 Heterogeneity of the strains in loaded conductor

a. Distributions of axial strains produced by the axial compression

Fig. 5.11 presents the distributions of the axial strain ε for ten different steps of the axial compression of the conductor (from 0 to -0.66 % applied strain). The colors stand for the successive steps of the computation. The most striking feature is the broadness of the

distributions. There is a great variability of possible strain due to the single axial compression of the cable. Moreover, the variability increases as the compression increases. For the reference thermal strain ε_a = -0.66 %, the distribution shows that the strands can locally sustain more that -1 % of compression and up to +0.3 % of tension, whereas the mean is equal to -0.41 %. This great variation result may lead to a reconsideration of the relevance of the smeared model for the description of the thermal induced strain of conductor by a single compressive value of strain. The broadness of the distributions shows that such description cannot be appropriate.

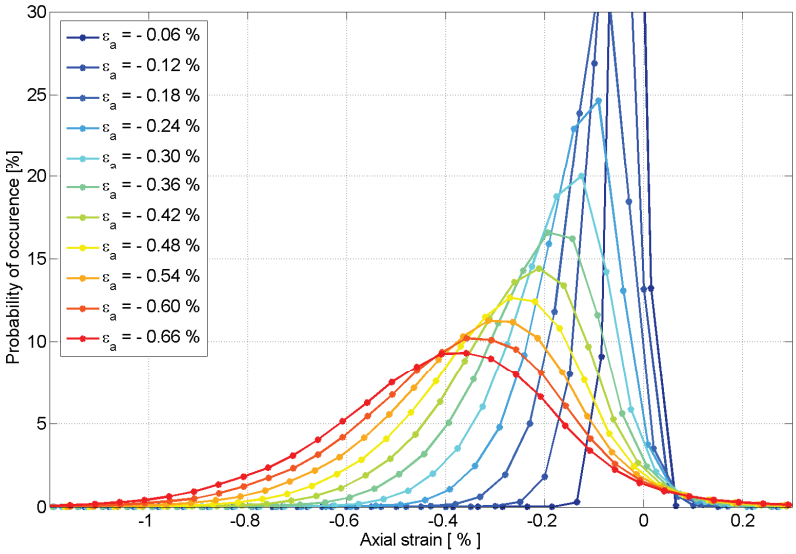

Fig. 5.11. Evolution of the axial strain distributions along the axial compression. The distributions become broader and broader as the axial compression increases.

b. Broadening of the axial strain distribution with the Lorentz loading

In the same way, the distributions corresponding to the application of the Lorentz forces from 0 to 1.7 N/mm at the reference thermal strain ε_a = -0.66 % are analyzed. In Fig. 5.12 a), the distributions are shown for 13 different steps of the computation. In b), a zoom on the highest positive strains, the tails of the distributions are shown. Unlike the axial compression, the Lorentz force loading does not affect much the aspect of the distributions. However, it induces an extra compression to the strands as illustrated by the progressive broadening of the distributions towards the negative and positive strains. In Fig. 5.12 b), it can be seen that the distribution tails, (for strains ranging from 0.3 % to 1.3 %), are remarkably impacted by the Lorentz loading. The percentage of values represented by these tails is rather low, with 0.34 % before and 1 % after F_L = 1.35 N/mm, but it already represents an increase of the number of points of factor 3 from 1539 to 4558 points. The question of the location of these critical tensile strains will be treated later.

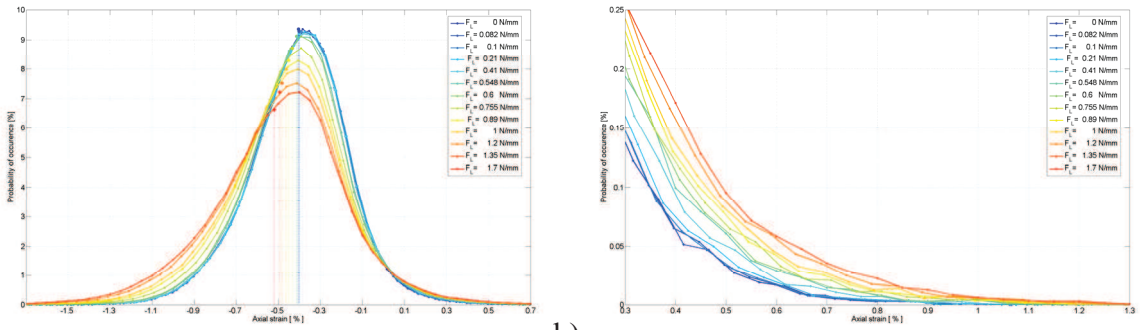

a) b)

Fig. 5.12. a) Evolution of the distribution of the local axial strains ε and their mean along the Lorentz loading (from 0 to 1.7 N/mm). The Lorentz forces cause extra compression of the strands. b) Evolution of the tails of the distributions (ε greater than 0.3%). The Lorentz forces raise the tensile strain on the strands by up to +1.3 % and induce extra compression by up to – 1.7 %.

c. Competition between pure compression and bending

During the axial compression of the cable inside the jacket, the strands can either compress or bend. As a result, the axial stiffness of the cable is logically lower than the strand material. Fig. 5.13 shows the computed global axial stress-strain curves of the conductor compared to the single strand behavior.

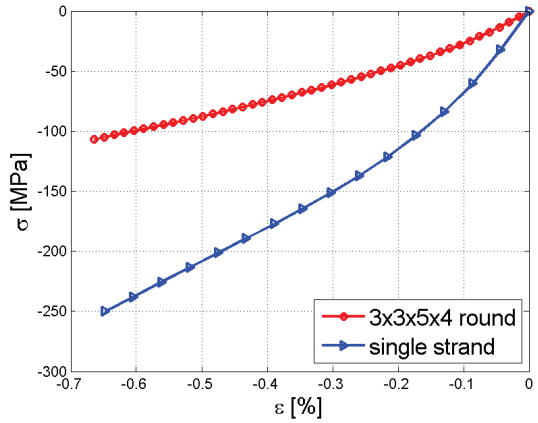

Fig. 5.13. Axial stress-strain curves of the 3x3x5x4 conductor and comparison with the single strand behavior. The axial stiffness of the cable is lower than the single strand due to the bending of the strands.

Fig. 5.14 a) illustrates the evolution of the mean axial strain $< \varepsilon >$ as a function of the applied strain. In order to quantify the competition between pure compression and bending, the mean value of the pure axial strains $< \varepsilon_0 >$ and the mean absolute value of the bending strains $< |\varepsilon_b| >$ are analyzed in the same way –see Fig. 5.14 b). The absolute value for the bending component is chosen since the mean is zero. On these two graphics, the standard deviation is plotted as the error bar. In Fig. 5.14 a), $< \varepsilon > = f (\varepsilon_{th})$ can be fitted by a linear function $< \varepsilon > = 0.62\ \varepsilon_{th}$. It indicates that, on average, only 62% of the applied compression is transmitted into pure compression to the strands. The rest is transmitted either into bending of the strands or into their transverse deformation by contact. In Fig. 5.14 b), the pink curve shows the increase of the bending with the loading. From the curves and for the reference axial compression $\varepsilon_{th} = -0.66\%$, one gets:

$< \varepsilon > = \ - 0.41\%$

$< |\varepsilon_b| > = \ 0.11\%$

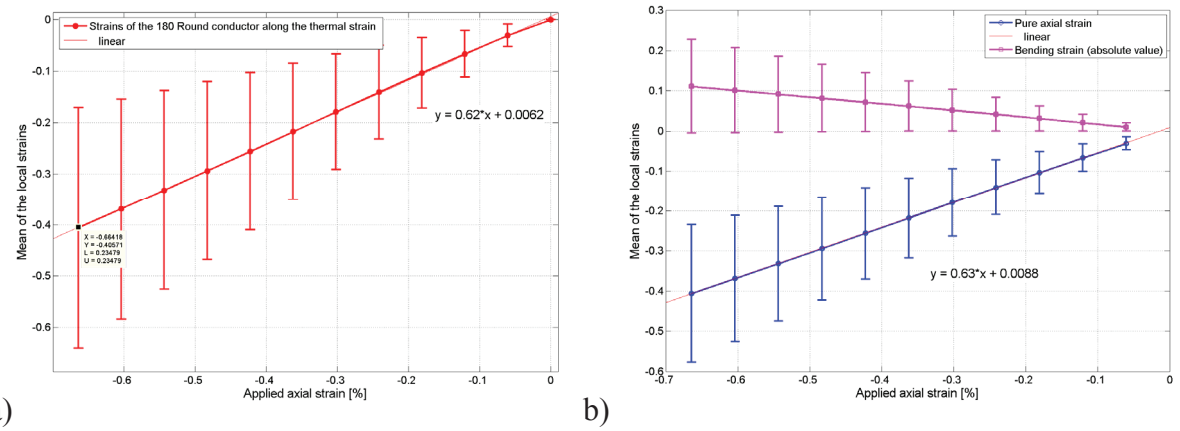

a) b)

Fig. 5.14. a) Evolution of the average axial strain value (< ε >) along the thermal axial compression for the 3x3x5x4 round conductor. A linear fit of the curve is shown with a slope of 0.62. b) Evolution of the average pure axial strains (< ε_0 >) and the average absolute value of the bending (ε_b). The error bars stand for the standard deviation.

In the same way, Fig. 5.15 a) and b) show the evolution of the mean strains as a function of the applied Lorentz force F_L. Unlike the axial compression, the evolution are not monotonic along the loading. If the mean axial strains are stable at the beginning, they suddenly decrease after F_L = 0.6 N/mm. In average, the Lorentz loading produces an extra axial compression of the strands – see < ε_0 > in Fig. 5.15 b). This effect can be understood by the fact that the axial displacements of the strands are locked at their ends by the boundary conditions. As a result, the strands cannot stretch themselves along the axial direction of the conductor as the forces globally push the cable in its transverse directions. The transverse displacements induced by the Lorentz loading are partly transmitted into local axial compression and partly into bending – see < $|\varepsilon_b|$ > increases in Fig. 5.15 b).

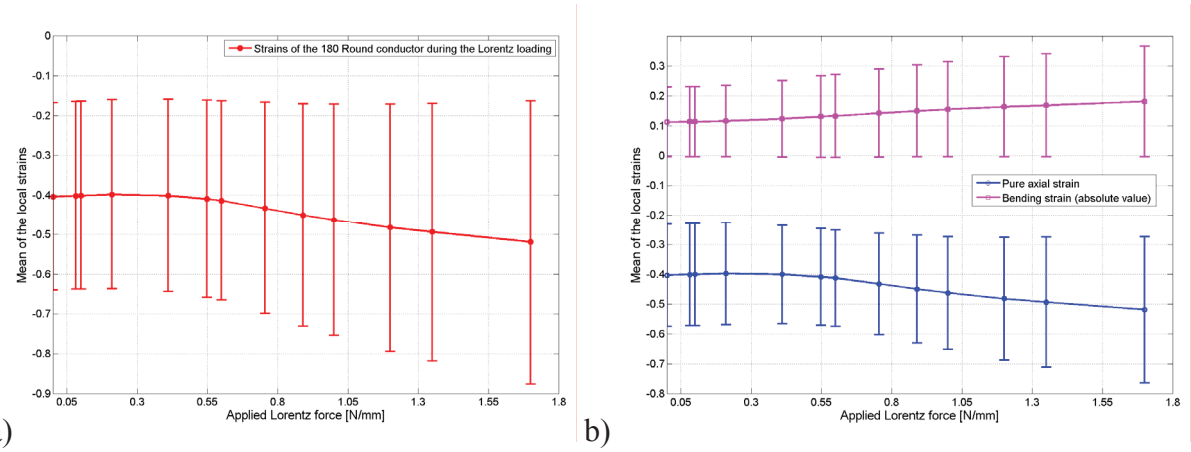

a) b)

Fig. 5.15. a) Evolution of < ε > along the Lorentz loading in the case of the 3x3x5x4 round conductor. b) Corresponding evolution of < ε_0 > and of <|ε_b|>.

In Fig. 5.16, the evolutions of the distributions of ε_0 and ε_b are observed along the axial compression. In Fig. 5.17, their evolutions along the Lorentz loading are presented. The ε_0 values are always negative and the distribution tails relative to ε_0 extends up to -1 %. In other words, a large part of the beam sections is sustaining compression. The bending strain can reach ± 0.6 % due to the sole -0.66 % applied axial compression. As already discussed, the Lorentz loading causes an extra compression of the strands and an increase of the bending.

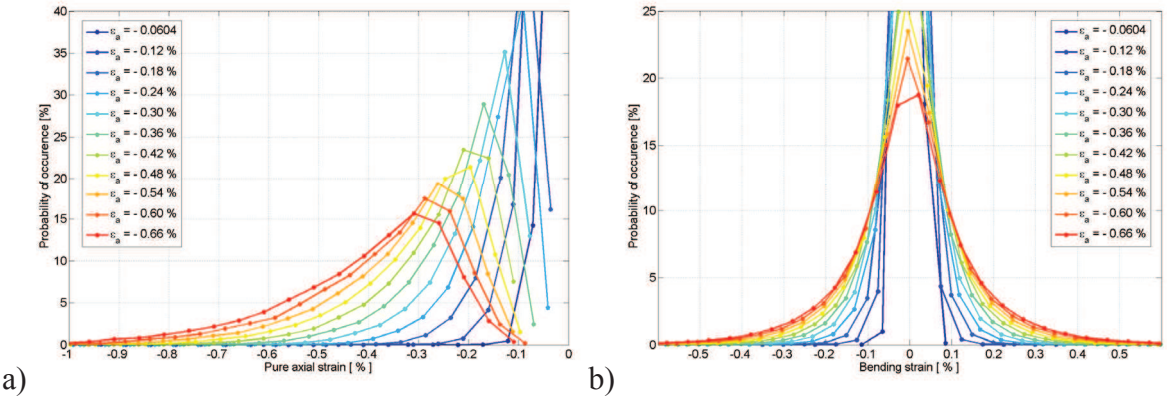

a) b)

Fig. 5.16. Evolution of a) ε_0 and b) ε_b along the steps of the axial compression up to -0.66%.

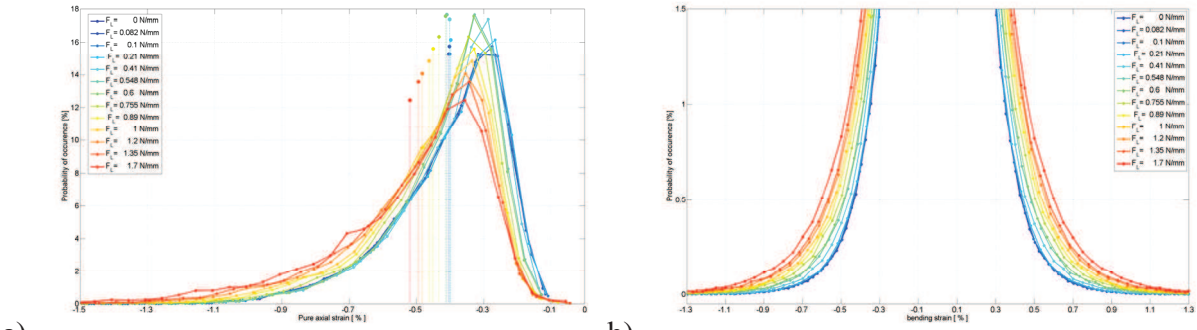

a) b)

Fig. 5.17. a) Evolution of a) ε_0 and b) ε_b along the steps of the Lorentz loading (from F_L = 0 to 1.7 N/mm).

2.2 Localization of the axial strains across the conductor section

2.2.1 The highest tensile strains are located at the core

The visualizations and the distributions have shown that the strains are not uniform in the conductor and that some points may present some critical tensile strain or high compression. However, it is still not clear where are the worse places for the strands to be in a cable in terms of these excessive strains. To answer this question, the strain maps representing either the average or the maximum of the axial strain quantities ε_0, ε_b, or ε_p, are used. These strain maps are obtained first by interpolating these quantities over cross-sections regularly distributed along the studied sample of conductor, and then by computing either the average or the maximum of these interpolated data along the axial directions. As result, 2D representations displaying the evolutions of maximum or average quantities in transverse directions are derived. The peak axial strain ε_p is the most representative strain regarding the filament breakage. For this reason the study will first focus on it. On the next four maps, the mean and the maximum of ε_p are presented before and after Lorentz loading. In Fig. 5.18, the mean values range from -0.7 % to +0.3 % (the zero is the orange color). In Fig. 5.19, the maximum values range from -0.3 % to +0.9 % (the zero is the light blue color).

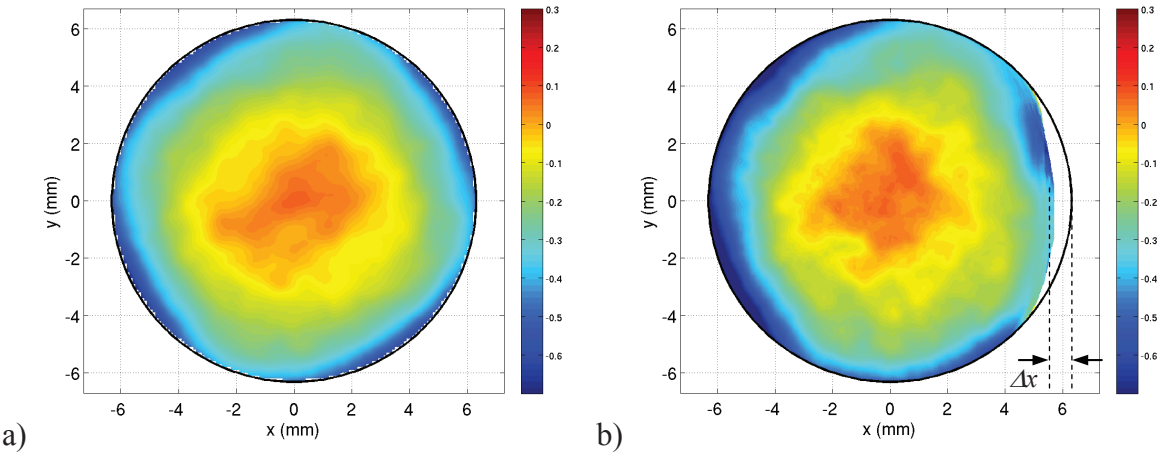

Fig. 5.18. Map of the *mean* peak strain ε_p. a) For ε_{th} = -0.66 %. b) For F_L=1.35 N/mm. The average peak strains calculated along the conductor axis are plotted at the interpolated positions (x, y) in the conductor cross-section.

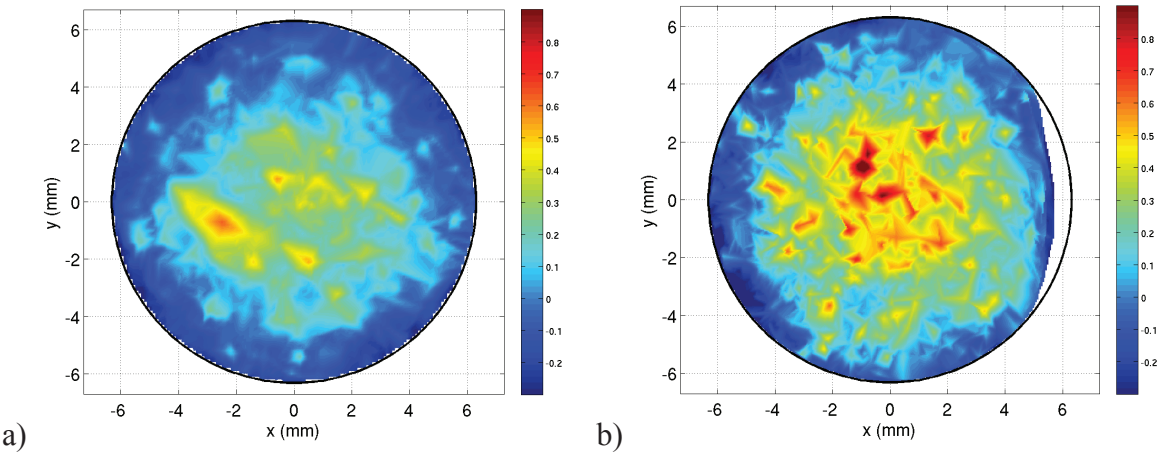

Fig. 5.19. Map of the *max* peak strain ε_p. a) For ε_{th} = -0.66 %. b) For F_L=1.35 N/mm. The maximum peak strains found along the conductor axis are plotted at their positions (x,y) in the cross-section.

The most important feature revealed by the plots is the non uniformity of the conductor's strain state across its section. The mean and the maximum peak strains increase from the outer periphery of the cable to its core. The maps prove that the strands are statistically sustaining more tensile strains at the core of the cable than at the periphery. At the core some points exhibit maximum peak strain greater than +0.6 %. The effect of the Lorentz loading causes a significant increase of the peak strains over the cross-section with amplified effect at the core. Some points of the strands can reach a maximum strain up to +0.9 %.

2.2.2 Maps of the pure compressive strain and the bending

In Fig. 5.20 and Fig. 5.21, the mean of the pure axial and bending components ε_0 and ε_b are presented. The compression, here ε_0, is higher at the periphery and gradually decreases toward the core of the conductor. But what was not obvious in Fig. 5.18 is the important influence of the Lorentz force loading on the strain state. The loading modifies the strain state introducing extra bending to the strands, as shown in Fig. 5.21 a) and b). The bending hardly exceeds +0.3% after the thermal compression in a very limited zone which greatly expands after the Lorentz force loading.

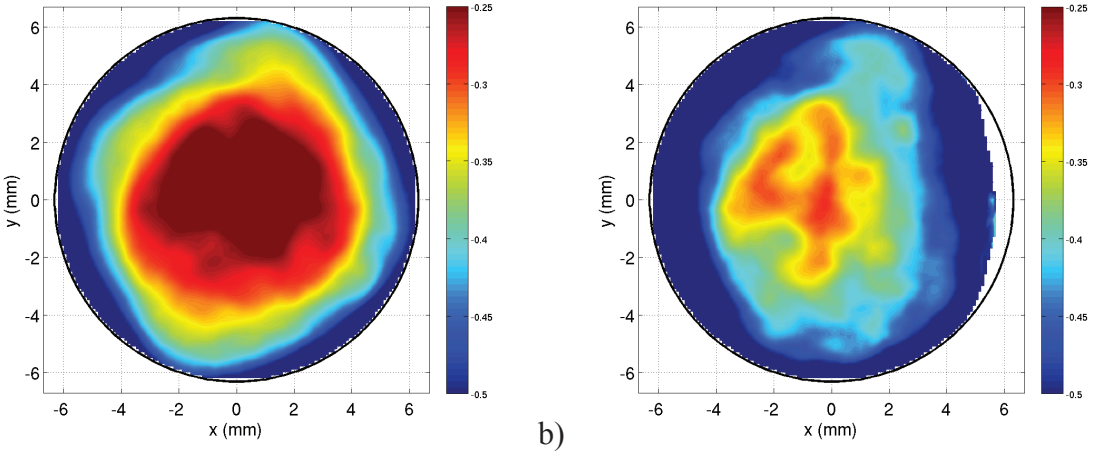

Fig. 5.20. Map of the *mean* ε_0. a) For ε_{th} = -0.66 %. b) For F_L = 1.35 N/mm. The strands are sustaining higher compression at the periphery compared to the core. The Lorentz forces increase the axial compression.

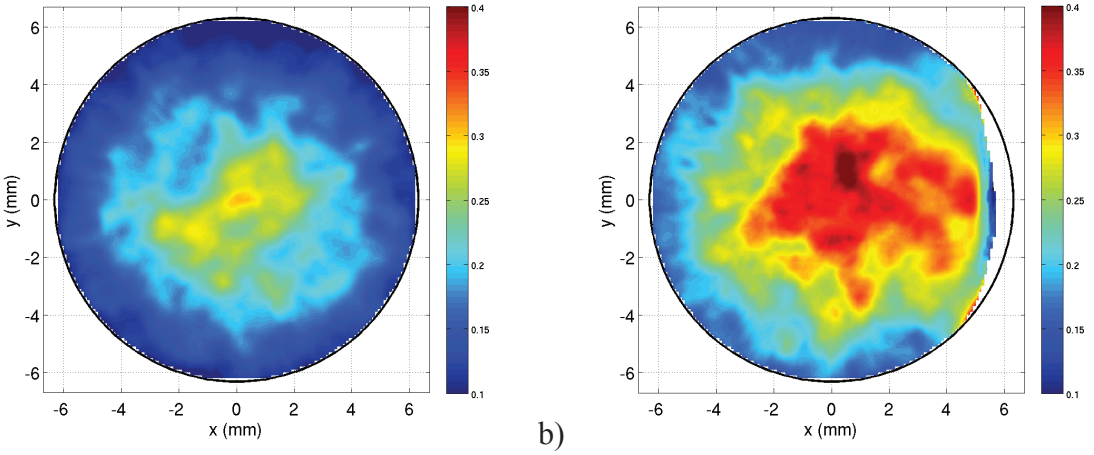

Fig. 5.21. Map of the *mean* ε_b. a) For ε_{th} = -0.66%. b) For F_L=1.35 N/mm. The strands show more bending at the core and the Lorentz force creates more bending.

In conclusion, the maps tend to show that the strands passing by the periphery of the cable are more likely sustaining pure compression whereas they probably experience more bending passing by the core. In anyway, the strain is not uniform through out the conductor section which could likely cause some current unbalance between the strands and thus possible current redistribution.

3 Evaluation of the critical strains along the strands

3.1 Evolution of the local peak strains along the strands

A complementary approach to the distribution of the axial strains and the strain maps is the plot of the peak strain along their curvilinear abscissa.

3.1.1 Effect of the Lorentz loading on the peak strains

In Fig. 5.22 a) and b), the maximum strains ε_p along the hundred and eighty strands of the conductor are shown before and after the Lorentz loading. The colors, all different, stand for

the strand number. Some peaks clearly pop out the average behavior both compressive and tensile. In that sense, there is an important effect of the Lorentz loading on the strains. Comparing Fig. 5.22 a) and b), it is visible that the number of strands seeing tensile strain greater than ε_c = 0.3 % is much greater after the Lorentz loading.

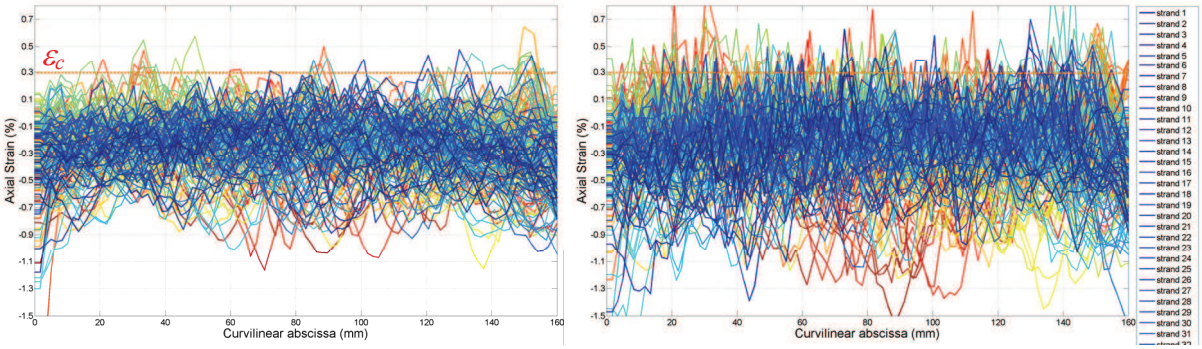

a) b)

Fig. 5.22. Peak strain ε_p along the strand for every strand. a) After the axial compression. b) After the Lorentz loading (F_L = 1.35 N/mm at ε_{th} = -0.66 %). Evidence of the effect of the Lorentz loading on the amplitude of the maximum strain.

Fig. 5.23 a) and b) show a zoom on the strains that range between 0.25 % and 0.9 %. After the sole thermal axial compression, some part of the filament region already presents strains greater than 0.3%. The Lorentz force generates both an increase of the maximum strains and a significant increase of the number of strands experiencing such strains. Along some strand, ε_p reach values greater than +0.9% for several different strands.

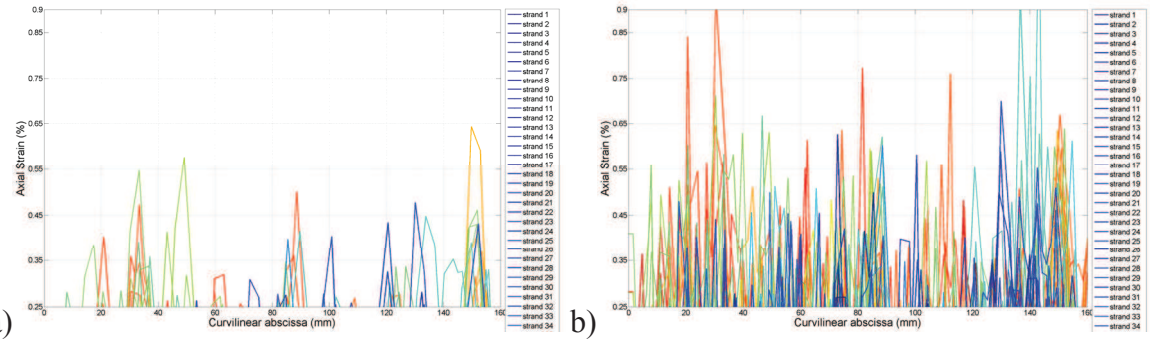

a) b)

Fig. 5.23. Evidence of the increase of the peak strains before (a) and after (b) the loading (F_L = 1.35 N/mm ε_a = - 0.66%). The variety of colors in b) indicates that numerous strands are seeing ε_p>0.3%.

3.1.2 Detailed analysis of selected strands

Fig. 5.24 a) and b) show the results for two strands that have been selected among others because they present particularly high peak strains. These are the strands 74 and 147. The blue curve represents ε_p (s) before the Lorentz force loading and the red one after. The curves show that the strain can be either released or amplified by the application of the Lorentz loading. On the one hand, for the strand #74, the strain located between 85 and 95 mm is ε_p = +0.2 % before but decrease to 0% after loading. On the other hand, between 115 and 155mm (black arrows), ε_p dramatically increases up to +0.9 %. The same remark can be made for the strand 147 which sees several times a critical strain along its length (at 60, 85, 110 and 147 mm). The evolution of the strain along the strands do not present regular pattern and it would be hard to derive an 'average' bending wave length as assumed by some other models

[Nijhuis 2008], [Zhai 2008]. The evolution should be now linked with the current transfer typical length in later work.

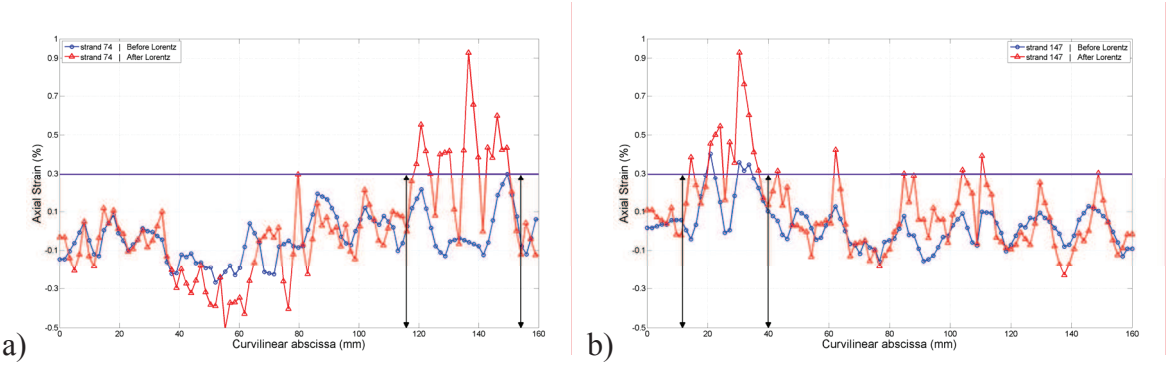

Fig. 5.24. Peak strain along the strands 74 and 147 before and after the Lorentz loading. The Lorentz loading amplifies the peak strains. ε_p can reach +0.3% at several points along the strands (indicated by the black arrows).

With the help of the $\varepsilon(s)$ curve and the visualization, it is possible to quickly target the part of strands concerned by the critical events. As an example, the set of pictures in Fig. 5.25 and Fig. 5.26 exposes the state of the strands #74 and #147 before any loading, after the thermal compression and after the Lorentz loading. For clarity, the strand cross sections are shown. There is an apparent rotation of the location of the maximum strains reflecting the variety of possible bending orientations. The impacted parts of strand can extend over few millimeters The bending phenomenon is three dimensional which is of great concern since the filaments inside are twisted.

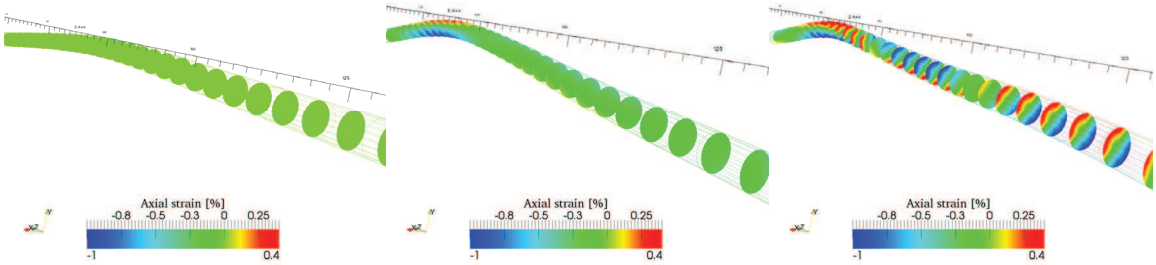

Fig. 5.25. Visualization of the strand 74 in between 115 and 155 mm along the cable axis.

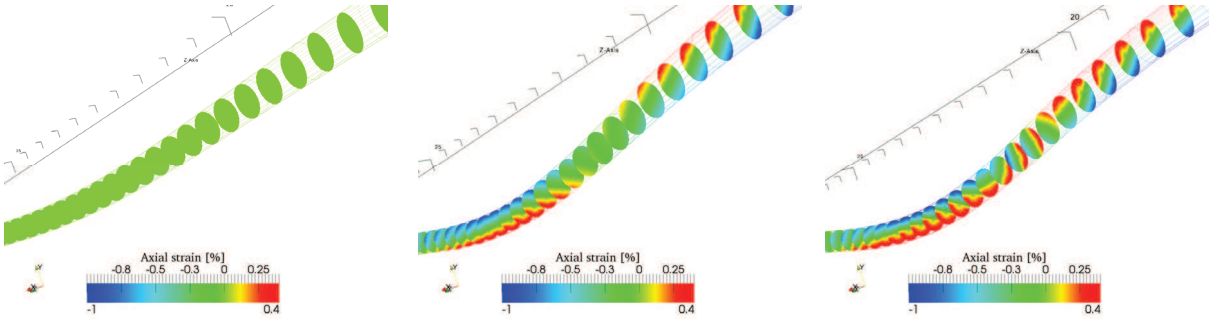

Fig. 5.26. Visualization of the strand 147 in between 15 and 40 mm along the cable axis.

3.1.3 The strands passing by the core of the conductor

In order to understand why the events seem to go wrong at these precise places, it is proposed to look at the strand bundles composed of the strands 73-74-75 at the abscissa comprised

between 115 and 155 – see Fig. 5.27. The simulation shows that the conductor cross-section particularly 'opens' there after the thermal compression.

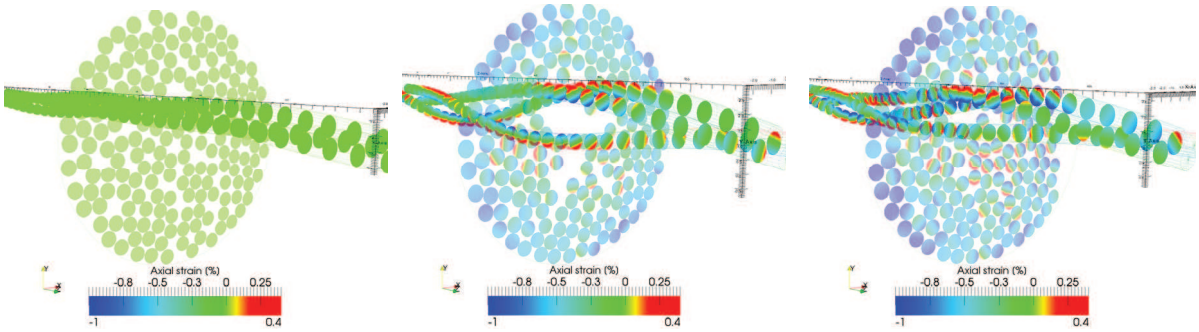

Fig. 5.27. Evidence of important bending at the "open" sections for the bundle that contains the strand 73-74-75.

In the same way, the strands 145 and 147 are more carefully observed at s=30mm. The pictures in Fig. 5.28 show that the strands pass by the core the conductors at this abscissa but the cable section is not particularly open there. The comparison between strands #74 and #147 indicates that high bending strains produced at the core of the conductor are not necessarily related to a local opening of strands.

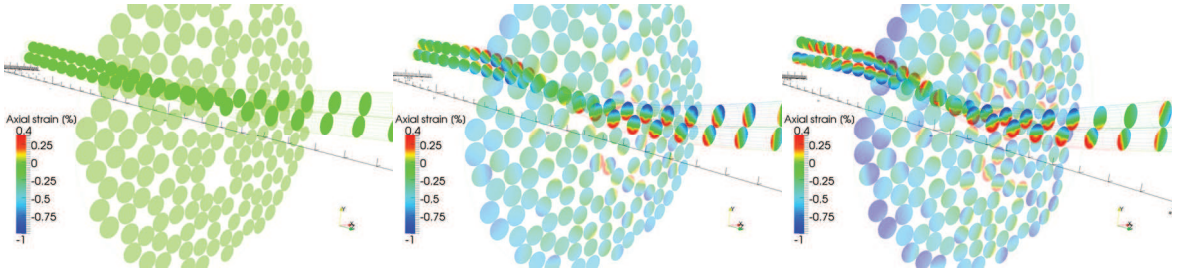

Fig. 5.28. Evidence of important bending of strands passing by the core of the conductor for the bundle that contains the strands 145-147(section at L=30mm).

3.2 Critical strains and number of damaged strands

3.2.1 Introduction of a crack criterion

Using dedicated Matlab routines, it is possible to select the strands of interest that have at least once along their length a maximum strain greater than a critical value ε_c. These precise strands are referred to now as the 'impacted strands' whereas the others are referred to as the 'clean strands'. The parameter ε_c may be a crack criterion set by the user. For this analysis, the reference ε_c is set to 0.3% in accordance to micrographic measurement on OST2 superconducting strand at 4.2 K [Jewell 2008].

3.2.2 Evolution of the number of damaged strands

In Fig. 5.29 a) and b), the colored lines are relative to the impacted strands and the grey lines to the clean ones. Their maximum strains are plotted before a) and after b) the Lorentz loading. The impacted strands are counted. 17.8 percent of the strands display at least one maximum strain greater than ε_c on the studied length after the thermal compression, and this proportion increases to 55.6 percent after the Lorentz loading. This means that after $F_L = 1.35$

N/mm, more than half of the strands are sustaining a critical strain at at least one point of their filament region.

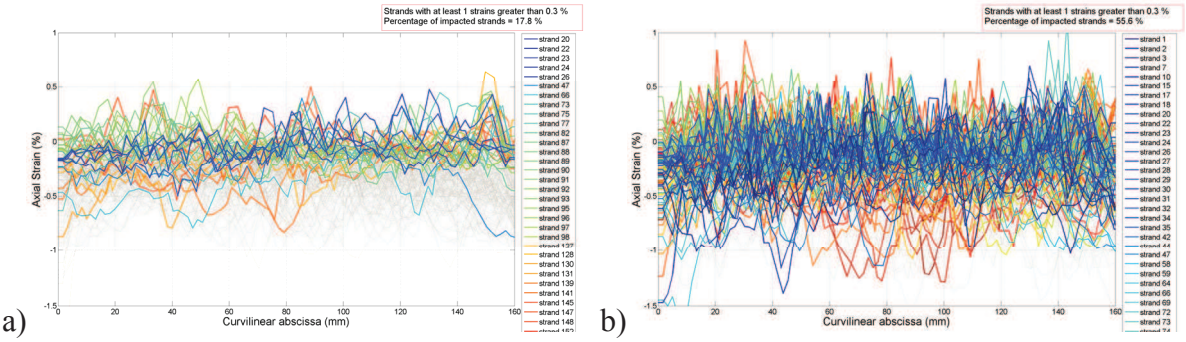

Fig. 5.29. a) After the thermal strain 17.8% of the strands see at least one time along their length a critical strain greater than 0.3%. b) It concerns 55.6% of the strands after the Lorentz loading.

If the ε_c is switched to +0.5 % and if a new condition is set, stating that at least two consecutive critical events should be registered along the length to be 'impacted', then one gets only one impacted strand after the thermal strain and 23 strands (12.8 %) after the Lorentz loading. The graphics in Fig. 5.30 present the result.

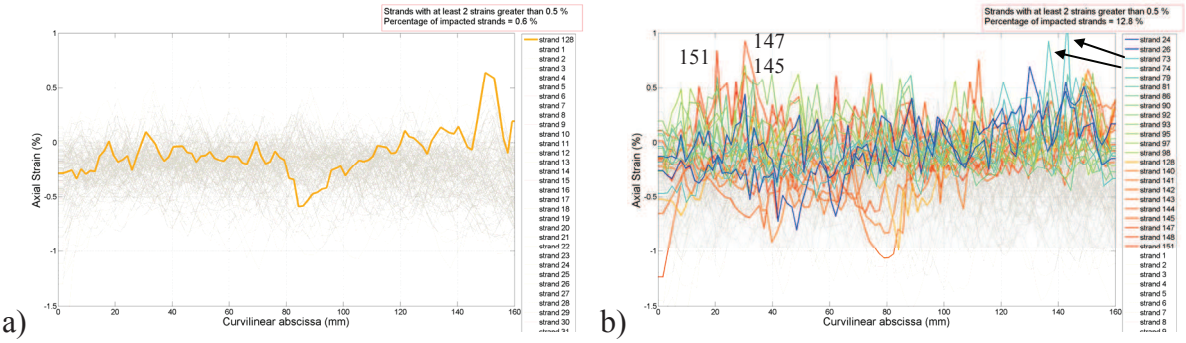

Fig. 5.30. a) After the thermal strain, only one strand see at least two times along its length a critical strain, saying greater than 0.5 %. b) These are 12.8 % of the strands after the Lorentz loading.

In order to clarify the situation, another graphic is used. By the means of stem representation, the number of critical events per strand is plotted. The clean strands get 0 in ordinate whereas the impacted strands get the number of times ε_p overrun ε_c. The results are presented in Fig. 5.31, with ε_c = +0.3%. The increase of the critical strain occurrence is clearly observed (from 17 to 55% of the strands are impacted after F_L = 1.35 N/mm).

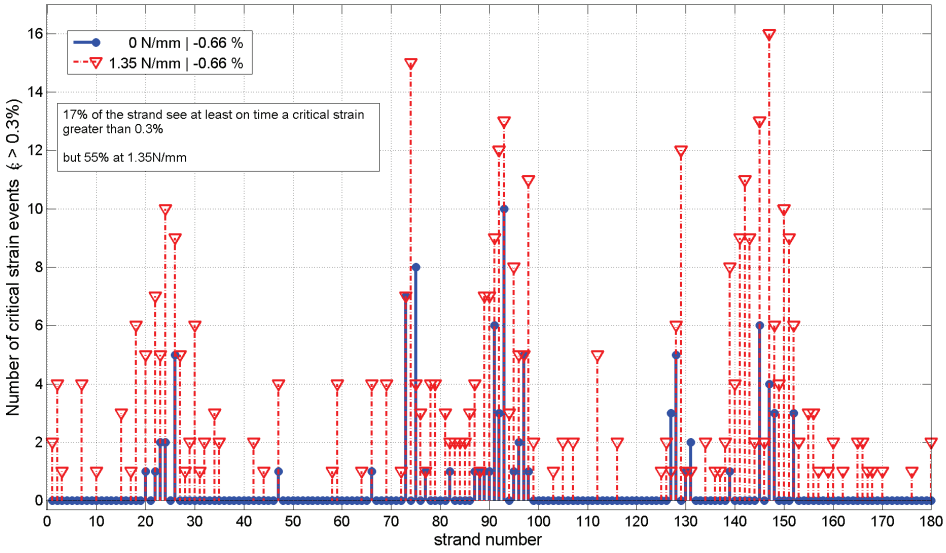

Fig. 5.31. Evolution of the number of critical events (ε_p > 0.3 %) before and after the application of the Lorentz loading.

The plot shows that some strand bundles are almost not impacted by any critical events. This is the case for example for the strands 48 to 57 or the strands 117 to 124. By the way, there are also bundles that are more particularly critical, e.g. the strands 15 to 35, 72 to 99 and 138 to 152. The reason of this is later discussed. Fig. 5.32 presents the percentage of impacted strands that increases with the Lorentz loading (F_L from 0 to 1.7 N/mm).

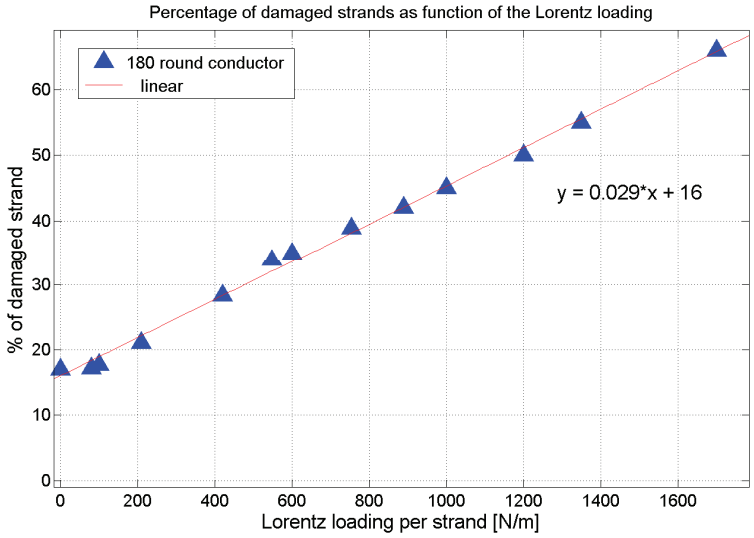

Fig. 5.32. Linear evolution of the number of impacted strands (ε_p > +0.3 %) as a function of the Lorentz force loading.

3.3 A determination of the cracked area

In this paragraph, a method to evaluate the damaged area of the Nb_3Sn filament region is presented. Depending on the value of the local strains (ε_0 and ε_p) measured at each beam section and according to a crack initiation criterion, here chosen equal to ε_c = +0.3 %, the area of the damaged zone can be derived.

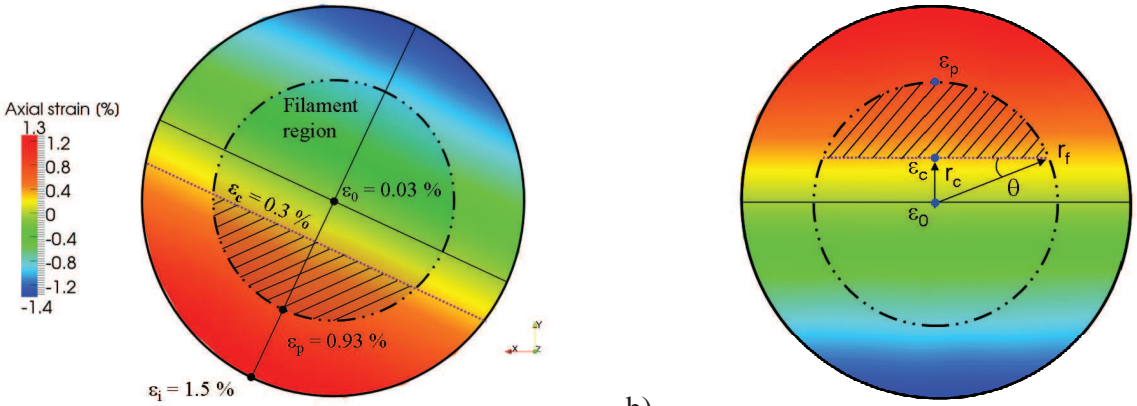

a) b)

Fig. 5.33. a) View of the cross-section of the strand 147 at L=31mm. Illustration on the filament region (light gray) of the critical strain limit and the damaged zone (hatched area). b) Parameters for the determination of the damaged area.

In order to calculate the damaged area S_d illustrated by the hatched area in Fig. 5.33, the parameter r_c should be calculated knowing the critical strain ε_c, the strain measured at the neutral axis ε_0 and at the maximum strain found around the outer filament perimeter ε_p. It reads:

$$r_c = r_f \left(\frac{|\varepsilon_c - \varepsilon_0|}{|\varepsilon_p - \varepsilon_0|} \right) \qquad \textbf{eqn. 5.5}$$

$$S_d = 2 \cdot \left[\frac{\pi}{4} r_f^2 - \left(\frac{\theta}{2} r_f^2 + \frac{1}{2} r_c \sqrt{r_f^2 - r_c^2} \right) \right] \qquad \textbf{eqn. 5.6}$$

with,

$$\theta = \sin^{-1} \left(\frac{r_c}{r_f} \right) \qquad \textbf{eqn. 5.7}$$

The relation should be modified in case the strain ε_0 is greater than ε_c. In that case, more than a half of the section is damaged and it is easier to just remove the clean area instead. It yields:

$$S_d = \pi r_f^2 - 2 \cdot \left[\frac{\pi}{4} r_f^2 - \left(\frac{\theta}{2} r_f^2 + \frac{1}{2} r_c \sqrt{r_f^2 - r_c^2} \right) \right] \qquad \textbf{eqn. 5.8}$$

The procedure can be repeated for all strand sections. The corresponding distributions relative to the impacted section of the strands, before and after Lorentz loading, are presented in Fig. 5.34. This graphics shows a significant increase of the damaged area with the Lorentz loading. The damaged areas extend up to 29 % of the total filament region with an average of 4 %. However, the twist of the filaments inside the strands may imply a more complex approach to estimate the loss of the superconducting area.

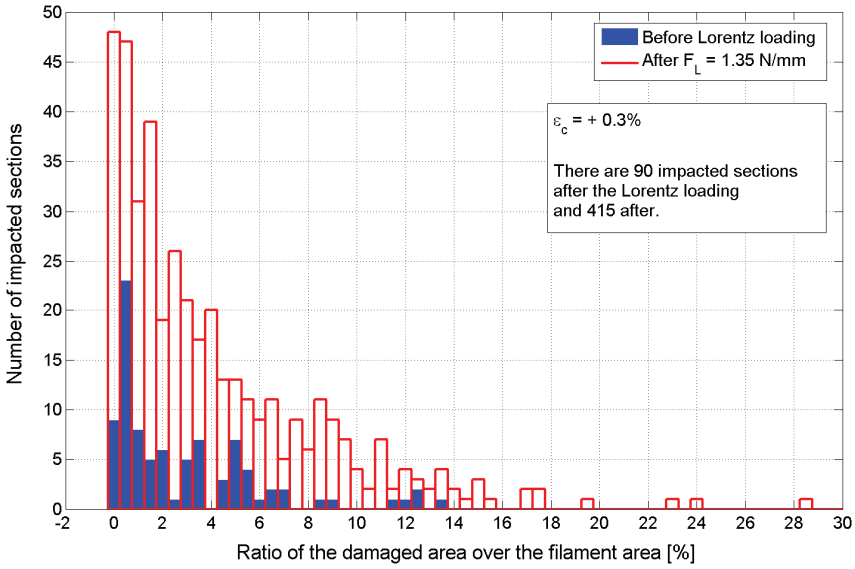

Fig. 5.34. Distribution of the ratio damaged area / filament region area. The damaged area goes up to 28.5% with a mean of 4.1% after the Lorentz loading.

4 Influence of the conductor design and operating conditions

The computations show that the model of conductors is able to handle various configurations of cable even using the orthotropic elasto-plastic behavior with friction consideration. The results of the complete simulation of the conductors described in Chapter II are presented in the next set of pictures – see Fig. 5.35. The following work proposes to compare those cables to one another.

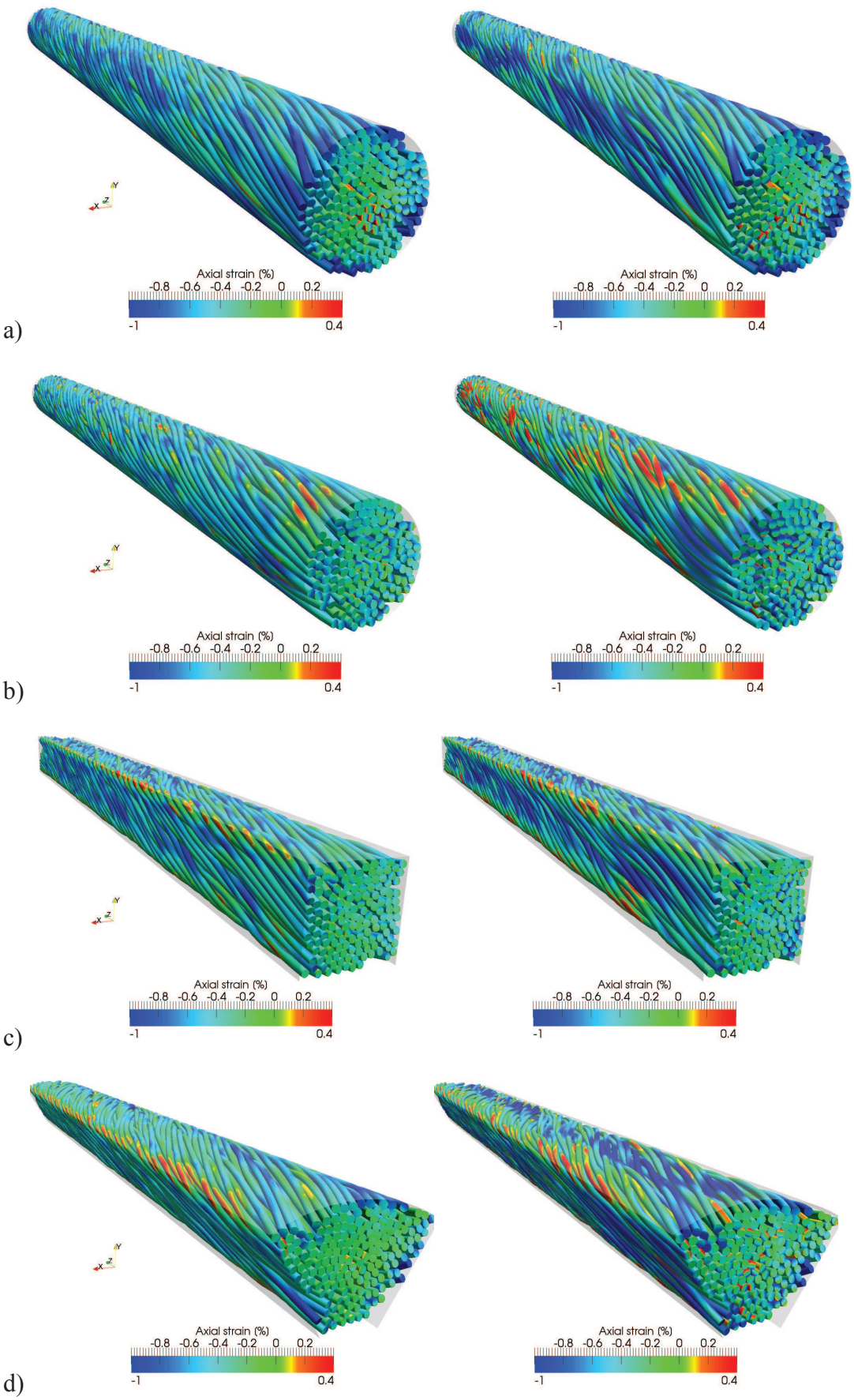

Fig. 5.35. Global visualisation of the simulation results for the four modelled conductors after the axial compression ε_{th} = -0.66 % and after the Lorentz loading F_L = 1.35 N/mm.

4.1 The cabling pattern

The purpose of the comparison of the 144 strand with the 180 strand cable is more about quantifying the effect of a change in the cabling pattern from 3x3x4x4 to 3x3x5x4 than a simple increase of the number of strands. For these two samples, the axial strain distributions are shown in Fig. 5.36. On these curves, notable effect is already visible. On the one hand, the 3x3x5x4 cabling pattern tends to exhibit extra compression compared with the 3x3x4x4 pattern and the mean values are respectively -0.49 % and -0.42 %. On the other hand, the tensile part is lower in the 3x3x5x4. The percentage of points in the structure that exhibit axial strain greater than 0.3 % is 0.15 % in the 3x3x5x4 conductor and 0.2 % in the 3x3x4x4 conductor.

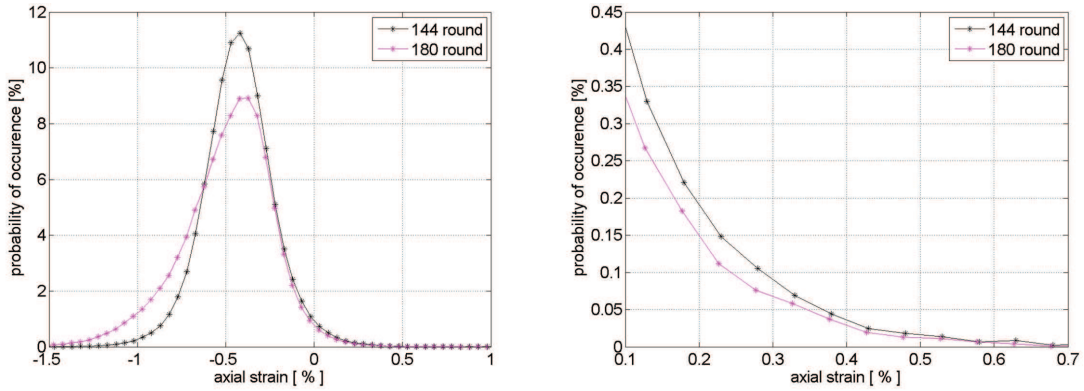

Fig. 5.36. Comparison between the 3x3x4x4 conductor and the 3x3x5x4 conductor. Distribution of the axial strain ε after both thermal and Lorentz loadings (ε_{th} = -0.66 % & F_L = 1.35 N/mm).

The different map relative to the peak strain, ε_p, the strain at the neutral axis ε_0 and the bending strain ε_b are presented in Fig. 5.37 to Fig. 5.39. After the axial loading, the compression at the periphery of the cable and the tension at its core are both amplified in the 3x3x5x4 compared to 3x3x4x4. After the Lorentz loading, F_L = 1.35 N/mm, the occurrence of the gap at the low pressure zone is almost non-existent for the 3x3x4x4 whereas reaches about 1mm in the 3x3x5x4 conductor. The maps of the maximum peak strain indicate that the highest strains are found in the 144 strand cable with almost only positive maximum strains. The highest strains localize at the low pressure zone and at the core in the 3x3x4x4 whereas only at the core in the 3x3x5x4.The Lorentz force increases the pure compression at the low pressure side in the 3x3x5x4 but decreases it in the 3x3x4x4. For the rest of the cross-section, the Lorentz force lowers the pure axial strains in both cases. The pure bending strains ε_b are lower in the 3x3x5x4 conductor than in the 3x3x4x4 after both the axial strain and the Lorentz loading. To conclude, it seems that a change in the cabling pattern produces non negligible effect on the strain state of the conductors. The different plots show that the 3x3x4x4 pattern allows more bending than the 3x3x5x4 and produces less homogeneous local strain maps. The highest peripheral compression in the 3x3x5x4 seems to protect against the effect of the Lorentz loading on the occurrence of tensile strain at the low pressure zone. It would be delicate to determine which of these two patterns is mechanically the best. Regarding the criterion of critical tensile strains, the 180 strand cable appears better than the 144 strand.

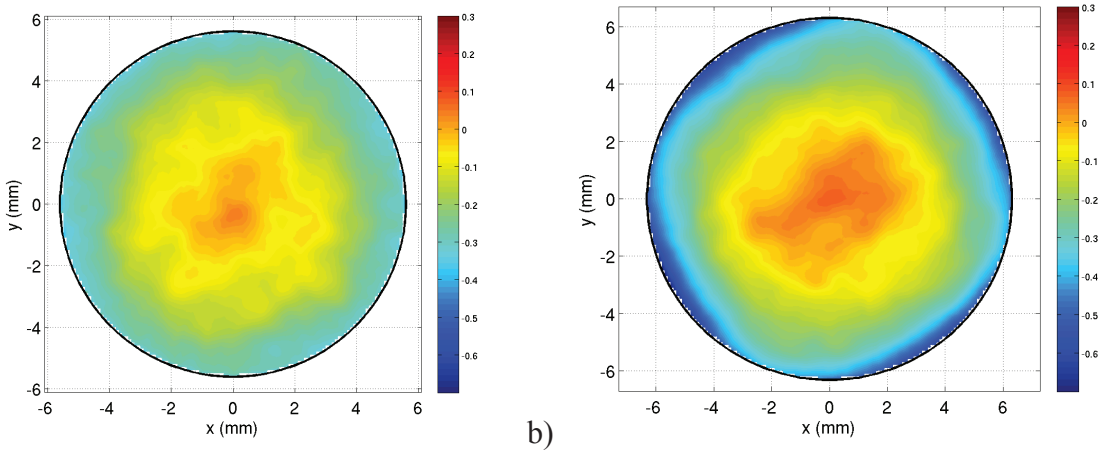

a) b)

Fig. 5.37. Map of the *mean* peak strain ε_p after the reference thermal strain ε_{th} = -0.66 %. a) 3x3x4x4. b) 3x3x5x4.

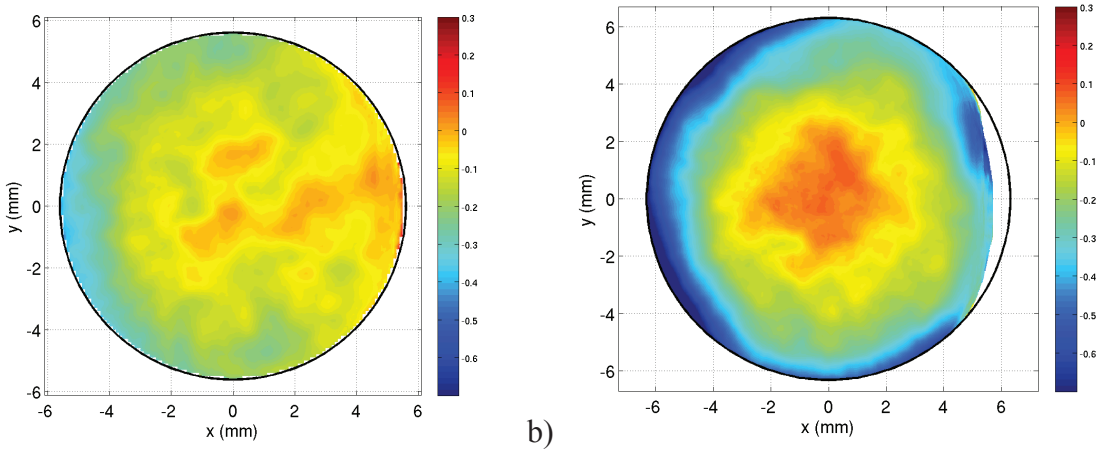

a) b)

Fig. 5.38. Map of the *mean* peak strain ε_p after the reference Lorentz loading F_L=1.35 N/mm. a) 3x3x4x4. b) 3x3x5x4.

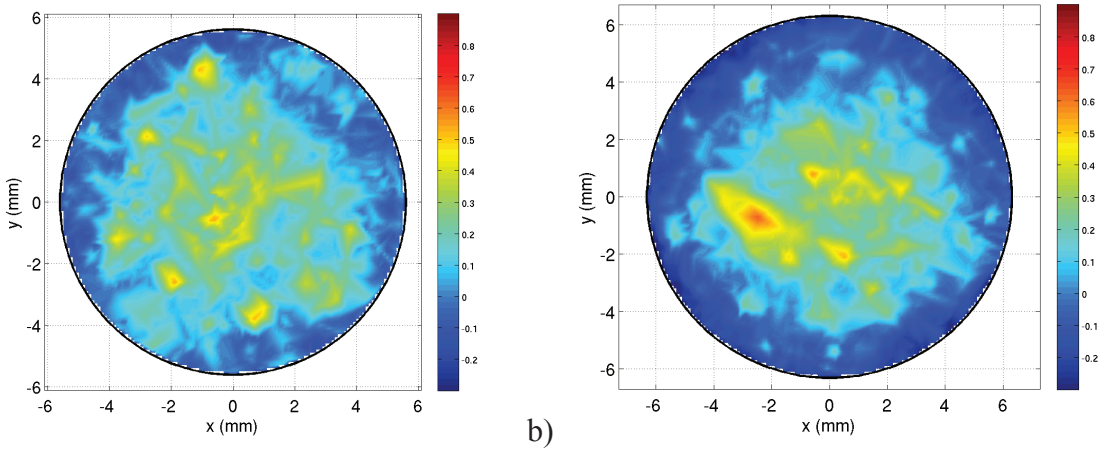

a) b)

Fig. 5.39. Map of the *max* peak strain ε_p after the reference thermal strain ε_{th} = -0.66 %. a) 3x3x4x4. b) 3x3x5x4.

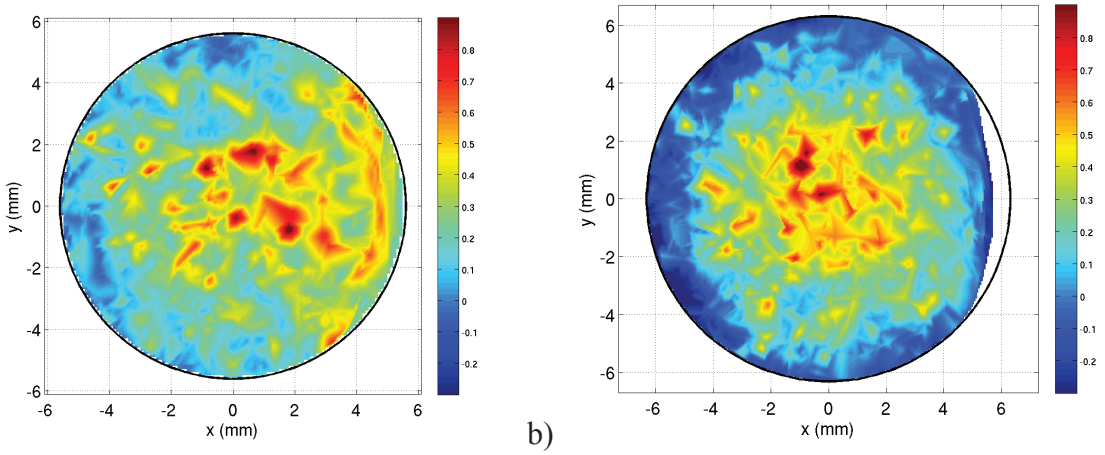

Fig. 5.40. Map of the *max* peak strain ε_p after the reference Lorentz loading F_L=1.35 N/mm. a) 3x3x4x4. b) 3x3x5x4.

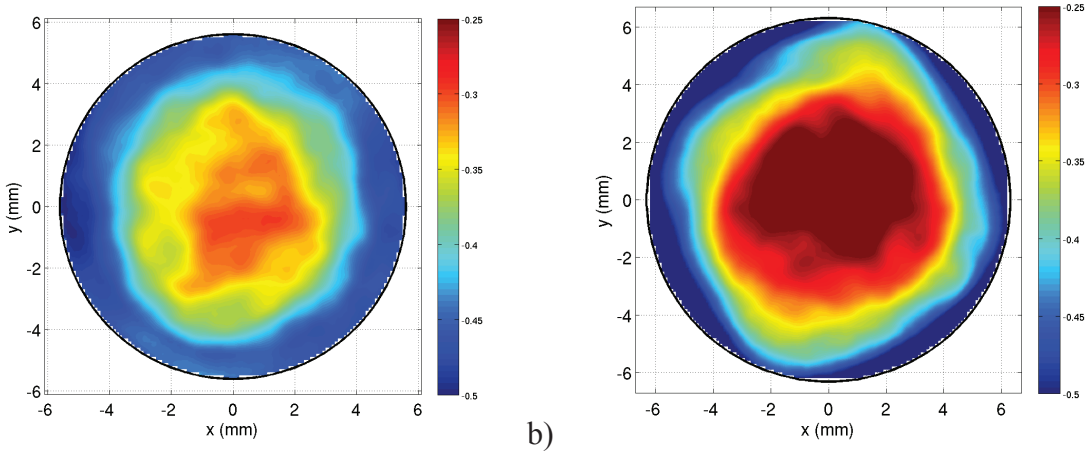

Fig. 5.41. Map of the *mean* pure axial strain ε_0 after the reference thermal strain ε_{th} = -0.66 %. a) 3x3x4x4. b) 3x3x5x4.

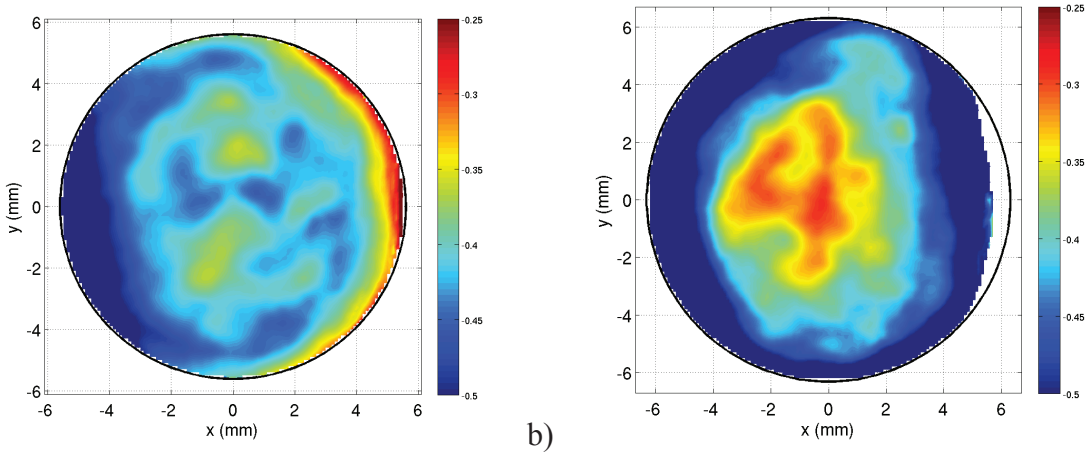

Fig. 5.42. Map of the *mean* pure axial strain ε_0 after the reference Lorentz loading F_L=1.35 N/mm. a) 3x3x4x4. b) 3x3x5x4.

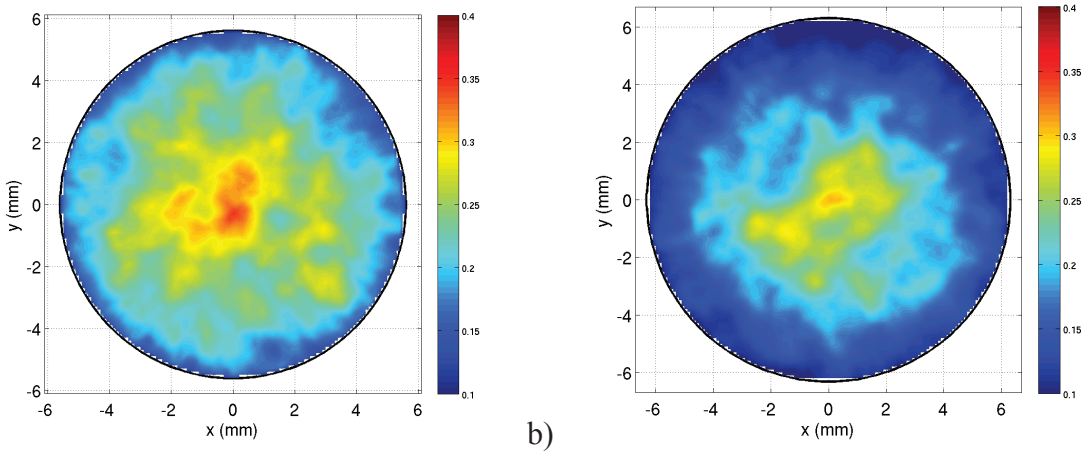

Fig. 5.43. Map of the *mean* pure bending strain ε_b after the reference thermal strain ε_{th} = -0.66 %. a) 3x3x4x4. b) 3x3x5x4.

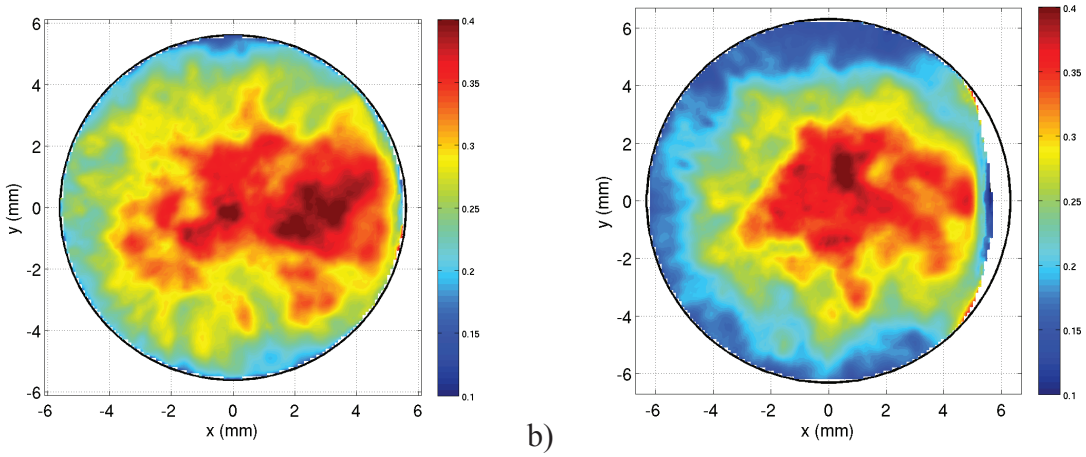

Fig. 5.44. Map of the *mean* pure bending strain ε_b after the reference Lorentz loading F_L=1.35 N/mm. a) 3x3x4x4. b) 3x3x5x4.

4.2 The shape of the conductor

4.2.1 Round versus petal

In this paragraph, the round and petal conductor are compared. It is reminded that the petal-like conductor gets slightly higher void fraction so that not only the shape is here tested. The distributions are presented in Fig. 5.45 and the corresponding *mean* values are respectively -0.49 % and -0.38 %. The percentage of values greater than 0.3 % are 0.15 % and 0.24 %.

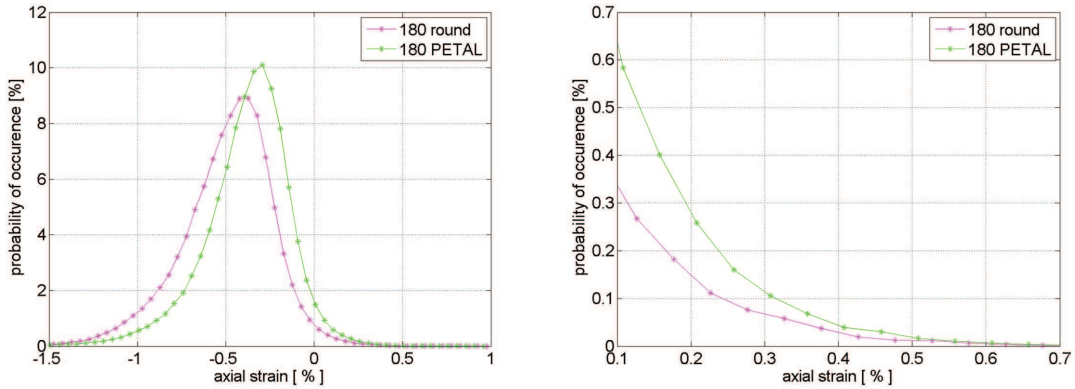

Fig. 5.45. Comparison between the 180 round conductor and the 180 petal conductor. Distribution of the axial strain ε after both thermal and Lorentz loadings (ε_{th} = -0.66 % & F_L = 1.35 N/mm).

In Fig. 5.46 to Fig. 5.49, the maps of the local strains tend to show that the strands are locally more compressed in the round conductor. Due to higher void fraction, the strands have more room to move and the strains in the petal conductor are in average higher than in the round conductor. Moreover, the interesting feature with the petal conductor is the localization of high bending strain at the corners.

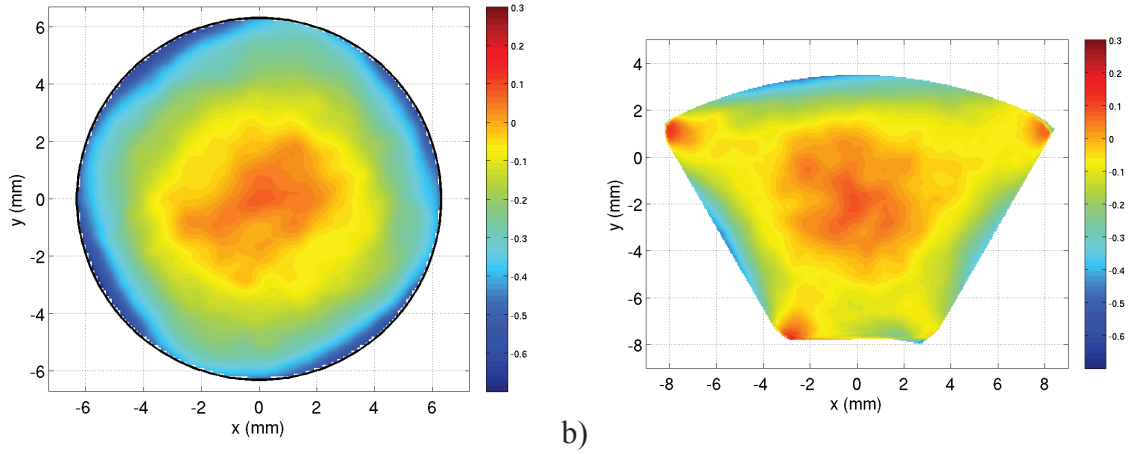

a) b)

Fig. 5.46. Map of the *mean* peak strain ε_p after the reference thermal strain ε_{th} = -0.66 %. a) Round (3x3x5x4). b) Petal (3x3x5x4).

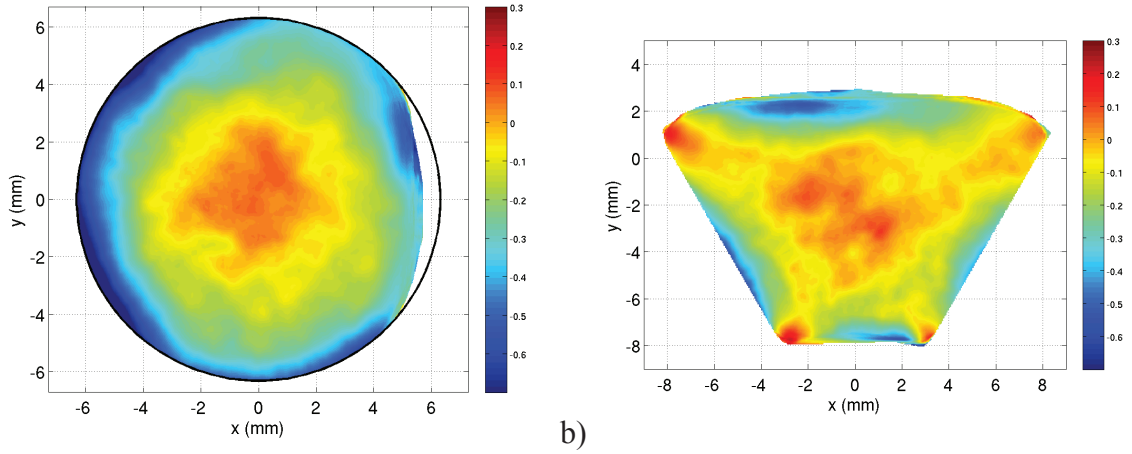

a) b)

Fig. 5.47. Map of the *mean* peak strain ε_p after the reference Lorentz loading F_L=1.35 N/mm a) Round (3x3x5x4). b) Petal (3x3x5x4).

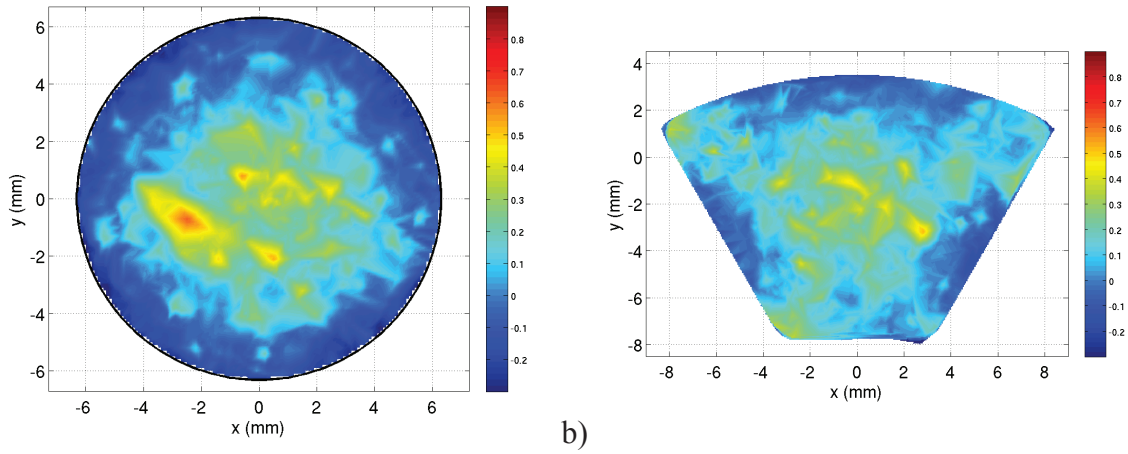

Fig. 5.48. Map of the *max* peak strain ε_p after the reference thermal strain ε_{th} = -0.66 %. a) Round (3x3x5x4). b) Petal (3x3x5x4).

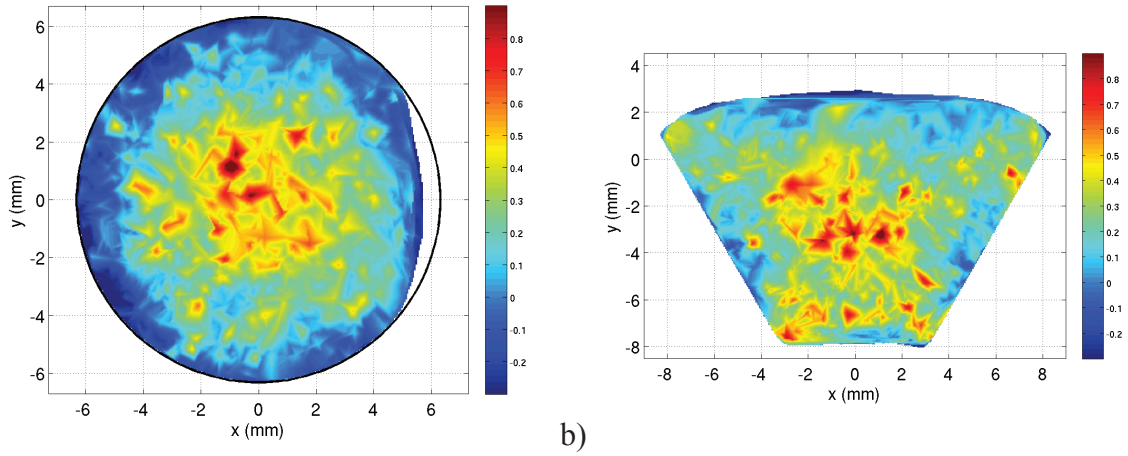

Fig. 5.49. Map of the *max* peak strain ε_p after the reference Lorentz loading F_L=1.35 N/mm along the x direction. a) Round (3x3x5x4). b) Petal (3x3x5x4).

4.2.2 Round versus square

In this paragraph, two conductors are compared that only differ by their shape from round to square cross-section. The distributions in Fig. 5.50 are similar and the means are respectively -0.42 % and -0.43 % for the round and the square conductor. However, the tails point at highest tensile strains in the case of the round conductor. The percentage of points in the structure that exhibits axial strain greater than 0.3 % is 0.2 % in the case of the round conductor and 0.06 % in the case of the square conductor. That is to say a factor 3 between both.

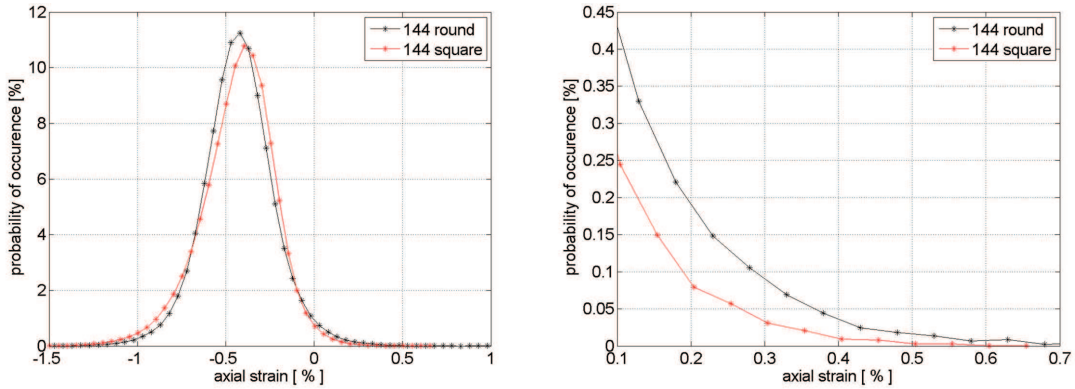

Fig. 5.50. Distribution of the axial strain ε after both thermal and Lorentz loadings (ε_{th} = -0.66 % & F_L = 1.35 N/mm). Comparison between the 144 round conductor and the 144 square conductor.

In Fig. 5.51 to Fig. 5.52, the different maps show that the square conductor tends to exhibit a localization of the strain at the corners and at the core. The effects of the Lorentz forces are very limited in this conductor compared to the round conductor. The square conductor displays much less critical strains than the round conductor. From a mechanical standpoint, the different graphics tend to show that square aspect ratio is more beneficial than round one when same twist pitch and void fraction are used. This is a noteworthy result that corroborates the actual good electrical behavior of existing square *CICC* compared with round one that seems not to degrade with electromagnetic cycles [Bruzzone 2006], [Miller 2003].

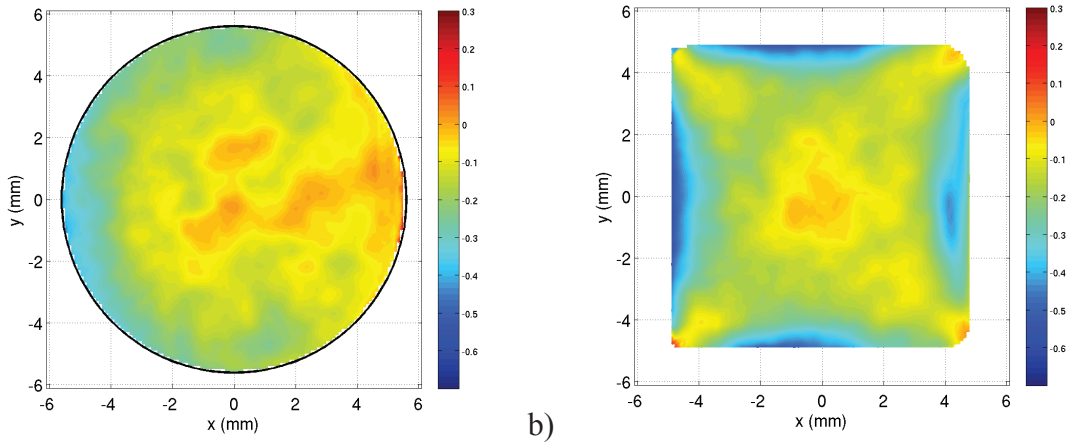

a) b)

Fig. 5.51. Map of the *mean* peak strain ε_p after the reference Lorentz loading F_L = 1.35 N/mm a) Round (3x3x4x4). b) Square (3x3x4x4).

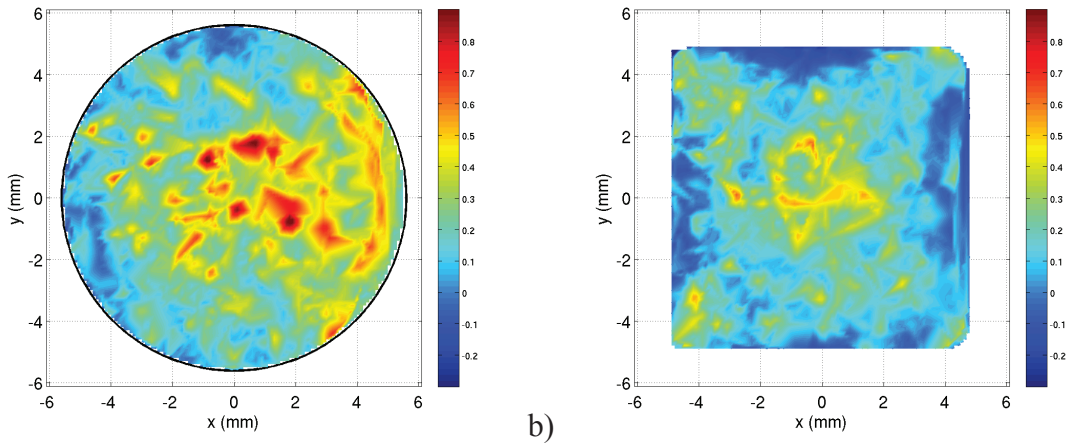

a) b)

Fig. 5.52. Map of the *max* peak strain ε_p after the reference Lorentz loading F_L = 1.35 N/mm a) Round (3x3x4x4). b) Square (3x3x4x4).

4.3 The effect of two different axial compressions

In this paragraph, the same conductor is tested with two different axial compressions of ε_{th} = -0.38 % and ε_{th} = -0.66% before the Lorentz force loading. The purpose here is to determine whether the initial strain state of the strands influences the mechanical behavior of the cable. The distributions are presented in Fig. 5.53 and the corresponding *mean* values are respectively -0.42 % and -0.29 %. The most striking effect that is here observed is that the distribution queues are very similar. In fact, the percentage of values greater than 0.3 % is 0.21 % in both cases.

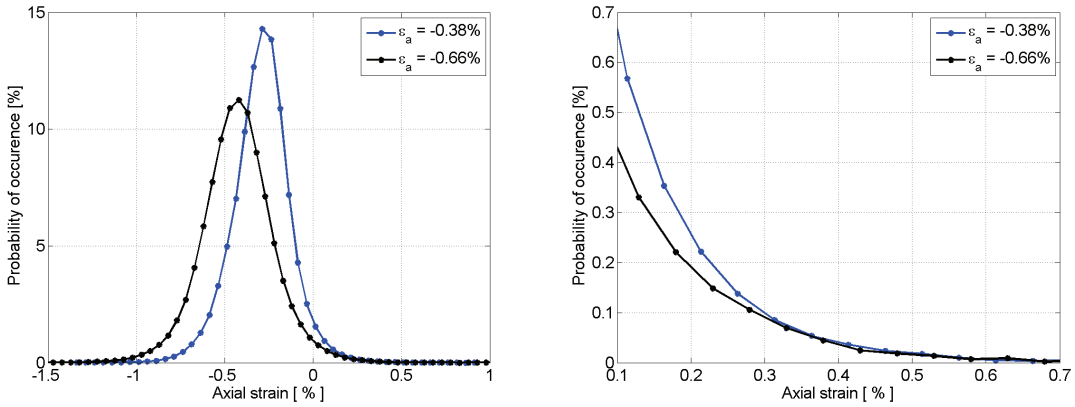

Fig. 5.53. Distribution of the axial strain ε for two different thermal loading, ε_{th} = -0.38 % vs. ε_{th} = -0.66 % but equal Lorentz loading (F_L = 1.35 N/mm). The conductors are both 3x3x4x4.

Regarding the peak strain map of the two conductors, Fig. 5.54 and Fig. 5.55 shows again that the highest strains are situated at the low pressure zone. It appears that the conductor that is the less axially compressed display the highest strain. This is interesting to note that the gap created by the Lorentz loading is greater for the cable which is the less axially compressed. The axial compression protects the cable against the occurrence of tensile strains. As far as the maximum strains are looked at, there is no much difference between the two conductors. The highest strains localize at the low pressure zone and at the core of the cable.

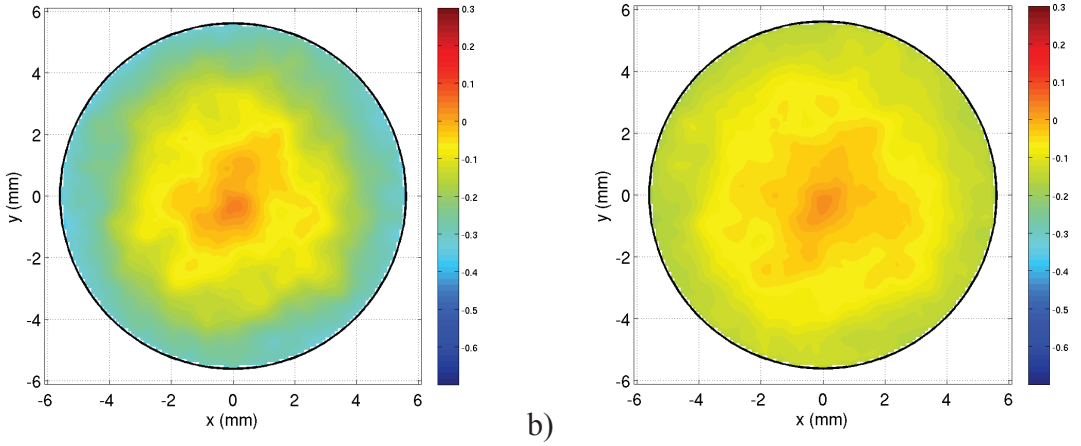

a) b)

Fig. 5.54. Map of the *mean* peak strain ε_p after thermal strain. a) 3x3x4x4 (ε_a = -0.66%). b) 3x3x4x4 (ε_a = -0.38%).

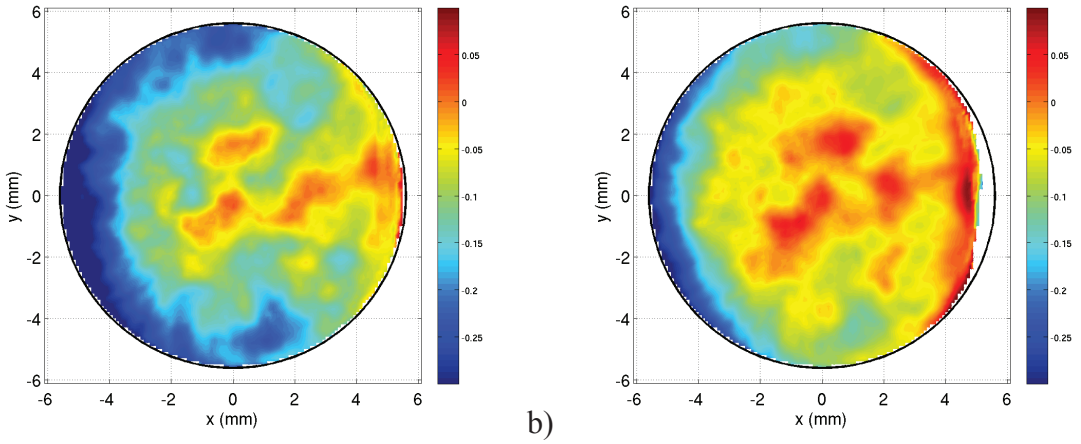

Fig. 5.55. Map of the *mean* peak strain ε_p after the reference Lorentz loading F_L=1.35 N/mm along the x direction. a) 3x3x4x4 (ε_a = -0.66 %). b) 3x3x4x4 (ε_a = -0.38 %).

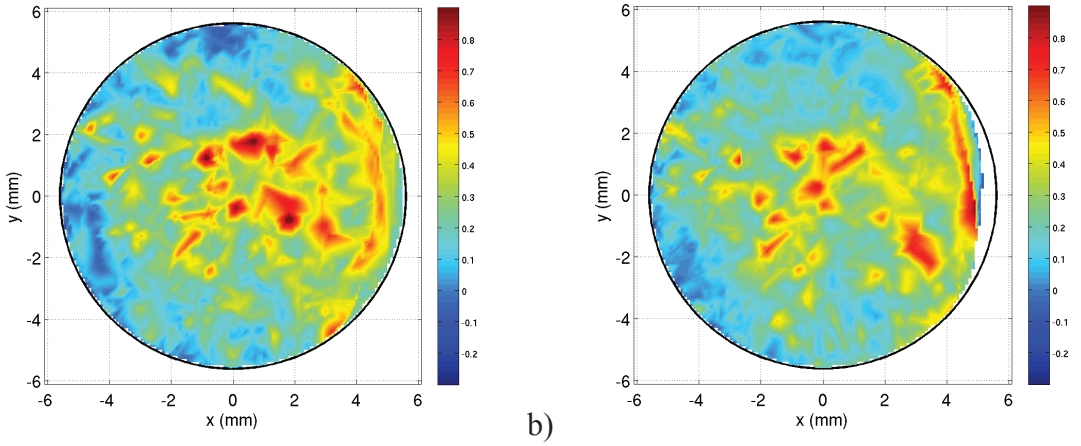

Fig. 5.56. Map of the *max* peak strain ε_p after the reference Lorentz loading F_L=1.35 N/mm along the x direction. a) 3x3x4x4 (ε_{th} = -0.66 %). b) 3x3x4x4 (ε_{th} = -0.38 %).

Fig. 5.57 shows the estimation of the damaged area in the case the crack criterion is ε_c = +0.3%. The conductor that is the most damaged is definitely the one which gets the lowest thermal axial compression with two cross-sections that are entirely broken and four sections that are damaged by more than half. It can be concluded that the pre-compression influences the impact of the Lorenz loading on the local strain state of the strands. Lower compression is detrimental in regard with the generation of critical strains.

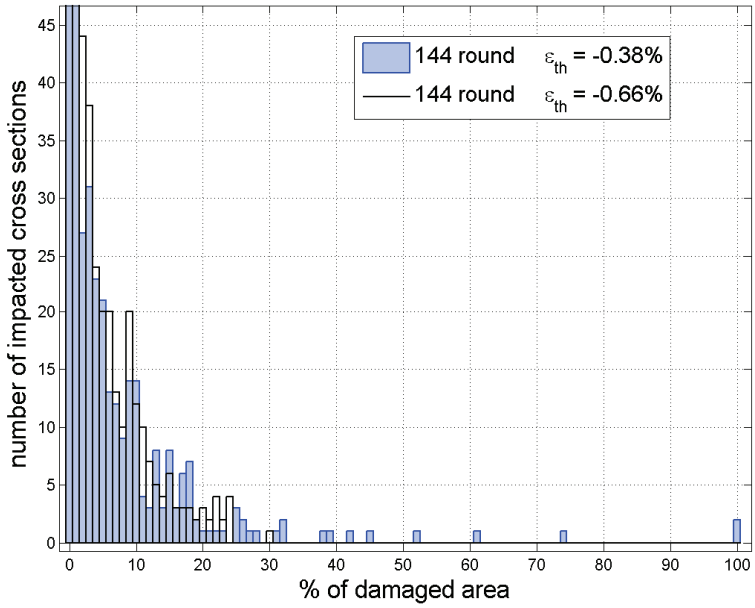

Fig. 5.57. Comparison of distributions of the damaged area for two identical conductor submitted to different axial compression. Both conductor are sustaining identical Lorentz loading F_L = 1.35 N/mm.

4.4 Global comparison of the four tested designs

To conclude about the different tested conductors, Fig. 5.58 displays the computation of the damaged area in the case the crack criterion is ε_c = +0.3 %. None of the conductor sees more than half of the strands cross-section that is damaged. Regarding the percentage of damaged area? the worst conductor would be the petal conductor and the best would be the square conductor.

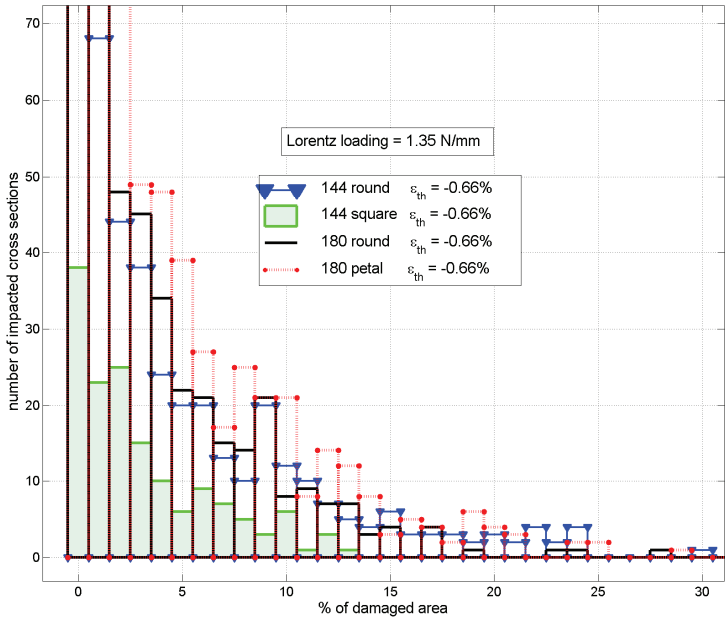

Fig. 5.58. Comparison of the four different conductors regarding the estimation of the damaged area distributions. The distribution shows that the petal conductor exhibits the greatest number of impacted sections whereas the square conductor gets the lowest number. At maximum, 30 % of the beam section can be damaged.

5 Question about the impact of the pinching

In this part, the amplitudes of the contact loads are analyzed. The purpose is to determine whether the contact loads that are generated by the thermal axial compression and the Lorentz loading are sufficient to cause any electrical loss. In Chapter I 1.3.2, it is indicated that from the TARSIS crossing strand experiment, a contact pressure greater than 100 MPa is causing irreversible current degradation. In this experiment, the strands are crossing at an angle of 90°. Such an angle is a limit case in the sense that in a cable the angles between strands are generally much lower.

5.1 Directions of the contact forces

The plots in Fig. 5.59 illustrate the various possible orientations of the contact loads in the conductor after the reference thermal strain and after the Lorentz loading. Their amplitudes may differ, but greater loads are found at the so-called high pressure zone.

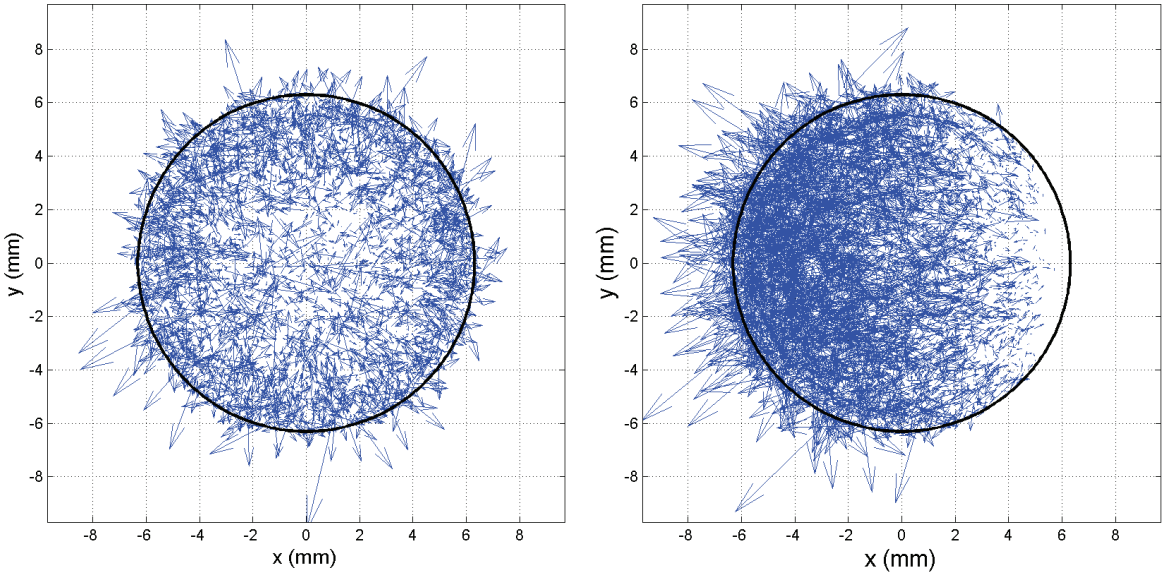

Fig. 5.59. Plot of the contact loads vectors across the conductor sections. a) After the reference thermal strain ε_{th} = -0.66%. b) After the reference Lorentz loading F_L=1.35 N/mm along the x direction.

5.2 Map of the contact forces

For the generation of the contact amplitude map of the conductor, the contact load can be post-treated using the same method as the one developed for the axial strains. It is possible to produce a map of the contact load across a typical conductor cross-section. Instead of using the finite element nodes (x, y, z, ε_p) as input of the Matlab routine, the contact points are chosen (x, y, z, f_c). In that case, f_c is taken as the norm of the contact force vectors. Fig. 5.60 shows the result right after the axial compression and after two different Lorentz loading, saying F_L = 0.89 & 1.35 N/mm. The plot indicates the accumulation of the contact loads in the direction of the Lorentz loading.

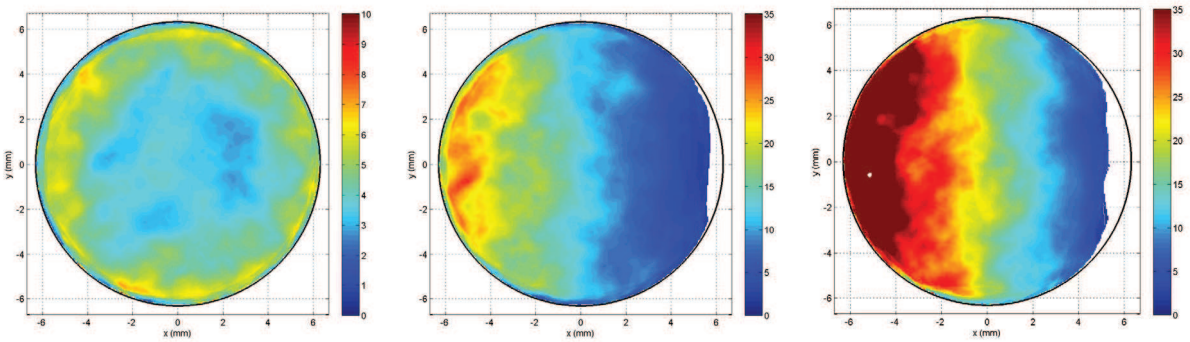

Fig. 5.60. Conductor map of the contact loads for three different Lorentz loadings: 0, 0.89 and 1.35 N/mm. The amplitudes of the forces (N) linearly vary across the conductor section.

5.3 Distributions of contact pressures

The contact loads measured by the contact elements of a proximity zone can be summed and divided by the length of the zone to get an equivalent line force. To get a pressure, it would be necessary to have access to the local width of the contact zone. Since the simulation does not allow this width to be computed, the diameter of the strand is taken as an arbitrary dimension to calculate the pressure. The presented pressures are thus obtained by dividing the lineic contact force by the strand diameter. The distributions of the contact pressureS are shown in Fig. 5.61 for four different applied Lorentz loadings (0, 0.89, 1.35 and 1.71 N/mm) in the case of the 3x3x5x4 round conductor. The plots indicate that most of the values lie between 0 and 40 MPa. However, the distribution tails are broad and reach up to 140 MPa which exceed the critical 100 MPa assigned by the TARSIS experiment.

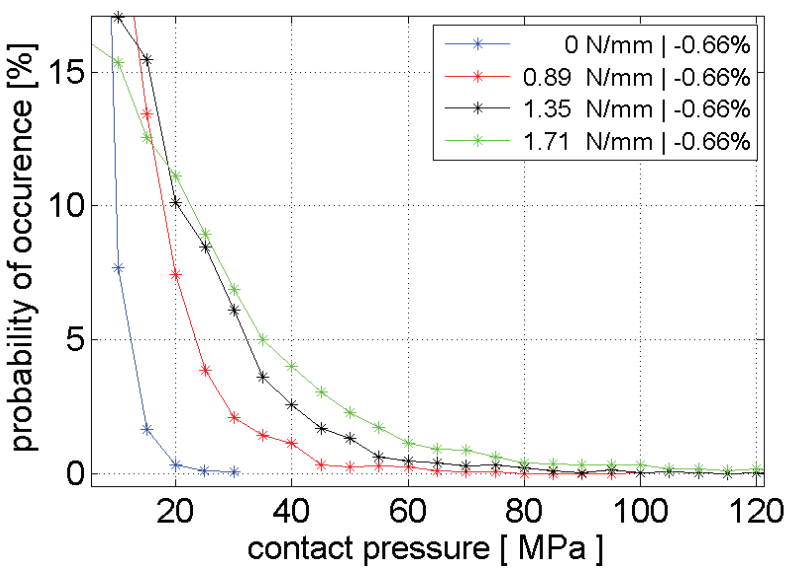

Fig. 5.61. Evolution of the contact pressure along the Lorentz loading.

6 Coupling with electromagnetic codes

During this thesis, the Multifil mechanical approach of conductor has been interfaced with two different electromagnetical codes These two dedicated codes, CARMEN (**C**oupled **A**lgorithm for **R**esistive **M**odeling of **E**lectrical **N**etworks) and JackPot (Jacket Potential) are presented in detail in [Zani 2007-09], [van Lanen 2010]. The codes are able to simulate the *V-I* and the *V-T* tests of sub-size and full-size conductors. Both models consider the conductor as

a three dimensional network of electrical resistances of two kinds, respectively standing for the contact resistances between the strands (that follows the ohmic law) and the superconducting behavior of the Nb_3Sn strand (that follow the $I_c(B,T,\varepsilon)$ law). The system is then solved using the Kirchoff laws. The magnetic and temperature fields are known from measurements but the strain should be assessed. Since the variations of the axial strain along and across the strands are not known, an average axial strain was only considered, as computed from the smeared model. The models suffer from the approximations made on the trajectories of the strands and the positions of the contact points. The contribution of Multifil to the electromagnetic codes is then simple. The Multifil output data gives the trajectories of strands within the conductor, the strains across the sections of the strands and the positions of the contacts points with their corresponding contact loads. The data are ordered in exchangeable files for the interface with the other codes.

The coupled simulations of CARMEN and Multifil have been performed on 45 strand cables with encouraging results published in [Torre 2010]. The simulation corresponds to the *Saman experiment* that is dedicated to measure the overall critical current of ITER sub-size conductors (triplet, 3x3, 3x3x5, 3x3x4x5) as a function of a tensile loading, described in [Vostner 2005], [Weiss 2007]. The stretching of the conductor aims to determine the $I_c(\varepsilon)$ curve as it is usually done for single strand – see Fig. 1.13. The Multifil simulation consists to submit the conductor to an axial compression (the cool-down) that is followed by the tensile test (the stretching) with regular applications and releases of the Lorentz force loading. Since the current evolves along the stretching, the Lorentz force loading should also increase. The amplitude of the force to apply in Multifil comes from the experimental measurements of the current for a constant field of 12T. Two models of cables are considered that correspond to the Saman n°11 which is entirely superconducting whereas the Saman n°14 contains one third of copper wire. The cables are 75mm long which is the length of the high field zone in the Saman test facility. The result of the simulation in terms of the evolution of the axial strain distributions with the loadings in presented in Fig. 5.62, from [Torre 2010]. The CARMEN computation of the critical current along the loading is presented in Fig. 5.63.

The Multifil results have allowed the experimental curves $I_c(\varepsilon)$ to be rescaled according to the mean axial strain $<\varepsilon>$ and no more on the applied axial strain. This rescaling highlights why the critical current of the conductor could exceed the $I_c(\varepsilon)$ of the single strands in the previous Saman results interpretation. However, the present models are still not explaining the large degradation of the properties of the Saman 11, even though the behavior of the Saman 14 (with much less degraded properties) is quite close to the experimental curve when low transverse resistivity (LTP) is used to depict the effect of the bending on the current transfer.

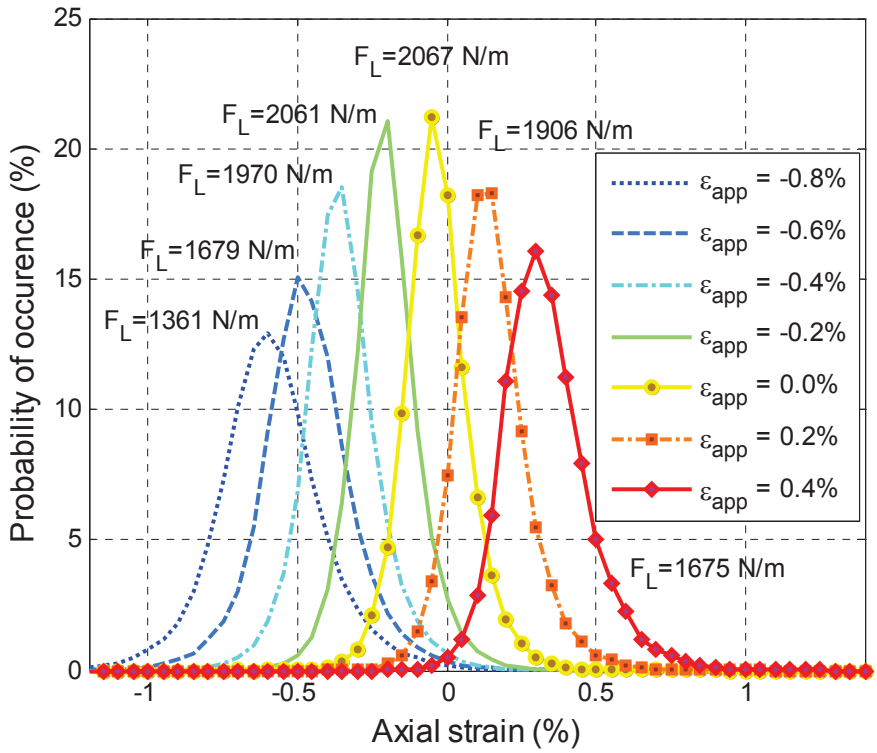

Fig. 5.62. Distributions of the local axial strains in the strands of the 3x3x5 conductor (Saman n11). The conductor is initially axial compressed up to -0.8 % and then stretched up to a total strain of 1.2%. The Lorentz force loading is applied and released every 0.2 %, according to the experimentally measured current critical current for a magnetic field of 12 T.

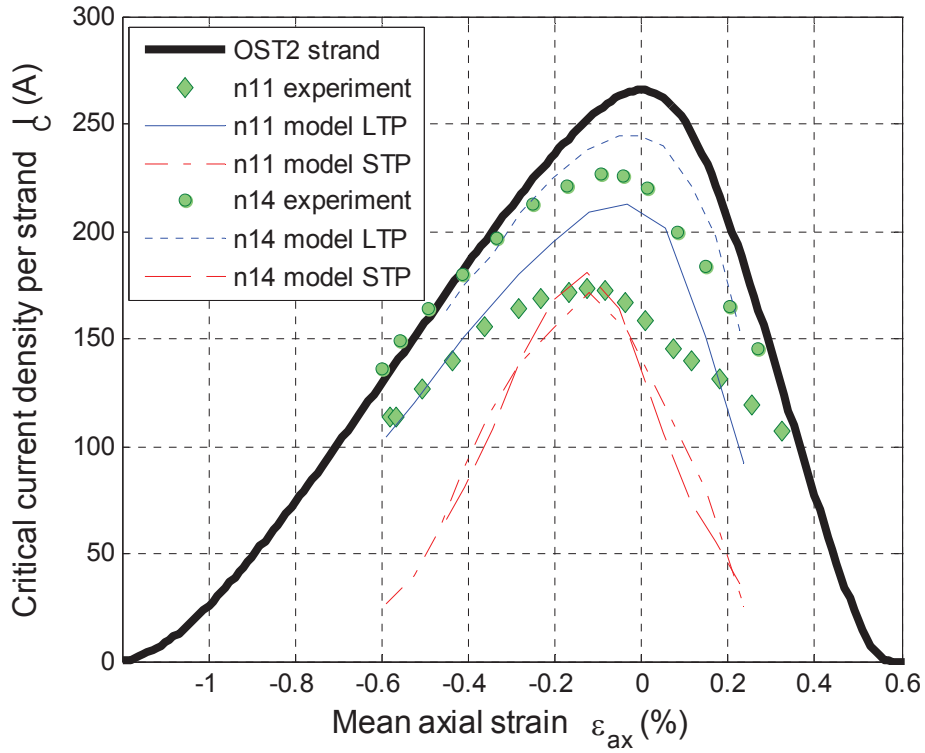

Fig. 5.63. Results of the CARMEN electrical code for the computation of critical current of the 3x3x5 conductor using the Multifil mechanical results for the axial strains along the strands of the cable. The cable I_c ($<\varepsilon>$) curves are compared with the single strand behavior.

Conclusion

The objectives for the thesis were to provide for an accurate description of the deformations occurring at the scale of the strands that may be responsible for degradation of conductivity properties in superconducting cable-in-conduit conductor subjected to the various loadings. Different approaches have been carried out to meet these objectives, both from an experimental and a numerical viewpoint. Two kinds of experimental investigations have been conducted during this thesis. The first ones were directed to identify the mechanical behavior of various wires that compose the conductors, in response to the loadings in the longitudinal and transverse directions. Experimental tests in longitudinal direction identified the cyclic constitutive laws of the considered materials and described cyclic hardening with proper functions. Transverse compression tests performed on two crossing wires showed an apparent linearity of the response on the loading path, even though large plastic strains of cross-sections were induced in the crossing zone.

In parallel, investigations through SEM microscopy have been conducted to observe breakage at the scale of microfilaments inside the strands caused by the applied loadings. These investigations confirmed previously established criteria for crack initiation, but also revealed interesting bending mechanisms at the scale of the strand that could be at the origin of degradations in the case of pinching loading.

Most of the effort focused on the improvement of the simulation code and the development of simulations with more realistic loadings, on a wide variety of cases, to better analyze and understand the underlying mechanisms responsible for electrical property degradation.

New transverse boundary conditions, referred to as the pseudo-periodic conditions have been developed and implemented in the code to tackle the problem of considering only a portion of limited length of the conductor and to limit the influence of the end effects, even if the layout of the conductor is not periodic. A parametric study about the influence of the penalty parameter used to account for this condition and about the length of the considered sample shows that these new boundary conditions have a satisfactory domain of validity. These new boundary conditions allow the initial forming to be simulated for a wide range of conductors in order to compute their a priori unknown initial configuration.

New constitutive laws, describing in particular the evolution of hardening identified on cyclic tensile tests, have been implemented to reproduce the axial behavior of the different materials constituting the wires of the conductors. The simulation of the mechanical response of a real conductor to cyclic axial loading was made possible by these new constitutive laws, with a good agreement between experimental data.

Additional difficulties arose regarding the transverse behavior of conductors. The limits of the current beam model employed in Multifil are reached as soon as the loading is likely to cause pinching of strands because only uniform transverse deformations of cross-sections can be considered. Nevertheless, transverse deformations of cross-sections could be taken into account using an elastic transverse isotropic model, with a transverse stiffness corresponding to the apparent transverse stiffness identified upon the transverse compression experiment between crossing wires. To reproduce the results of the transverse experiment performed on a 45 strand conductor, it appeared necessary to consider an initial pinching of wires caused by the forming process. With the help of the apparent transverse stiffness and the consideration of the initial pinching, the obtained numerical results are in good agreement with

experimental data, accounting for the complex mechanisms involved in the cyclic transverse compression experiment.

Complete simulations of the successive loadings encountered during the conductor service-life, from the initial shaping to the application of the magnetic loading forces, have been finally conducted for different conductors. Post-treatment tools have been developed to analyze the Multifil output data in order to characterize the occurrence of critical strains possibly responsible for conductivity losses. The quantification of these critical strains may help to discriminate different conductor designs.

The analysis of axial strains in terms of pure axial and bending strain brings a better understanding of the global behavior of conductors. It can be seen, in particular, that the global axial compression caused by the thermal loading, results in an inhomogeneous distribution of strains in conductor cross-sections, with the conversion of a part of the global compression into bending strains at the scale of strands. This inhomogeneous distribution and the conversion of part of the global compression into local bending are two important results of the presented simulations that question some of the previously accepted assumptions.

The trajectories of the strands in the conductor, the description of the contact interactions between strands and the determination of the axial strains at any point of the strands are standard results from Multifil. These data can be easily retrieved by the electrical simulation codes to model the distribution of current in the loaded strands of the conductor, taking into account the dependence of local conductivity on the local strains. This coupling between the mechanical behavior computed by Multifil with the simulation of the electrical behavior is a first step to assess the conductivity of cable-in-conduit conductors subjected to a wide range of loadings.

During this thesis, the conducted studies have also emphasized some limits of the models currently used in Multifil, particularly regarding the representation of the transverse mechanical behavior of the beam model. An enrichment of the kinematical beam model, with a corresponding increase of the computational cost, could be envisaged to describe in more details the actual deformations of cross-sections, and to make the model able to account for plastic effects in transverse directions.

Even though improvements are still needed on particular points, the model provides a large amount of data that are still to be analyzed to get a deeper understanding of mechanisms responsible for conductivity losses in conductors. Parametric studies on design parameters should help optimizing the conductors' electrical performances.

References

[Arbelaez 2009] – D. Arbelaez, A. Godeke and S.O. Prestemon. *An improved model for the strain dependence of the superconducting properties of Nb_3Sn*. Supercond. Sci. Technol., 22, (2009), 025005

[Bajas 2010] – Bajas, H. Durville, D. Ciazynski, *et al. Numerical Simulation of the Mechanical Behavior of ITER Cable-In-Conduit Conductors*. IEEE Trans. Appl. Supercond., (2010), vol. 20, n°3

[Boso 2005 a] – D Boso, M. Lefik, B.A. Schrefler. *A multilevel homogenised model for superconducting strand thermomechanics*. Cryogenics, 45 (2005) 259–271

[Boso 2005 b] – D.P. Boso, M. Lefik, B.A. Schrefler. *Multiscale analysis of the influence of the triplet helicoidal geometry on the strain state of a Nb_3Sn based strand for ITER coils*. Cryogenics 45 (2005) 589–605

[Boso 2009] – D Boso , M. Lefik. *A thermo-mechanical model for Nb_3Sn filaments and wires: strain field for different strand layout*. Supercond. Sci. Technol., 22, (2009), 125012

[Bottura 2008] – L. Bottura. *Jc (B,T,e) parameterization for the ITER Nb_3Sn production*. Iter Organization internal communication

[Bottura 1995] – L. Bottura. *Numerical aspects in the simulation of thermohydraulic transients in CICCs.* Journal of Fusion Energy, Volume 14, Number 1, 13-24, DOI: 10.1007/BF02214030

[Bruzzone 2003] – P. Bruzzone, R. Wesche, B. Stepanov. *The Voltage/Current Characteristic (n Index) of the Cable-in-Conduit Conductors for Fusion*. IEEE Trans. Appl. Supercond., (2003), vol. 13, n°2, pp. 1452-1455

[Bruzzone 2004] – P. Bruzzone. *The index n of the voltage–current curve, in the characterization and specification of technical superconductors*. Physica C, 401 (2004) 7–14

[Bruzzone 2006] – P. Bruzzone, B. Stepanov, E. Zapretilina. *A Critical Review of Coupling Loss Results for Cable-in-Conduit Conductors*. IEEE Trans. Appl. Supercond., (2006), vol. 16, n°2

[Bruzzone 2007] – P. Bruzzone, M. Bagnasco, D. Ciazynski, *et al. Test Results of Two ITER TF Conductor Short Samples Using High Current Density Nb_3Sn Strands*. IEEE Trans. Appl. Supercond., (2007), vol. 17, n°2

[Bruzzone 2008] – P. Bruzzone, B. Stepanov. *Results of a new generation of ITER TF Conductors samples in SULTAN*. IEEE Trans. Appl. Supercond., (2008), vol. 18, n°2

[Bruzzone 2009 a] – P. Bruzzone, B. Stepanov, R.Wesche. *Qualification tests for ITER TF conductors in SULTAN.* Fusion Engineering and Design 84 (2009) 205-209

[Bruzzone 2009 b] – P. Bruzzone, B. Stepanov, R.Wesche. *Test results of a Nb_3Sn CICC with variable pitch sequence.* IEEE Trans. Appl. Supercond., (2009), vol. 19, n°3

[Cheggour 2002] – N. Cheggour, D. P. Hampshire. *The unified strain and temperature scaling law for the pinning force density of bronze route Nb_3Sn wires in high magnetic fields*. Cryogenics, 42 (2002) 299–309

[Cheggour 2010] – N Cheggour, L.F. Goodrich, T. C. Stauffer, *et al. Influence of Ti and Ta doping on the irreversible strain limit of ternary Nb_3Sn superconducting wires made by the restacked-rod process*. Supercond. Sci. Technol., 23, (2010), 052002

[Ciazynski 1985] – D. Ciazynski. *Transient current distribution inside asuperconducting composite subjected to a fast changing magnetic field.* Proc. 9th Int. Conf. on Magn. Technol., pp 605–8

[Ciazynski 1985] – D. Ciazynski. *Distributions de courant et pertes à l'intérieur d'un composite multifilamentaire supraconducteur soumis a un champ magnétique variable.* Thesis Presented at University Pierre et Marie Curie, Paris 6

[Ciazynski 2000] – Ciazynski D, Duchateau J L, Schild T and Fuchs A M. *Test results and analysis of two European full-size conductor samples for ITER.* IEEE Trans. Appl. Supercond., (2000), vol. 10, n°1, pp. 1058–61

[Ciazynski 2007] – D. Ciazynski. *Review of Nb_3Sn conductors for ITER*.Fusion Engineering and Design, 82, 488–497, 2007

[Ciazynski 2008] – D. Ciazynski, L. Zani, P. Bruzzone, *et al. Influence of cable layout on the performance ITER-type Nb_3Sn conductors.* Journal of Physics: Conference Series 97, (2008), 012027

[Ciazynski 2010] – D Ciazynski, A Torre. *Analytical formulae for computing the critical current of an Nb_3Sn strand under bending*. Supercond. Sci. Technol., 23, (2010), 125005

[Dresner 1995] – L. Dresner. *Twenty years of cable-in-conduit conductors: 1975–1995*. Journal of Fusion Energy, Volume 14, Number 1, 3-12

[Duchateau 2002] – J.L. Duchateau. *Cryoélectricité des courants forts. Câbles en conduit supraconducteurs*. Techniques de l'ingénieur, RE10, 2002

[Duchateau 2004] – J.L. Duchateau, D. Ciazynski, O. Guerber, *et al. Exploring the limits of a very large Nb_3Sn conductor: the 80 kA conductor of the International Thermonuclear Experimental Reactor toroidal field model coil*. Supercond. Sci. Technol., 17, (2004), S241–S249

[Durville 2003] – D. Durville, Numerical simulation of the mechanical behaviour of textile structures at a mesoscopic scale. Structural Membranes 2003, Textile composites and inflatable structures, E. Oñate and B. Kröplin (Eds.), CIMNE, Barcelona, Spain, 310–315, (2003)

[Durville 2004] – D. Durville, *Modelling of contact-friction interactions in entangled fibrous materials*, Computational Mechanics, WCCM VI, Sept 5-10 2004, Beijing, China, 2004.

[Durville 2005] – D. Durville, *Numerical simulation of entangled materials mechanical properties*. Journal of Materials Sciences, vol. 40, no. 22, 5941–5948, 2005.

[Ekin 1978] – J. Ekin. *Current transfer in multifilamentary superconductors.* Theory J. Appl. Phys., (1978), 49 3406–9

[Ekin 1980] – J. Ekin, M. Suenaga, M. Clark. *Strain scaling law and the prediction of uniaxial and bending strain effects in multifilamentary superconductors*. Filamentary A15 Superconductors Plenum Press, New York, USA (1980), 187-203

[Ekin 1980] – J. Ekin. *Strain scaling law for flux pinning in practical superconductors: Part 1. Basic relationship and application to Nb_3Sn conductors*; Cryogenics, (1980), 20, 611

[Ekin 1981] – J. Ekin, S. Foner , B.B. Schwartz. *Mechanical properties and strain effects in superconductors*. Superconducting Materials Science: Metallurgy Fabrication and Applications Plenum Press, New York, USA (1981) 455-510

[Ekin 1987] – J. Ekin. *Effect of transverse compressive stress on the critical current and upper critical field of Nb_3Sn*. Journal of Applied Physics, 62, 4829-4834, (1987)

[Ekin 2006] – J. Ekin. *Experimental Techniques for Low-Temperature Measurements: Cryostat Design, Material Properties and Superconductor Critical-Current Testing*. Oxford Univ Pr

[Fisher 2002] – C. Fischer, P. Lee, D. Larbalestier. *Irreversibility field and critical current density as a function of heat treatment time and temperature for a pure niobium Powder-in-Tube Nb_3Sn conductor.* Adv. Cryogenic Eng., 48(B):1008–15, 2002

[Godeke 1999] – Godeke, A.; ten Haken, B.; ten Kate, H.H.J. *Scaling of the critical current in ITER type niobium-tin superconductors in relation to the applied field, temperature and uni-axial applied strain*. IEEE Trans Appl Supercond., (1999), vol. 9, n°. 2, pp. 161-164

[Godeke 2004] – A. Godeke, M. Dhalle, A. Morelli, *et al.A device to investigate the axial strain dependence of the critical current density in superconductors*. Review of scientific instrument, vol. 75, n°12, 2004

[Godeke 2005 a] – A. Godeke. *Performance boundaries in Nb_3Sn conductors*. PhD Thesis University of Twente, Enschede, The Netherlands, 2005

[Godeke 2005 b] – A. Godeke, B. ten Haken, H.H.J. ten Kate. *The deviatoric strain description of the critical properties of Nb_3Sn conductors.* Physica C, 372–376, (2002), 1295–1298

[Godeke 2005 c] – A. Godeke, M. C. Jewell, C. M. Fischer, *et al.The upper critical field of filamentary Nb_3Sn conductors.* J. Appl. Phys., 97, 093909, (2005)

[Ilyin 2006] – Y. Ilyin, A. Nijhuis A, J. Wessel, *et al*. *Axial Tensile Stress-Strain Characterization of a 36 Nb_3Sn Strands Cable*. IEEE Trans. Appl. Supercond., (2006), vol. 16, n°2, pp. 61-1890.

[Ilyin 2007 a] – Y. Ilyin, A. Nijhuis, E. Krooshoop. *Scaling law for the strain dependence of the critical current in an advanced ITER Nb_3Sn strand*. Supercond. Sci. Technol., 20, (2007), 186–191

[Ilyin 2007 b] – Y. Ilyin, A. Nijhuis. *Review of Current Distribution Measurements and Reconstruction in Cable-in-Conduit Conductors for ITER*. IEEE Trans Appl Supercond., vol. 17, n°2, pp. 1465

[Jewell 2003] – M.C. Jewell, P. Lee, D. Larbalestier. *The influence of Nb_3Sn strand geometry on the filament breakage under bend strain as revealed by metallography.* Supercond. Sci. Technol., 16, 1005

[Jewell 2004] – M.C. Jewell, A. Godeke, P. Lee, *et al.The upper critical field of stoichiometric and off-stoichiometric bulk, binary Nb_3Sn.* Adv. Cryogenic Eng., 50(B):474–81, 2004

[Jewell 2008] – M.C. Jewell. *The effect of strands architecture on the fracture propensity of Nb_3Sn composite wires.* PhD thesis for the University of Wisconsin, Madison, 2008

[Kato 2001] – T. Kato, H. Tsuji, T. Ando, *et al. First test results for the ITER central solenoid model coil.* Fusion Engineering and Design, 56–57, (2001), 59–70

[Lee 2000] – P. Lee, A. Squitieri, D. Larbalestier.*Nb_3Sn: macrostructure, microstructure, and property comparisons for bronze and internal Sn process strands.* IEEE Trans. Appl. Supercond., (2000), Vol. 10, n°1, 979–82,

[Lee 2001] – P. Lee, D. Larbalestier. *Compositional and microstructural profiles across Nb_3Sn filaments produced by different fabrication methods.* IEEE Trans. Appl. Supercond., (2001), vol. 11, n°1, pp. 3671–4

[Lee 2005 a] – P. Lee, D. Larbalestier. *The microstructure and microchemistry of high critical current Nb_3Sn strands manufactured by bronze, Internal Sn and PIT technique*. IEEE Trans. Appl. Supercond., (2005), vol. 15, n°2, pp. 3474–7

[Lee 2005 b] – P. Lee, D. Larbalestier. *Microstructural and Microchemical Homogeneity for High Critical Current Density in Nb_3Sn.* National Institute For Materials Science, 0, 1-8 (2005)

[Lee 2008] – P. Lee, D. Larbalestier. *Microstructural factors important for the development of high critical current density Nb_3Sn strand.* Cryogenics (2008), vol. 48, n^o 7-8, pp. 117

[Lemaître Chaboche 1988] – J. Lemaître J., J.L. Chaboche, *Mécanique des matériaux solides*. Dunod, *1988*

[Libeyre 2009] – P. Libeyre, N. Mitchell, D. Bessette, *et al. Detailed design of the ITER central solenoid.* Fusion Engineering and Design, (2009), 84, 1188–1191

[Markiewicz 2002] – W. Markiewicz, R. Goddard. *Bronze Tin Content and Grain Size in Nb_3Sn Composite Superconductors.* IEEE Trans Appl Supercond., (2002), vol. 12, n°. 1.

[Martovetsky 2004] – N. Martovetsky. *ITER Model Coil tests overview: Nb_3Sn strand properties in cable-in-conduit conductors.* Physica C, 401, (2004), 22–27

[Martovetsky 2005 a] – N. Martovetsky, P. Bruzzone, B. Stepanov, *et al. Effect of Conduit Material on CICC Performance Under High Cycling Loads.* IEEE Trans Appl Supercond., (2005), vol. 15, n°. 2, pp. p. 1367-1370

[Martovetsky 2005 b] – N. Martovetsky. *Stability and design criterion for cable-in-conduit-conductors with a broad transition to normal state*. Fusion Engineering and Design, 75–79, (2005), 215–219

[Mitchell 1999] – N. Mitchell. *Analysis of non-uniform current distribution effects in multistage cable-in-conduit conductors.* Cryogenics, (1999), 39, 539–556

[Mitchell 2000 a] – N. Mitchell. *Steady state analysis of non-uniform current distributions in cable-in-conduit conductors and comparison with experimental data*. Cryogenics, (2000), vol. 40, n°2, pp. 99-116

[Mitchell 2000 b] – N. Mitchell. *Steady state analysis of non-uniform current distributions in cable-in-conduit conductors and comparison with experimental data*. Cryogenics, (2000), vol. 40, pp. 99-116

[Mitchell 2001] – N. Mitchell, E. Salpietro. *ITER R&D: Magnets: Toroidal Field Model Coil*. Fusion Engineering and Design, 55, (2001), 171–190

[Mitchell 2002] – N. Mitchell. *Analysis of the effect of the Nb_3Sn strand bending on CICC superconductor performance.* Cryogenics, 42, 311–325, 2002

[Mitchell 2003 a] – N. Mitchell. *Mechanical and magnetic load effects in Nb_3Sn cable-in-conduit conductors*. Cryogenics, 43, 255–270, 2003

[Mitchell 2003 b] – N. Mitchell. *Summary, assessment and implications of the ITER model coil test results*. Fusion Engineering and Design 66 /68 (2003) 971 /993 2003

[Mitchell 2004] – N. Mitchell. *Two-way interaction between the strand voltage–current characteristic and the overall conductor behaviour in cabled low temperature superconductors*. Physica C, 401, 28–39, 2004

[Mitchell 2005 a] – N. Mitchell. *Finite element simulations of elasto-plastic processes in Nb_3Sn strands*. Cryogenics, 45, 501–515, 2005

[Mitchell 2005 b] – N. Mitchell. *Modelling of the Effect of Nb_3Sn Strand Composition on Thermal Strains and Superconducting Performance*. IEEE Trans. Appl. Supercond., (2005), vol. 15, n^o 2, pp. 1380

[Mitchell 2005 c] – N. Mitchell. *Operating strain effects in Nb_3Sn cable-in-conduit conductors*. Supercond. Sci. Technol., 18, (2005), S396–S404

[Mitchell 2006] – N. Mitchell. *Quality control in the design, fabrication and operation of the ITER magnets*. Fusion Engineering and Design, 81, (2006), 2325–2339

[Mitchell 2008] – N. Mitchell, D. Bessette, R. Gallix, *et al. The ITER Magnet System*. IEEE Trans Appl Supercond., (2008), vol. 18, n°2

[Mitchell 2008] – N. Mitchell. *Comparison between predictions and measurements of the superconducting performance of Nb_3Sn cable in conduit conductors with transverse load degradation*. Supercond. Sci. Technol., 21, (2008), 054005, (9pp)

[Mitchell 2009] – N. Mitchell, P. Bauer, D. Bessette, *et al. Status of the ITER magnets*. Fusion Engineering and Design, 84, (2009), 113–121

[Miyoshi 2009] – Y Miyoshi, E P A van Lanen, M M J Dhall´e, *et al. Distinct voltage–current characteristics of Nb_3Sn strands with dispersed and collective crack distributions*. Supercond. Sci. Technol., 22, (2009), 085009, (7pp)

[Mizoguchi 2001] – T. Mizoguchi, N. Mitchell. *ITER R&D: Magnets: Introduction*. Fusion Engineering and Design, 55, (2001), 139–140

[Naus 2002] – M.T. Naus. *Optimization of internal-Sn Nb_3Sn composites*. PhD thesis, The University of Wisconsin-Madison, 2002.

[Nevov 2010] – A.S. Nemov, D.P. Boso, I.B. Voynov, A.I. Borovkov, B.A. Schrefler. *Generalized stiffness coefficients for ITER superconducting cables, direct FE modeling and initial configuration*. Cryogenics, 50, (2010), 304–313

[Nijhuis 2004 a] – A. Nijhuis A, Y. Ilyin, W. Wessel, *et al. Effect of Periodic Cyclic Deformation on the Voltage Current Transition of Nb_3Sn Strands Tested in the Novel 'TARSIS' Setup*. IEEE Trans. Appl. Supercond., (2005), vol. 14, n°2, pp. 1464-1467

[Nijhuis 2004 b] – A. Nijhuis A, Y. Ilyin, W. Abbas, *et al. Performance of an ITER CS1 Model coil conductor under traverse cyclic loading up to 40,000 cycles*. IEEE Trans. Appl. Supercond., (2005), vol. 14, n°2, pp. 1489-1494

[Nijhuis 2005 a] – A. Nijhuis, W. Wessel, H. Knoopers, *et al. Compressive Pre-Strain in Nb_3Sn Strand by Steel Tube and Effect on the Critical Current Measured on Standard ITER Barrel*. IEEE Trans. Appl. Supercond., (2005), vol. 15, n°2, pp. 3466-3469

[Nijhuis 2005 b] – A. Nijhuis A *et al. Impact of void fraction on mechanical properties and evolution of coupling loss in ITER Nb_3Sn conductors under cyclic loading*. IEEE Trans. Appl. Supercond., (2005), vol. 15, n°2, pp. 1633–6.

[Nijhuis 2006 a] – A. Nijhuis A, Y. Ilyin, W. Wessel, *et al. Critical current and strand stiffness of three types of Nb_3Sn strand subjected to spatial periodic bending.* Supercond. Sci. Technol., 19, (2006), 1136–1145

[Nijhuis 2006 b] – A. Nijhuis A, Y. Ilyin, W. Wessel. *Spatial periodic contact stress and critical current of a Nb_3Sn stran measured in TARSIS*. Supercond. Sci. Technol., 19, (2006), 1089–1096

[Nijhuis 2006 c] – A. Nijhuis A, Y. Ilyin. *Transverse load optimization in Nb_3Sn CICC design; influence of cabling, void fraction and strand stiffness;* Supercond. Sci. Technol., 19, (2006), 945–62.

[Nijhuis 2008 a] – A. Nijhuis, Y. Ilyin, H.J.G. Krooshoop, *et al. ITER Nb_3Sn strand bending and strain test program at the University of Twente*; Final Report UT-ITER 2008-2

[Nijhuis 2008 b] – Nijhuis A. *A solution for transverse load degradation in ITER Nb_3Sn CICCs, effect of cabling on Lorentz forces response.* Supercond. Sci. Technol., 21, (2008), 054011

[Nijhuis 2009 a] – A. Nijhuis, Y. Ilyin, W. Abbas, *et al. Summary of ITER TF Nb_3Sn strand testing under axial strain, spatial periodic bending and contact stress.* IEEE Trans. Appl. Supercond., (2009), vol. 19, n°3, pp, 1516-1520

[Nijhuis 2009 b] – A. Nijhuis and Y. Ilyin; *Transverse cable stiffness and mechanical losses associated with load cycles in ITER Nb_3Sn and NbTi CICCs*. Supercond. Sci. Technol., 22, (2009), 055007, (13pp)

[Nunoya 2007] – Y. Nunoya, T. Isono, N. Koizumi, *et al. Development of Strain-Applying Apparatus for Evaluation of ITER Nb_3Sn Strand.* IEEE Trans Appl Supercond., 2007, vol. 17, n°2

[Salpietro 1999] – E. Salpietro, R. Maix, G. Bevilacqua, *et al. The ITER toroidal field model coil (TFMC).* Fusion Engineering and Design, 46, (1999), 151–158

[Summers 1991] – L. Summers, M. Guinan, J. Miller, *et al. A model for the prediction of Nb_3Sn critical current as a function of field, temperature, strain and radiation damage.* IEEE Trans. Magn., (1991), 27, 2041–4

[Taylor 2002] – D. Taylor, S. Keys, D. Hampshire. *Reversible and irreversible effects of strain on the critical current density of a niobium–tin superconducting wire*. Cryogenics, 42, (2002), 109–112

[Taylor 2005 a] – D. Taylor and D. Hampshire. *Properties of helical springs used to measure the axial strain dependence of the critical current density in superconducting wires*. Supercond. Sci. Technol., 18, (2005), 356–368

[Taylor 2005 b] – D. Taylor and D. Hampshire. *The scaling law for the strain dependence of the critical current density in Nb_3Sn superconducting wires*. Supercond. Sci. Technol., 18, (2005), S241–S252

[Taylor 2005 c] – D. Taylor and D. Hampshire. *Relationship between the n-value and critical current in Nb_3Sn superconducting wires exhibiting intrinsic and extrinsic behaviour*; Supercond. Sci. Technol., 18, (2005), S297–S302

[Tixador 1995] – P. Tixador. *Les supraconducteurs*. Collection matériaux Paris, Hermes 1995

[Torre 2010] – A. Torre, H. Bajas, D. Ciazynski, *et al. Mechanical-Electrical Modeling of Stretching Experiment on 45 Nb_3Sn Strands CICCs.* To be published in Trans Appl Supercond., 2010

[Ulbricht 2005] – A. Ulbricht, J.L. Duchateau , W.H. Fietz, *et al.The ITER toroidal field model coil project.* Fusion Engineering and Design, 73, 189–327, 2005

[van den Eijnden 2005] – N. van den Eijnden, A. Nijhuis, Y. Ilyin, *et al. Axial tensile stress-strain characterization of ITER model coil type Nb_3Sn strands in TARSIS*. Supercond. Sci. Technol., 18, (2005), 1523–1532

[van Lanen 2010] – E.P.A. van Lanen, A. Nijhuis. *JackPot: A novel model to study the influence of current non-uniformity and cabling patterns in cable-in-conduit conductors*. Cryogenics, 50, (2010), 139–148

[Vostner 2005] – A. Voster, E. Salpietro, K. Weiss, *et al.The FBI facility – A test rig for critical current measurement on CICC as a function of strain*. Supercond. Sci. Technol., (2005), vol. 1, n°2

[Vostner 2006] – A. Vostner, E. Salpietro. *Enhanced critical current densities in Nb_3Sn superconductors for large magnets.* Supercond. Sci. Technol. 19 (2006) S90–S95

[Weiss 2007] – K. Weiss, J.L. Duchateau, A. Vostner. *Systematic approach to examine the strain effect on the critical current of Nb_3Sn CICC.* IEEE Trans. Appl. Supercond., (2007), vol. 17, n^o 2, pp. 1529

[Wilson 1986] – M.Wilson. *Superconducting Magnets.* Oxford University Press, 1986

[Zani 2007] – L. Zani, D. Ciazynski, A. Torre, P, *et al. Analysis of DC Properties and Current Distribution in TFAS ITER Conductor Samples Using High J_C Nb_3Sn Advanced Strands*. IEEE Trans Appl Supercond., (2007), vol. 17, n^o 2, pp. 1374 - 1377

[Zani 2009] – L. Zani, P-E. Gille, C. Gonzales, *et al. Code Development and Validation Towards Modeling and Diagnosing Current Redistribution in an ITER-Type Superconducting Cable Subject to Current Imbalance*. Fusion Science and Technology, (2009) vol. 56, n°2, pp. 690-694

[Zanino 2000] – L. Savoldi, R. Zanino. *M&M: Multi-conductor Mithrandir code for the simulation of thermal-hydraulic transients in superconducting magnets.* Cryogenics, 2000, 40:179–89.

[Zanino 2003 a] – R. Zanino, L. Savoldi Richard. *Performance evaluation of the ITER Toroidal Field Model Coil Phase I Part 1: current sharing temperature measurement*. Cryogenics, 43, (2003), 79–90

[Zanino 2003 b] – R. Zanino, L. Savoldi Richard. *Performance evaluation of the ITER Toroidal Field Model Coil phase I Part 2: M&M analysis and interpretation*. Cryogenics 43, (2003), 91–100

[Zanino 2003 c] – R. Zanino, N. Mitchell, L. Savoldi Richard. *Analysis and interpretation of the full set (2000–2002) of TCS tests in conductor 1A of the ITER Central Solenoid Model Coil*. Cryogenics, 43, (2003), 179–197

[Zanino 2005] – R Zanino, D Ciazynski, N Mitchell, *et al. Coupled mechanical–electromagnetic–thermal–hydraulic effects in Nb_3Sn cable-in-conduit conductors for ITER.* Supercond. Sci. Technol., 18, (2005), S376–S382

[Zanino 2006] – R. Zanino, L. Savoldi Richard. *A review of thermal-hydraulic issues in ITER cable-in-conduit conductors.* Cryogenics, 46, (2006), 541–555

[Zanino 2008] – R. Zanino, L. Savoldi Richard. *Application of calorimetry to the assessment of the performance of ITER Nb_3Sn TF conductor samples in SULTAN tests.* Supercond. Sci. Technol., 21, (2008), 105004, (12pp)

[Zhai 2008 a] – Y. Zhai and M. Bird. *Florida electro-mechanical cable model of Nb_3Sn CICCs for high-field magnet design*. Supercond. Sci. Technol., 21, (2008), 115010, (15pp)

[Zhai 2008 b] – Y. Zhai and M. Bird. *Modeling of the Performance of Nb_3Sn CICCs for High Field Magnet Design.* IEEE Trans. Appl. Supercond., 2008, vol. 18, n°2

[Zhai 2010 c] – Y. Zhai. *Electro-mechanical modeling of Nb_3Sn CICC performance degradation due to strand bending and inter-filament current transfer*. Cryogenics, 50, (2010), 149–157